SNAPSHOT MULTISPECTRAL OXIMETRY USING IMAGE REPLICATION AND BIREFRINGENT SPECTROMETRY

Javier A. Fernandez Ramos
B.Sc. Physics
School of Physics and Astronomy
College of Science and Engineering
University of Glasgow

This dissertation is submitted for the degree of
Doctor of Philosophy

May 2017

Abstract

This thesis describes the improvements to the image replicating imaging spectrometer (IRIS) and the development of novel applications in the field of oximetry. IRIS is a snapshot multispectral device with a high transmission output and no need of inversion for data recovering, hence, with high signal-to-noise ratio (SNR). IRIS shows great versatility due to the possibility of choosing multiple contiguous or non-contiguous wavelengths inside its free spectral range.

IRIS uses a set of waveplates and Wollaston prisms to demultiplex the spectral information of an object and replicate the image of such object in different wavelengths. The birefringent nature of IRIS means that different wavelengths are separated by the Wollaston prisms with different angles, introducing multiple images of the same object. In addition, the spectral transmission function shows multiple spectral sidelobes that contaminate each IRIS band with light belonging to other wavelengths. These issues can lower the performance of IRIS as a multispectral imaging device. In this thesis, these problems were assessed with the introduction of a filter plate array placed in the image plane of the optical system. This filter array is a set of narrow-band filters (Full Width Half Maximum (FWHM) $= 10 \pm 2$ nm) that removes undesired wavelengths from each IRIS band. Since the spectral transmission of IRIS is replicated along the free spectral range, the filters can be designed to match any of the present spectral lobes in IRIS. The design and fabrication of a filter array enhance the performance of IRIS as a multispectral imaging device: it allows wavelength selection and improves spectral and spatial image quality. The design and manufacture of the corresponding filter holder and camera adapter were critical in terms of offering an easy filter-camera implementation. The filter plate allowed the removal of other dispersed wavelengths by the Wollaston prisms, improving image registration between the set of spectral images created by IRIS, and so, improving the quality of the registered spectral 3-D cube.

The implemented improvements on IRIS allow high quality, calibration-free oximetry using eight different wavelengths optimised for oximetry. Two main experiments were performed: 1) Using an inverted microscopy interfaced with IRIS and a linear spectral unmixing technique, we measured the deoxygenation of single horse red blood cells (RBC) *in vitro* in real time. The oximetry was performed with a subcellular spatial resolution of $0.5\,\mu$m, a temporal resolution of 30 Hz, and an accuracy (standard error of the mean) of $\pm 1.1\%$ in oxygen saturation. 2) Eight-wavelength calibration-free retinal oximetry performed in nine

healthy subjects demonstrated an increase in the stability of the oxygen saturation measurements along retinal vessels when compared with more traditional analysis methods such as two wavelengths oximetry. The stability was measured as the standard deviation along the retinal vessels of the nine subjects and was found to be $\sim 3\%$ in oxygen saturation for eight-wavelengths oximetry and $\sim 5\%$ in oxygen saturation for two-wavelengths oximetry.

A modified physical model was used to improve the characterization of light propagation through the eye, retina, and blood vessels by applying a set of feasible physiological assumptions. This model was optimised by an algorithm which solves for the different variables involved in the retinal vessels transmissions in order to accurately calculate the oxygen saturation. The oximetry algorithm was applied in retinal vessels, in collaboration *in vivo* on rat spinal cord to assess hypoxia in inflammatory diseases such as multiple sclerosis and rheumatoid arthritis and on mice legs to assess hypoxia on autoimmune diseases.

A third experiment using a microscope interfaced with IRIS was performed. The experiment aimed to replicate laminar flow conditions observed in retinal vessels and to calculate oxygen diffusion between adjacent streams of blood with different oxygen saturation. For this purpose a PDMS multichannel flow cell with cross sections of 40x100 μm was designed and fabricated allowing us to replicate conditions found in retinal blood vessels. Laminar flow was replicated but the experiment failed in calculating oxygen diffusion due to flaws in the experiment. The experiment with the results and recommendations on how to improve it can be found in Apendix B for future researchers

Acknowledgements

This work has been funded by SUPA, I am grateful to this organisation for making this research possible.

I would like to thank my supervisor Professor Andrew Harvey for his guidance and helpful discussions on this research.

I would also like to thank all my research group colleagues for all their provided help, feedback and good times, especially on off-topic discussions that made the research to be more enjoyable.

I would also like to thank my family and friends back in Spain for their support from the distance. Finally, thanks to Laura for her understating and unconditional support.

Declaration

I hereby declare that the contents of this dissertation are original and have not been submitted for consideration of any other degree or qualification in this or any other University. This dissertation also includes work performed in collaboration with other researchers. Laurence R. Brewer[1] collaborated in Chapters 2, 3 and Appendix B , where his parts are acknowledged in the main text of the respective chapters. David Bragason[2] and Marc Rodriguez[3] collaborated in Appendix B providing the original idea and experimental equipment respectively.

Javier A. Fernandez Ramos
B.Sc. Physics
May 2017

[1]SUPA Advanced Fellow, School of Physics and Astronomy, University of Glasgow
[2]Ophthalmology, University of Iceland/Landspitali University Hospital, Reykjavik, Iceland
[3]WestCHEM, School of Chemistry, University of Glasgow, University Avenue, Glasgow G12 8QQ, UK

Contents

List of Figures

List of Tables

Nomenclature

Roman Symbols

A-V Arteriovenous difference

A-V Arteriovenous difference

ALI Advance Land imager

AVIRIS Airborne Visible/Infrared Imaging Spectrometer

BGA Blood Gas Analyser

CASSI Coded Aperture Snapshot Spectral Imager

cSLO Confocal Scanning Laser Ophthalmoscope

CTIS Computer Tomography Imaging Spectrometer

CW Central Wavelength

EVR Extravascular Light Reflection

FEP Fluorinated Ethylene Propylene

FHI Foveal Hyperspectral Imaging

FLIM Fluorescence Lifetime Imaging

FoV Field of View

FTIS Fourier-Transform Imaging Spectrometer

FWHM Full Width at Half Maximum

Hb Deoxyhaemoglobin

HbO2 Oxyhaemoglobin

ICA Independent Component Analysis

IFS Integral Field Spectrometry

ILM Inner Limiter Membrane

IMS Image Mapping Spectrometer

IRIS Image Replicating Imaging Spectrometer

ISS Image Slicing Spectrometer

LCTF Liquid Crystal Tunable Filter

LED Light-Emitting Diode

LSU Linear Spectral Unmixing

MAFC Multiaperture Filtered Camera

MTF Modulation Transfer Function

N-H Normoxia-Hypoxia difference

N-H Normoxia-Hypoxia difference

NA Numerical Aperture

OCT Optical Coherence Tomography

OD Optical Density

ODR Optical Density Ratio

OS Oxygen Saturation

PBS Phosphate-Buffered Saline

PCA Principal Component Analysis

PDMS Polydimethylsiloxane

PLA Polylactic Acid

PLL Poly-L-Lysine

PSF Point Spread Function

PTFE Polytetrafluoroethylene

RBC Red Blood Cell

ROI Region of Interest

ROP Retinopathy of Prematurity

RPE Retinal Pigment Epithelium

SAM Spectral Angle Mapper

SHIFT Snapshot Hyperspectral Imaging Fourier Transform Spectrometer

SIFT Scale-Invariant Feature Transform

SLM Spatial Light Modulator

SNR Signal to Noise Ratio

Chapter 1

Introduction

Summary: This chapter provides first a literature review in spectral imaging techniques in order to put the image replicating imaging spectrometer (IRIS) in context. In second place follows a literature review of oximetry applied to retinal vessels and red blood cells (RBCs).

1.1 The need for a snapshot spectral retinal oximetry technique

Oximetry is an experimental technique which calculates oxygen saturation in blood by taking advantage of the different spectral behaviour of haemoglobin under oxygenated and deoxygenated conditions. Oxygen is transported by blood in two forms: 1. dissolved in plasma (2%); 2. by haemoglobin contained in RBCs (98%)[8]. Blood carries oxygen across the body where needed to satisfy the metabolic requirements of the different tissues, so oximetry is a useful technique to monitor tissue metabolism. Failure on effective oxygen delivery produces hypoxia (low oxygen saturation), which can end with serious health problems. Hypoxia detection can be critical in the treatment of diseases which disturb oxygen supply. Hypoxia can be developed in diseases such as diabetes[9], tumour hypoxia[10], glaucoma[11], sickle cell anaemia[12], Alzheimer's disease[13] and multiple sclerosis[14].

In principle, oximetry could be performed in any part of the body, but human tissue is a highly scattering material, making it extremely challenging to retrieve information by non-invasive optical based techniques, being more challenging the deeper in tissue we go. Fortunately, the eye is highly transparent in the visible part of the spectrum, making it possible to obtain high quality spatial and spectral information from retinal vessels and retinal tissue. Performing oximetry in the retina can provide critical information in diseases such as glaucoma, diabetic retinopathy and retinopathy of prematurity (ROP), where hypoxia indicates how the disease is progressing. Oximetry would allow an early diagnosis and continuous monitoring of these diseases, which could prevent potential loss of sight.

The importance of oximetry as a snapshot technique resides in the need of recording dynamic phenomena. The use of a snapshot technique allows the analysis of the exact same blood volume in all the wavelengths, as opposed to scanning techniques, where the flowing blood changes during the data acquisition and there is no guarantee that different volumes of blood have the same characteristics. Another argument in favour of snapshot oximetry is the lack of movement artefacts, which can be problematic in imaging the retina due to eye movement. Finally, when oxygen delivery by RBCs is studied, it is important to do it at high acquisition speeds in order to capture the process and be able to do oximetry. In conclusion, snapshot oximetry allows calculating oxygen saturation of transient phenomena in real time with no artefacts.

The literature review in this chapter is structured in two different parts. The first part provides a general overview of spectral imaging devices that could be potentially useful to perform oximetry. This literature review briefly describes advantages and disadvantages of each spectral imaging device and puts IRIS into context as a suitable device to perform retinal oximetry. This first part also includes a description of spectral analysis techniques that are applied to oximetry in this thesis. The second part of the literature review covers oximetry. It first describes how light absorption can be used to calculate oxygen saturation and then different proposed physical methods that model light absorption by blood in the retina are showed. Some of these models are used in Chapter 4 to perform retinal oximetry and evaluate their behaviour when used with retinal images obtained with IRIS. Finally, a literature review of oximetry performed in red blood cells is provided. This review techniques and results obtained from other researchers.

1.2 Review of spectral imaging techniques

Spectral imaging devices create a 3-D spectral cube from a scene. This 3-D cube contains the spatial and spectral information (x, y, λ) of the sample. These spectral techniques can be classified in different ways[1], but in this thesis, we focus on scanning, Fourier-Transform imaging spectometers and snapshot devices.

1.2.1 Scanning devices

Scanning devices are those time sequential devices which sample a scene spectrally and/or spatially. Scanning devices are fundamentally limited by the impossibility of recording transient phenomena, but they allow the acquisition of a high number of spectral bands with high spectral resolution.

The spatial scanning can be performed using rotating mirrors in order to sample in the x and y directions sequentially. These devices are called Whiskbroom (Fig. 1.1(a)). Each scanned portion of the scanned sample is passed through a dispersive element which gener-

ates the desired spectrum of the scanned object over a linear sensor array. This method is used by the Airborne Visible/Infrared Imaging Spectrometer (AVIRIS)[15]. AVIRIS images Earth's surface using 224 bands in the 400-2500 nm spectral range. Whiskbroom devices can be used in microscopy to analyse biological samples[13, 16].

Pushbroom devices are those which scan an image of the scene across a slit[17] (Fig. 1.1(b)). This method uses the same principle as in Whiskbroom devices, in which the image of the sample is dispersed. In the case of Pushbroom devices, the use of a slit allows simultaneous acquisition in one spatial dimension, while the other dimension is scanned. The dispersed image is finally recorded using a 2-D detector. The spectral 3-D cube is generated with the computer-recovered dispersed images through the scanned sample. This scanning method is used in satellites like the Advanced Land Imager (ALI). Pushbroom techniques capture more spatial data in one sample than the whiskbroom, meaning that it can image an object for longer and capture more light. This method can be implemented with other techniques such as line confocal microscopy[18] or with a static coded aperture mask[19].

Finally, other multispectral devices create the 3-D spectral cube by acquiring the scene over a 2-D (x,y) detector sequentially for a set of different wavelengths (Fig. 1.1(c)). Rather than using dispersive components to capture the different wavelengths, staring methods use elements such as filters and tunable filters to select them. This technique offers great versatility in terms of wavelength selection and allows capturing different wavelengths with different exposure time, which optimises signal to noise ratio (SNR) and overall performance.

1.2.2 Fourier-Transform Imaging Spectrometer (FTIS)

Fourier-Transform Imaging Spectrometer is a set of spectral imaging methods that generates an interferogram of a scene, which is then inverted by Fourier transformation in order to obtain the spectral data of the imaged sample. There are two main scanning methods: spatial and temporal FTIS[20], and snapshot FTIS.

Spatial FTIS[21, 22] is often based in a Sagnac interferometer configuration. This method spatially scans an image through a slit while the interferometer creates the corresponding interferometry pattern over a row (or column) of pixels of a 2-D array. Since it is possible to obtain the whole spectrum from the imaged sample slice, it can be considered as snapshot FTIS.

Temporal FTIS[23] is generally based in Michelson interferometers with a scanning mirror. In this case, the image of the sample is imaged through the interferometer, which creates an interferogram of each point of the sample at the detector array. The scanning mirror is then scanned in order to obtain the complete interferogram per pixel. Each (x,λ) interferogram is then Fourier transformed to recover the spectral data. Another example of temporal FTIS is the birefringent FTIS[24]. This version of FTIS uses a Wollaston prism in exchange of the Michelson interferometer. This allows the construction of a more stable device which is less

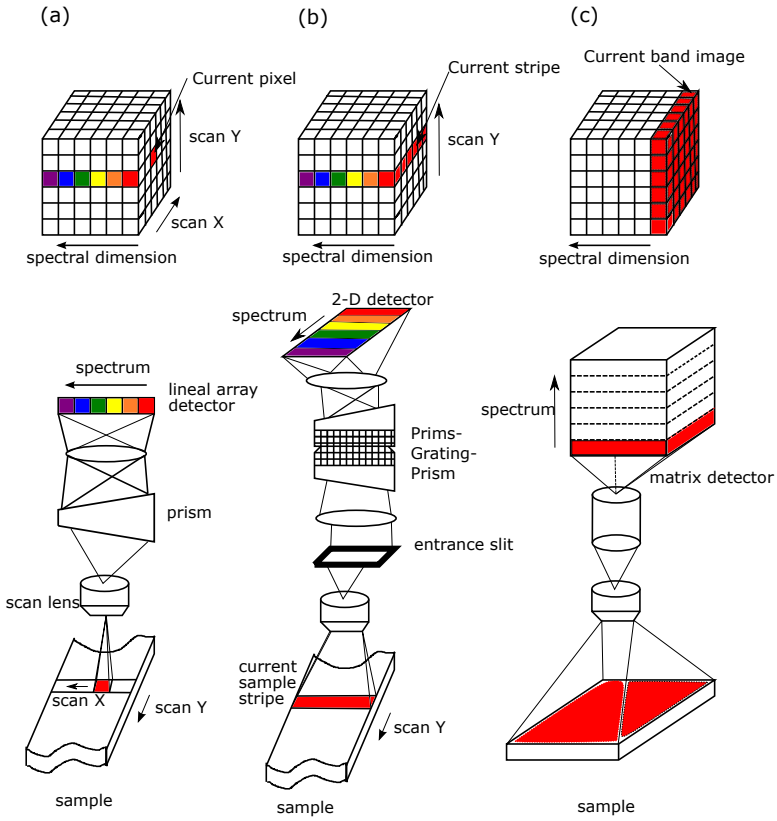

Figure 1.1: Scanning devices (the spectrum is shown in discrete form for simplicity). (a) Whiskbroom. (b) Pushbroom. (c) Spectrally-sequential approach. Figures reproduced from Reference[1].

affected by vibrations. The Wollaston prism generates a two beam interferogram by creating two beams with different relative pathlengths. The interferogram pattern is produced by translating the Wollaston prism normal to the optic axis.

In FTIS devices based on Michelson and Sagnac interferometer half of the light is returned to the source, so the transmission output is 50% of the input, while in the birefringent FTIS there are not light losses.

Snapshot Hyperspectral Imaging Fourier Transform Spectrometer (SHIFT) (Fig. 1.2(e))[25] exchanges the Michelson interferometer with a set of birefringent interferometers in order to generate an interferogram. The main components of a SHIFT system are a lenslet array and a birefringent polarisation interferometer, which consists of two Nomarski prisms. These prisms separate the polarised light beams from the lenslet array and make them converge to a focal point after exiting the birefringent block. In the case of the birefringent-FTIS[24], different parts of the prism introduce different pathlengths, changing the interferogram. In the SHIFT case, each beam created by each lenslet passes through a different part of the prisms, which introduces the pathlength difference. The output of the system over the 2-D sensor is an array of interferograms from the sample, which can be converted in a 3-D cube of interferograms. Each pixel interferogram is then Fourier transformed to obtain the spectral 3-D cube.

Similarly to the birefringent-FTIS, SHIFT has more stability to vibrations than Michelson or Sagnac based interferometers, but it suffers from parallax effects introduced by the lenslet array[25].

1.2.3 Snapshot devices

Although scanning devices can image in as many wavebands as required for the application, they are limited by the impossibility of recording transient phenomena which occur on time scales shorter than the complete sampling process.

On the other hand, snapshot devices excel in imaging dynamic scenes such as in surveillance[26, 27], microscopy, Fluorescence Lifetime Imaging (FLIM)[28], combustion dynamics[29], machine vision and medical imaging, as for example retinal oximetry[30]. In order to achieve snapshot spectral imaging, it is desirable to record the spatial and spectral information at the same time and ideally in the same detector. These requirements limit the number of possible wavebands which can be recorded. In the following subsections, some of the currently available snapshot techniques are described.

1.2.3.1 Computer Tomography Imaging Spectrometer (CTIS)

Computer Tomography Imaging Spectrometer (Fig. 1.2(a))[31, 32] is based in a phase grating to generate the 3-D cube. This computer generated hologram grating disperses light in a 2-D detector array. In computed tomography, various directions of a two-dimensional cross-section image are projected on one dimension and then the image is reconstructed. The same is applicable by increasing the dimension on one and imaging 3-D objects. In CTIS, wavelength replaces one of the dimensions and the reconstruction generates the spectral 3-D cube. CTIS can be either work in transmission[32]or in reflection in Offner configuration[33].

The reconstruction using computer tomography reconstruction algorithms introduces artefacts, degrading the overall quality of the data. Another associated problem is the manufacturing of the desired phase grating, which can be technically challenging. Furthermore, the use of a dispersive element introduces light losses. The required inversion and light losses reduces the SNR, so CTIS does not benefit from the Fellgett's advantage (multiplexed measurements improves SNR[20]).

1.2.3.2 Coded Aperture Snapshot Spectral Imager (CASSI)

Coded Aperture Snapshot Spectral Imager (Fig. 1.2 (b)) uses compressive sensing introducing a binary-coded mask and a single[34] or double[35, 36] dispersive element. The objective of this mask is to create transmission patterns which make each band to be uncorrelated to the others, so it is possible to reconstruct the image by computing means.

On the single dispersive element design, the mask is applied to the image once, which then passes through the disperser. The output is a disperse sheared image, with the bands being overlapped and uncorrelated over the detector. The image shear and the shape of the coded-mask allows the reconstruction of the 3-D cube.

On the double dispersive element configuration, the two dispersive elements and mask are placed on the focal planes of a 4-f system. The first dispersive element spectrally disperses and shears the image, which is then imaged over the mask. Due to the introduced shear, the bands are differently coded by the mask. Finally, the second dispersive element corrects the shear, producing an image of all the bands overlapped and physically uncorrelated. The knowledge of the mask pattern allows the 3-D cube reconstruction.

Due to the compressive nature of the technique, the reconstruction is computationally demanding and presents spatial losses.

1.2.3.3 Multiaperture Filtered Camera (MAFC)

Multiaperture Filtered Camera (Fig. 1.2(c)) uses a lenslet array[37, 38] with an array of individual interference filters mounted over a 2-D detector. Each lenslet creates an image of the sample at the wavelength specified by the attached filter. While this method is relatively simple to implement, there are some drawbacks. One drawback is the effect of nonuniform angular irradiance, which could lead to interpreting intensity variations in the images as spectral variations. Another problem is the spatial parallax displacement produced by each lenslet, so when the 3-D cube is reconstructed there might be spatial information missing on some bands.

1.2.3.4 Image Mapping Spectrometer (IMS)/Image Slicing Spectrometer (ISS)

Image Mapping Spectrometer (Fig. 1.2(d))[39, 40] is a reformatting method. The most relevant component of this technique is the image mapper, which spatially decompose the image by slicing it. The image mapper is a microfaceted mirror with each mirror tilted in different orientations. Once the image is sliced, each slice is spectrally decomposed by a dispersive element and finally it is reimaged over the detector by a lenslet array. This set of spectral spatially sliced images is then reformatted to reconstruct the 3-D cube.

The main drawback of this technique is the need of high precision cutting in order to produce a high-quality image mapper[2].

Integral Field Spectrometry (IFS) is a set of reformatting techniques used to perform spectral imaging with the same principle as IMS. It can be subdivided in IFS with lenslets (IFS-L), with slicing mirrors (IFS-M) and with fibre arrays (IFS-F)[41].

In the IFS_L design, an array of lenslets segments and reimages the scene. These segments are passed through a dispersive element to produce the spectrum over a 2-D detector.

IFS-M is based on slicing mirrors. Each sliced image of the field is passed through a dispersive element to produce the spectrum.

IFS-F (FRIS) uses a set of reformatting fibres to produce the 3-D cube. The scene is reimaged over a bundle of fibres, so each one captures only one part of the sample. The fibre bundle reformats the captured light in a linear fibre array. The light from the array passes through a disperser and the 3-D cube can be obtained by reversing the reformatting process.

1.2.3.5 Foveal Hyperspectral Imaging (FHI)

FHI[26] is a reformatting technique. FHI simulates the human eye, in which most of the field of view has poor spatial and spectral resolution, while the central region, the fovea, has high spatial and spectral resolution. This is achieved with FHI by using a monochromatic CCD for the whole scene and a small central high-resolution hyperspectral region. This technique would be useful in surveillance as a means to record only the hyperspectral data of a region of interest while the rest of the scene is captured monochromatically (or panchromatically if an RGB sensor is used).

In FHI, the central part of the field of view is reimaged to a fibre bundle which reformats the 2-D input into a linear array output. The output is then passed through an Offner spectrometer with a holographic dispersive element which creates the dispersed image containing the spectrum of the linear array. This spectral information is then captured by a different CCD. Finally, a panchromatic image is created from both the monochromatic and the reformatted hyperspectral output.

1.2.3.6 Image-Replicating Imaging Spectrometer (IRIS)

IRIS (Fig. 1.2(f))[42] is the spectral imaging system used in this research. IRIS is a birefringent block constituted by a collinear set of waveplates and Wollaston prisms. These act as multiple cascaded birefringent interferometers, which replicate images and spectrally filter them. The input light is linearly polarised 45º with the optic axis of the waveplates. The waveplates introduce a wavelength dependent phase retardation, which changes the polarisation state to linear, circular or elliptical depending on wavelength. Once the light arrives at the Wollaston prism, this separates the two polarisation states and split them in different angles. This process is repeated for each waveplate and Wollaston prism pair, producing an output of 2^Nreplicated images with distinct and orthogonal spectral transmission functions, where N equals to the number of Wollaston prisms. The images are replicated directly over the detector, so there is no need for inversion to recover the 3-D cube (Fellgett's advantage). Furthermore, IRIS does not reject any light, offering high efficiency in that 50% of unpolarised light is used, rising to 100% in linearly polarised light (high Etendue). The use of a linear polariser eliminates reflection in the scene, which enhances the spectral information since specularly reflected light does not carry significant spectral information of the imaged

object composition. These properties make of IRIS one of the most efficient and reliable imaging spectral devices.

Although IRIS shows higher SNR capabilities and a more efficient use of light than other devices, IRIS suffers from two main issues that need to be solved before being used as an imaging spectral device. The interferometric nature of IRIS means that the same spectral pattern is replicated along the free spectral range, so multiple spectral lobes introduce spectral contamination on each waveband. The second problem is the birefringent dispersion from the Wollaston prisms, which split the image of each sidelobe in a different angle, generating "ghost" images corresponding to other wavelengths. These replicated images in each waveband introduce spatial and spectral contamination. These issues explained in more detail in Chapter 2 and can be sorted out by introducing a filter plate (Chapter 2).

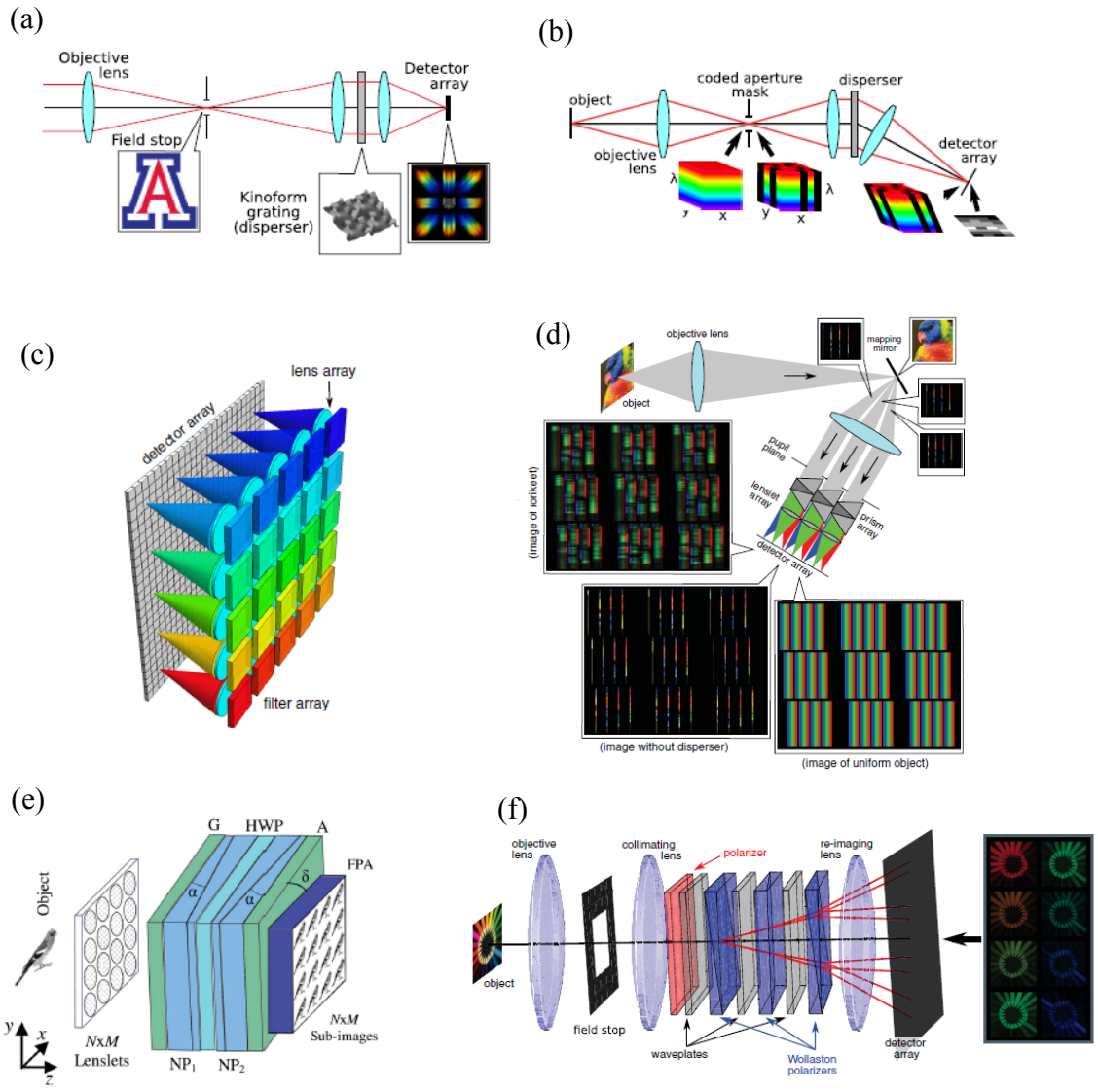

Figure 1.2: (a) CTIS. (b) CASSI. (c) MAFC. (d) IMS. (e) SHIFT. (f) IRIS. Figures extracted from Reference [2]

1.2.4 Spectral analysis techniques

All imaging spectral devices described in the previous sections generate a 3-D cube which includes the spatial and spectral information of a scene. From the 3-D cube, it is possible to retrieve the spectral information of any substance or material which absorbs, transmit, reflects, emits and/or fluoresces in a scene. This allows the identification of chemicals, minerals, vegetation, fluorescent dyes and any chromophore by applying different analysis techniques. I will now discuss some of the main spectral analysis techniques.

1.2.4.1 Spectral Angle Mapper (SAM)

Spectral Angle Mapper[43] allows the identification of spectral features in a scene from a 3-D cube. To do so, it calculates how similar is the spectral profile of the pixel (x,y) to a reference spectrum. This is performed using:

$$cos^{-1}\left(\frac{\sum_{i=1}^{nb} t_i r_i}{\sqrt{\sum_{i=1}^{nb} t_i^2}\sqrt{\sum_{i=1}^{nb} r_i^2}}\right), \tag{1.1}$$

where nb is the number of bands, r is the reference spectrum and t is the spectrum recorded at each pixel. Given a number of reference spectra, Eq. 1.1 is applied pixel by pixel to find to which reference spectrum the angle between them (considering the spectra as vectors) is smaller. This result is then used to classify the pixels according to the reference spectrum.

1.2.4.2 Linear Spectral Unmixing (LSU)

Linear Spectral Unmixing[44] finds the abundance of each reference spectrum in each recorded pixel. This method is based on:

$$I(\lambda) = \sum c_i R_i(\lambda), \tag{1.2}$$

where $I(\lambda)$ is the recorded intensity at each pixel, c is the abundance of the reference chromophore or endmember, and $R(\lambda)$ is the reference spectral profile of the corresponding chromophore. By performing a non-linear-least-squares optimisation on Eq. 1.2, it is possible to find the spectral abundances of each spectral reference from the pixel intensity values.

1.2.4.3 Principal Component Analysis (PCA)

Principal Component Analysis[45] can reduce the dimensionality of the acquired data in the spectral dimension. PCA applies an orthogonal linear transformation to the 3-D cube in order to obtain a new 3-D cube which is an uncorrelated linear combination of the input data. The transformation is performed by finding the covariance between the inputs bands

(eigenvectors) and maximising the covariance in the new linear combination. Then the new eigenvectors are sorted from highest to lowest variance. In this context, the eigenvectors with the highest variance correspond to significant spectral features in the input data, and the lowest variance corresponds to noise. With this knowledge, it is possible to reduce the problem dimensionality by eliminating the bands with the lowest variance, which contain the less significant spectral information.

1.2.4.4 Independent Component Analysis (ICA)

Independent Component Analysis[46] uses high order statistics to separate independent signals based on a non-Gaussian assumption of independent sources. ICA can reveal and identify spectral features of interest in the original 3-D cube without any previous knowledge of the signals (blind deconvolution). The new bands are independent of each other.

1.3 Oximetry principles

Oximetry is the calculation of oxygen saturation in blood. This can be achieved using the Beer-Lambert law and the transmitted light through blood (Fig. 1.3):

$$I(\lambda) = I_o(\lambda)\, 10^{-cd\varepsilon(\lambda)}, \tag{1.3}$$

where $I(\lambda)$ is the light intensity after passing through an absorbing medium of constant thickness d while $I_o(\lambda)$ is the intensity before the sample. c and $\varepsilon(\lambda)$ are the solution concentration in $^{\text{mole}}/_{\text{litre}}$, and the extinction coefficient in $^{\text{litre}}/_{(\text{cm}\cdot\text{mole})}$ respectively.

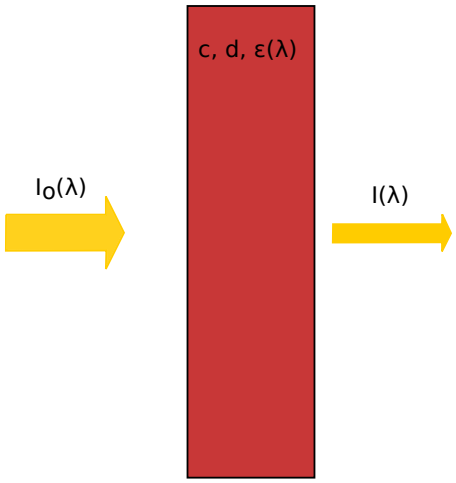

Figure 1.3: Light transmission by an absorptive medium.

In the case of blood, the Beer-Lambert law is used in conjunction of the oxyhaemoglobin and deoxyhaemoglobin extinction coefficients[47] (Fig. 1.4).

The main chromophore of whole blood is the haemoglobin contained in RBCs, being up to 98% oxyhaemoglobin and deoxyhaemoglobin while other components such as meth-

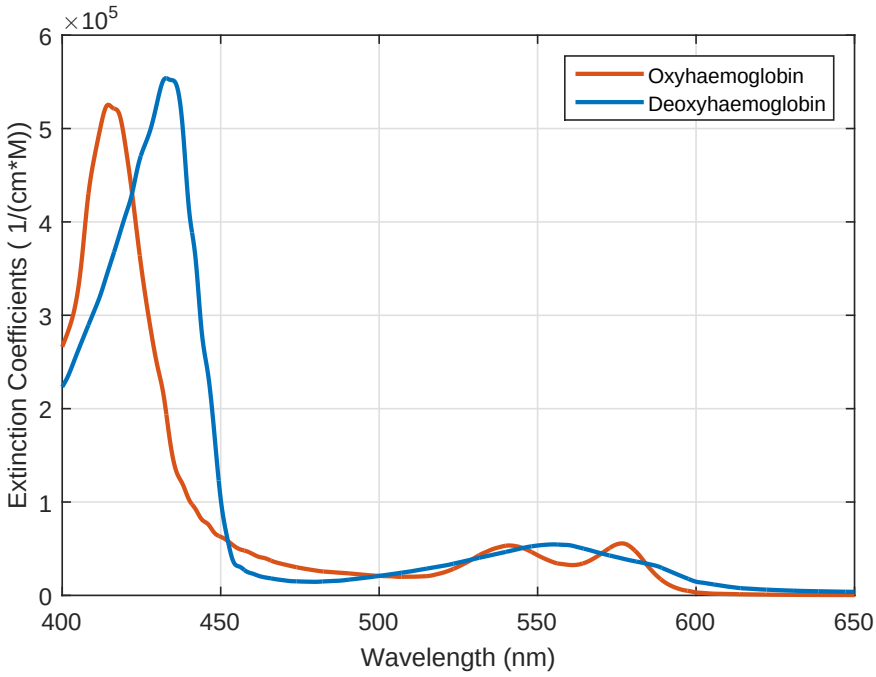

Figure 1.4: Oxygenated (red) and deoxygenated (blue) haemoglobin extinction coefficients.

aemoglobin and carboxyhaemoglobin make the other 2% in healthy patients and are usually ignored. If the concentration of both haemoglobin states is known, it is possible to calculate the blood oxygen saturation (OS) with:

$$OS = \frac{c_{HbO_2}}{c_{HbO_2} + c_{Hb}}, \tag{1.4}$$

where c_{HbO_2} and c_{Hb} are the oxyhaemoglobin and deoxyhaemoglobin concentration respectively and OS is the oxygen saturation. Combining Eq. 1.3 and Eq. 1.4 produces an expression which allows finding the blood OS from transmission measurements:

$$T(\lambda) = \frac{I_o(\lambda)}{I(\lambda)} = 10^{-cd\left[\left(\varepsilon_{HbO_2}(\lambda) - \varepsilon_{Hb}(\lambda)\right)OS + \varepsilon_{Hb}(\lambda)\right]}, \tag{1.5}$$

where $c = c_{HbO_2} + c_{Hb}$ is the total haemoglobin concentration in blood.

One of the first attempts to characterise blood OS by photometric means was realised by Hickam *et al.*[48]. By using haemolysed blood and a spectrometer with nominal wavelength 600 nm, they found a linear relationship between the change in OS and the optical density of the sample. In 1951, Kramer *et al.*[49] showed in the infrared and with haemolysed blood, how with two wavelengths, one isosbestic and one sensitive to OS changes, it is possible to find a linear relation between optical densities ratios and oxygen saturation. This was the first attempt of performing two-wavelength oximetry. This method is based on Eq. 1.5 and the spectral difference between the oxy- and deoxyhaemoglobin extinction coefficients (Fig. 1.4). In order to perform this method, it is necessary to do the ratio of the logarithm of Eq.

1.5 (Optical Density, *OD*), which produces:

$$\begin{aligned} ODR &= \frac{-\log\left(10^{-cd\left[\left(\varepsilon_{HbO_2}(\lambda_1)-\varepsilon_{Hb}(\lambda_1)\right)OS+\varepsilon_{Hb}(\lambda_1)\right]}\right)}{-\log\left(10^{-cd\left[\left(\varepsilon_{HbO_2}(\lambda_2)-\varepsilon_{Hb}(\lambda_2)\right)OS+\varepsilon_{Hb}(\lambda_2)\right]}\right)} \\ &= \frac{cd\left[\left(\varepsilon_{HbO_2}(\lambda_1)-\varepsilon_{Hb}(\lambda_1)\right)OS+\varepsilon_{Hb}(\lambda_1)\right]}{cd\left[\left(\varepsilon_{HbO_2}(\lambda_2)-\varepsilon_{Hb}(\lambda_2)\right)OS+\varepsilon_{Hb}(\lambda_2)\right]}, \end{aligned} \tag{1.6}$$

where $\varepsilon(\lambda)$, c and d the haemoglobin extinction coefficients, the haemoglobin concentration and the sample thickness respectively. Eq. 1.6 can be simplified by making one of the wavelengths to be isosbestic, $\varepsilon_{HbO_2}(\lambda_2) = \varepsilon_{Hb}(\lambda_2)$, giving place to:

$$ODR = \frac{\left[\left(\varepsilon_{HbO_2}(\lambda_1) - \varepsilon_{Hb}(\lambda_1)\right)OS + \varepsilon_{Hb}(\lambda_1)\right]}{\varepsilon_{Hb}(\lambda_2)}. \tag{1.7}$$

Finally, rearranging Eq. 1.7 a linear relation between *ODR* and *OS* is found:

$$\begin{aligned} OS &= \frac{ODR*\varepsilon_{Hb}(\lambda_2)-\varepsilon_{Hb}(\lambda_1)}{\left(\varepsilon_{HbO_2}(\lambda_1)-\varepsilon_{Hb}(\lambda_1)\right)} \\ &= a\cdot ODR + b, \end{aligned} \tag{1.8}$$

where $a = \varepsilon_{Hb}(\lambda_2)/\left(\varepsilon_{HbO_2}(\lambda_1)-\varepsilon_{Hb}(\lambda_1)\right)$ and $b = -\varepsilon_{Hb}(\lambda_1)/\left(\varepsilon_{HbO_2}(\lambda_1)-\varepsilon_{Hb}(\lambda_1)\right)$ are calibration parameters which are found with the measured (or assumed) blood *OS* and their corresponding *ODR*. Eq. 1.8 is independent of haemoglobin concentration and diameter and is meant to have a linear relationship with *OS*. In reality, experimental results show otherwise. Using an integrating sphere, Anderson *et al.*[50] showed how linearity is lost with changes in haematocrit and sample depth, being light scattered from RBCs the main reason behind this effect. The same group showed how reflected (or backscattered) light from the sample[51] is also dependant on depth and haematocrit, increasing nonlinearities between *OS* and *ODR*. Blood reflectance is related to transmission as:

$$R = c_1 T + c_2, \tag{1.9}$$

where $c_1$and c_2 are fitting parameters dependent on haematocrit and sample depth. Reflectance is shown to increase with sample depth up to 300 μm and then it has an asymptotic behaviour. These nonlinearities can lead to a mischaracterization of *OS*.

Scattering from RBCs was introduced in the blood transmission model by Twersky after developing the theory of scattering through a suspension of particles[52, 53]. The new formulation included absorption and scattering on the optical density:

$$OD = \varepsilon cd - \log\left[10^{-sH(1-H)d} + \frac{q\alpha}{q}\left(1 - 10^{-sH(1-H)d}\right)\right], \tag{1.10}$$

where H is the haematocrit, s is a factor depending on the wavelength, particle size and

orientation, q_α/q is a light detection efficiency factor, ε is the molar extinction coefficient, d is the sample depth, and c is the molar concentration. The second part of Eq. 1.10 represents the scattering, which only depends on haematocrit and sample depth so it can be simplified as[50]:

$$OD = \varepsilon cd + B, \tag{1.11}$$

where B represents the scattering component of blood, which is constant for a fixed haematocrit and pathlength. Eq. 1.11 was used by Pittman *et al.*[54, 55] for oximetry using three wavelengths, 2 isosbestic and 1 sensitive to *OS* changes. The *OD* of two samples with equal haematocrit and depth using 2 isosbestic wavelengths close to each other are obtained, then the scattering component B is considered to be equal for the three wavelengths. This factor is then subtracted from the *OD*, giving place to Eq. 1.12, which is similar in form to Eq. 1.8 and needs calibration previous to application.

$$OS = a\frac{OD_1 - B}{OD_2 - B} + b. \tag{1.12}$$

1.4 Retinal oximetry

There are two approaches regarding retinal oximetry, both based on the Beer-Lambert law. The first approach and more widely used is a calibration based method using two wavelengths (Eq. 1.8). The second approach is to use Eq. 1.5 or modified versions of it to find OS without any need of calibration.

1.4.1 Calibration-based oximetry

The principle behind calibration-based oximetry is the linear relation between *OS* and *ODR* when one isosbestic and one sensitive to OS changes wavelengths are used as shown in Eq. 1.8.

One of the first attempts was done by Hickam *et al.*[56]. In their study, they used a fundus camera to obtain pictures of human retinas breathing air at different oxygen concentrations. First, linearity between OS vs ODR was showed *in vitro* with blood filled glass capillaries using two different sets of filters: red/green (640 nm and 510 nm, full width half maximum (FWHM) FWHM = 10 nm) and red/infrared (640 nm and 720 nm, FWHM = 10 nm). The demonstration on retinal vessels was performed by breathing normal air and 10% O_2 for the red/infrared and normal air, 15, 11 and 9% $O_2$for the red/green. While imaging the subject, brachial arterial blood was extracted, and the stability of *OS* was monitored using an ear-lobe oximeter. The obtained *OS* from the extracted blood was plotted against the retinal arteries *ODR* and a linear fit was performed, obtaining the calibration factors. The calibration was later applied on retinal vessels, producing retinal venous *OS* of $59 \pm 11\%$.

The gold standard of calibration-based oximetry was introduced by Beach *et al.* in 1999[57]. In their method, the *OD* was obtained by analysing the reflectance at two wavelengths on digital images, which facilitates the image analysis. Using a dichroic filter and a system of mirrors, two equal images at two different wavelengths were created over the same detector array. The two wavelengths are 569 nm (isosbestic) and 600 nm (sensitive to *OS* changes), with FWHM = 4.5 nm. A method for pigmentation calibration was also presented. This method corrects the OD(569 nm) by considering the extravascular light reflection (*EVR*):

$$EVR = \frac{I_{569}}{\eta I_{600}}, \tag{1.13}$$

where η is the ratio between the intensities of the two created images from a neutral reflective surface. By default, Eq. 1.8 considers that in both wavelengths the pigmentation effect is the same, which can lead to misleading *OS* values. The introduction of *EVR* takes into account and corrects the effect of wavelength on pigmentation absorbance:

$$OD_{cor,569} = \log\left(\frac{I_{out,569}}{EVR \cdot I_{in,569}}\right) = \log\left(\frac{\eta I_{out,600}}{I_{in,569}}\right). \tag{1.14}$$

Once the correction was applied, Eq. 1.8 was calibrated using the OS values obtained from an earlobe oximeter while the subjects were breathing air with different O_2 concentrations during the retinal images acquisition. Venule diameter calibration was also performed by introducing a corrective factor which made the slope of *ODR* vs *OS* of both arteries and veins to be equal.

Hammer *et al.*[58] added a linear relation in Eq. 1.8 with Eq. 1.14 to correct the systematic effects of pigmentation and vessel diameter over retinal vessels *OS*.

Oximetry calibration can also be performed by using known averaged venular and arteriolar oxygenation[59]. For arterioles the standards are 92%[60], 97%[61] and 98%[62], while for venules the standards are 45%[62], 55%[57], 58%[60] and 59%[56].

This calibration method has been widely used by other groups for retinal oximetry[58, 59, 63]. It is of interest to remark the use of two wavelengths oximetry to research diseases such as diabetes[64, 65], glaucoma[66, 67], retinitis pigmentosa[68] and Alzheimer's disease[69], all of them showing differences in OS between healthy and disease affected subjects.

1.4.2 Calibration-free oximetry

Although two wavelengths oximetry is widely used and can effectively detect changes on blood *OS*, it is still a calibration based method. This means that it relies on assuming a standard *OS* for veins and arteries for the calibration. Other problems are the loss of linearity due to scattering and systematic changes in OS due to vessel diameter and pigmentation, as explained in previous sections.

Two wavelengths oximetry also relies on using one isosbestic wavelength in order to simplify calculations. This was established because the extinction coefficients were not well known and it was possible to do calibration oximetry accurately (Eq. 1.8). However, as stated by Smith[70], this does not offer any mathematical advantage once these coefficients have been properly characterised. In addition, isosbestic wavelengths do not offer any *OS* related information, so choosing *OS* sensitive wavelengths would improve oximetry results.

Another problem with two wavelengths oximetry is the assumption that light passes only once through the vessel after being reflected by the retina. Monte Carlo simulations of photon transport through the eye shows that for vessels of a calibre larger than 50 µm, most of the collected light belongs to photons which have been backscattered by the blood vessel without reaching the fundus[71, 72].

Several attempts have been done in terms of achieving calibration-free retinal oximetry.

1.4.2.1 Cohen

One of the first approaches was performed by Cohen *et al.*[73]. Their system uses a Zeiss fundus camera, which includes a film camera with a dichroic and two interference filters λ_1= 470 nm and λ_2= 515 nm with FWHM = 20 nm, none of the wavelengths being isosbestic.

The model is based on Twersky's scattering theory[53]:

$$I_t(\lambda) = I_o(\lambda)\, e^{-N\sigma_a d}\left[e^{-\beta d} + q(\alpha)\left(1 - e^{-\beta d}\right)\right], \tag{1.15}$$

where $e^{-N\sigma_a d}$ is the absorption of light by particles of density N, σ_a is the particle absorption cross-section, $e^{-\beta d}$is the scattering effect, $q(\alpha)(1-e^{-\beta d})$ is the incoherent scattering into the collection half-cone angle α, and $\beta = sH(1-H)$ from Eq. 1.10. Applying Eq. 1.15 to a retinal vessel, *OS* can be obtained from:

$$\begin{aligned} OS &= \frac{ODR\mu_{Hb}(\lambda_0) - \mu_{Hb}(\lambda_1)}{\left[\mu_{HbO_2}(\lambda_1) - \mu_{Hb}(\lambda_1)\right] - ODR\left[\mu_{HbO_2}(\lambda_0) - \mu_{Hb}(\lambda_0)\right]} \\ &= \frac{\frac{1}{2cd}\left[\log\left(1-1.32\lambda_1^2\right) - ODR\log\left(1-1.32\lambda_0^2\right)\right]}{\left[\mu_{HbO_2}(\lambda_1) - \mu_{Hb}(\lambda_1)\right] - ODR\left[\mu_{HbO_2}(\lambda_0) - \mu_{Hb}(\lambda_0)\right]}, \end{aligned} \tag{1.16}$$

where $1 - 1.32\lambda^2$ corresponds to scattering from RBCs[53]. This model assumes that double pass is the dominant component. This assumption comes from Twersky's scattering theory[53], which states that for infinitely thick layers of blood, the reflected intensity is $I_r(\lambda) = R_\infty I_0(\lambda)$, where $R_\infty \cong 10^{-7}$ is the reflectance of the layer of blood. When this reflectance is smaller than the fundus reflectance[74], the backscattered light can be neglected. In addition, the single pass contribution is neglected due to the assumption of the fundus being specular reflective, which implies no light diffusion from the adjacent fundus to the vessel. These assumptions were proven wrong later on by experimental results[51] and Monte Carlo simulations[71, 72], which show that the backscattered component cannot be

neglected and in retinal vessels is usually dominant. The reflective fundus assumption is also inaccurate since the different layers of the fundus scatter and spread the incoming light[75], generating a wavelength-dependent tissue PSF.

1.4.2.2 Modified Beer-Lambert law

Delori[62] introduced the modified Beer-Lambert law

$$OD(\lambda) = S + scd\left[\left(\varepsilon_{HbO_2}(\lambda) - \varepsilon_{Hb}(\lambda)\right) OS + \varepsilon_{Hb}(\lambda)\right], \tag{1.17}$$

where S[50, 54] is a wavelength independent parameter which depends on light scattered by RBCs, being $S = 0$ for haemolysed blood. s[76] is a geometric factor which depends on the illumination and light collection geometry, being $s = 1$ for haemolysed blood. S and s are empirical factors added to the simple Beer-Lambert law in order to improve data fits.

Delori used three wavelengths, two isosbestic at 569 nm and 586 nm (isosbestic according to Ref. [77], although according to Ref. [47], 570 nm and 584 nm are isosbestic), and one sensitive to OS changes at 558 nm, with FWHM between 7 and 9 nm. The ODs at the three chosen wavelengths are meant to have a linear relationship with OS. With three wavelengths and Eq. 1.17, OS can be calculated with:

$$OS = 100\frac{\left(\varepsilon_{Hb,569} - \varepsilon_{Hb,558}\right) + \left(\varepsilon_{Hb,586} - \varepsilon_{Hb,569}\right) RP}{\left(\Delta_{558} - \Delta_{569}\right) + \left(\Delta_{569} - \Delta_{586}\right) RP}, \tag{1.18}$$

where $\Delta_\lambda = \varepsilon_{HbO_2,\lambda} - \varepsilon_{Hb,\lambda}$ and $RP = {}^{(OD_{569} - OD_{558})}/_{(OD_{569} - OD_{586})}$. RP eliminates S and scd from the equation system, simplifying the OS calculation.

1.4.2.3 Modified Beer-Lambert law and wavelength dependent scattering

Schweitzer *et al.*[78] extended Eq. 1.17 by adding a wavelength dependent component in order to further compensate the difference between the haemolysed extinction coefficients and the extinction produced by whole blood:

$$OD(\lambda) = S + n\log\left(\frac{1}{\lambda}\right) + scd\left[\left(\varepsilon_{HbO_2}(\lambda) - \varepsilon_{Hb}(\lambda)\right) OS + \varepsilon_{Hb}(\lambda)\right]. \tag{1.19}$$

Eq. 1.19 was tested on new-born piglets brains and compared with blood tested by a haemoximeter. No retinal data was obtained due to the complexity of modelling light transport in retinal vessels.

1.4.2.4 Introduction of multiple light paths

Smith *et al.*[79] introduced the effect of multiple light pathlengths in retinal vessels. In their model, single and double pass are implemented on Eq. 1.5. The model also includes the

reflected light (or backscattered) by incident light in a blood sample[51]. When all the paths are considered, the intensity over the vessel can be written as:

$$I_v = \alpha R_f I_0 \exp(-\varepsilon cd) + \beta R_f I_0 \exp(-2\varepsilon cd) + a_1 I_0 + a_2 I_0 \exp(-\varepsilon cd), \tag{1.20}$$

where α and β are the fraction of transmitted light for single and double pass respectively; $a_1$and $a_2$are fitting parameters for the transmitted-backscattered light relation, and are dependent on haematocrit and pathlength; I_0 and R_f are the incident intensity and the fundus reflectance respectively. All the previously defined parameters from Eq. 1.20 are potentially wavelength dependent.

Eq. 1.20 can be rewritten for transmission by dividing it by the background intensity $I_0 R_f$, which correspond to light reflected by the fundus:

$$\begin{aligned} T_v = \left(\alpha + \tfrac{a_2}{R_f}\right) \exp\left\{-\left[OS\varepsilon_{HbO_2} + (1-OS)\,\varepsilon_{Hb}\right] cd\right\} \\ +\beta \exp\left\{-2\left[OS\varepsilon_{HbO_2} + (1-OS)\,\varepsilon_{Hb}\right] cd\right\} + \tfrac{a_1}{R_f}. \end{aligned} \tag{1.21}$$

Eq. 1.21 has seven unknowns: OS, cd and R_f plus the 4 pathlengths factor contributions. In order to simply the model, Smith *et al.*[79], expanded Eq. 1.21 using Taylor series and explored two cases: negligible backscattered component and negligible double pass. The negligible backscattered approximation is based on the hypothesis that the backscattered component is small compared to the others in vessels smaller than $50\,\mu$m, high-reflectance regions as the optic disc and at high absorption wavelengths (green or blue wavelengths). The negligible double pass approximation would be applicable to vessels larger than $160\,\mu$m. Although both approximations are physically different, they yield the same mathematical expression:

$$T_v(\lambda) = T_s(\lambda) \exp\left[-\chi(\lambda)\, cd\, \varepsilon(\lambda)\right], \tag{1.22}$$

where T_s is the scattering transmittance and χ the effective pathlength. In the negligible backscattering case, $0 \leq T_s \leq 1$ and $1 \leq \chi \leq 2$, while in the negligible double pass case, $T_s > 0$ and $\chi < 1$

The model in Eq. 1.22 requires wavelength dependent calibration *in vitro* in order to produce accurate oximetry. Although is was not applied to human retinas by this author, another group used this model in healthy humans, without calibration and using an LCTF and wavelengths from 500 nm to 650 nm in 2 nm steps[80]. The results were >100% for arteries and <40% in healthy humans, which are far from the standard values 96% and 54% oxygen saturation used on 2 wavelengths oximetry[59].

1.4.2.5 Blue-green spectral shift

Denninghoff *et al.*[81] demonstrated a technique to estimate *OS* on blood independently of pathlength, concentration and pH. According to the haemoglobin extinction coefficients (Fig. 1.4), the *OD(λ)* of a blood sample at a determined *OS* has an approximately parabolic shape in the green region of the spectrum (476 nm to 516 nm). The minimum of this parabola shifts from shorter to longer wavelengths with increasing *OS*, being this shift independent of any other blood properties.

This method was later on applied to human eyes[82]. By obtaining images with a confocal scanning laser ophthalmoscope (cSLO) at 5 wavelengths (457.9 nm, 476.5 nm, 488 nm, 496.5 nm and 514.5 nm) and fitting a parabola to the *OD(λ)* it was possible to identify the minimum of the parabola, and hence, the corresponding *OS*.

This method requires previous spectral calibration in order to find the minimum *OD* and its corresponding wavelength for each *OS*[83].

1.5 Red blood cell oximetry

A number of different spectroscopy techniques have been used to perform oximetry measurements of blood vessels, but most have not measured the OS of individual RBCs.

Raman spectroscopy was used to perform non-imaging oximetry on whole blood[84, 85]. However, sufficient irradiance of a single RBC to obtain Raman spectra can damage the cell and increase its background fluorescence[86]. Furthermore, surface specific interactions with the RBC can alter the Raman spectra[86]. These problems make it difficult to obtain quantitative measurements of RBC oxygen saturation using Raman spectroscopy.

RBC oximetry was also performed with optical coherence tomography OCT on RBCs *in vitro* on a gel phantom[87]. Their validation was used by first recording the spectrum by diffusive spectroscopy and calculating the *OS* by fitting the data to a model. The results showed good agreement with the *OS* measured with a probe. The *OS* values were then compared with the *OS* obtained from the OCT data, which yielded -15% *OS* for a $\sim 0\%$ *OS*. A correction factor of $\sim 1/0.86$ was then included to match the OCT results to the diffusive spectroscopy results.OCT offers the possibility of performing oximetry *in vivo.* Using a supercontinuum laser centred at 585 nm (FWHM = 85 nm) oximetry was performed in the retina of rats *in vivo* in the visible portion of the spectrum[88]. A complex model incorporating oxygen dependent scattering and absorption was required to analyse the resulting data. The OCT technique was used to measure oxygen saturation of blood vessels between 30 and 130 μm, but could not be used for smaller vessels (<30 μm) or RBCs because the absorption of light was too weak, resulting in a poor signal-to-noise ratio (SNR).

Magnetic resonance imaging was used to measure *OS* of major blood vessels in the brain[89] but the inherent spatial resolution of the technique (240 μm)[90] is insufficient

to image single RBCs.

Photoacoustic oximetry of mouse brain RBCs was performed *in vivo* in reflection mode[91, 92]. Two pulsed lasers were sequentially focused onto a sample and scanned in two dimensions. The photoacoustic signal generated by the energy deposited in the sample was proportional to absorption of laser light by RBC haemoglobin. Mean values of RBC *OS* were obtained from 500 measurements averaged over 30 capillaries and 1 second[91]. Although the limited spatial resolution (3.5 μm) of RBCs was due to the ultrasound transducer[93], the technique has the distinct advantage of being able to image flowing RBCs *in vivo* in capillaries that are 300 μm beneath the surface of tissue.

Abundance maps of oxyhaemoglobin, methaemoglobin and haemozoin in individual blood cells were obtained from a monolayer of RBCs using multispectral imaging in conjunction with an endmember analysis[94]. The spectrum was taken from 450-700 nm at 5 nm intervals using a tunable light engine coupled to a microscope. Because the spectral data points were taken sequentially, this technique cannot be classified as video-rate (even for exposure times as low as 5 ms, the time required to obtain multispectral images at a given point in time is 0.3 seconds). The abundance of deoxyhaemoglobin was not measured, thus, the oxygen saturation for each RBC was not determined.

Two-wavelength oximetry (431 nm and 420 nm, where absorption is highest) measurements of RBCs were performed *in vivo* within hamster muscle tissue capillaries[95]. *ODR* differences were observed between 100% *OS* and 0% *OS* and calibration was performed, but accurate oximetry of single RBCs was not possible, mainly due to not having enough data points in single RBCs to compensate the low SNR of the measurements.

Two-wavelength oximetry of individual RBCs was performed *in vitro* in a custom PDMS flow cell[96]. This was achieved by sequentially imaging the RBCs with two LEDs, $\lambda_1 = 410\,\text{nm}$ and $\lambda_1 = 430\,\text{nm}$ (FWHM = 20 nm for both), which corresponds to the maximum absorption of oxyhaemoglobin and deoxyhaemoglobin respectively. The RBC was simultaneously illuminated by a red LED (630 nm). The flow cell contained an index matching light absorbing dye (transmits at 633 nm, approximately the same as the red LED) in order to remove scattering and refractive effects from the RBC, so when the RBC was imaged with the red LED, only absorption would affect the image of the RBC. The RBC image in the red plus an image without RBC allowed the calculation of the pathlength, or RBC thickness using the Beer-Lambert law, which in return made possible the calculation of the RBC volume. The blue LEDs were used to calculate the mass of oxyhaemoglobin and deoxyhaemoglobin by using the obtained absorbance and RBC volume and thickness. Finally, *OS* can be calculated using the mass of both oxygenated and deoxygenated haemoglobin. Measured *OS* values of RBCs that were fully oxygenated (21% oxygen partial pressure) equalled 80% rather than 100% as expected. Each RBC *OS* value was therefore multiplied by a correction factor of 1.28.

1.6 Conclusions

This chapter includes a literature review of the most relevant ideas covered in this thesis, being some of them expanded in their corresponding chapter. As previously stated, the main objective of this thesis is to perform oximetry, more precisely retinal oximetry. To accomplish high-quality retinal oximetry it is necessary to acquire high-quality data.

The first part of the literature review describes a set of spectral imaging devices potentially useful for retinal oximetry. In the context of the eye, rapid eye movements, the importance or recording dynamic phenomena and the high absorption from the tissue layers of the eye, a device such as IRIS offers snapshot capabilities, high SNR and higher light efficiency when compared with the other described devices. However, the existence of spectral lobes and the dispersion of the Wollaston prisms reduces the spatial and spectral quality of IRIS. Chapter 2 describes how with the implementation of a filter array these problems can be solved because each waveband is replicated in different parts of the sensor. This approach would not be applicable in devices such as CASSI and CTIS.

This chapter also provides a description of three spectral analysis techniques: PCA, LSU and ICA. In this thesis, LSU is used in Chapter 3 as the main analysis technique to perform oximetry, while ICA is used as an independent auxiliary technique to identify spectral components in Chapter 3 and Chapter 4.

The final sections of this chapter cover the basic principles of oximetry and how it is applied to retinal oximetry and red blood cells. Regarding retinal oximetry, calibration-based methods are widely used in eye related diseases (Subsection 1.4.1), while calibration-free methods have yet to be successfully applied in such studies. Since the main objective of this thesis is to perform calibration-free retinal oximetry using IRIS, the performance of these models and two-wavelengths oximetry (calibration-based) are evaluated in Chapter 4. Finally, the literature review finishes showing examples in which oximetry is applied to RBCs. Chapter 3 performs oximetry in RBCs and the results are then compared with the literature.

The following chapters implement a solution of the inherent problems of IRIS (sidelobes and dispersion) and the application of IRIS to study oxygen saturation of blood on RBCs and retinal vessels.

Chapter 2

IRIS Improvement

Summary: This chapter describes the existing issues in IRIS and how they have been solved. In the first place, the IRIS design used in this research is described, showing its inherent problems. This is followed by the proposed and implemented solutions and how the spectral and spatial information retrieved from IRIS are improved.

2.1 Retinal IRIS

Retinal IRIS is a 8 wavebands imaging spectral device specially designed for oximetry by A. Gorman[3] (Fig. 2.1).

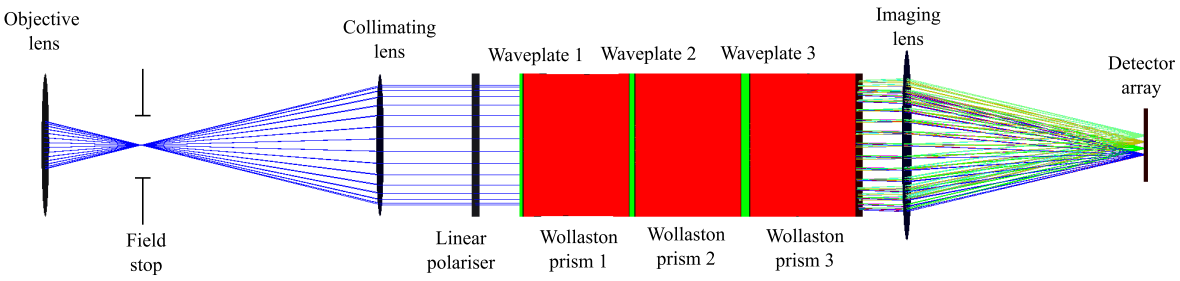

Figure 2.1: Retinal IRIS *Zemax* model. Indicating waveplates in green and Wollaston prisms in red.

This IRIS system consists of a 3 set of collinear pairs of quartz waveplates and calcite Wollaston prisms. The thickness of the waveplates is optimised for oximetry in the 560-600 nm range, with the target of having 2 isosbestic points and 6 sensitive to *OS* changes in order to characterise the haemoglobin absorption. In addition, it is of interest to maximise the orthogonality among the spectral bands and to obtain maximum mean peak power. Under

these constraints, the transmission functions[42] are optimised:

$$\begin{aligned}
T_1 &= \cos^2(l_1k)\cos^2(l_2k)\cos^2(l_3k)\\
T_2 &= \sin^2(l_1k)\sin^2(l_2k)\sin^2(l_3k)\\
T_3 &= \cos^2(l_1k)\sin^2(l_2k)\cos^2(l_3k)\\
T_4 &= \sin^2(l_1k)\cos^2(l_2k)\sin^2(l_3k)\\
T_5 &= \cos^2(l_1k)\cos^2(l_2k)\sin^2(l_3k)\\
T_6 &= \sin^2(l_1k)\sin^2(l_2k)\cos^2(l_3k)\\
T_7 &= \cos^2(l_1k)\sin^2(l_2k)\sin^2(l_3k)\\
T_8 &= \sin^2(l_1k)\cos^2(l_2k)\cos^2(l_3k)
\end{aligned} \tag{2.1}$$

where $l_1 = B_1D_1$, $l_2 = B_2D_2$ and $l_3 = B_3D_3$, B_i and D_i being the waveplate birefringences and thicknesses respectively, and $k = \pi/\lambda$. The optimisation results, as seen in Fig. 2.2, are one isosbestic point at 571 nm, two quasi-isosbestic at 567 nm and 586 nm, and finally five sensitive to *OS* changes at 560 nm, 576 nm, 580 nm, 591 nm and 599 nm, all of them with FWHM $\approx$ 8 nm. The interferometric nature of IRIS produces sidelobes around the wavelength of interest, furthermore, this pattern is replicated along the free spectral range. These transmission functions are achieved with $D_1 = 617\,\mu$m, $D_1 = 951\,\mu$m and $D_1 = 1615\,\mu$m for the waveplates thickness as seen in Fig. 2.1.

In order to evenly distribute the 8 replicated images over a 15.15×15.15 mm detector using a 50 mm f/1.4 SLR lens, the splitting angles are $\phi_{x1} = 8.87°$ for the first Wollaston prism, $\phi_{y1} = 8.87°$ for the second and $\phi_{x2} = 4.43°$ for the third prism.

From Fig. 2.2 it is evident that the spectral information of each waveband is contaminated by the existence of sidelobes. In addition to this problem, the dispersion in the birefringence of the Wollaston prisms introduces wavelength dependent image dispersion, degrading the spatial information.

2.1.1 Sidelobes and spectral information

IRIS by itself contains multiple spectral lobes along its spectral range (Fig. 2.3), making difficult the use of IRIS as a device capable of identifying spectral signatures of chromophores. However, IRIS is capable of measuring spectral abundances if a set of reference spectra are previously recorded with the same system.

To show the effects of the side lobes, the IRIS transmission spectra in Fig. 2.2 was used to simulate two capillaries of $d = 150\,\mu$m, $c = 100\,$g/l, $OS_1 = 100\%$ and $OS_2 = 0\%$. In order to take into account the contribution of the FWHM of the spectral lobes, it was necessary to rewrite Eq. 1.5 in integral form as shown in:

$$T = \frac{\int S(\lambda)\, 10^{-cd\left[\left(\varepsilon_{HbO_2}(\lambda)-\varepsilon_{Hb}(\lambda)\right)OS+\varepsilon_{Hb}(\lambda)\right]}d\lambda}{\int S(\lambda)\, d\lambda}, \tag{2.2}$$

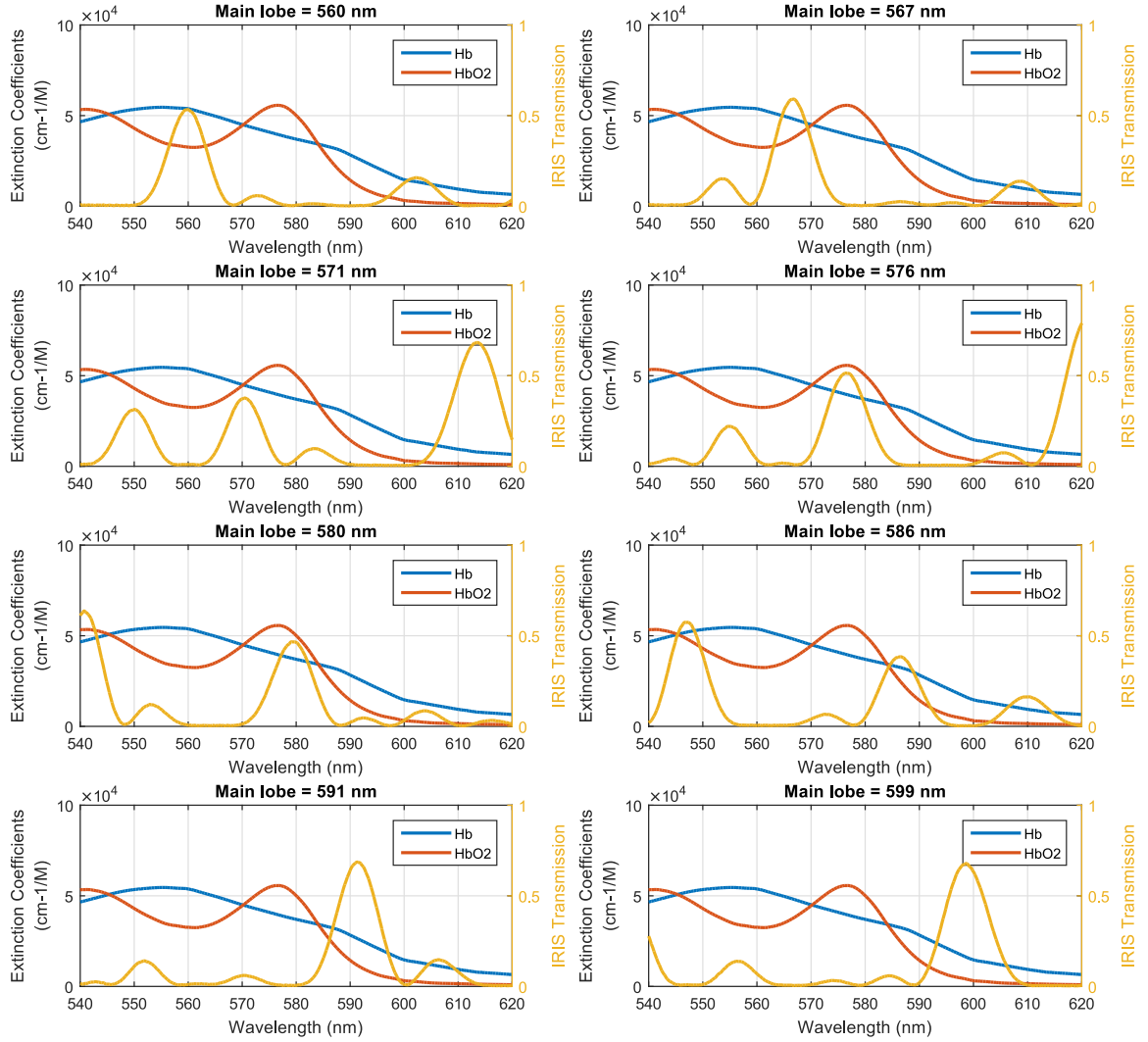

Figure 2.2: IRIS bands transmission (yellow) with oxyhaemoglobin (red) and deoxyhaemoglobin (blue) extinction coefficients in the 540-620 nm range.

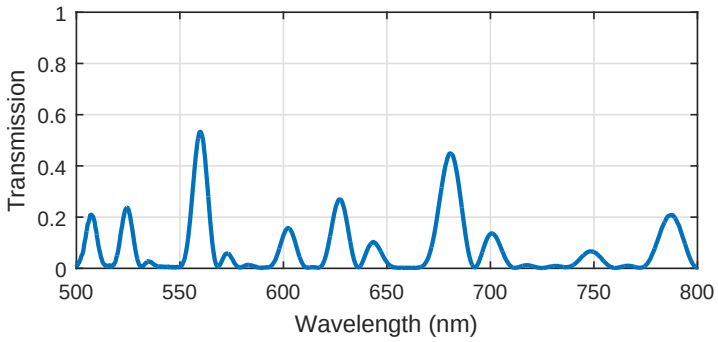

Figure 2.3: IRIS transmission of the 560 nm waveband along the free spectral range.

where $S(\lambda)$is the source spectrum, IRIS transmission, detector sensitivity and background reflectance, although, for simplicity, source, detector sensitivity and background reflectance were considered to be equal to 1 in the whole spectral range. For comparison, the two capillaries were also simulated with Eq. 2.2 considering the spectral range of IRIS in the 540

nm to 620 nm and monochromatic light, using only the main wavelength of each waveband (Fig. 2.2). The results are displayed in Fig. 2.4.

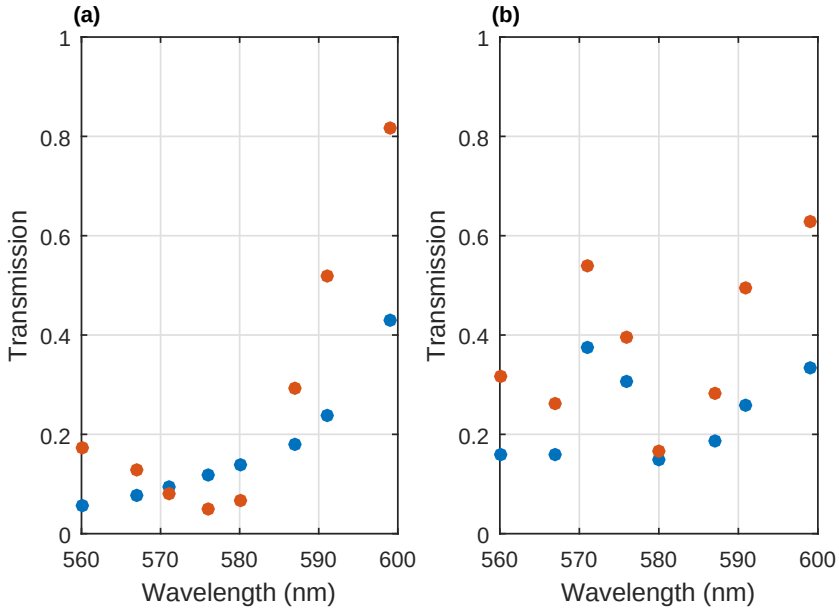

Figure 2.4: Blood transmission model for OS = 100% (red) and OS = 0% (blue): (a) considering IRIS spectral transmission in the 540-620 nm range; (b) considering monochromatic light for the main IRIS wavelengths.

Fig. 2.4(a) shows the transmission of 0% and 100% oxygenated blood using monochromatic light, which has a clear resemblance with the haemoglobin extinction coefficients on Fig. 2.2. Although the real isosbestic point is at 570.2 nm[47], the 571 nm wavelength offers a good isosbestic point, since the difference in transmission for this modelled case is 1.2% between the oxygenated and deoxygenated case.

When the IRIS transmission spectra is used to obtain the blood transmission (Fig. 2.4 (b)), it bears little resemblance with the extinction coefficients. In addition 576 nm isosbestic (1.8% transmission difference between oxygenated and deoxygenated blood), while 571 nm becomes sensitive to OS changes.

As a spectral reference, Fig. 2.4(b) would be appropriate to perform oximetry for capillaries under similar conditions and similar characteristics using a linear spectral unmixing technique, but it would not be valid when performed in the eye. In retinal vessels, the transmission depends on pathlengths, pigmentation, contrast, scattering, haematocrit and vessel size, which would make it necessary to have a set of different references of oxyhaemoglobin and deoxyhaemoglobin for each set of conditions. As an example, Fig. 2.5 displays the mean transmission profiles belonging to two different arteries on the same eye. In this case, having a different diameter and being in different pigmentation background makes both arteries to have different transmissions, meaning that the use of the same reference would produce different oxygenation results for each artery.

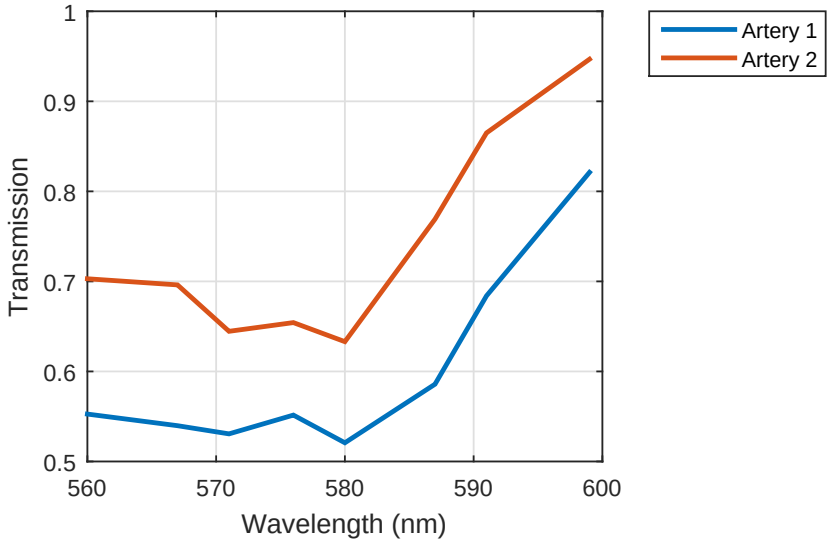

Figure 2.5: Arteries transmission from the same retina. Artery 1 corresponds to a large capillary of $\sim 120\,\mu$m diameter after exiting the optic disc. Artery 2 corresponds to a small capillary of $\sim 70\,\mu$m diameter and 2 mm far from the optic disc. The different allocated regions showed small differences in pigmentation, which in addition of the diameter difference, created the different transmission spectrum for both vessels.

2.1.2 Sidelobes and birefringent dispersion

As previously explained, IRIS is made of birefringent blocks. In the case of the calcite Wollaston prisms, their birefringence (Fig. 2.6) means that different wavelengths are split in different angles:

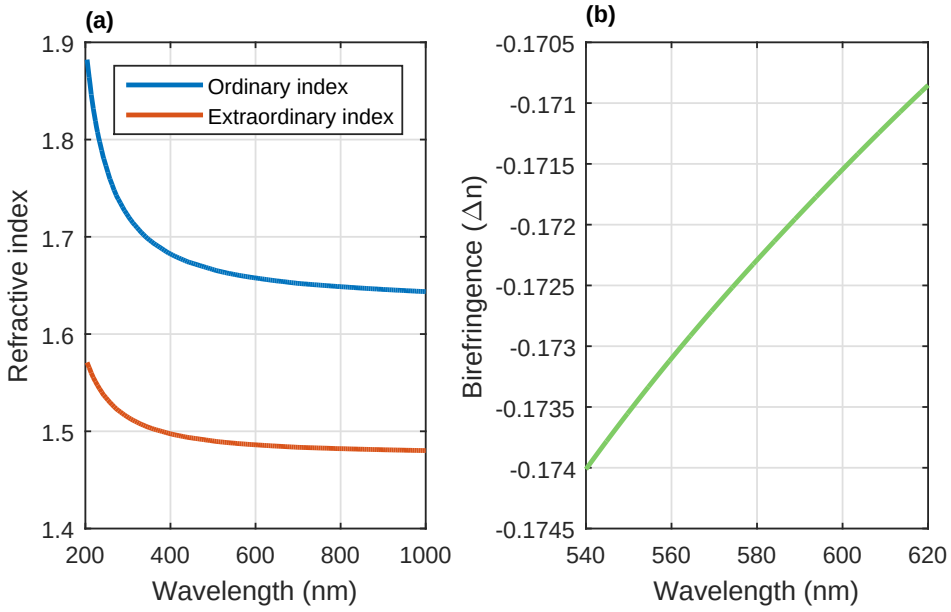

Figure 2.6: Calcite Wollaston prism: (a) extraordinary and ordinary refractive index; (b) birefringence

$$\psi \simeq 2B \tan\theta. \tag{2.3}$$

In Eq. 2.3[3], ψ is the split angle, B the birefringence and θ the wedge angle of the Wollaston prism.

As an example of the birefringence dispersion, Fig. 2.7 shows an image of two red blood cells (RBCs) obtained with IRIS at 571 nm band (Fig. 2.2) using a broadband filter (585 nm, FWHM = 40 nm). In this image it is very clear how IRIS splits the main wavelength (571 nm) and the secondary wavelength (613 nm) in different angles. The final image is then a composite of the wavelength of interest with an overlapped "ghost" image, which degrades the spectral and spatial information.

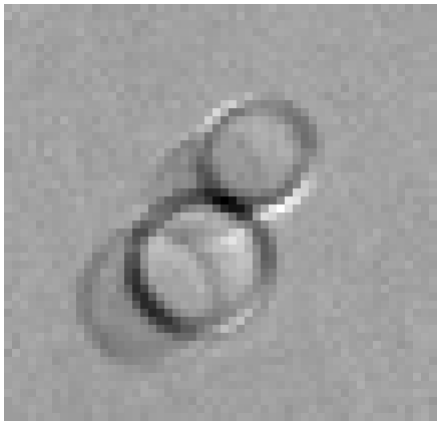

Figure 2.7: Red Blood Cells image taken with IRIS at 571 nm. Image obtained using the system shown in Fig. 3.1 (Section 3.2).

IRIS dispersion can be mitigated by implementing Wollaston prisms with different birefringence so they compensate the dispersion of each other[97]. The use of different birefringent materials (high and low dispersion) to form the Wollaston prism would also achromatise the Wollaston prism[3].

In the next section it is explained how the filter plate is used and effectively solves the issues derived from the side lobes and the Wollaston prisms dispersion.

2.2 Filter plate design and implementation

As shown in Subsection 2.1.1 and Subsection 2.1.2, the performance of IRIS is degraded due to the existence of sidelobes and the fact that is not achromatised. Fortunately, the sidelobes can be removed by filtering the individual spectral bands[3]. In order to achieve this, a filter plate was designed. This filter plate needed to be easy to implement in any optic system, easy to align and to replace. This design would provide a more compact design than using beam splitters and filters to separate and replicate over the same sensor eight images at different wavelengths.

The filter plate ideal position is where the images are smallest after the imaging lens. Ideally, this plane corresponds to the imaging plane. However, *Zemax* simulations of some double Gaussian lenses interfaced with IRIS showed a narrower beam at distances before the image plane[3].

In order to test where the beam is narrowest, we designed an experiment with the configuration shown in Fig. 2.1, using a halogen lamp, a 0.75 mm pinhole, two *Nikon* AF NIKKOR 50 mm F1/4 SLR lens for the collimating and imaging lenses, IRIS and a Retiga-4000R (*QImaging*, Canada) detector. The camera was translated in 1 mm steps from the image plane towards the imaging lens. The pinhole image size was measured in terms of area and diameter. The results showed the images being smallest at the image plane (Fig. 2.8(a) and (b)), where the replicated pinhole images were in focus over the detector. Since the smallest image size corresponds to the image plane, which is on the detector, the filters were placed as close to the sensor as possible, which in the case of the Retiga-4000R was in contact with the protective glass over the sensor, being this 5 mm away from the sensor, which could lead to the different bands overlapping in the plane of the filter, but this effect could be eliminated using an aperture stop in the collimating lens of IRIS. In the case of a Zyla 5.5 (*Andor*, Ireland), the distance between the sensor and the protective glass is of 15 mm, which would require a smaller aperture stop if overlapping in the filter plate plane wants to be avoided.. On the other hand, light from other bands that would be larger than its own filter would be attenuated by the adjacent filters and is not expected to have an effect on the replicated images over the sensor.

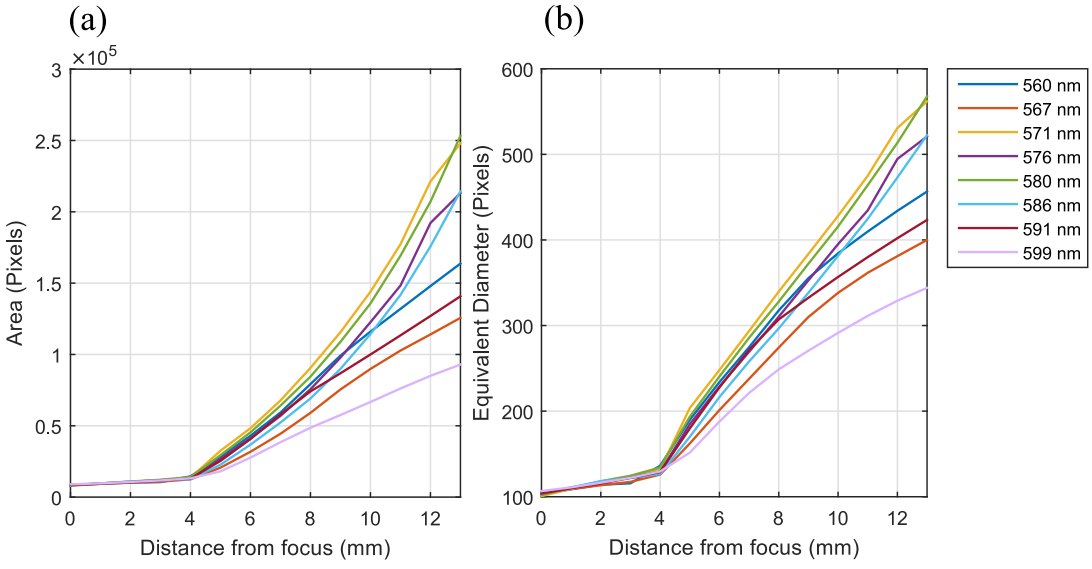

Figure 2.8: Beam behaviour with distance to the imaging lens focal plane. (a) Area of the 8 replicated images of the pinhole. (b) Equivalent diameter of the replicated images of the pinhole.

Another advantage of placing the filter plate as close as possible to the detector is to minimise vignetting from the filter edges and light scattering. An IRIS system needs an aperture stop to avoid overlapping between the bands and to optimise the used area over the

detector. The discontinuities between adjacent filters introduce a shadow over the detector, that is more dispersed and larger the farther the filter plate is displaced from the detector. Since the aperture stop is reimaged over the detector, it can be resized in order to eliminate the vignetting from the filters.

As shown in Fig. 2.2, the wavelengths of interest are 560 nm, 567 nm, 571 nm, 576 nm, 580 nm, 586 nm, 591 nm and 599 nm. In order to filter them, a set of individual filters were manufactured by *Envin Scientific Limited* (UK). The individual filters were ordered with the previously specified wavelength with a ± 2 nm tolerance, transmission$T \geqq 80\%$ at the central wavelength (CW), FWHM = 10 ± 2 nm and blocking with $OD = 3$ outside the 540-620 nm region. The filters were dielectric hard coated only on one surface, to allow easy attachment to a glass substrate. The dimensions of each filter were 25 mm diameter and 1.35 ± 0.15 mm thickness.

Since the filters only blocked light in a narrow spectral region around the central wavelength (Fig. 2.9), we included in our system a 545-625 nm broadband filter (hq585/80x, *Chroma Technology Corporation*, USA) so any unwanted wavelength was cleaned.

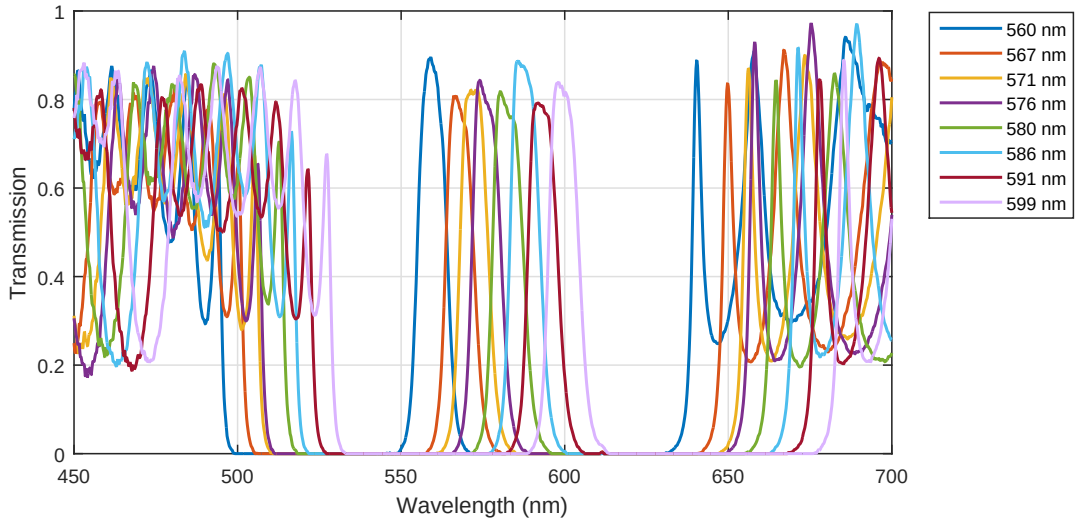

Figure 2.9: Measured filter transmissions, showing how they transmit light outside the 545-625 nm range, which is blocked by the broadband filter.

2.2.1 First filter plate design

The first filter plate was designed by Laurence R. Brewer[1]. The filters were cut by *Helia Photonics* (UK) to be $(3.79 \pm 0.02\,\text{mm}) \times (7.58 \pm 0.1\,\text{mm})$ (Fig. 2.10(a)) so they would cover the full extension of the 15.15×15.15 mm detector of a Retiga-4000R (QImaging) camera. The filters were then assembled over a $18.58 \times 18.58 \times 1$ mm B270 glass substrate by *Helia Photonics* (Fig. 2.10(a)), which produced three filter plates using the same wavelength

[1]SUPA Advanced Fellow, School of Physics and Astronomy, University of Glasgow

configuration. The final result can be seen in Fig. 2.10(b).

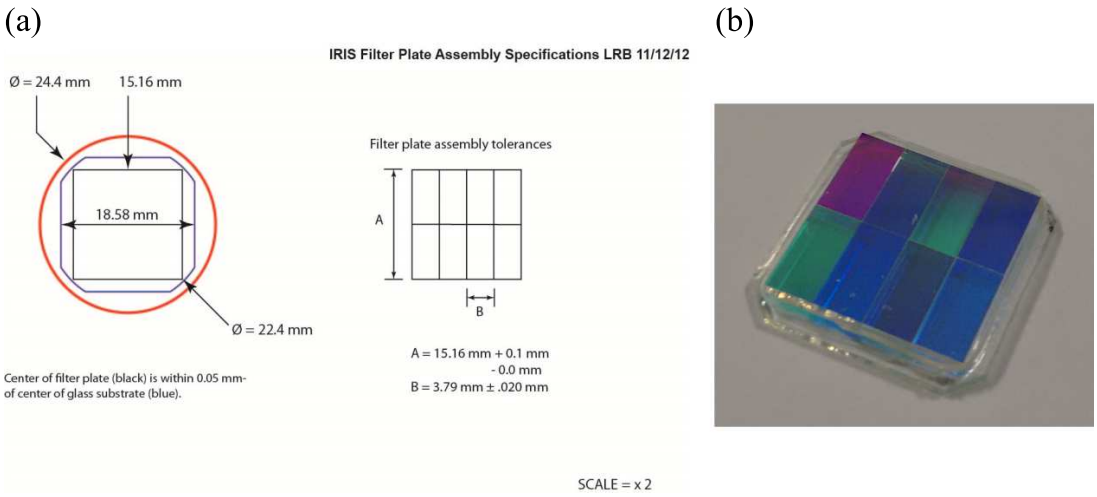

Figure 2.10: First filter plate assembly design. (a) Specification designs for cutting and assembling the filters in the substrate. (b) Final assembly.

This filter plate was attached to the camera by means of a filter plate holder. Two versions of the same model were designed: one for a 15.15×15.15 mm sensor of a CCD Retiga-4000R (*QImaging*) camera (Fig. 2.11), and a second one for a 16.6×14.0 mm sensor of a Zyla 5.5 (*Andor*, Ireland) camera (Fig. 2.12). Each holder was made of a single phosphor-bronze piece with ± 0.05 mm tolerance, with the dimensions specified in their respective figures.

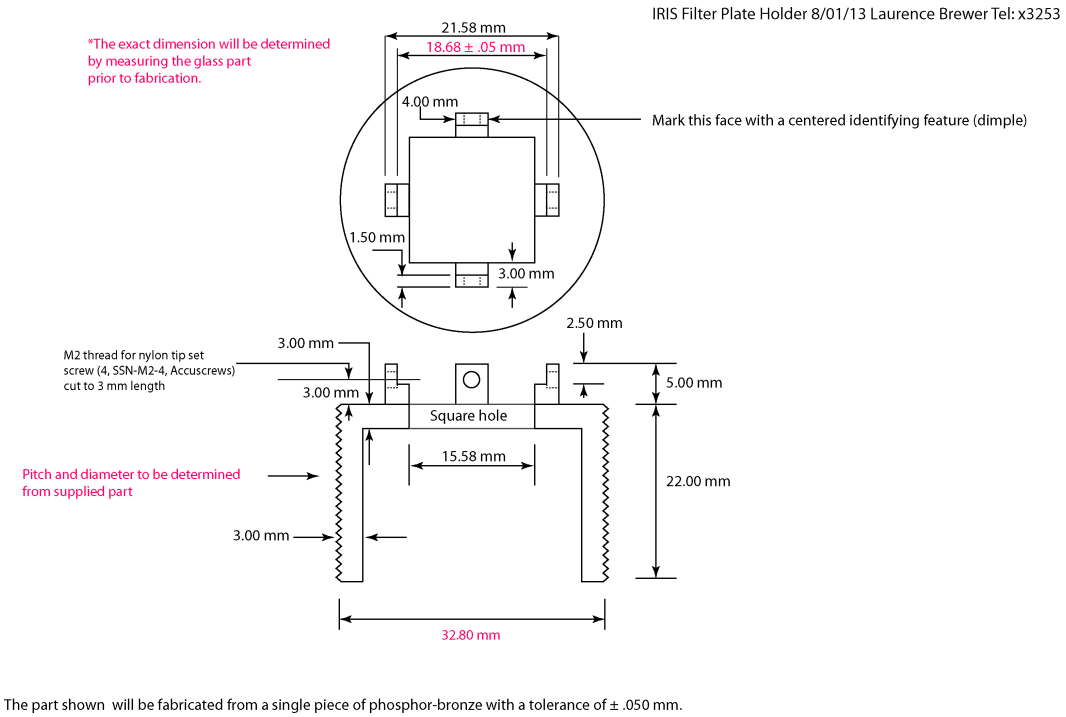

Figure 2.11: Filter plate holder design for a Retiga-4000R camera.

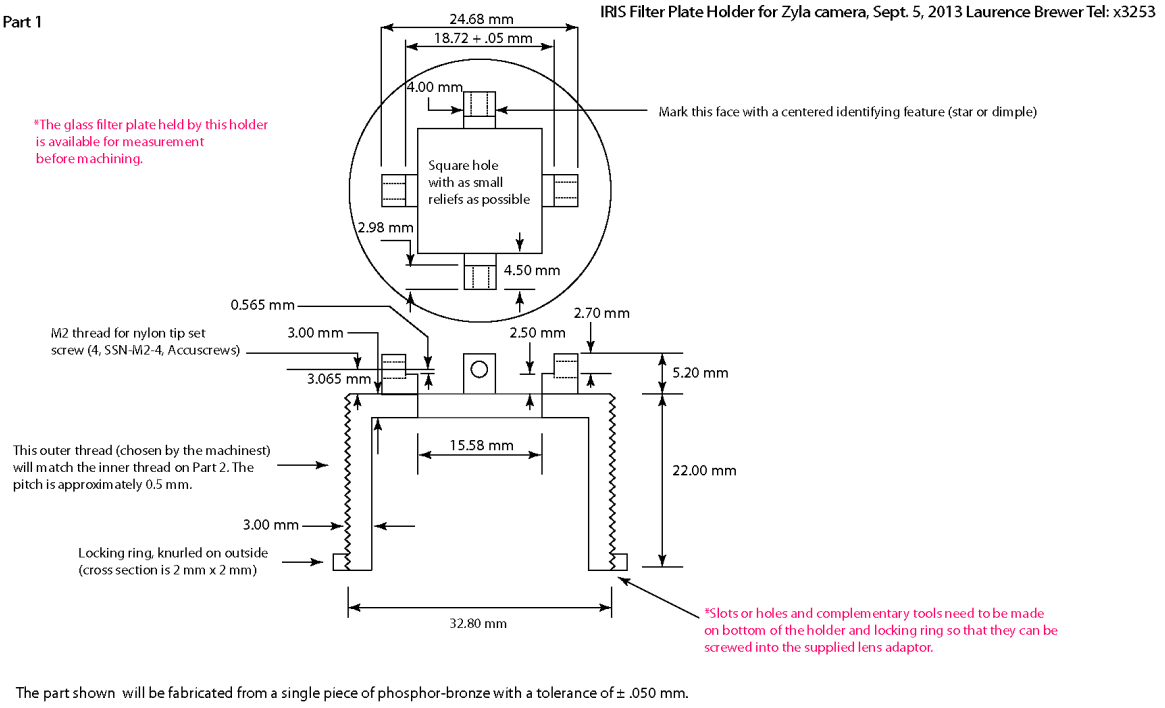

Figure 2.12: Filter plate holder design for a Zyla 5.5 camera.

The finished holders for both cameras are shown in Fig. 2.13. Once the filter plate was attached to the holder, it was attached to a T-mount SLR lens adaptor (Fig. 2.13), modified so the internal threads of the mount would match the external threads of the holder.

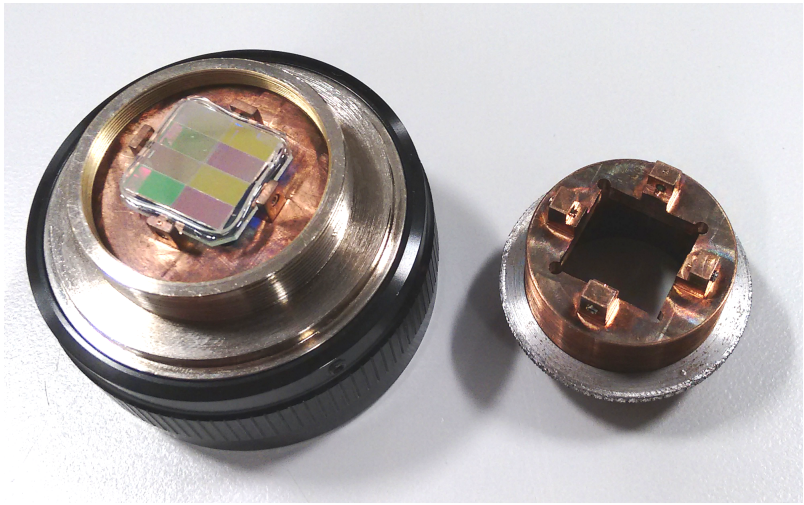

Figure 2.13: Finished filter plate holders. On the left: full filter plate assembly for a Retiga-4000R camera. On the right: filter plate holder for a Zyla 5.5 camera.

In order to assess the quality of the filters, they were attached to a CCD camera by means of the filter plate holder. Then, using a pinhole, collimated white light from a halogen lamp was directed towards them. Although the filter assemblies manufactured by *Helia* were appropriate once they were handed to us, the quality degraded after a few months. Fig. 2.14 shows one of the three assembled filter plates on the day of arrival (Fig. 2.14(a)) and two

months after (Fig. 2.14(b)). Both images were obtained with different cameras because the first one (Retiga 4000-R) was replaced by a higher sensitivity and frame rate camera (Zyla 5.5). Since the second camera had a smaller detector in one dimension, some features of the filter on Fig. 2.14(a) are not visible on Fig. 2.14(b).

There were three main features in the filter plate as shown in Fig. 2.14. The first one were reflections, which are more visible in Fig. 2.14(a) than in Fig. 2.14(b). These reflections were produced by the window in the filter plate holder (Fig. 2.11). This window is a non-coated metallic piece, so it reflected/scattered light back to the sensor. The reflections between filters were probably due to light reflected/scattered by the filter walls. The second feature were manufacturing defects on the filter surface. These defects do not change with time, and might be due to debris from sputtering in the filter manufacture or from the filters cutting. The third feature was bubbles in the filter-substrate interface and between the filters themselves. Since the aperture stop of any IRIS system would block these regions, these defects were not disruptive at the beginning (Fig. 2.14(a)), but with time they became worse by getting farther inside the filters (Fig. 2.14(b)). The same problem was observed in all three manufactured filters, which gave way to the design of the second filter plate on Subsection 2.2.2.

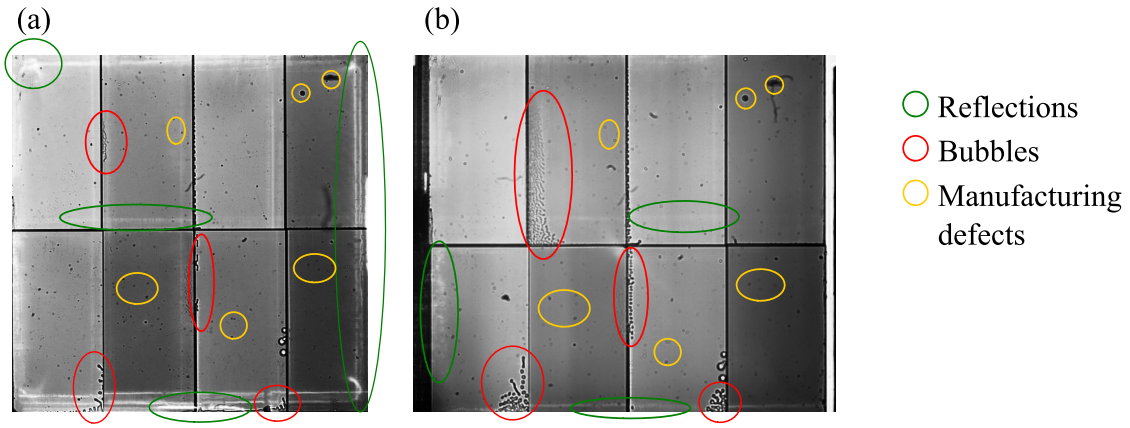

Figure 2.14: Filter plate image through collimated light, showing reflections (green), bubbles in the filter-substrate interface (red) and manufacturing defects (yellow). (a) On the day of arrival (obtained with Retiga-4000R). (b) After two months of use (obtained with a Zyla 5.5).

The second filter manufactured by *Helia* is shown in Fig. 2.15(a), where the bubbles were clearly disrupting three of the filters. In this case, doing accurate spectral analysis was not possible, since these features would change the apparent intensity of the image, giving a false spectral signature that would also vary spatially. The third filter (Fig. 2.15(b)) interfaced with IRIS shows how due to bubbles affecting four bands, spectral imaging could only be done accurately in the ROI highlighted in red, being the usable area reduced by $\sim 53\%$ of the full waveband area.

Once it was evident that the filters were not suitable for spectral imaging, *Helia* offered to re-do them, but they suffered from the same issues after a few months. We believe that the epoxy used was not properly cured, but it was not possible to verify it. In order to bypass any

need of glueing filters to a substrate, we designed a newer version of the filter plate holder, shown in Subsection 2.2.2.

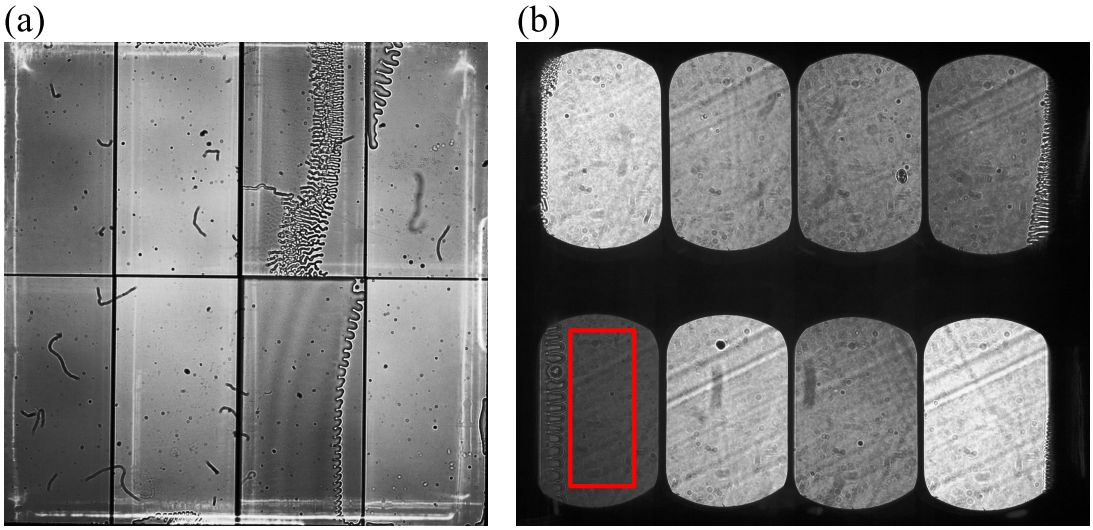

Figure 2.15: Filters-substrate bubbles of two different filter plates. (a) Severely affected filter plate. (b) Effect of bubbles in a filter plate being used with IRIS, showing in red the usable ROI of any image taken with the system.

2.2.2 Second filter plate design

To avoid the problems experienced with the first design, we decided to eliminate the need of epoxy and substrate and use a 3-D printer in order to obtain good quality pieces. The elimination of the substrate would also improve the image quality, since the addition a 1 mm glass increases spherical aberrations on the system as explained in Subsection 2.4.

This design (Fig. 2.16) was created using *OpenSCAD* and consisted of several parts, being the one which holds the filters (Fig. 2.16(c), (designed in collaboration with Laurence. R. Brewer[2])) the most critical.

The part holding the filters (Fig. 2.16(c)) are two window-frame-like pieces. The dimensions of the piece are shown in Fig. 2.17. In our experience, 3-D printers tend to reduce the dimension of sockets, so, although the specified (and measured) dimensions for the filter tiles were 3.79×7.58 mm, the sockets where the filters are placed were designed slightly larger in the x and y dimensions in order to compensate this effect. This piece was printed using an *Objet30 Prime* (*Stratasys* Ltd., UK) and was made of polypropylene. The characteristics of the material produced a piece which good elasticity, which allowed the filters to be easily placed while the piece was exerting pressure on them, effectively fixing them on place.

Parts (a) and (b) from Fig. 2.16, required less quality and a more rigid material, so they were printed of PLA using an *Ultimaker2* (*Ultimaker* B.V., UK). The flange of part (a) was designed slightly larger than the T-mount adaptor where was attached. The flange

[2]SUPA Advanced Fellow, School of Physics and Astronomy, University of Glasgow

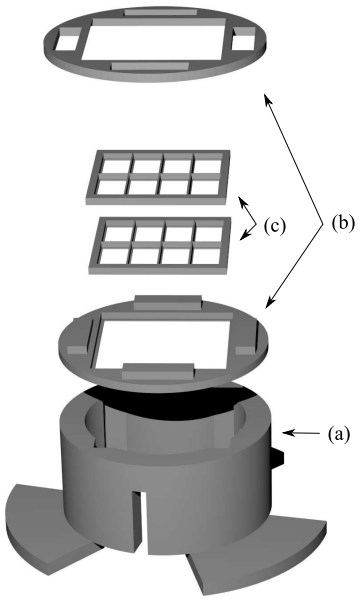

Figure 2.16: Complete 3-D filter plate holder assembly. (a) Main body attachable to a T-mount SLR lens adapter. (b) Attachable parts which hold in place part (c), being the inferior part glued to part (a). (c) Window-frame-like piece which holds in place the individual filter tiles.

complemented with the gaps allowed fixing the piece inside the mount since it made pressure against the T-mount adaptor walls. Once everything was in place and the inferior component of part (b) was glued to part (a), part (c) was then fixed in place through the pins and apertures of part (b).

The main advantage of this design over the previous one is the lack of substrate and glue in the final assembly. With this design it is possible to easily change and replace the individual filters, facilitating the selection of other wavelengths from the IRIS spectra. This increases the applicability of IRIS to other multiple spectral imaging applications since the desired wavelengths can be easily selected (Fig. 2.3).

2.3 Improved IRIS applied to oximetry

Once the filters were in place, the IRIS transmission spectra did not have any sign of spectral contamination (Fig. 2.18), but since the filters had an average of 80% transmission, the central wavelengths were reduced.

As a proof of concept, we show two examples of how IRIS performance was improved. The first example shows how the spatial information was improved by imaging a horse blood sample with a Nikon Ti-Eclipse (*Nikon*, Japan) interfaced with IRIS (more details in Chapter 3). Fig. 2.19(a) shows an image of an RBC without the filter plate next to an image of the same sample (but different cells) imaged using the filter plate (Fig. 2.19(b)). In both cases, the image corresponds to the 571 nm band. Without filter, the overlapped image corresponds to a side lobe at 610 nm (Fig. 2.18), which impedes any possibility of accurate spectral

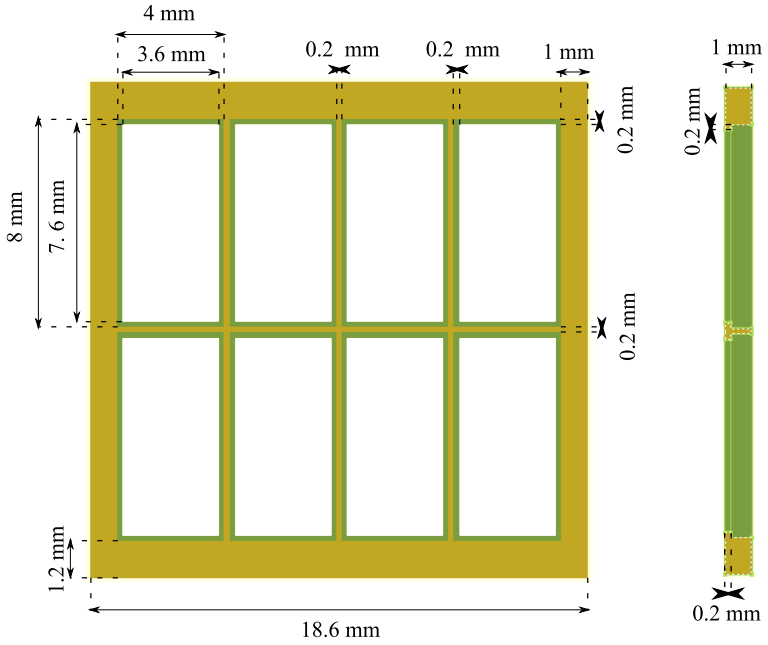

Figure 2.17: Filter tiles frame, including dimensions.

and spatial analysis, furthermore, it disrupts any attempt of registration with the other bands, specially because other bands have different wavelengths and they split in different angles. However, as can be observed, the replicated images due to the side lobes disappeared from the image taken using the filter plate.

The second example shows in more depth the effect of the side lobes and the introduced improvements. For this case, two 150 μm quartz capillaries filled with defibrinated horse blood were placed in a model eye (Fig. 2.20) with a Spectralon (*Labsphere*, US) background to simulate the sclera. One of the capillaries was 100% oxygenated while the other was deoxygenated to 0% using sodium dithionite[98] and checked using a blood gas analyser (BGA) (*OS* accuracy = 1.6%, GEM OPL blood gas analyser manual, Instrumentation Laboratory, Rev.02, 2003). The capillaries were imaged using a commercial fundus camera (*TOPCON* TRC-50DX, Japan). The sample was imaged with and without filter plate, with the broadband filter always in place, using a flash lamp as illumination and a sCMOS camera.

The results in Fig. 2.21 show the spectral improvement when the filter plate was introduced. As a first point of the analysis, it is important to consider the 571 nm band, which is meant to be isosbestic. Isosbestic points show no difference in absorption between oxygenated and deoxygenated blood, so it is a good indicator of the accuracy on the retrieved spectral information. In the case of IRIS, the 571 nm band has a FWHM of 8 nm, meaning that it is no longer an isosbestic point, although experimentally it shows a quasi-isosbestic behaviour as shown on Fig. 2.21(b). In Fig. 2.21(a) both capillaries, deoxygenated above and oxygenated below, show different intensity values in the case where the filter plate was not used (left image), while they show apparently similar intensities when the filters were in place (right image). This can be seen clearer in Fig. 2.21(b), where it is shown a line profile

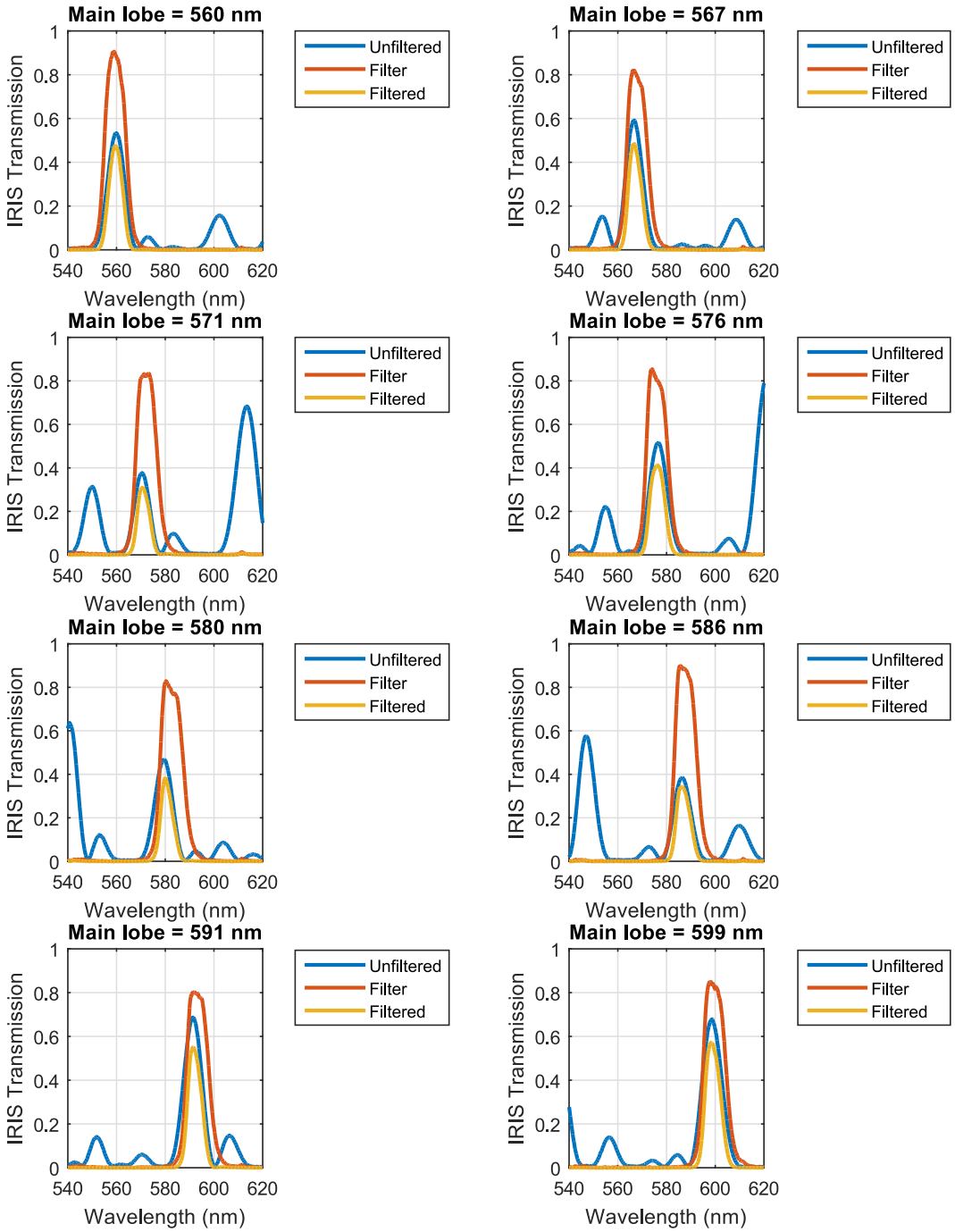

Figure 2.18: Effect of the filter plate implementation over IRIS transmission. In blue we have the raw IRIS transmission, in red we have the narrow-band filters, and in yellow we have the filtered IRIS transmission.

(red line in Fig. 2.21(a)) for both cases. In this image, the left graph corresponds to the captured image without filter plate, and both intensity profiles show different intensity minimum being 0.3 the transmission for the deoxygenated vessel and 0.44 for the oxygenated vessel, which verifies that the 571 nm is not isosbestic (Fig. 2.4(b)). On the other hand, the right graph shows how both oxygenations have approximately the same minimum. In fact, the deoxygenated vessel has a transmission of 0.176 while the oxygenated is 0.167. The reason

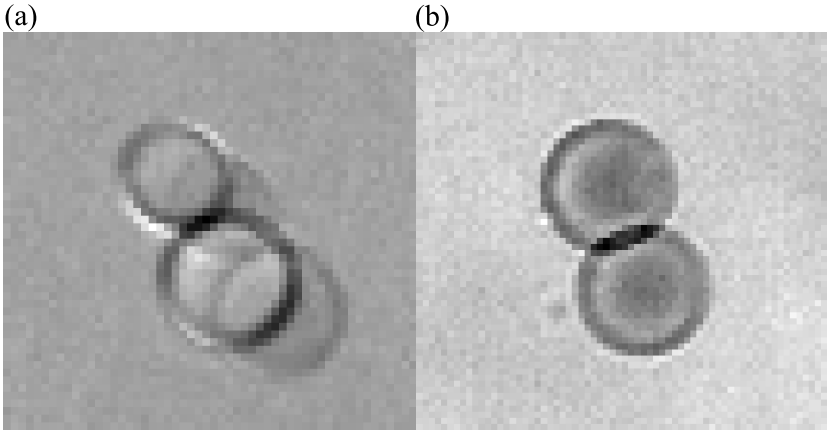

Figure 2.19: Image of horse RBCs using IRIS at 571 nm. (a) Without filter plate. (b) With filter plate.

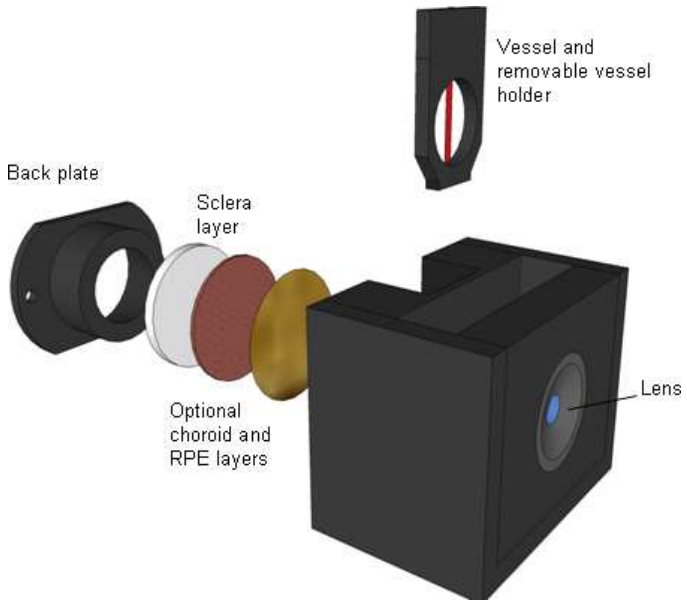

Figure 2.20: Model eye diagram. Includes a 22 mm focal length lens. In this research only the sclera layer, simulated with Spectralon, was included[3].

why they are not completely isosbestic is because the real isosbestic point is at 570.2 nm and because it is necessary to integrate across the whole transmission spectrum of the 571 nm IRIS bands. This effect is shown on Fig. 2.4(a), in which two equal modelled vessels with 0% and 100% oxygenation do not have the same transmission at 571 nm.

Finally, the complete spectral improvement is shown in Fig. 2.21(c), where the transmission spectrum of a 150 μm quartz capillary filled with 0% *OS* shows a clear resemblance with the extinction coefficient for deoxyhaemoglobin shown in Fig. 2.2 when the filter plate was used. In contrast, IRIS without the filter plate performed poorly in terms of spectrally identifying deoxyhaemoglobin, although it could be used to measure abundances if the spectra of the corresponding chromophores was previously characterised with IRIS.

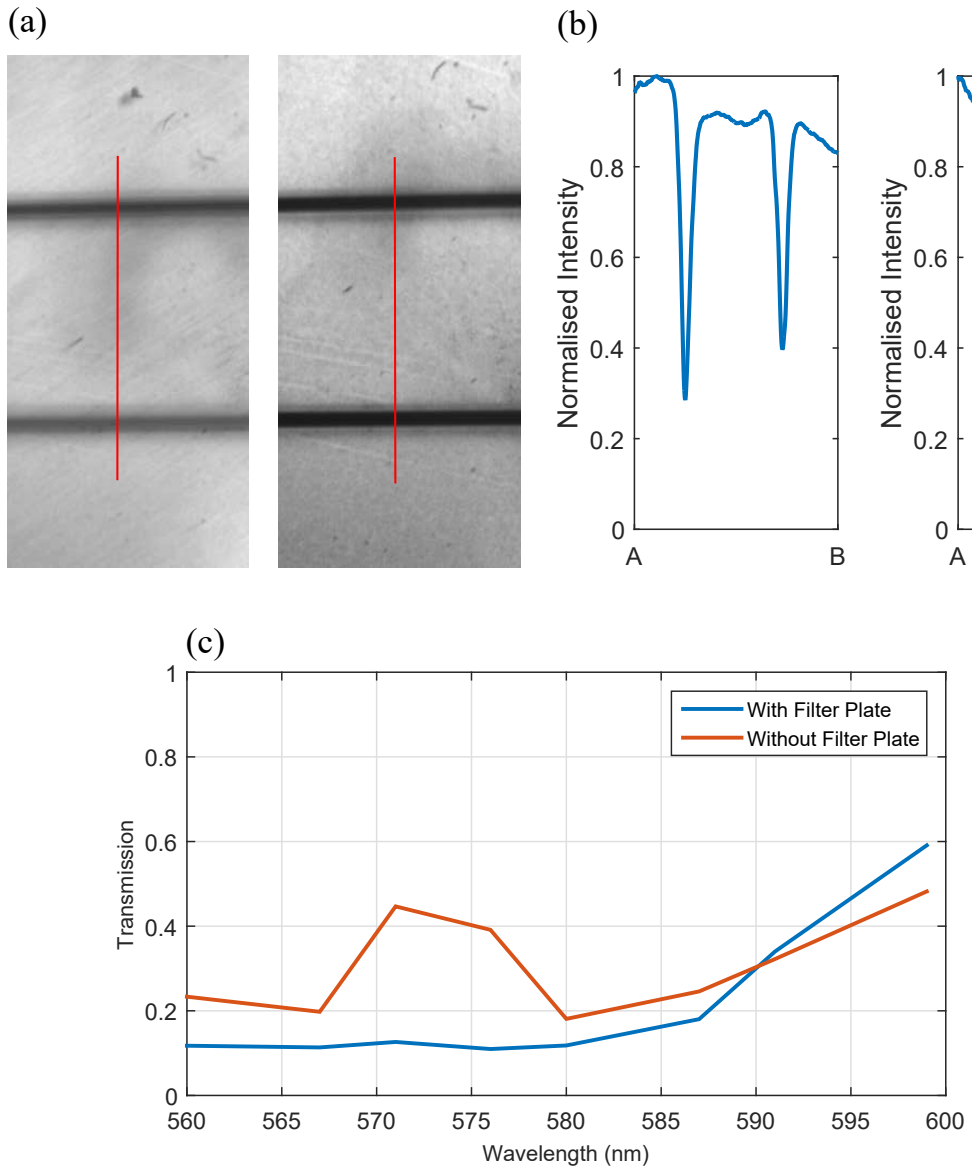

Figure 2.21: Filter plate effect on IRIS images. (a) 150 µm quartz capillary filled with 100% (lower capillary) and 0% (superior capillary) oxygenated blood imaged without filter plate (left) and with filter plate (right) at 571 nm (isosbestic point). (b) Normalised intensity profile of (a) (line profile in red) being the left one the corresponding to imaging without the filter and the right one the image captured using the filter plate. (c) 0% *OS* capillary transmission with (blue) and without (red) filter plate.

2.4 Spherical aberrations from the filter plate tiles and substrate

One concern about adding a piece of glass in the optical path where light is not collimated is the introduction of spherical aberration. In our case, the filter tiles are 1.35 ± 0.01 mm and are placed in front of the sensor, before the image comes to a focus, so it is of interest to analyse how significant these aberrations could be.

The analysis was done using *Zemax* (*Zemax* LLC, US), by modelling a system which in-

cluded a paraxial 50 mm lens of F# = 1.4 to simulate a Nikon 50 mm 1.4D lens. The model also included a glass tile of 2.26 mm thickness B270 glass to simulate filter + substrate. A second system with a 1.35 mm thickness glass was used to simulate the case without substrate. The wavelength used for the simulation was 560 nm, which is the smallest wavelength on IRIS and has the smallest Airy Disc. The results are summarised in Table 2.1 and show how the aberrated PSF is larger than the diffraction limited PSF (Airy Disc). However, these results could not be compared with a real IRIS system since this model only represented the imaging lens part of the system and was oversimplified by the use of a paraxial lens.

	Glass Tile + Substrate (2.26 mm)	Glass Tile (1.35 mm)
R_A (μm)	1.016	1.016
R_G (μm)	7.084	3.538
W_{040} (waves)	-3.08	-1.83

Table 2.1: Spherical aberrations effect for two glass thickness. R_A = Airy Radius, R_G = Geometric Radius, W_{040} = Seidel Spherical Aberration Coefficient.

For comparison with a real system, a pinhole should have been imaged through our imaging system and then the MTF analysed. This was not done because the obtained images were not qualitatively degraded. But it is important to show that some consideration has to be given to the design of the filter plate in terms of thickness.

In reality, the F# (which determines the magnitude of the introduced spherical aberrations) is ruled by the relation between the optical system F# (F_o) and the focal lengths of the collimating (f_C) and imaging (f_I) lenses in the IRIS system. If there is no vignetting by the IRIS system, the whole system F# can be expressed as:

$$F_s = F_o \frac{f_I}{f_C}. \tag{2.4}$$

A microscope objective of 100x $NA = 1.45$ has $F\# = 0.34$ in the object space, while in the image space it is $F_o = 34$. When the microscope is interfaced with an IRIS system (Chapter 3) containing two lenses $f_I = 50\,\text{mm}$ and $f_C = 200\,\text{mm}$, the F# of the system would be $F_s = 8.5$ using Eq. 2.4. Considering the imaging lens $f_I = 50\,\text{mm}$ and the system F#, the effective pupil is 5.88 mm in diameter. The spherical aberrations are shown in Table 2.2. In this case, the diffraction limited spot (Airy Radius) is larger than the Geometric Radius, which includes the geometrical aberrations. This means that spherical aberrations are negligible and the system can be considered to be diffraction limited.

A retinal camera with a $F\# = 1.2$ and 1.84x magnification has an image f-number $F_o \approx 2.2$. When the retinal camera is interfaced with an IRIS system consisting of two lenses $f_I = 50\,\text{mm}$ and $f_C = 80\,\text{mm}$, the F# of the system would be $F_s \approx 1.38$ (Chapter 4). Considering the imaging lens $f_I = 50\,\text{mm}$ and the system F#, the effective pupil is 36.2 mm in diameter. A lens aperture for a 50 mm f/1.4 SLR Nikon lens is 35.7 mm, so a small amount of vignetting

	Glass Tile + Substrate (2.26 mm)	Glass Tile (1.35 mm)
R_A (μm)	5.82	5.82
R_G (μm)	0.029	0.017
W_{040} (waves)	-0.002	-0.001

Table 2.2: Microscope-IRIS system spherical aberrations effects for two glass thickness. R_A = Airy Radius, R_G = Geometric Radius, W_{040} = Seidel Spherical Aberration Coefficient.

is to be expected, and the limiting F# is then from the imaging lens, producing the same spherical aberrations as in Table 2.1.

For the same retinal camera but considering $f_I = f_C = 50\,\text{mm}$, $F_s = F_o \approx 2.2$. This would correspond to an effective pupil of 22.7 mm in diameter, so there would not be any vignetting by the imaging lens. In this case, the spherical aberrations are smaller than in the previous retinal camera setup (Table 2.3). For the case with glass tile + substrate, the aberrated spot is $\sim 4\%$ larger in radius than the diffraction limited and might not be problematic. In the glass tile case, the Airy radius is larger than the geometrical, so it is considered to be diffraction limited.

	Glass Tile + Substrate (2.26 mm)	Glass Tile (1.35 mm)
R_A (μm)	1.543	1.543
R_G (μm)	1.601	0.952
W_{040} (waves)	-0.5	-0.299

Table 2.3: Fundus camera-IRIS system spherical aberrations effects for two glass thickness. R_A = Airy Radius, R_G = Geometric Radius, W_{040} = Seidel Spherical Aberration Coefficient.

2.5 Conclusions and future work

In this chapter IRIS has been briefly described, focusing mainly on the issues introduced by the existence of spectral sidelobes in each waveband and the Wollaston prism dispersion. It is also shown how these problems degrade the spectral and spatial resolution of IRIS as a multispectral device. Then we have shown how these problems can be easily solved by introducing a filter plate assembly. We have shown how, although the first filter holder was successful, due to external causes, it failed after a few months of being assembled and received from the company responsible for manufacturing it.

The second design improved the system in the sense that there is no need of substrate or glue, which reduces spherical aberrations and facilitates the change of filters, so IRIS can be easily adapted to other multispectral imaging applications.

Finally, we tested IRIS with the filter plate by imaging RBCs and blood-filled capillaries. These experiments showed improvements on spatial and spectral quality, effectively boosting the performance of IRIS as a snapshot multispectral imaging device.

In the future, the filter array will be adapted to different imaging applications by swapping the filters. As an example, this 8-band IRIS can be used with a filter array containing wavelengths in the blue (high haemoglobin absorption) and the red (low haemoglobin absorption) to simultaneously image red blood cells and the microvasculature.

Chapter 3

Video-Rate Oximetry of Single Red Blood Cells

Summary: This chapter describes the application of the modified retinal IRIS to oximetry of single RBCs in real time. It describes the importance of RBC oximetry and how it is possible to do it accurately and in real time thanks to IRIS. The results are shown for individual RBCs while they deoxygenate and for prepared RBC samples with a known oxygenation. The results are then compared with other techniques.

3.1 Introduction

Oxygen is transported by RBCs to other cells in the body via the circulatory system on a rapid time scale. Each RBC takes approximately 1 minute to pass through the circulatory system (capacity of the human circulatory system is ~5 L and speed of blood pumped through circulatory system by heart at rest is 5L/minute) and releases approximately half its oxygen to other cells in approximately 150 ms[99, 100]. Therefore, quantitative optical imaging of the oxygen saturation (*OS*) of individual RBCs with high temporal resolution is necessary for obtaining a fundamental understanding of how oxygen is metabolised *in vivo*. Performing oximetry of RBCs with subcellular spatial resolution may be useful for studying diseases like sickle-cell anaemia, where changes in an erythrocytes shape reflect a decrease in *OS*[101], and malaria, where haemoglobin is degraded by parasites to form the biocrystal haemozoin[102]. However, performing such oximetry can be challenging. The complex optical environment for *in vivo* measurements, including strong refraction, absorption and scattering effects[94, 103], make accurate quantification challenging, while RBC flow speeds in capillaries up to 1mm/s[104] require integration times less than 1ms, to prevent the individual RBCs from moving significantly during a measurement.

3.2 Optical system

In order to perform RBC oximetry we used a Nikon Ti-E inverted microscope with a 100x 1.45NA immersion oil objective. The image was cropped by a 23×14 mm stop aperture and collimated by a 200 mm 1:4D SLR lens. The collimated light passed through IRIS and was brought to focus by a 50 mm 1:4D SLR lens on a sCMOS (*Zyla*, *Andor*). The filter plate was placed in front of the sensor (see Fig. 3.1). The divergence angle of a collimated beam is expressed as $\theta = {}^{A}/_{f}$, being A the aperture stop dimensions and f the focal length of the collimating lens. In this case, a 50 mm focal length showed a beam with a high divergence angle, which caused vignetting from IRIS. To avoid vignetting, a 200 mm lens was used as a collimating lens. Using a shorter focal length lens would also implicate the use of a smaller aperture stop, which would have reduced the field of view. The use of a 200 mm lens demagnified the microscope output image, allowing a field of view (FoV) big enough as to include a minimum of 50 sparse RBCs in the sample and a maximum of ~ 200 packed RBCs, providing more reliable data regarding the *OS* of the sample. In this case, the stop aperture limited the FoV to $226.46 \times 138.84\,\mu$m.

A side effect of demagnifying the image was the introduction of aliasing. In a case without the IRIS system, a 100x 1.45NA microscope objective has a cut-off frequency ($f_c = \frac{2NA}{\lambda} \approx \frac{1}{\lambda F_\sharp}$) $f_c = 4.83\,\mu\text{m}^{-1}$ at λ = 0.6 μm. In order to know if it was being sampled without aliasing, it was necessary to consider the magnification of the system, which in this case is 100x. Considering magnification, the cutoff frequency was $f_c = 0.0483\,\mu\text{m}^{-1}$. The camera used was a Zyla 5.5 with a pixel size of $6.5 \times 6.5\,\mu$m, which determined the sampling frequency to be $f_c = 0.154\,\mu\text{m}^{-1}$. With this information, according to Nyquist, $2f_c < f_s$ is required to avoid having aliasing, which in this case was satisfied.

On the other hand, once the IRIS system was introduced and the image demagnified, there was aliasing. In the IRIS part of the system the beam was not vignetted, so it can be considered that the cutoff frequency was not degraded. However, the 200:50 mm lens system demagnified the image by 4, making the cutoff frequency to be $f_c = 0.193\,\mu\text{m}^{-1}$, which did not satisfy Nyquist. The existence of aliasing was not expected to be problematic. As it is seen later in this chapter, imaged RBCs (average of 5 μm diameter) are around 15 to 19 pixels in the sensor, and since most of the cell is homogeneous (especially the central part), there should not be any major negative effects due to aliasing.

3.3 Image registration

The elimination of the side lobes and ghost images by the filter plates allowed improved image registration in order to obtain a good quality spectral 3-D cube. Registration of IRIS images can be complex since they are differently affected by pincushion distortion introduced by the imaging SLR lens. In our case, the central IRIS wavebands (567 nm, 576 nm, 580 nm

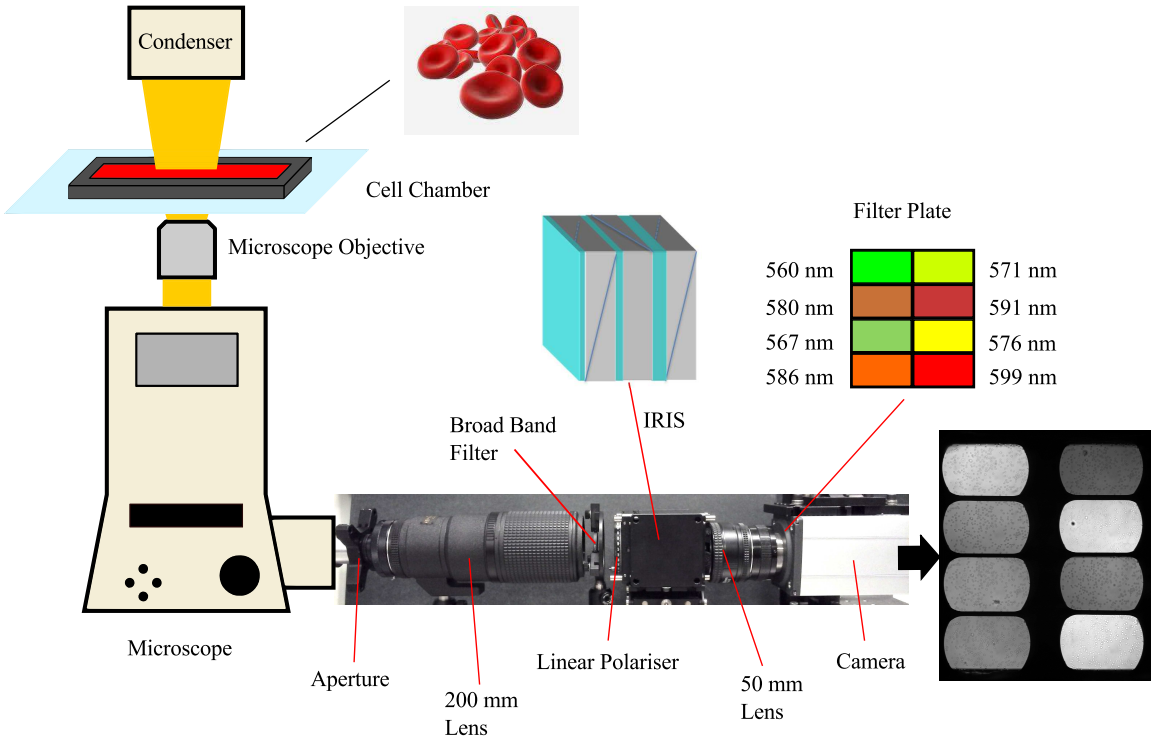

Figure 3.1: Snapshot Multispectral Imaging Oximetry. A 100x microscope objective was used to image a monolayer of RBCs attached to a coverslip in a cell chamber. Light exiting a microscope image port passed through a rectangular aperture, collimating lens, linear polariser, broadband filter (hq585/80x, *Chroma Technology Corporation*, USA), IRIS, imaging lens and filter plate before being imaged onto a camera.

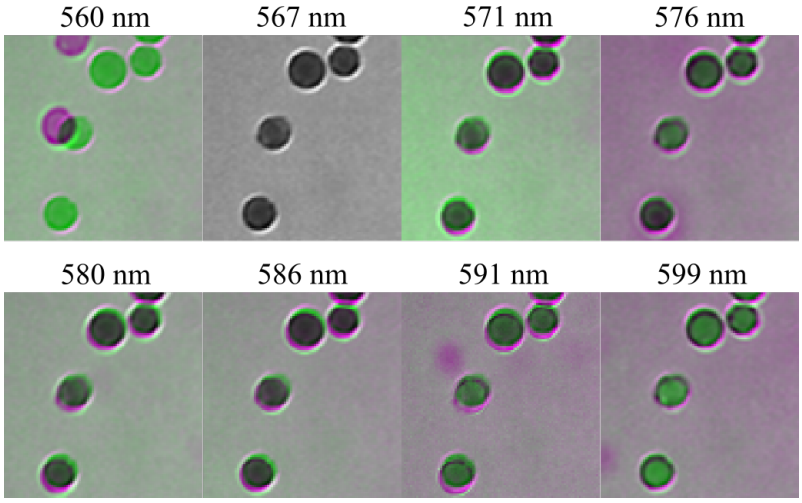

Figure 3.2: Registered RBCs through an intensity-based method. The image shows the reference image 567 nm (green) against the other wavelengths (magenta).

and 591 nm) were the less distorted bands. 567 nm was the chosen waveband to be used as a reference because it had the highest transmission of these four bands (Fig. 2.18) and was closest to the isosbestic point 570.2 nm, so it was less likely to have intensity changes under different *OS* conditions.

Image registration can be performed in an intensity-based approach, applying a high-order polynomial correction[3]. This method finds the coefficients which maximise the correlation between the IRIS images, one of them being used as a reference. In the case of RBCs, the difference in appearance due to spectral variations and the high transmission ($OD \approx 0.03$ at 560 nm and 100% *OS*), image registration tended to produce poor results (Fig. 3.2), where the RBCs was an average of 3 pixels off when compared with the reference at 567 nm and without taking into account the image at 560 nm.

Image registration was improved using a distortion target, which would allow obtaining an image transformation independent of spectral variations between wavebands. The chosen distortion target (SL3, *Photo Data Ltd* , UK) contained arrays of lines and dots with different sizes. For this application, the 5 μm-dot array was used. Maximising the correlation between corrected images by optimising the coefficients of a high-order polynomial yielded a significant improvement using the distortion target, the mean distance between the weighted centroids of the dots being $D = 0.6 \pm 0.3$ pixels, achieving subpixel resolution. However, the resulting registered image (Fig. 3.3) shows how the dots were slightly displaced, which would introduce systematic errors on spectral analysis. Another issue was that the intensity-based method used the image correlation as a metric. The main problem was that registration can fail when the features were too regular or similar, as in Fig. 3.2 at 560 nm, in which the registration produced high correlation values, but the resulting image registration is clearly poor.

Other tested methods included features detection using a SIFT[105] algorithm built in

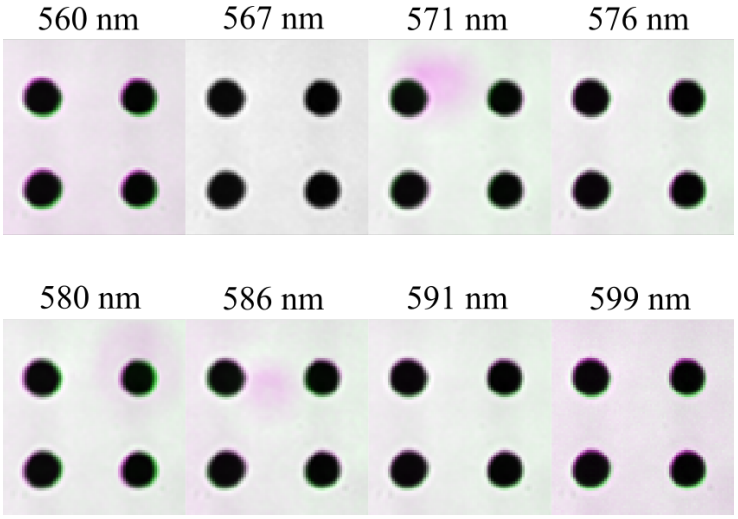

Figure 3.3: Registered distortion target through an intensity-based method. The image shows the reference image 567 nm (green) against the other wavelengths (magenta).

Matlab, but an image consisting of RBCs or dots did not offer significantly different features, making it practically impossible to match them.

In order to improve the registration, another registration method was developed, as described in the next steps:

1. Record image from dot distortion target. Using $5\,\mu$m or $10\,\mu$m dots did not provide any significant difference.

2. Obtain image without distortion target in order to obtain background.

3. Divide dots image by background image in order to flatfield the image. This removed intensity variations in the FoV. Imperfections and dust on the optical system and filter plate were eliminated or mitigated.

4. Crop regions of interest (ROI) of each waveband containing the same imaged dots.

5. Identify and sort dot centroids for each waveband.

6. Find the local weighted mean geometric transformation (built in *Matlab*) of the wavebands to the 567 nm reference. The transformation used the 20 closest points to each control point (detected centroid) to infer a second degree polynomial transformation. This produced 7 transformation structures which moved the pixel coordinates from the 7 images to match those on the 567 nm image.

7. Apply transformations using the *imwarp Matlab* function to each spectral image in order to obtain the registered 3-D cube. This function uses the obtained polynomial coefficients from step 6 to transform and correct the distorted images. The transformation is performed by applying a cubic interpolation.

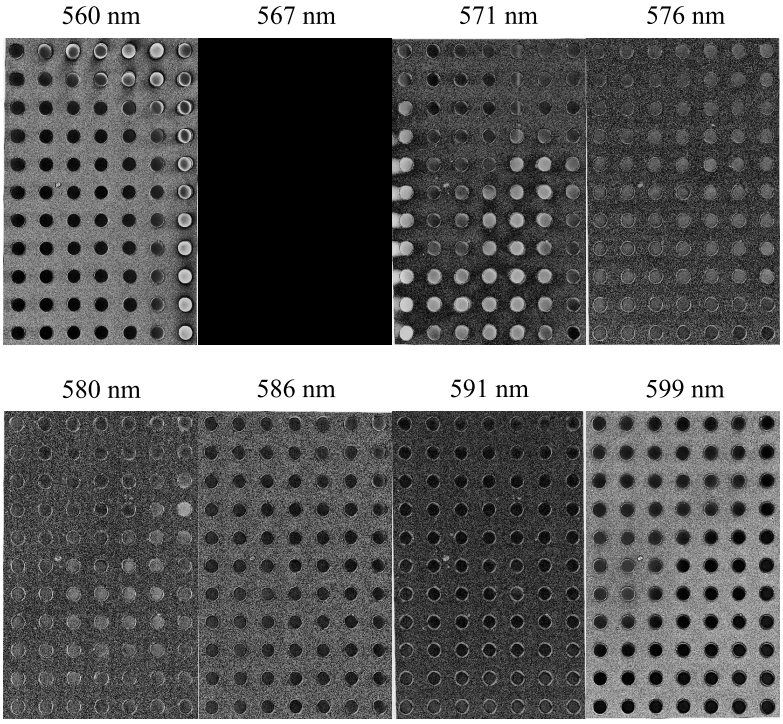

Figure 3.4: Centroid-based registration results of a distortion target. The images are created by subtracting the normalised reference (567 nm) from the other normalised images.

The results of this centroid-based transformation method are shown in Fig. 3.4. In the figure, the brighter dots belong to regions affected by filter plate defects. These dots had a different relative intensity after normalisation when they were compared with the 567 nm image. A mismatch registration or displacement would be highlighted in Fig. 3.4, but these effects were minimal. A more quantitative way of characterising the registration quality is comparing the centroids positions of the registered images. In this case, the average mismatch among dots belonging to different wavebands was of $D = 0.06 \pm 0.02$ pixels, which means a 10% improvement compared with the results obtained with other methods.

The image registration *Matlab* code can be found in the path specified in Appendix C under the names *CalibrationImWarp_Normalization_1* and *Undistort_PLUS_NORM_ImWarpImageSequence* for the calibration and the image correction respectively.

3.4 Sample preparation and image acquisition

Diluted blood was created by mixing 5 μl of defibrinated horse whole blood (*E&O Laboratories Ltd*, Scotland) in 10 ml of phosphate buffered saline (PBS) (*Fisher BioReagents*, *Fisher Scientific,* UK). The open RBC container consisted of a $40 \times 5 \times 5$ mm rectangular stainless steel frame attached to a poly-l-lysine (PLL, $1\,\mathrm{mL}/25\,\mathrm{cm}^2$, Sigma-Aldrich Co.) coated microscope cover slide (*Corning*, USA) using Parafilm (*Bemis Company*, USA). RBCs were attached to PLL, making it harder for them to move through the FoV. 1 ml of diluted blood

solution was poured into the prepared cell chamber. Removal of unattached RBCs was accomplished by removing 0.9 ml of the diluted solution and adding 0.9 ml of fresh PBS (repeated three times). The sample was imaged for 2 minutes, adding 2.7 mg of sodium dithionite to the cell chamber to deoxygenate the RBCs after 10 seconds of starting acquisition. 2.7 mg of sodium dithionite is the quantity required to deoxygenate 1 ml of whole blood[98]. In this case, a mixture of PBS and RBCs would require less sodium dithionite than 1 ml of whole blood, but it was not possible to estimate the diluted O_2in PBS so it was decided to consider the solution as whole blood to ensure complete oxygen depletion on the chamber. The extra sodium dithionite plus the 5 mm of solution between the RBCs and air minimised the chances of the RBCs reoxygenating during the 2 minutes of imaging.

The RBC container was filled with buffer exactly to the top to prevent a meniscus from forming which would modify the microscope condenser illumination. The images of individual RBCs were recorded at 30 Hz (full frame), 11-bits and global shutter, as they were deoxygenated by sodium dithionite. This rate was limited to 30 Hz by the camera used (Andor Zyla) but faster video rates are possible using other cameras.

After finishing the image sequence acquisition, an image of a PBS filled chamber was taken under the same conditions as the video sequence. The image was then used as background and the RBC images were flatfielded in order to obtain the optical density map of the video sequence (Eq. 3.1).

3.4.1 Sensor bit depth

An important factor to consider for image acquisition is the bit depth of the sensor being used. The capacity of the sensor to distinguish between two different intensity levels might be critical for accurate representation of the spectral signature of a chromophore. In addition, the bit depth might limit the data transfer and acquisition between the camera and computer, which limits the available frame rate.

The ability of different bit depths to characterise the spectral signature of RBCs can be tested by calculating the transmission of a layer of haemoglobin using Eq. 1.5 and assuming a thickness of $3\,\mu$m. Once the transmission is calculated, is then multiplied by 2^N, where N is the bit depth, and the obtained values are rounded. The results in Fig. 3.5 show how an 11 and 16-bit sensor would correctly sample the spectral signature of the RBC, while the 8-bit sensor would assign the same grey level to different wavelengths. However, an 8-bits sensor would still produce an adequate sampling of the transmission for the wavebands of IRIS (560 nm, 567 nm, 571 nm, 576 nm, 580 nm, 586 nm, 591 nm and 599 nm) because they are far apart and the transmission is different enough for these wavelengths.

In addition to accurately reproducing the transmission profile of blood, it is important to be able to differentiate between different oxygenations. To do so, Eq. 1.5 is used to generate 11 transmission profiles for 11 oxygenations from 100% to 90% in steps of 1%.

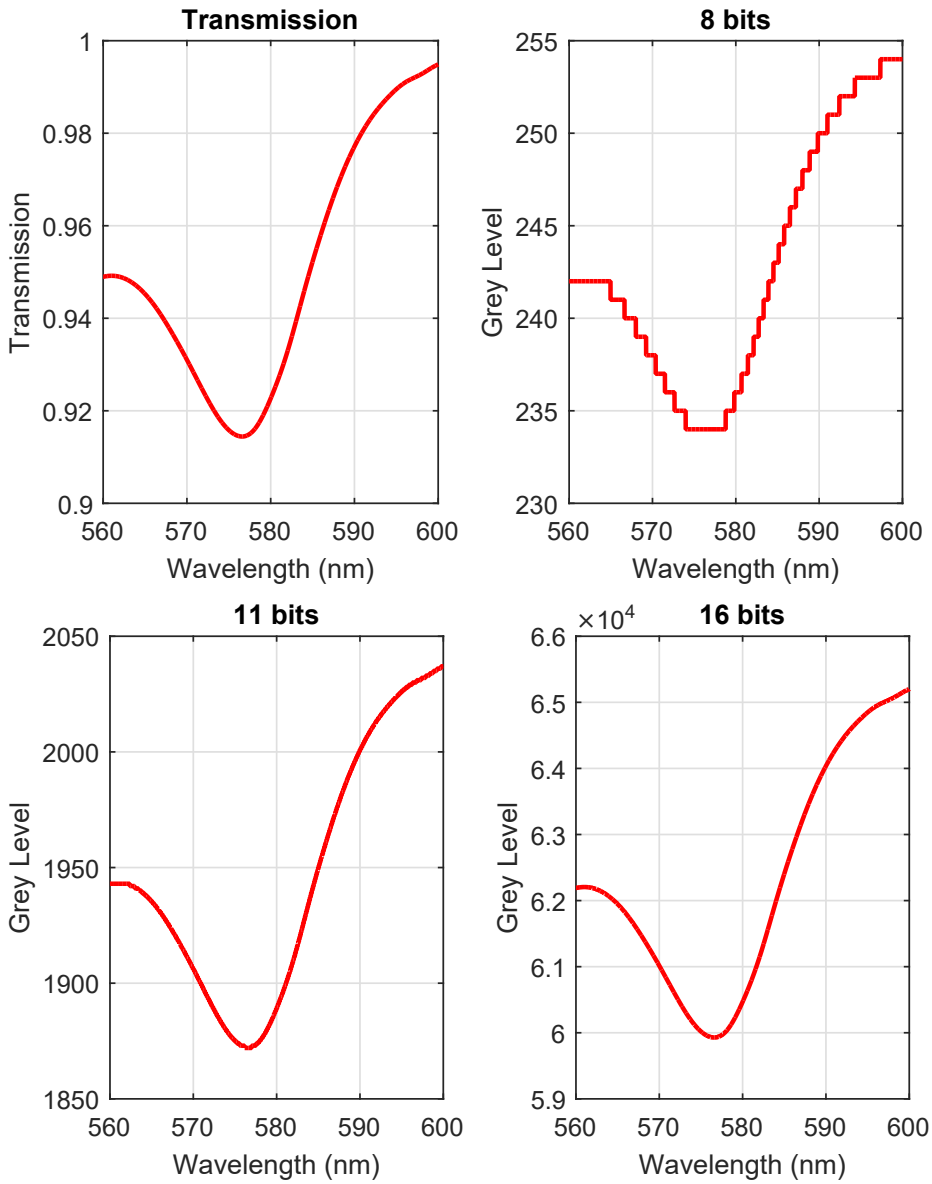

Figure 3.5: Simulated transmission of a oxyhaemoglobin layer of 3 μm and how it would be sampled by sensors of 8, 11 and 16 bits.

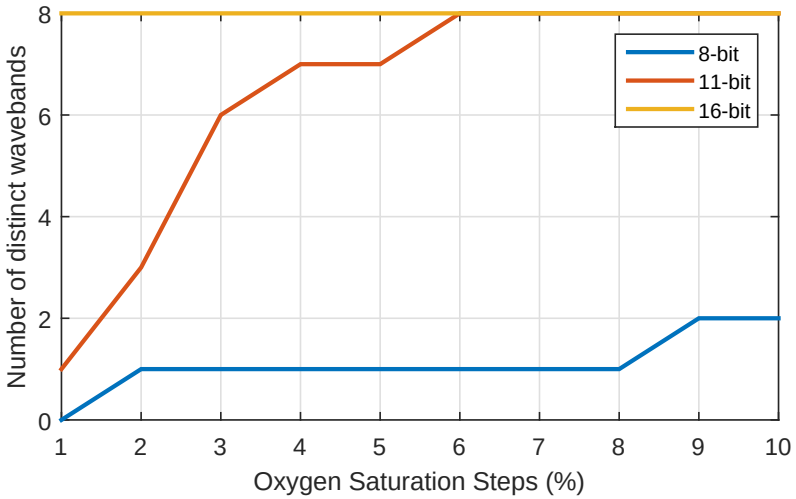

Figure 3.6: Oxygenation steps needed to fully differentiate (8 distinct wavebands) between transmissions measured by sensors with different bit depth.

Each transmission profile is multiplied by 2^N and the values are rounded as in Fig. 3.5. Using the 100% oxygenation transmission profile as a reference, the other 10 transmissions are subtracted to this reference to check how many of the 8 IRIS wavelengths produce a transmission that can be distinguished by the sensor bit depth. These measurements will show how large the oxygenation has to be so the transmission is different in the 8 wavelengths of IRIS. Fig. 3.6 shows the oxygenation steps needed so the 8 produced transmissions, one per each IRIS waveband, are different to the reference oxygenation. This figure shows how an 8-bit sensor would not be enough to differentiate between oxygenations 10% apart from each other. An 11-bit sensor would be able to distinguish between oxygenations 6% apart from each other. However, since the 571 nm waveband is quasi-isosbestic, the 11-bit sensor would have problems to distinguish between close oxygenations, so considering this factor, the 11-bit sensor would be able to distinguish oxygenations up to 4% apart. Finally, the 16-bit sensor is sensitive enough as to assign different grey levels to each waveband and each oxygenation.

This section shows how an 8-bit sensor would be unsuitable for measuring oxygen saturation variations in RBCs, while the 16-bits sensor would be the ideal candidate. However, the objective of this chapter was to observe and calculate oxygen saturation changes in real time, for which is needed frame rates up to 30 Hz. These frame rates were not achievable using a 16-bit sensor with our current camera and computer during the experiment due to problems capturing and transferring the data, so an 11-bit sensor was used instead. The use of an 11-bit sensor is expected to introduce uncertainty in the oxygenation measurements and lowers the ability to distinguish oxygenations closer than 4-6% oxygenation.

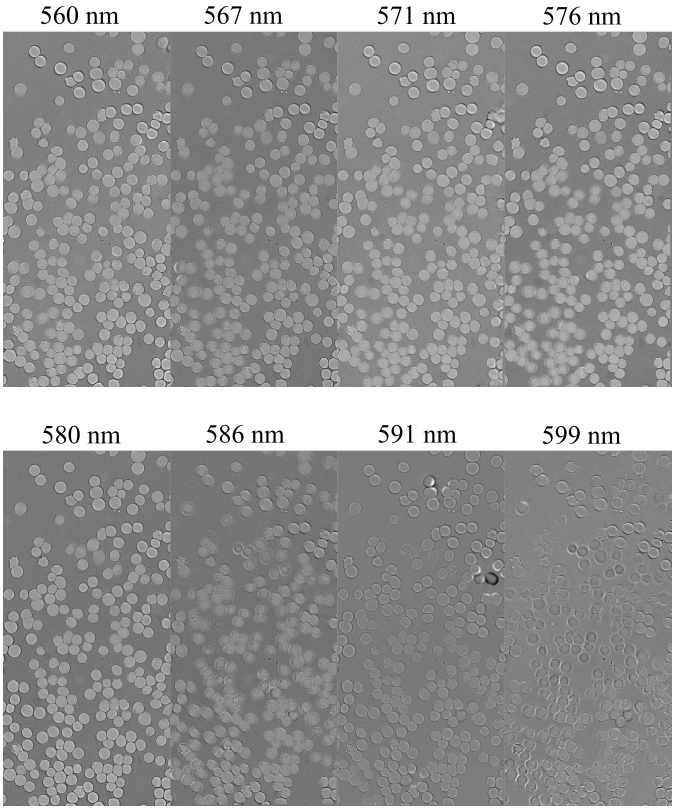

Figure 3.7: *OD* map of a 100% oxygenated RBC sample.

3.5 Data analysis

In principle, it should be possible to calculate the *OS* pixel by pixel from the RBCs using Eq. 1.5. However, each cell had an average of 170 pixels, there was an average of 50 RBCs per image and 3600 frames were taken. If the fitting process of Eq. 1.5 to the transmission of one pixel takes 10 ms, processing all the pixels belonging to RBCs would take a minimum of 3.5 days of computing time, without taking into account the RBC labelling and tracking computing time. In addition, concentration and depth are unknown and can vary from cell to cell. Instead, a linear spectral unmixing (LSU) (Eq. 1.2) approach was considered. This approach was possible because the light diffusion (only single pass) and spectral components involved in the imaging was simple when compared to that found on retinal vessels. An LSU approach was also more simple in the sense that it is not necessary to know the haemoglobin concentration, depth, extinction coefficients, scattering, illumination spectrum and bandwidth of the wavebands. In order to be able to perform an LSU analysis, the logarithm was applied to the recorded images divided by the obtained background (Eq. 3.1, Fig. 3.7). Once the *OD* map was obtained, the spectral components of blood (haemoglobin and deoxyhaemoglobin) behaved linearly with *OD:*

$$OD = -\log_{10}\left(\frac{I_{RBC}}{I_{Background}}\right). \tag{3.1}$$

For the LSU analysis to work, it was necessary to introduce the spectral components that were expected to contribute to the *OD* of each pixel in the whole image or analysed region. In our case, we identified four possible endmembers: oxyhaemoglobin, deoxyhaemoglobin, background and RBC edges. Other haemoglobin components such as methaemoglobin and carboxyhaemoglobin are usually found in small concentrations (<3%) and were ignored in the analysis. From the four endmembers, the first three are the most obvious. However, the fourth one, called edges, is most likely to result from defocus[103], refraction and scattering effects[94]. Previous work by other researchers [94, 103] show that when the RBCs are modelled as spheres, light is seen to be scattered and refracted more strongly from the edges, which is a consequence of light being propagated through a sphere and also from being imaged through a short depth of field objective such as the 1.45 NA objective used in this chapter.

In order to obtain accurate endmembers, two samples of the same blood container were obtained and one of them was deoxygenated to be 0% using sodium dithionite. The oxygen saturation was checked with a commercial blood gas analyser (GEM OPL) and 100% was obtained with the oxygenated sample while the deoxygenated showed 0% *OS*. Physiologically, arterial blood (oxygenated blood) is in the range of 96% to 98% due to the oxyhaemoglobin dissociation curve[106], which corresponds to a 100 mmHg pO_2 on the alveoli. On ambient air the partial pressure of oxygen is expected to be around 160 mmHg, which provides more oxygen that can bind with haemoglobin, producing slightly higher oxygen saturations on RBCs due to the sigmoidal behaviour of the oxyhaemoglobin dissociation curve. In our experiments it was decided to use the 100% value provided by the BGA in order to have a measured reference. 5 μl of each sample were then imaged on a microscope slide covered with a coverslip. The background was obtained with a sample containing only PBS. Both samples had 150 RBCs approximately. Using the image analysis software for remote sensing applications *ENVI* (Exelis, US), the central region of 50 RBCs (average of 100 pixels per RBC) was analysed to obtain the endmembers for oxyhaemoglobin and deoxyhaemoglobin (Fig. 3.8), which followed the behaviour shown by their corresponding extinction coefficients (Fig. 2.2). Special care had to be taken so when both endmembers were obtained 571 nm was an isosbestic point. The generated optical density map using the background and sample could differ between the oxygenated and deoxygenated references used to obtain the endmembers. These changes were produced by different water and haemoglobin concentrations between the image of the sample and the image used as background, which was obtained from a sample without RBCs. In addition, the two reference samples could have had different free haemoglobin concentrations, affecting the calculated optical density. When the oxy and deoxyhaemoglobin reference endmembers were compared the 571 nm point did not show an isosbestic behaviour. This effect was observed in multiple obtained references, so it was decided to correct the reference endmembers by adding or subtracting the appropriate *OD* to make the 571 nm band to be isosbestic.

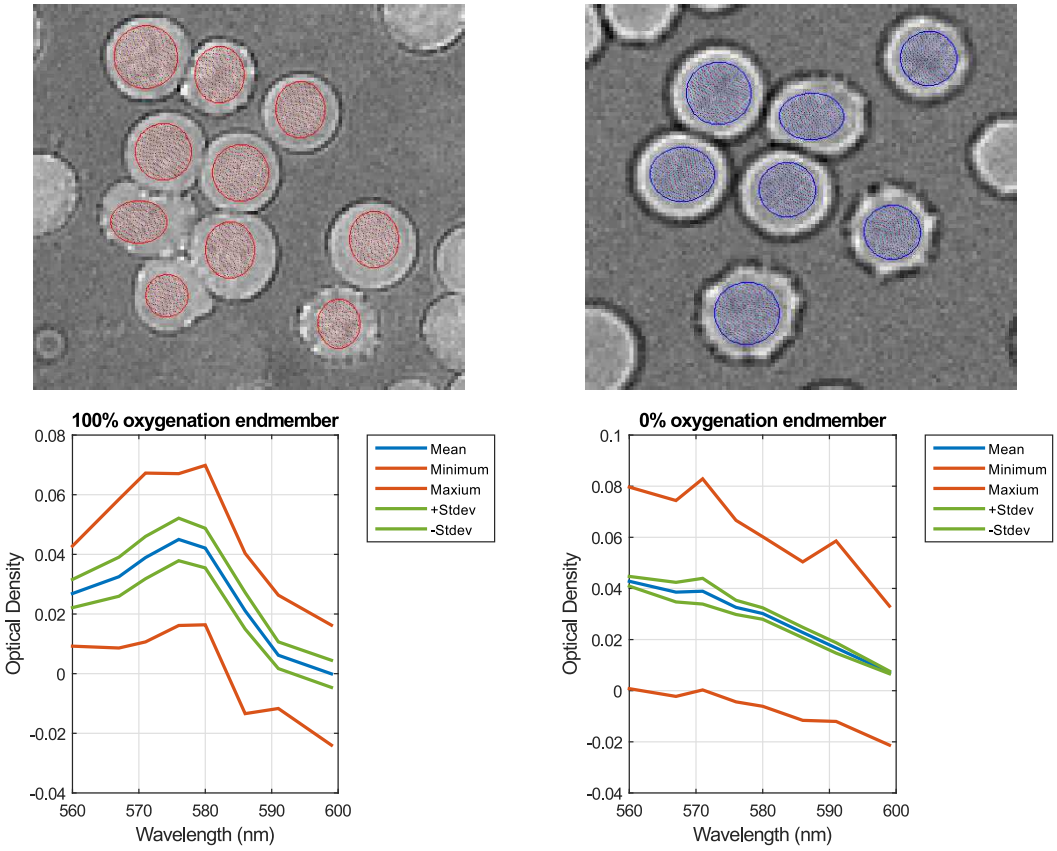

Figure 3.8: 100% and 0% oxygenation endmembers. The images of RBCs show the ROIs used to estimate the endmembers for the oxygenated (red) and deoxygenated (blue) samples. Below it is shown the retrieved optical densities, with the mean value (blue), maximum and minimum values (red) and standard deviation (green). The measured standard deviation is believed to be mainly produced by detector noise (Subsection 3.8.1, Fig. 3.19)

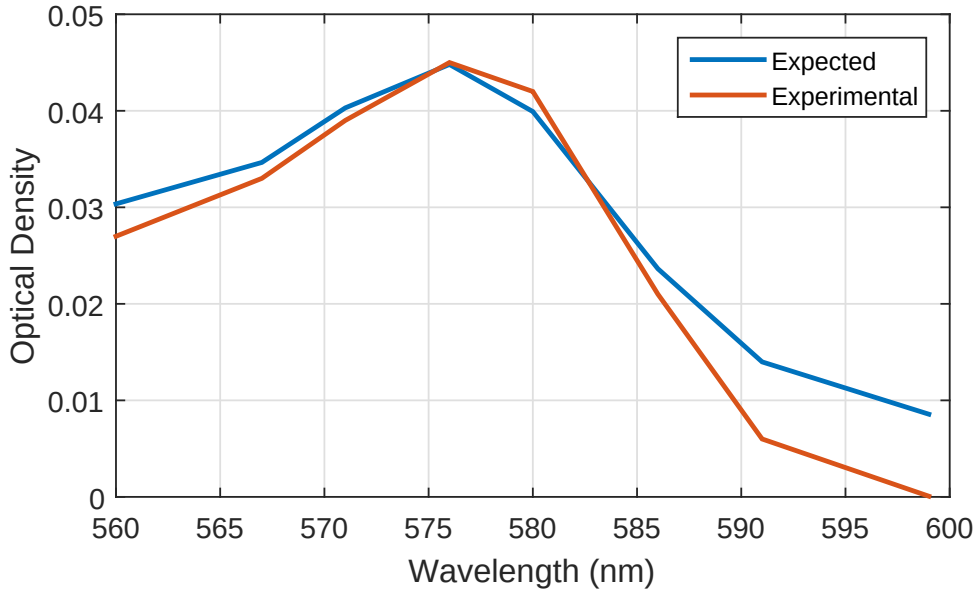

Figure 3.9: Expected (Eq. 3.2) and experimental (Fig. 3.8) optical densities.

The optical density for 100% oxygenated RBC can be compared with the expected behaviour calculated using the extinction and scattering coefficients of a layer of oxyhaemoglobin:

$$OD(\lambda) = c_{HbO_2} d \left(\varepsilon_{HbO_2}(\lambda) + \alpha_{HbO_2}(\lambda)\right), \tag{3.2}$$

where $\varepsilon_{HbO_2}(\lambda)$ and $\alpha_{HbO_2}(\lambda)$ are the extinction and scattering coefficients for oxyhaemoglobin. Horse RBCs have a shallower central pallor when compared with human RBCs, so the horse RBC is simulated by a $3\,\mu$m thickness layer of oxyhaemoglobin. The expected *OD* obtained with Eq. 3.2 is compared with the measured *OD* (Fig3.8) in Fig.3.9. Although both the expected and experimental attenuation shows a similar behaviour, there are large differences in *OD* values for the more transparent wavelengths, especially at 599 nm, showing the experimental less attenuation than the expected. The difference between the modelled and the experimental *OD* is probably due to the assumption of the RBC being a constant oxyhaemoglobin layer with a thickness of $3\,\mu$m. This assumption ignores any possible lensing effects introduced by a real RBC, which would produce a light distribution different from a layer of haemoglobin. For better comparison between the expected and experimental behaviour, a shape characterisation of horse RBCs should be performed using techniques such as OCT[107]. Once the real shape of the RBCs is known, a mathematical model including thickness variations in the RBC and the effect of lensing could be developed for a better evaluation of the experimentally obtained results.

Regarding the background and edges endmembers, these were obtained for each dataset individually (see Fig. 3.10). Illumination, focus or blood sample could vary among data sets, making the endmembers differ. As an example, a sample with more free haemoglobin

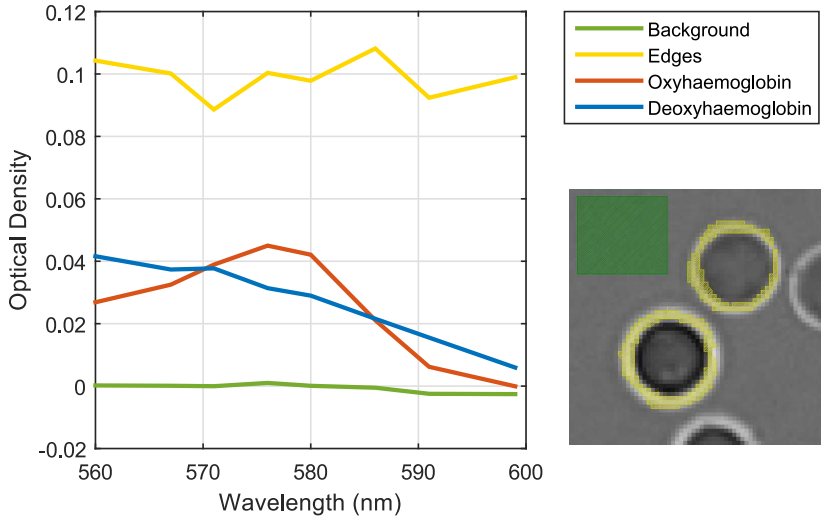

Figure 3.10: Endmembers of a typical RBC sample in the cell chamber, showing the common regions used for the background and edges endmembers.

would show a different background spectral transmission. In addition, the free haemoglobin changes the refractive index of the solution, tending to match it to the refractive index of the RBCs. As a result, refractive effects and scattering from RBCs are mitigated[108]. Fig. 3.10 shows a typical example of endmembers obtained from RBCs in a cell chamber.

Once the endmembers were characterised, an LSU algorithm built in *ENVI* was applied to the 3-D cube. In order for the results to have physical meaning, the sum of the abundances had to be equal to 1. Since there was 8 wavelengths and 4 endmembers, the system was overdetermined, being a_i the endmember abundances, C_i the endmembers and ε the residuals produced by the LSU, which should be small if the endmembers in the sample were correctly identified.

$$OD(\lambda) = a_1 C_1(\lambda) + a_2 C_2(\lambda) + a_3 C_3(\lambda) + a_4 C_4(\lambda) + \varepsilon. \tag{3.3}$$

The output of Eq. 3.3 were four abundance maps plus a residual (ε) map. For a 100% *OS* sample, the endmember maps are shown in Fig. 3.11, in which the brightness of the pixels is proportional to the abundance of the corresponding endmember. In this case, it is clear how the oxyhaemoglobin endmember was the main component in the bulk of the RBCs (Fig. 3.11(a)), while the deoxyhaemoglobin endmember was practically non-existent in the sample (Fig. 3.11(b)). Regarding the background and edges endmember, they were correctly identified in Fig. 3.11(c) and (d). Finally, the residuals (ε) (Fig. 3.11(e)) is only visible on the perimeter of the RBCs and in regions corresponding to filter plate defects.

The resulting information from the abundance maps was then used to identify the pixels belonging to RBCs. The regions identified as background and edges were in principle independent of oxygenation, so their corresponding abundances should remain constant, before, during and after deoxygenation. Because of this characteristic, the regions with a high abund-

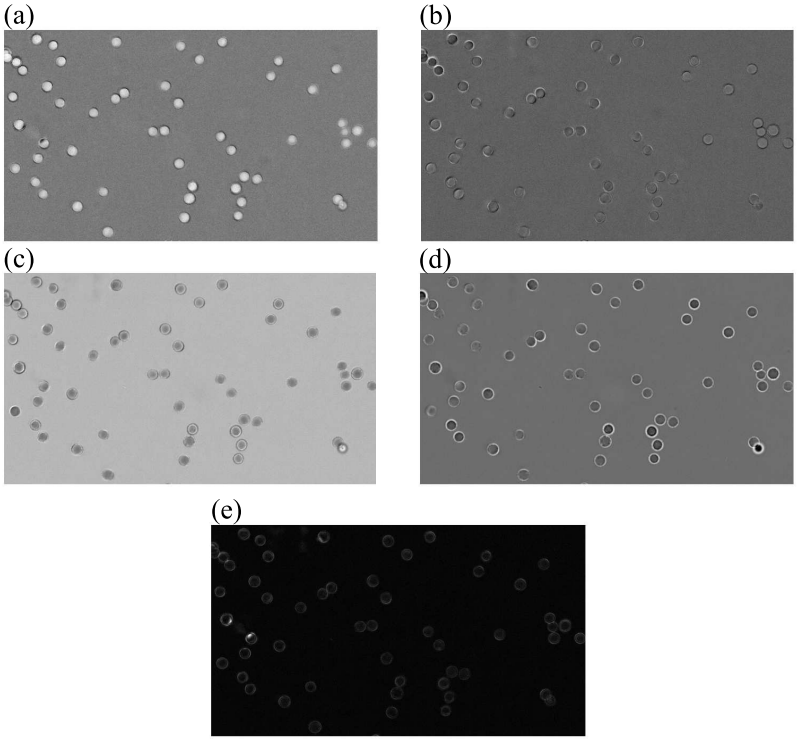

Figure 3.11: Linear Spectral Unmixing abundances results. (a) Oxyhaemoglobin. (b) Deoxyhaemoglobin. (c) Background. (d) Edges. (e) Residuals (ε) .

ance of background and edges were used to reject pixels that did not belong to RBCs. These exclusion criteria were applied by calculating the mean value of the edges and background abundances in their respective regions. Every image pixel above this threshold was then rejected from the *OS* analysis. The residuals (ε) map was also used to reject pixels since these were less likely to be formed by a combination of the introduced endmembers. Ideally, the pixels belonging to background and edges should have had a value of 1 in their corresponding abundance maps, but this was not always the case. Usually, there was free haemoglobin and there could be other RBCs floating far from the depth of field. These two factors could add some haemoglobin endmember contribution to the background, which decreased the amount of background endmember in the actual background. This effect was small and the actual background pixels usually presented background abundances higher than 0.9. In the case of the edges, since it belongs to the cell, it contained some information about the haemoglobin state. This information was masked by refractive and scattering effects, which were enhanced with defocus, so there was less information available about the haemoglobin state in defocused RBCs. This can be observed in Fig. 3.12, where the smaller abundances correspond to better-focused regions of the RBCs.

More in-depth analysis of the LSU results showed how the abundances varied for different regions of the sample. In Fig. 3.13 there are four characteristic regions. The background is shown in green, and the spectral abundance corresponding to the background is 1, while the others endmembers have abundances ~ 0 in the same region. The central region of the

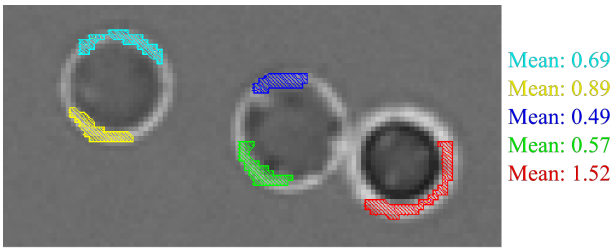

Figure 3.12: Edge abundance map showing how different regions of different RBCs have different edge abundances depending on focus. The brighter the edge abundance is, the more defocused is the RBC.

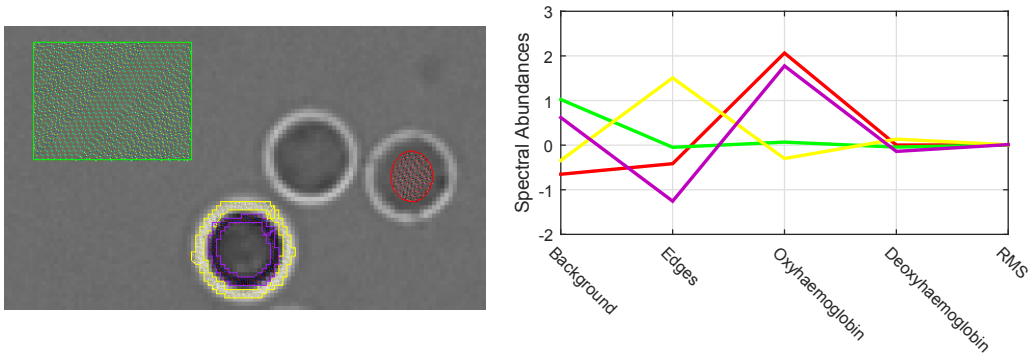

Figure 3.13: Spectral abundances of different ROIs from a 100% *OS* sample. The ROIs belong to background (green), central region of the cell (red), external part of the cell (yellow) and a region between the centre and edges (purple).

100% *OS* RBC is shown in red and there are only positives abundances for the oxyhaemoglobin endmember. The edges are shown in yellow and were also correctly identified. A more interesting case is the region in purple. This region followed an inverse behaviour to the edge region regarding the edges endmember, having < -1 abundance for this specific endmember. Although this region showed a similar behaviour to the central region in terms of oxyhaemoglobin endmember, it had negative values for the deoxyhaemoglobin endmember and, as shown in Eq. 3.6, it contributed to produce *OS* values higher than 100%. Taking into account this behaviour, pixels could be rejected to improve the oximetry as previously explained. In addition, the edges endmember was used to remove pixels belonging to regions like the purple ROI on Fig. 3.13. Another conclusion from Fig. 3.12 and Fig. 3.13 is that the edges (positive and negative values) tended to be more prominent in terms of area when the RBCs were more defocused, which matches results from the literature[103, 109, 110].

Once the pixel rejection was applied, it was possible to do oximetry using the oxyhaemoglobin and deoxyhaemoglobin abundances on the RBCs. These endmembers are defined as:

$$OD_0 = cd\,(\varepsilon_{Hb} + \alpha_{Hb})\,,$$
$$OD_{100} = cd\,(\varepsilon_{HbO_2} + \alpha_{HbO_2})\,, \tag{3.4}$$

where OD_0 and OD_{100} refer to experimentally measured endmembers for 0% and 100%

OS. c, d, ε_{Hb}, ε_{HbO_2}, α_{Hb} and α_{HbO_2} correspond to haemoglobin concentration, pathlength, oxyhaemoglobin and deoxyhaemoglobin extinction and scattering coefficients[111]. Each pixel has a combination of these two endmembers, represented by their abundance:

$$\begin{aligned} A \cdot OD_0 &= c_{Hb} d \left(\varepsilon_{Hb} + \alpha_{Hb}\right), \\ B \cdot OD_{100} &= c_{HbO_2} d \left(\varepsilon_{HbO_2} + \alpha_{HbO_2}\right), \end{aligned} \tag{3.5}$$

where A, B, c_{Hb} and c_{HbO_2} are the abundances and concentrations of oxy- and deoxyhaemoglobin respectively. Using Eq. 3.4 and Eq. 1.4 yields:

$$OS = \frac{c_{HbO_2}}{c_{HbO_2} + c_{Hb}} = \frac{B}{B+A}, \tag{3.6}$$

which allows the calculation of *OS* from the oxy- and deoxyhaemoglobin abundance maps generated by the LSU (Fig. 3.11(a) and (b)). This *OS* map contains only pixels belonging to RBCs thanks to the application of the pixel rejection previously explained.

3.6 Measurements of oxygen saturation of deoxygenating RBCs

Once the *OS* map of the sample was generated, it was possible to characterise the *OS* distribution and evolution in the sample and in individual RBCs.

In the first place, *OS* distribution in an individual RBC is shown. Fig. 3.14 shows an oximetry image of a single RBC with nominal 100% *OS* and a histogram of the pixel oximetry frequencies. The camera frame rate (30 Hz) was limited only by the maximum allowed by the camera maximum frame rate, the camera link transfer speed and the computer writing speed. Frame rates as fast as 100 Hz are possible using other cameras. The most consistent determination of the *OS* of each cell was obtained by taking the mean value of the *OS* values within a circle of radius 4 pixels centred in the middle of the cell (see the justification in Section 3.8). An example of this circular ROI is shown in Fig. 3.14(a) in yellow. This region contains 69 pixels, which is $\sim 30\%$ of an RBC with a radius of 9 pixels ($\sim 5\,\mu$m). The *OS* of these pixels had a mean and standard deviation of $102.0 \pm 9.0\%$. Ideally, with our system it should have been possible to observe *OS* changes with a spatial resolution of $0.2\,\mu$m (100x objective 1.45 NA, at 600 nm). However, there was aliasing due to the demagnification introduced by the IRIS system as previously shown and it was not possible to distinguish features smaller than $0.5\,\mu$m. *OS* changes on this scale could be recorded, although it was not possible to artificially induce *OS* changes at this spatial scale in order to verify it. Another reason why it was not possible to record internal *OS* changes is that the haemoglobin oxygen uptake is ~ 3 ms[99] which suggest that oxygen interchange among haemoglobin proteins happens in this timescale, making it impossible to observe internal *OS*

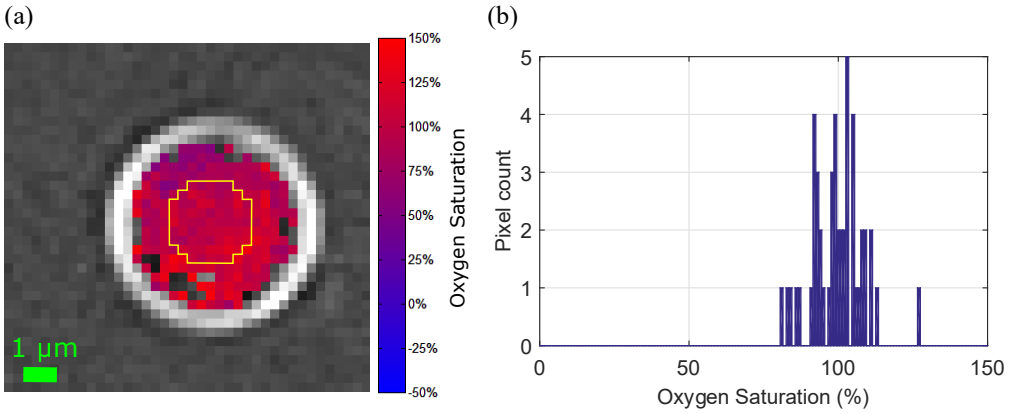

Figure 3.14: (a) Image of a single RBC with nominal 100% *OS* (determined by blood-gas analyser measurement of blood). The oximetry of each pixel within the cell is indicated by the legend on the right. The pixelated yellow circle indicates the region used for consistent oximetry. The black, grey and white pixels correspond to values of optical density. (b) Histogram of pixel oximetry *OS* values inside the yellow circle displayed in (a).

changes using an exposure time of 33 ms. In addition, RBCs are $\sim 92.8\,\text{fL}$ and during the experiment 2.7 mg of sodium dithionite are dissolved without control so it was unlikely that any gradient would have been observed by sampling at 30 Hz.

The distribution of haemoglobin *OS* values within the RBC is displayed in the histogram in Fig. 3.14 (b). The histogram shows dispersion around the main value, which could be explained by detector noise due to its apparent Gaussian-like shape. This distribution produces oxygenation values higher than 100% (and below 0% for deoxygenated RBCs), which do not have physiological sense, but because the LSU can produce negative abundance values of the oxy- and deoxyhaemoglobin endmembers, *OS* can reach these values for some pixels (Eq. 3.6). A more detailed explanation can be found in Section 3.8.

Once the *OS* map of a single RBC was characterised, the RBC deoxygenation process could be analysed. Previously it has been stated that images were recorded for 120 seconds, but the deoxygenation of the RBC took approximately 2.6 seconds, so the data shown here is for a period of 24 seconds, with the deoxygenation happening in approximately the central region of the sequence (Fig. 3.15(d)). Fig. 3.15 (a)-(c) shows three characteristic states of the same RBC during the deoxygenation process. The first image corresponds to the beginning of the image sequence when the RBC was completely oxygenated, with $OS = 102.0 \pm 9.0\%$. 10 seconds later the sodium dithionite was added. The second image corresponds to 12.5 seconds after the beginning of the recording, with $OS = 40.0 \pm 9.0\%$. 12.5 seconds correspond to the time when the whole sample was $\sim 50\%$ oxygenated. Finally, the third image corresponds to the end of the sequence, when it was completely deoxygenated, having $OS = -2.0 \pm 9.0\%$. Fig. 3.15(d) shows how the deoxygenation took approximately 2.6 seconds after the dissolved sodium dithionite reached the imaged RBC.

During the equilibrium states, it can be argued that the RBCs do not change their *OS*, so the uncertainty in the mean oxygenation of the single RBCs and the whole sample can

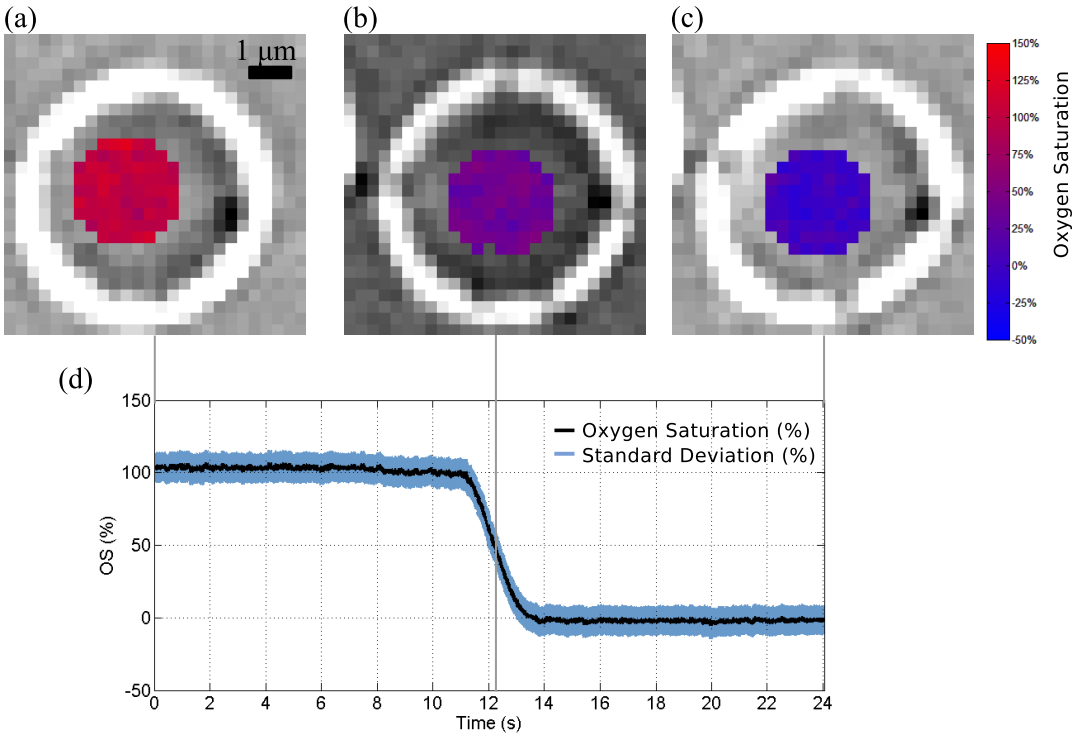

Figure 3.15: Single RBC deoxygenation (a)-(c) Oximetry images taken from a 30 fps video segment of the deoxygenation of a single RBC in buffer containing sodium dithionite (2.7 mg/ml, added at 10 seconds). Selected images recorded at 0, 12.5 and 24 seconds are indicated by grey lines. (d) Change in oxygen saturation as a function of time. The mean *OS* (black line) and the standard deviation (blue region) are displayed.

be given by the standard error of the mean. Considering the standard error of the mean, the uncertainty was $\pm 1.1\%$ *OS* for the three analysed cases, which showed the accuracy of the method.

For comparison purposes, the same RBC was analysed using a 2 wavelengths calibration method based on the Beer-Lambert law (Eq. 1.8). Using the 571 nm and 599 nm wavebands and the *ODR* for 0% and 100% *OS* as references, we obtained $OS = 284 \pm 875\%$ prior to deoxygenation and $OS = 20 \pm 611\%$ after deoxygenation. The error is produced mainly by the fact that RBCs are highly transparent, with $OD \approx 0.03$ at 560 nm and 100% *OS*, which made them highly sensitive to noise effects. Using eight wavelengths rather than two produces a better spectral characterization of the haemoglobin spectrum, reducing errors in *OS*. The addition of wavelengths should reduce the error in $\sqrt{N}$, being N the number of used wavelengths. In this case, we believe that the use of only two wavelengths, the low *OD* of the RBCs and the detector noise tend to introduce high variability in the two used points, producing errors in oximetry as the ones shown previously.

The RBC in Fig. 3.15 was analysed from a region of the sample that contained a population of 40 RBCs in the FoV, although this quantity varied during the image sequence. Some RBCs were pushed through the FoV by the addition and dissolution of the sodium dithionite. Some RBCs also spontaneously haemolysed, releasing haemoglobin and leaving only the

cell membrane. Since internal changes were expected to be faster (~ 3 ms [99]) than the exposure time (33 ms), in this analysis only the mean *OS* of the individual cells was used. The *OS* evolution of the RBCs on the FoV is shown in Fig. 3.16. The shown images correspond to 0, 12.5 and 24 seconds as in Fig. 3.15. In the first image there was no sodium dithionite in the solution (Fig. 3.16(a)), so the RBCs were highly oxygenated, with the analysis showing $OS = 103.7 \pm 14\%$. In these cases the error is the standard deviation of the mean *OS* from the RBCs population in the FoV. At 10 seconds the sodium dithionite was added, then at 12.5 the RBCs reached medium deoxygenation (Fig. 3.16(b)) with $OS = 49 \pm 15\%$. Finally, when they were fully deoxygenated (Fig. 3.16(c)) (24 seconds to make sure the measurement is stable) the oximetry analysis showed $OS = -5 \pm 9\%$. Fig. 3.16(d) shows the *OS* evolution of the sample, which was generated by using the mean *OS* of the individual RBCs, then the black lines correspond to the mean *OS* of the mean corresponding to all RBCs in the FoV. In this case, the standard error of the mean was $\pm 2.2\%$, $\pm 2.4\%$ and $\pm 1.4\%$ *OS* for the oxygenated image, the deoxygenation image and the deoxygenated image respectively.

The excess of sodium dithionite in the RBC buffer might have minimised the standard deviation at the deoxygenated stated compared to the standard deviation at 100% *OS*. This excess would reduce the chances of any free O_2 in the solution and would have forced the RBCs to be completely deoxygenated. Since the RBCs are in PBS, in the oxygenated case the partial pressure might be lower than the atmospheric, meaning that it might be lower than 100%, probably being distributed around 97% *OS*. In this case, there was not an independent method of checking the oxygenation of the RBCs such as a blood gas analyser (BGA), so it was assumed that the sample had the measured oxygenation by the BGA prior to prepare the sample with PBS.

The existence of values higher than 100% and below 0% can be also explained by how the analysis was performed. The endmembers were obtained by averaging the *OD* in a reference sample, which then was applied to a different sample, so differences in *OD* can be expected, especially in terms of spatial differences, which would introduce systematic errors.

The use of the first and last frame in the sample from Fig. 3.16 as endmembers should have produced values of 100% and 0% *OS* at least for the first and last frame. The oximetric analysis showed $OS = 105.9 \pm 14.3\%$ at $t = 0$ s, $OS = 50.8 \pm 14.4\%$ at $t = 12.5$ s and $OS = -4.2 \pm 10.2\%$ at $t = 24$ s. The main reason behind this effect is that production of the endmembers was pixel based while the calculation of the *OS* values was the mean of the mean *OS* of the RBCs in the FoV. Systematic errors introduced by the imaging system across the FoV would imply that the behaviour might differ between a pixel-based analysis and an RBC analysis.

In order to assess the stability and repeatability of the measurement, the *OS* variation of the frames from 0 to 8 seconds and from 16 to 24 seconds in Fig. 3.15 (d) and Fig. 3.16(d) were considered. These temporal regions are chosen because the first corresponds to the sample before adding sodium dithionite, and the second corresponds to the sample

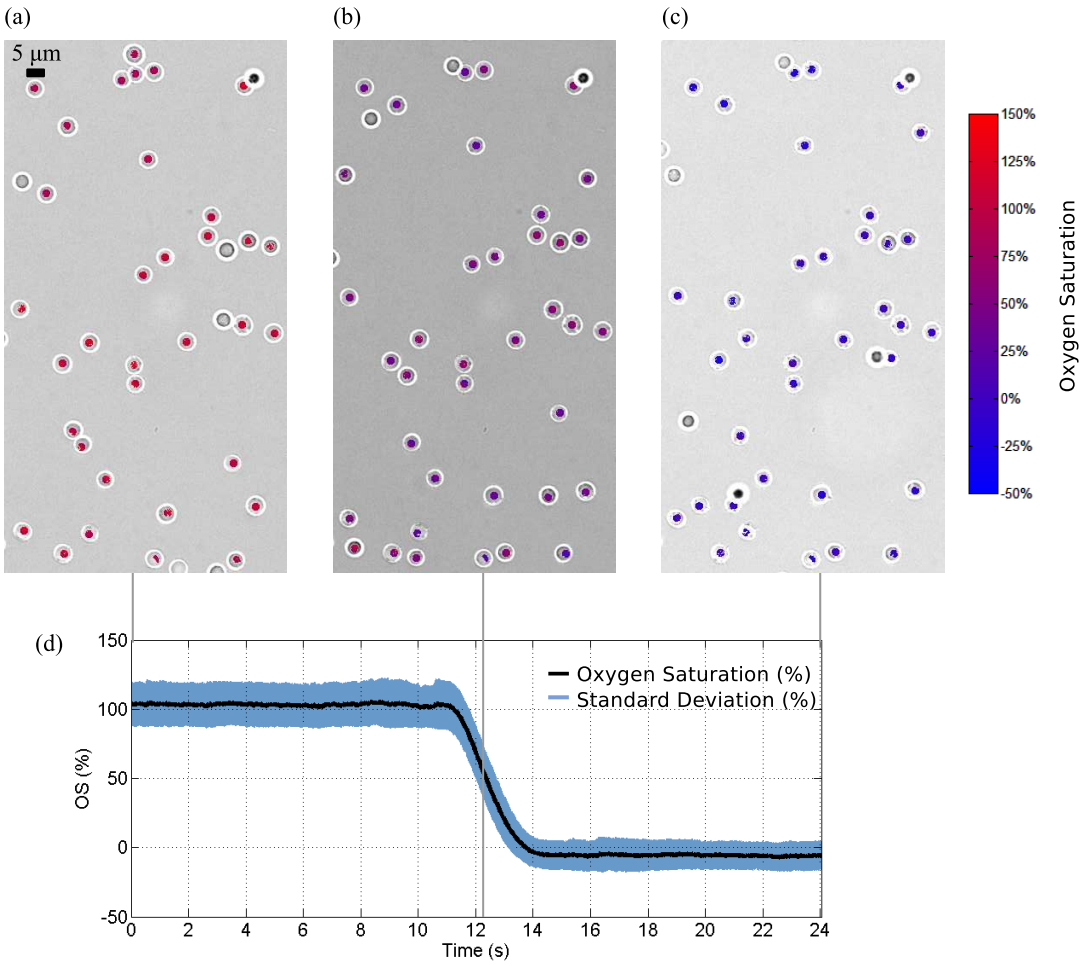

Figure 3.16: Deoxygenation of 40 RBCs. (a)-(c) Images of the deoxygenation of 40 RBCs in PBS containing sodium dithionite at 0, 12.5 and 24 seconds as indicated by grey lines. The *OS* of the RBCs is represented by the legend shown on the right. Uncoloured cells contained pixels with significant errors and abundances belonging to endmembers other than oxy- and deoxyhaemoglobin. (d) Mean oxygenation of the RBCs (black line) and standard deviation (blue region). The standard deviation was 14% prior to the start of the deoxygenation (<10 seconds) and 9% after deoxygenation (>14 seconds).

once it has been deoxygenated. Each region contains 234 frames, so the analysis of how the *OS* varies in these regions is a good repeatability and stability metric of the technique. The analysis produced an oxygenation standard deviation of 1.17% and 0.88% for the single cell (Fig. 3.15) at the oxygenated and deoxygenated states respectively. In this case, the standard error of the mean is 0.55%, which is in the same order of magnitude as the standard deviation, showing that the *OS* is stable during the experiment. In the case of the whole sample (Fig. 3.16), the oxygenation standard deviations were 0.66% and 0.56% for the oxygenated and deoxygenated states while the standard error of the mean are 0.86% and 0.55% for the oxygenated and deoxygenated cases respectively. These results show how this technique offers optimal repeatability and stability. No other techniques have performed oximetry over the same RBCs with this repeatability.

3.7 Accuracy of individual RBC oximetry

To determine the accuracy of the technique, the oximetry measurements were compared with a blood gas analyser (BGA) (*OS* accuracy = 1.6%, GEM OPL blood gas analyser manual, Instrumentation Laboratory, Rev.02, 2003). This was achieved by controlled deoxygenation using sodium dithionite, being 100%, 89.2%, 79.4%, 58.9%, 37.3%, 19.4% and 0% the oxygenations measured with the BGA. The seven samples were prepared in the same way the 0% and 100% reference samples in Section 3.5: 10 μl of the bulk blood was laid between a microscope slide and a coverslip to produce a monolayer of approximately 150 RBCs. Fig. 3.17 shows a graph comparing the *OS* values obtained using these two different methods, being the BGA measured *OS* used as a reference since the oxygenation could not be obtained through more reliable methods at the moment. The standard error of the estimate (a measure of repeatability obtained from the data and the corresponding regression line) of each sample was 10.7% and the standard deviation, averaged over the seven different sample *OS* measurements was 6.7%. When considering the repeatability, it is also important to consider the standard error of the mean, which in this case is 0.5% when the average standard deviation and 150 RBCs are considered, showing high repeatability on the spectrally calculated *OS*.

In overall, the spectrally calculated oxygenations on Fig. 3.17 were higher than the measured with the BGA. This effect might have been produced by reoxygenation of the sample. Since we used a 10 μl blood sample, such a small volume had high chances of being partially reoxygenated during the sample preparation. The spread in mean oxygenation in the sample, represented by the standard deviation, might be explained by size differences between cells, defects on the cell membrane and other systematic errors as is explained in the following section.

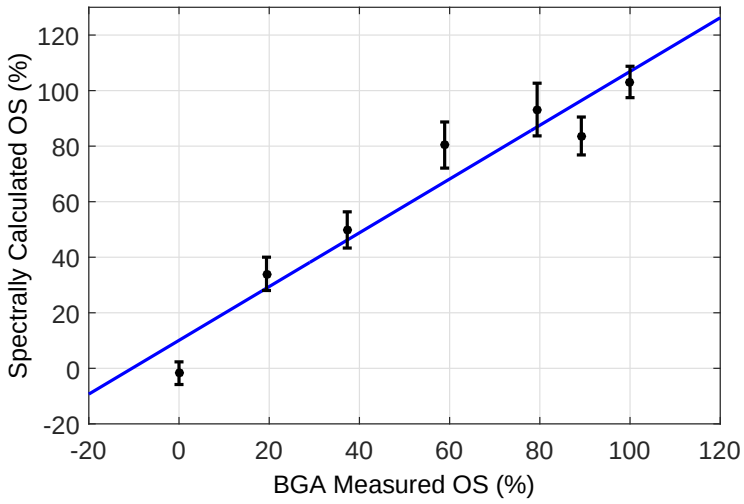

Figure 3.17: Comparison of the spectrally calculated *OS* with the measured values provided by the blood gas analyser (BGA). Average *OS* of $\sim$ 150 RBCs (black dots) values taken at 33 ms exposure time are displayed and compared to seven different bulk blood oxygen saturation values determined using a BGA. The standard deviation is obtained from the individual mean oxygenations of the 150 RBCs. The blue regression line is fit to the *OS* data for the 150 RBCs. The repeatability of the measurement of *OS* (standard error of estimate) for the RBCs was 10.7% while the mean standard deviation of the seven *OS* measurements was 6.7%.

3.8 Sources of errors

The previous section has shown how the LSU produced values higher than 100% and lower than 0%. This was due to negative calculated values of the deoxyhaemoglobin abundance for the first case, and negative calculated values of the oxyhaemoglobin for the second case. Another contribution was non-uniform measured *OS* distribution inside the same RBC (Fig. 3.14 (b)). Although these non-uniformities were measured in several RBCs it is likely that they were produced by tilted RBCs or systematic errors introduced by the system, because from a physiological point of view each RBC should be in oxygenation equilibrium if undisturbed. In the following sections, the sources of these errors are analysed.

In Fig. 3.18 are shown the *OS* histograms of a sample in the cell chamber at different oxygenations. Fig. 3.18 (a)-(c) shows the histogram for a single RBC, with a standard deviation of 9% *OS*. Fig. 3.18(d)-(f) show the histogram of all the pixels belonging to RBCs in the FoV, with a standard deviation of 18% at $t = 0\,\mathrm{s}$ and $t = 12.5\,\mathrm{s}$, while $t = 24\,\mathrm{s}$ had a standard deviation of 14% *OS*. Fig. 3.18(g)-(i) shows the histogram of the mean OS of each RBC in the sample with a standard deviation of 14%, 15% and 9% *OS*. As stated before, undisturbed RBCs from the same sample should all have approximately the same *OS* and there should not be any spatial differences on oxygenation, but these histograms show otherwise, pointing to systematic errors.

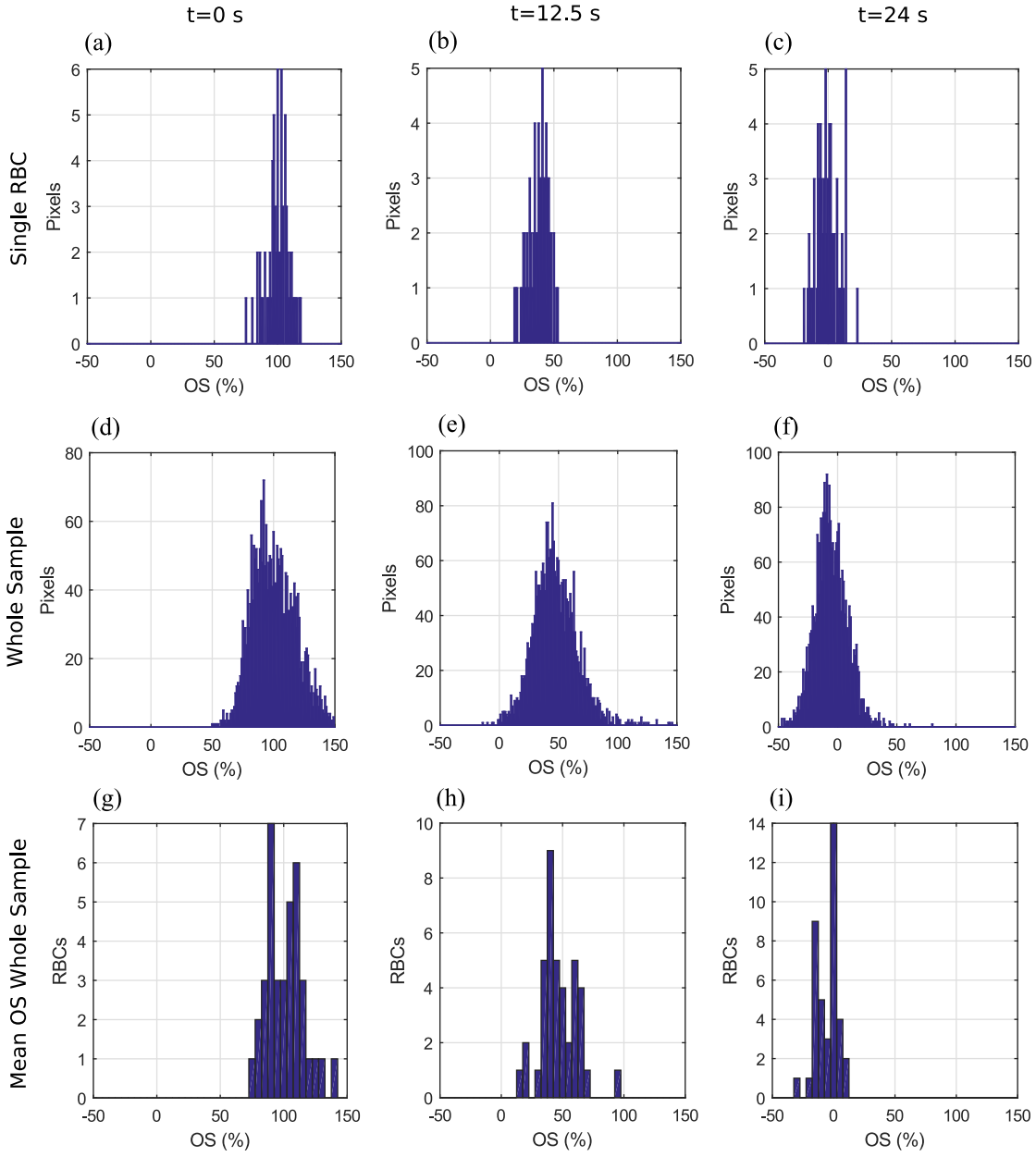

Figure 3.18: Oximetry histograms at 0, 12.5 and 24 seconds, using a radius of 4 pixels. (a)-(c) Histogram of the calculated pixel by pixel oxygenations on a RBC (Fig. 3.15). (d)-(f) Histogram of the calculated pixel by pixel oxygenation for all the displayed RBCs (Fig. 3.16). (g)-(i) Histogram of the mean oxygenations of all the displayed RBCs on Fig. 3.16.

3.8.1 Detector readout noise

One characteristic of the histograms on Fig. 3.18 is the Gaussian-like distribution shape, especially in Fig. 3.18(a)-(f), which could be explained by detector readout noise. This can be tested by showing how adjacent pixels belonging to the same RBC have different *OD*. In Fig. 3.19(a) an *OD* map of a 100% oxygenated RBC cell is shown, with four adjacent pixels being highlighted. These pixels have different *OD* (Fig. 3.19(b)) and in three of four cases, the *OD* diverges from the endmember by 0.01 *OD* while pixel 4 (purple) is the most similar to the endmember (green). Fig. 3.19(c) shows the LSU results of the four pixels. Pixel 1 (blue) shows negative deoxyhaemoglobin abundances. Pixel 2 (red) shows abnormally high deoxyhaemoglobin abundance while background and edges are higher in absolute value than for the other pixels. Pixel 3 (yellow) also shows deoxyhaemoglobin abundances higher than 0, which should not be possible on a 100% oxygenated sample. Finally, pixel 4 shows a deoxyhaemoglobin abundance value of ~ 0. The oxy- and deoxyhaemoglobin abundances can be used to find the *OS* using Eq. 3.6. The oximetry results are shown in Fig. 3.19(d), where the effect of having negative or high values of deoxyhaemoglobin is shown on pixel 2 and 3, which are below 100% *OS* and pixel 1 with 110% *OS*. Pixel 4 is the closest to 100% since the deoxyhaemoglobin endmember is closest to 0. Exclusion criteria could be applied to eliminate situations such as pixel 2 by ignoring pixels with edges endmembers higher than a certain absolute threshold. However, no clear exclusion criteria can be applied to eliminate pixels such as number 1 and 3, because they tend to have a similar behaviour as "well behaved" pixels such as pixel 4. LSU frequently assigns negative values to the deoxyhaemoglobin endmember, so rejecting them is not a viable option because a high portion of pixels belonging to RBCs (>70% on Fig. 3.18(d)) would be out of the oximetry analysis.

Further analysis of the image showed that the background region of the *OD* map had a standard deviation of ± 0.005 *OD* and maximum values of ± 0.02 *OD* on all wavelengths. Taking the standard deviation value of the background as a measurement of the readout noise and using the oxyhaemoglobin endmember as the signal, the SNR of the RBC spectral signal can be estimated (Table 3.1):

$$SNR(\lambda) = \frac{OD_{100\%}(\lambda)}{SD(background)}, \tag{3.7}$$

where $OD_{100\%}(\lambda)$ is the mean optical density of all RBCs in the FoV when they are oxygenated and $SD(background)$ is the standard deviation of the background (regions of the FoV without RBCs).

The SNR value was 9 in the best case (576 nm) and 0.014 in the worst case (599 nm), which are considered to be low SNRs values.

Fortunately, the absorption signal can be boosted and the effect of noise reduced. This can be achieved by imaging the RBCs in the blue, because oxyhaemoglobin has a maximum in absorption at 415 nm (Fig. 3.20(a)). In order to achieve imaging at this wavelengths,

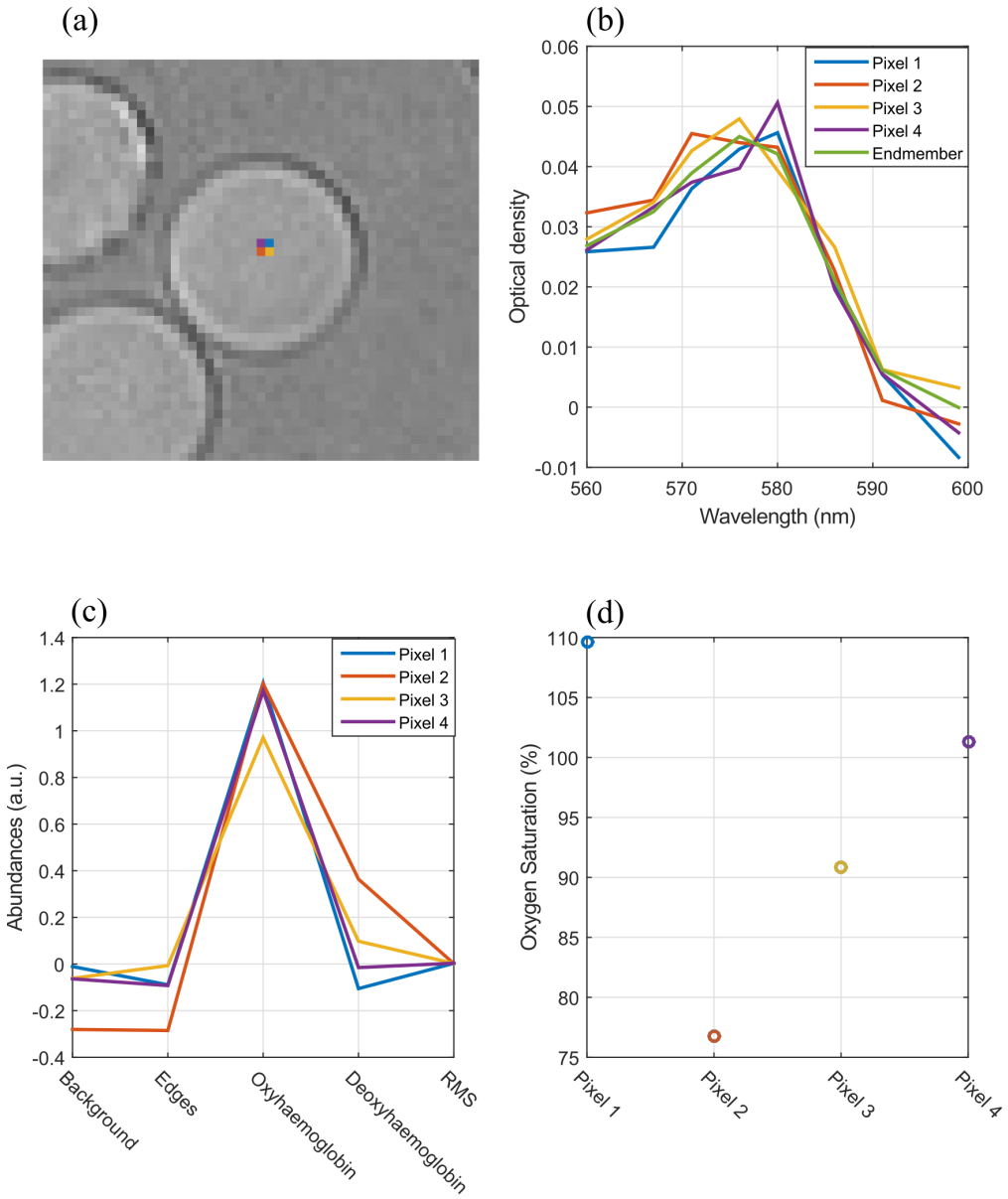

Figure 3.19: Noise effect on the spectral analysis. (a) *OD* map of a 100% oxygenated sample at 560 nm showing four different pixels. (b) Spectral *OD* and oxygenated endmember (green) of the pixels on (a). (c) LSU results from the highlighted pixels. (d) *OS* values for each pixel.

Wavelength (nm)	Optical Density	SNR
560	0.027	5.4
567	0.033	6.6
571	0.039	7.8
576	0.045	9
580	0.042	8.4
586	0.021	4.2
591	0.006	1.2
599	0.00007	0.014

Table 3.1: SNR of the RBC signal considering the *OD* of the oxyhaemoglobin endmember and a noise of 0.005 *OD*

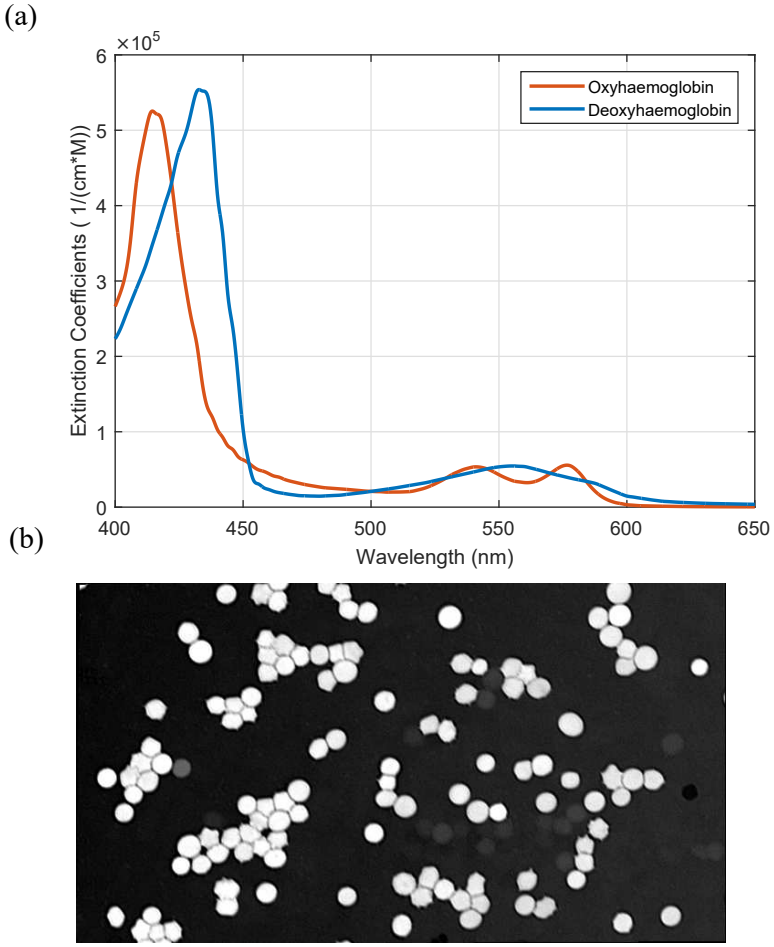

Figure 3.20: (a) Haemoglobin extinction coefficients, showing maximum absorption in the blue region. (b) *OD* map of a 100% oxygenated blood sample imaged at 415 nm.

a *VariSpec* Liquid Crystal Tunable Filter (LCTF) (PerkinElmer) set at 415 nm (FWHM $\approx$ 10 nm) was placed in the imaging path, after the microscope objective and before the IRIS lenses. For this case, the filter plate was removed. The resulting *OD* image of a 100% oxygenated RBC sample is displayed in Fig. 3.20(b). In this case, the standard deviation of the background was 0.007 *OD*, which was considered as the readout noise, while for the RBCs it was 0.46 *OD*, which is ten times higher than at 576 nm (highest absorption on the system using the filter plate). In this case, the SNR is 65.7, which is 7.3 higher in terms of signal than using IRIS at 576 nm. At this stage of the project, this was not considered a priority and was proposed to be done in the near future as another project.

3.8.2 Optical system defects

The data obtained for this section was obtained with the first design of the filter plate (Fig. 2.10(b)), so one of the concerns was the effect the defects may have in the analysis. Since most of the defects were on the periphery of the filters, it was easy to bypass them by reducing the analysed area (Fig. 2.15(b)). Other defects from the filter such as the highlighted black

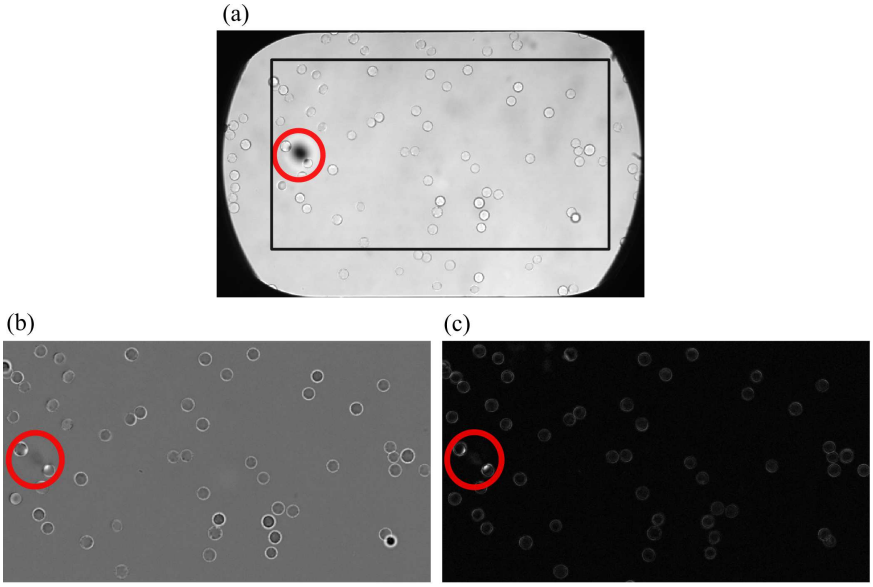

Figure 3.21: Filter plate defects and data analysis. (a) Raw image at 591 nm, showing the analysed FoV (black rectangle) and highlighting the filter plate defect (red). (b) *OD* map at 591 nm with the defect circled in red. (c) Residuals (ε) abundance map circled in red the filter defect.

spot on Fig. 3.21(a) can be eliminated from the analysis by other means. In this case the defect was a small hole in the filter surface. Normalising the RBC image with respect an image without sample made it possible to attenuate the effect (Fig. 3.21(b)), although it modified the transmission of the affected pixels, especially if these pixels belonged to RBCs. Once the LSU was applied, since the transmission of the RBC pixels affected was different to any of the endmembers, they had high values in the residual map (Fig. 3.21(c)), so they were identified and rejected as explained in Section 3.5.

Another effect was introduced by IRIS itself. By reducing the field diaphragm aperture on the illumination path of the microscope, the extent of the illumination source is reduced and the light source starts acting as a point source, enhancing the contrast and increasing the depth of field by modifying the illumination NA, but a side effect is an increase on the spatial coherence of the illumination at the sample. An increase in image contrast is desirable since RBCs are highly transparent, but the defects in the optical system become more defined. As an example, two images were taken, one with the field diaphragm almost closed and another being completely open (Fig. 3.22 (a) and (b)). On Fig. 3.22(a) straight lines crossing the FoV are highlighted in red. When the diaphragm is opened, the spatial coherence is lost and the illumination behaves as an extended source, then the lines become blurred until they are not visible, as shown in Fig. 3.22(b). These lines were not replicated, being different or non-existing in some wavebands, which led to the conclusion that they were introduced by IRIS. This idea is supported by the fact that translating IRIS horizontally and vertically changed the positions of these lines. Fig. 3.23 shows a false coloured image of the registered bands, in which magenta and green belongs to the reference (567 nm) and the registered images, and grey corresponds to identical regions. As can be observed, most of the defects

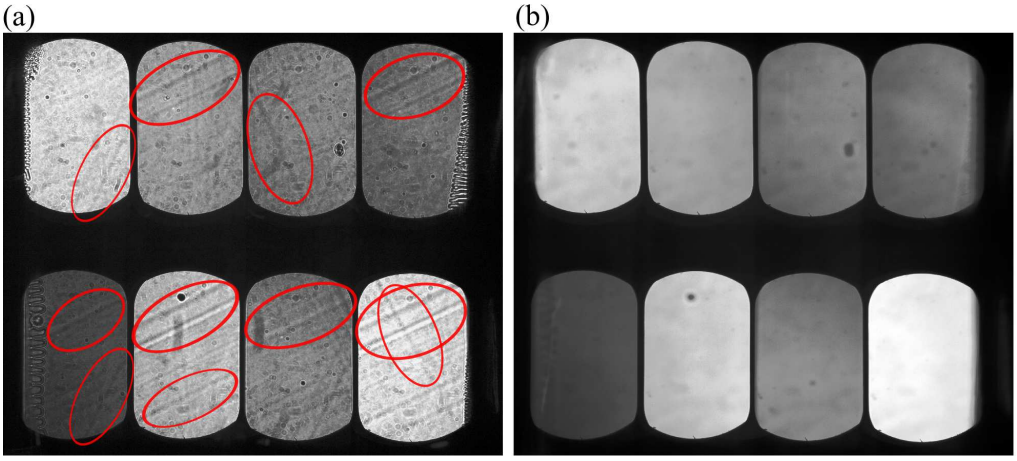

Figure 3.22: Images through the Microscope-IRIS system. (a) Field diaphragm closed, with IRIS defects circled in red. (b) Field diaphragm open.

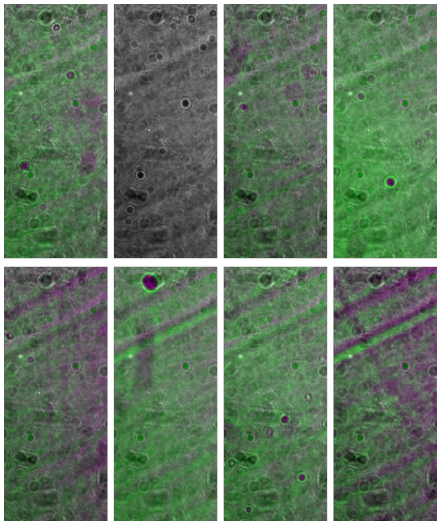

Figure 3.23: False colour composite of registered IRIS bands using 567 nm as reference. Intensity differences between the individual images and the reference are displayed as magenta and green (567 nm with itself does not have differences, so it is displayed as grey).

have a different colour, so they do not match while the image in grey corresponds to 567 nm compared with itself. The defects were identified as manufacture serration from the IRIS prisms production. Since the internal surfaces are index matched, they were expected to contribute in less degree than the external surfaces.

The serrations were in different positions in the FoV, so they were expected to modify the RBC *OD* on some wavelengths and on certain directions. In order to test this, a 5 μl 100% *OS* horse blood sample was imaged between a microscope slide and a coverslide. Fig. 3.24(a) shows how in the direction of the red regions the RBCs had brighter edges while this did not happen on the other RBCs of the sample. For comparison, Fig. 3.24(b) shows the *OD* belonging to the marked ROIs. Both spectra are similar, 591 and 599 nm being the wavelengths in which the red group of RBCs have higher *OD*.

Eliminating edges from the analysis removed the brighter external pixels, but the defects

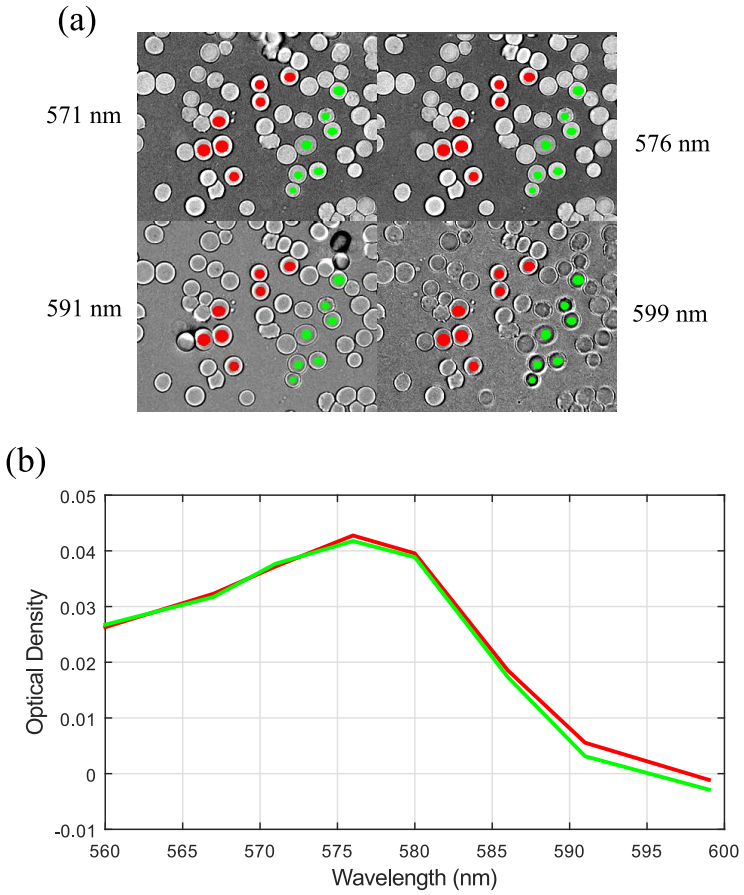

Figure 3.24: (a) *OD* images showing directional effects over the RBCs on the edges, with 4 pixels radius ROIs of two group of RBCs (red and green). (b) Spectral *OD* of the ROIs belonging to the two RBCs groups.

were expected to introduce systematic errors on the oximetry results of the remaining pixels. This might explain the reason why there were regional *OS* variations across the FoV in the same sample as shown in Fig. 3.25(a). The whole figure has $97 \pm 26\%$ *OS*, while the squared regions have (from left to right) $OS = 91 \pm 24\%$, $OS = 95 \pm 26\%$ and $OS = 102 \pm 25\%$, showing how the oxygenation varied from region to region. This can be better understood observing the deoxyhaemoglobin abundances map on Fig. 3.25(b). The RBCs on (a) which have pixels >100% *OS* (red) belong to RBCs with negative abundances (darker pixels), while RBCs with <90% *OS* have positive non-zero values for deoxyhaemoglobin abundance. The fact that there are groups of RBCs with similar *OS* and endmembers abundances characteristics along the FoV argues in favour of systematic errors introduced by IRIS serrations or other defects (Fig. 3.23). However, the relation was not thoroughly proved and only a comparison of the directional effects of the endmembers abundances, the *OD* map and the *OS* map was performed. This effect was harder to analyse in the cell chamber, since different PLL coating thickness could change the position on z of the RBC, placing them slightly out of focus, which makes it harder to identify regions affected by the same defects.

The effect of the serrations was not found to be repeatable since different samples showed different patterns and oxygenation distributions along the FoV. This is likely to be produced by IRIS being often removed from the microscope between experiments to be used in other systems, so the effect of the serrations would not be in the same positions. The samples were also moved along the FoV using the microscope stage, but changes in oxygenation could not be attributed to the serrations because it was not possible to control the oxygenation of the RBCs during the experiment. To assess the effect of the serrations in the analysis, a control experiment using $\sim 5\,\mu$m micro-beads should be performed. Such experiment would show the impact in terms of *OD* of having different defects on the different wavebands of IRIS. The advantage of using micro-beads is that it would not suffer physiological changes during the experiment.

A simple solution for the serrations problem would be to attach thin glass tiles to each external surface and index match them with oil. Unfortunately, these defects were detected after the experimental part of this chapter was finished and the project moved on to the next stage, so it was not solved.

3.8.3 Systematic errors from the RBC shape

Between a microscope slide and coverslip, RBCs are compressed, making them flat and reducing possible lensing due to their lenticular shape, but in a cell chamber, they preserve their shape, acting as lenses. Human RBCs have a characteristic lenticular shape, but in this research horse blood was used instead. Horse RBCs have shallower central pallors, so their behaviour as lenses differs from that of human RBCs. Furthermore, different buffer osmolarity can make them more spherical (low osmolarity) or shrink them (high osmolarity).

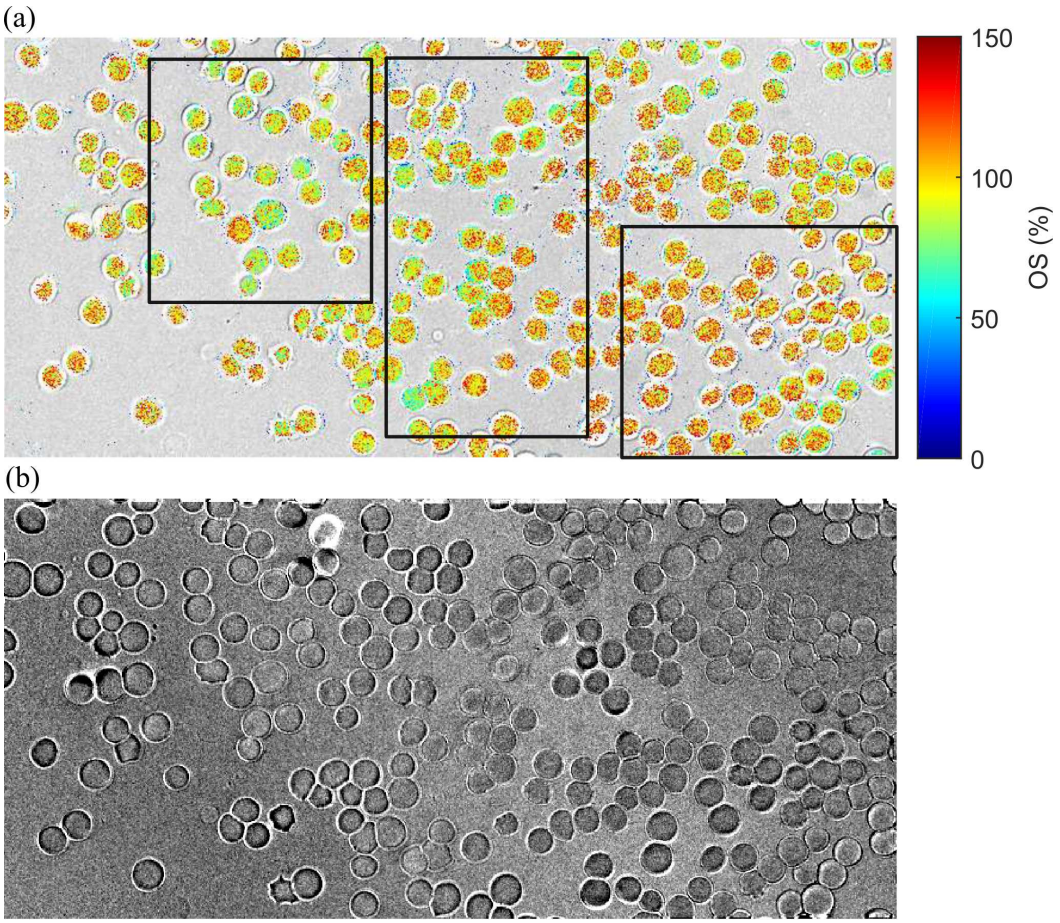

Figure 3.25: Regional variations on FoV. (a) Map of *OS* values, showing regions where RBCs have more than 70% pixels with higher than 100% *OS*, and regions where RBCs contain 90% of pixels with *OS* below 90% oxygenation. The three squared regions have, from left to right, $OS = 91 \pm 24\%$, $OS = 95 \pm 26\%$ and $OS = 102 \pm 25\%$. (b) Map of deoxygenated haemoglobin abundances, showing regional variations on RBCs, with dark values (negative abundances) and light values (positive abundances).

Lensing from RBCs creates a darker central region, a lighter external part, and dark edges in terms of intensity, which is the opposite in terms of *OD*. Fig. 3.26 shows how the *OD* changes for the three described regions of the same cell. In blue (Fig. 3.26), the edges show no information about the haemoglobin content because is the most affected region by refractive effects and defocus, in addition, there is little change between the oxygenated and deoxygenated case. The central part of the cell (Fig. 3.26 in red), however, shows a clear resemblance with the endmembers on Fig. 3.8, having a correlation of 0.98 for the oxygenated case and 0.97 for the deoxygenated case. The negative OD corresponds to the most transparent wavelengths. Because of their shape and higher refractive index, RBCs tend to act as positive lenses and appear to be brighter than the background since they are focusing light on another plane. On the other hand, the region between the central part and the edges (Fig. 3.26 in green) shows a certain resemblance with the endmembers with correlations of 0.96 and 0.93 for the oxygenated and deoxygenated cases respectively. The green regions are expected to produce higher errors in terms of *OS* farther from the centre and this is the reason why only the central region was used to report the results. More detail about the extent of this region is shown in Subsection 3.8.5. The reason behind this phenomena is most likely the lensing effect of the RBC since this does not happen when the RBCs are compressed between a microscope slide and a coverslide.

In an attempt to characterise and take into account the change of *OD* due to the RBC shape, different curves were fitted to the *OD* and *OS* maps of single RBCs. Two different equations were used for the fitting, a second-degree polynomial and a hyperGaussian:

$$Z = p_{00} + p_{10}x + p_{01}y + p_{20}x^2 + p_{11}xy + p_{02}y^2, \tag{3.8}$$

where Z is the *OD* or *OS*, p_{ij} multiplicative coefficients to be fitted and x and y the corresponding pixel position on the image for the polynomial expression on Eq. 3.8.

$$Z = A\exp\left(-\left(\left(\frac{x-d}{w}\right)^2 + \left(\frac{y-t}{g}\right)^2\right)^n\right), \tag{3.9}$$

where Z is the *OD* or *OS*, d, w, t, g and n fitting parameters of the hyperGaussian (Eq. 3.9) and x and y the pixel position on the image. The choice of models corresponds to empirical observations, in which there is a radial distribution of *OD*s, being higher in the centre, and getting lower towards the external part of the RBC (excluding edges).

Background and pixels were removed from the fitting by identifying the corresponding abundances from the LSU analysis. The fitting was applied over the region shown in Fig. 3.27, by applying weight 0 to the pixels belonging to background and edges endmembers. Fig. 3.28 and Fig. 3.29 show the fits of Eq. 3.8 and Eq. 3.9 respectively. In general, fits for both models tend to have r^2 values below 0.8, the best being achieved at 576 nm, which corresponds to the highest absorption for a 100% *OS* cell. Since the SNR is low, fitting

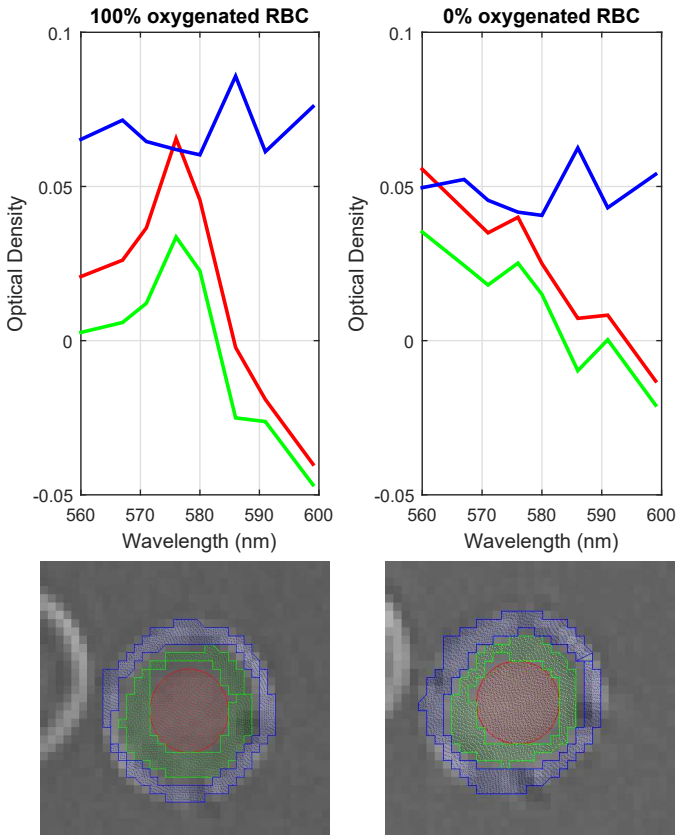

Figure 3.26: *OD* of a 100% (left) and 0% (right) oxygenated RBC at three ROIs highlighted over the *OD* map at 560 nm. Blue belongs to the most external part, the edges. Green belongs to the region between the centre and the edges. Red corresponds to the central part of the cell.

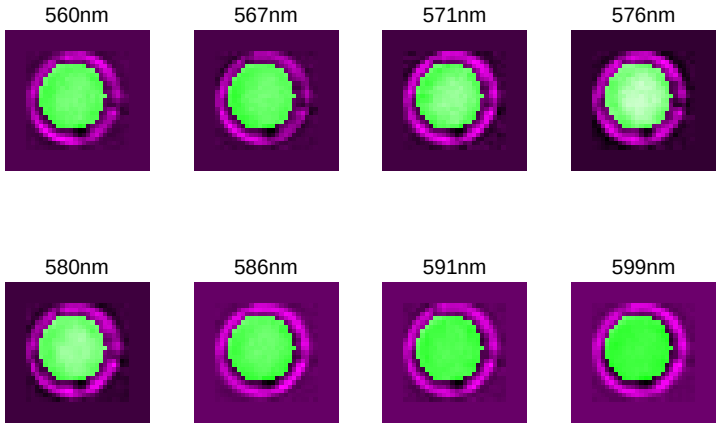

Figure 3.27: *OD* image (magenta) fused with the fitted region (green), which excludes edges and background.

becomes challenging and produces poor results, especially at low absorption wavelengths. A good example is found for, 586 nm, 591 nm and 599 nm as shown in Fig. 3.28 in which the r^2 are below 0.6. The same wavelengths on Fig. 3.29 are unable to produce any fit at all. Poor fits and the inability to fit on some wavelengths eliminates the possibility of using this method to characterise the *OD* changes in the same cell.

3.8.4 Regional oxygenation distribution inside RBCs analysis

The RBC displayed in Fig. 3.14 and some RBCs in Fig. 3.25 show regions with different oxygenations inside the same cell. Ideally, the fits introduced in Subsection 3.8.3 would allow taking into account changes on *OD* due to RBC shape or orientation, but it proved unsuccessful. As seen on the obtained r^2 values from Fig. 3.28 and Fig. 3.29, the fits are highly inaccurate, specially on the more transparent wavelengths, since they are more affected by noise.

To provide a more robust analysis, an independent components analysis (ICA) approach was applied. ICA removes the need of endmembers and would discard problems with the endmembers analysis. To achieve this, an RBC showing different *OS* distribution was selected (Fig. 3.30). In this cell, an *OS* gradient is observed, indicated by a green arrow from high *OS* to low *OS*.

Attempts were made to characterise the gradient, but due to noise and non-uniformities in the cell, these fits had low r^2 and were proved unreliable as seen in Fig. 3.31, where the *OS* of the cell on Fig. 3.30 and a second RBC from the same sample were fitted by Eq. 3.9.

ICA provides a set of independent spectral components that compose the *OD* image. In this case, since IRIS produces a set of eight wavebands, the output was set to eight, although it can be set to fewer bands if the amount of existing spectral components is known. The

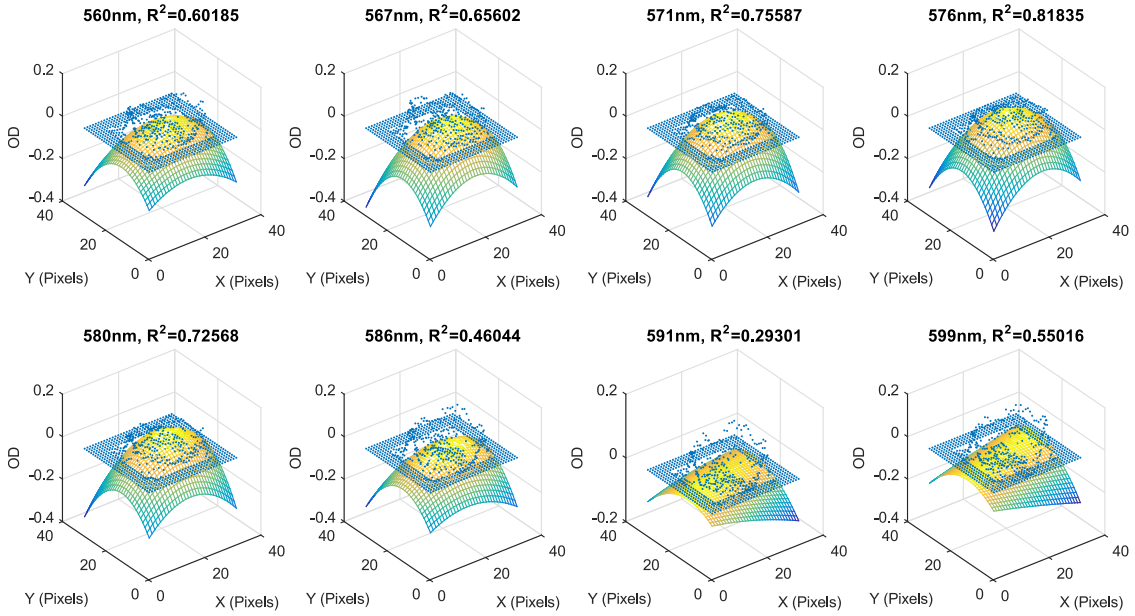

Figure 3.28: Parabolic (Eq. 3.8) fit results for the RBC on Fig. 3.27, including the wavelength, the r^2 of the fit, and the RBC *OD* data represented as dots.

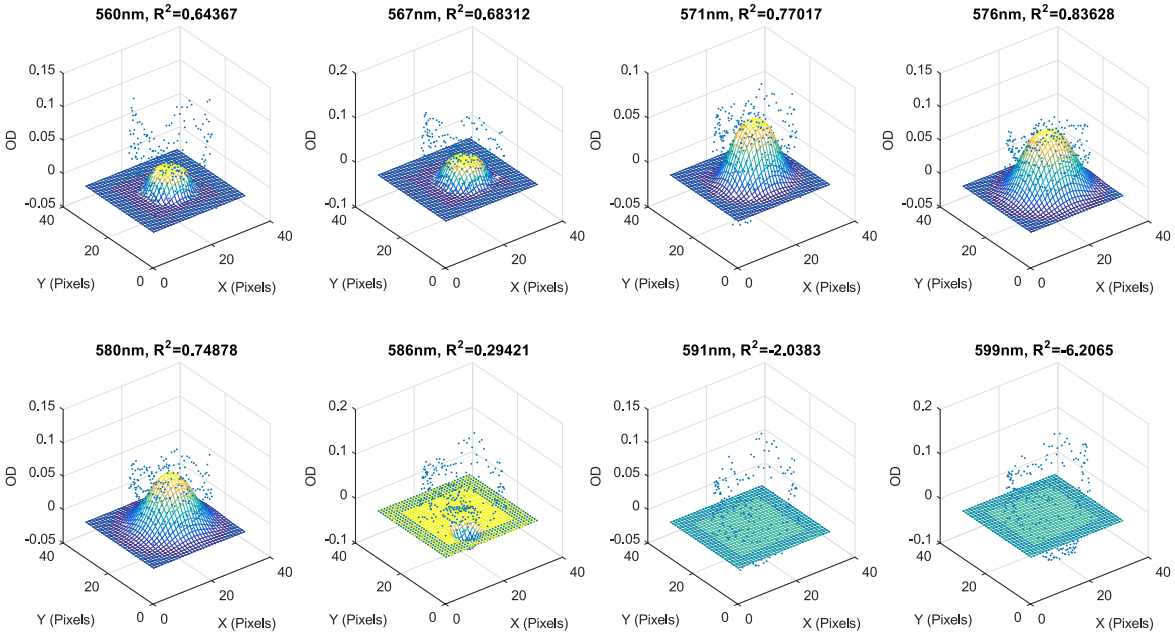

Figure 3.29: HyperGaussian (Eq. 3.9) fit results for the RBC on Fig. 3.27, including the wavelength, the r^2 of the fit, and the RBC *OD* data represented as dots.

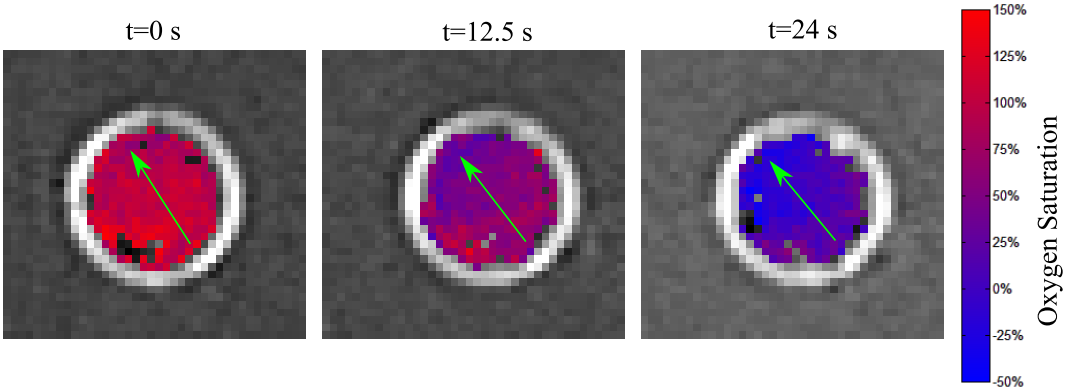

Figure 3.30: RBC oxygen saturation map during deoxygenation, showing how the oxygenation is not homogeneous in the cell. *OS* from left to right are $OS = 102.0 \pm 9.0\%$, $OS = 40.0 \pm 9.0\%$ and $OS = -2.0 \pm 9.0\%$.

objective of this analysis was to detect spectral components that would have an effect on the *OS* calculation, so all the eight components were kept. ICA was applied to the cell when completely oxygenated (Fig. 3.32) and completely deoxygenated (Fig. 3.32(b)) and the eight spectral components maps were obtained. In addition, the Linear Spectral Unmixing analysis (LSU) results were added in order to identify the ICA components with the LSU endmembers, since the oximetry calculations are obtained from the LSU results. The *OS* gradients are produced by the LSU results, which show an abnormally high abundance of deoxyhaemoglobin in the oxygenated case and oxyhaemoglobin in the deoxygenated case.

Fig. 3.32(a) shows a 100% oxygenated cell and the ICA components. The first component corresponds to the main spectral component, which is oxygenated haemoglobin and approximately matches the oxyhaemoglobin abundances map of the corresponding LSU analysis. This band was not homogeneous, which would not be a problem unless the deoxyhaemoglobin component had values other than 0 (Eq. 3.6). Regarding the *OS* gradient shown in Fig. 3.30 the deoxyhaemoglobin map obtained from the LSU analysis would correspond to component 4 from the ICA analysis. The bright pixels on this band would produce lower than 100% *OS*, while the dark pixels (negative values), would produce values higher than 100% *OS*. Components 2 and 5 highlights regions outside the RBC and defects on the RBC surface. Since the LSU assumes only 4 components, edges and background abundances from the LSU show more spatial coherence than the rest of components on ICA.

Fig. 3.32(b) shows the ICA components for a 0% oxygenated RBC. In this case, the *OS* gradient is more pronounced than in the 100% oxygenated case. As in the previous case, component 1 from ICA matches the abundance map obtained from LSU for deoxyhaemoglobin. In this case, there are two clear gradients in components 3 and 5, where 5 is the one that would correspond to oxyhaemoglobin on the LSU analysis.

The conclusion of the ICA analysis is first that the LSU analysis and the ICA analysis produce analogous results in terms of oxyhaemoglobin and deoxyhaemoglobin identification for the oxygenated and deoxygenated cases respectively. Secondly, there are spectral

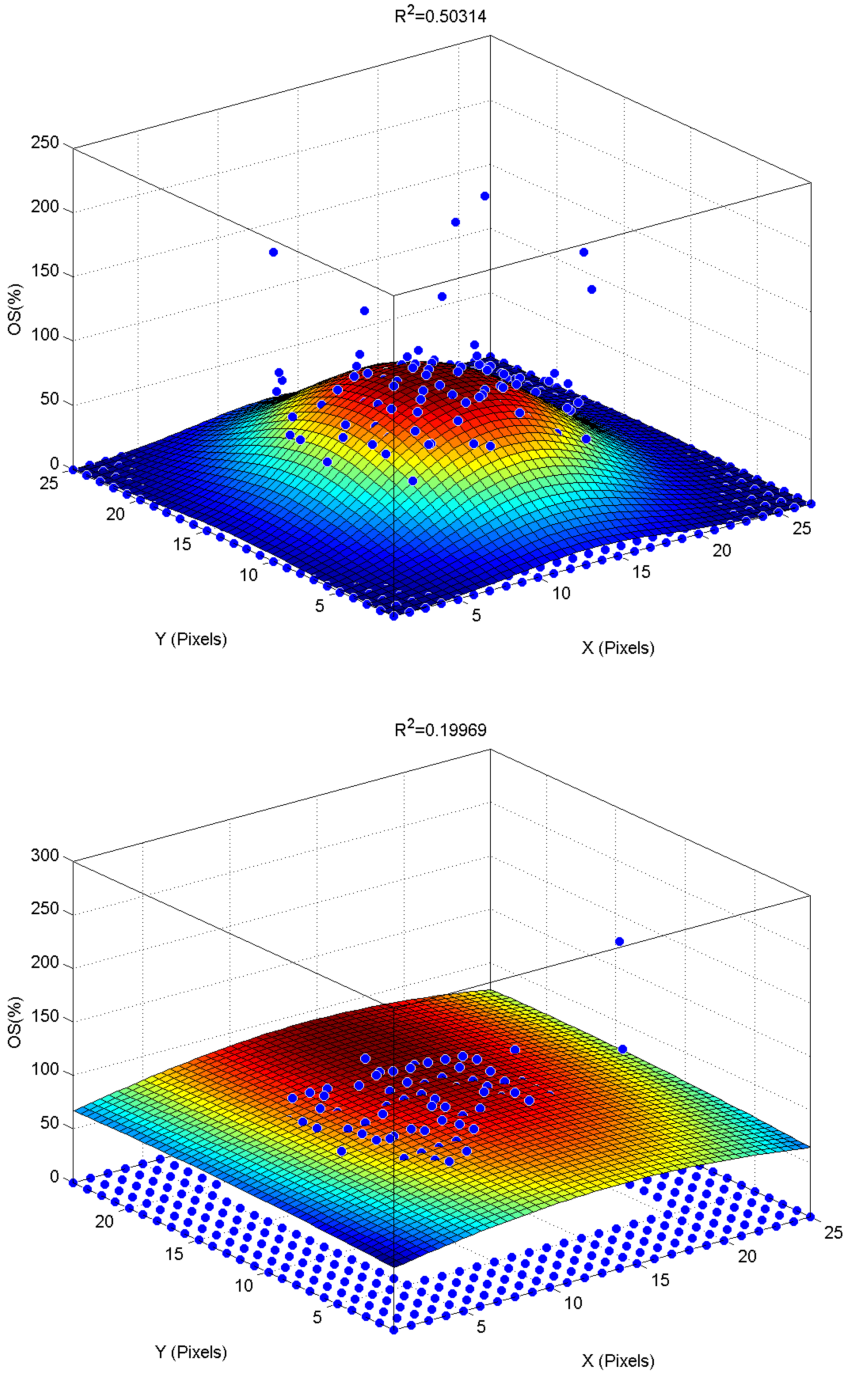

Figure 3.31: HyperGaussian fit to the *OS* map of two different RBCs. Weight 0 is assigned to any pixel not containing *OS* information.

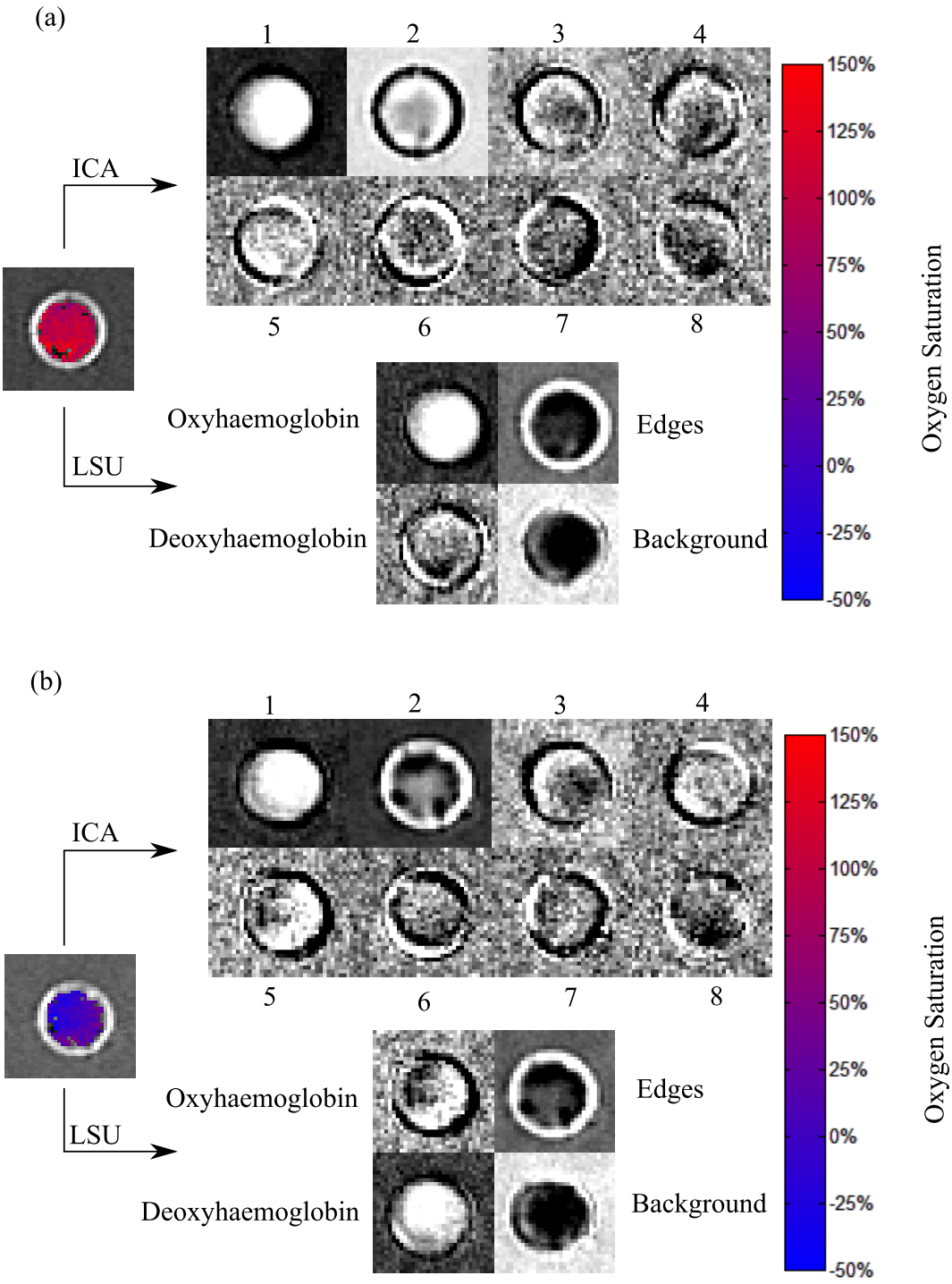

Figure 3.32: ICA results of the same RBC at different oxygenations compared with LSU results. (a) 100 % oxygenated RBC, with the ICA bands sorted by coherence. (b) 0% oxygenated RBC, with ICA bands sorted by coherence.

components distributed in the form of gradients on the RBCs. These non-uniformities are included in the LSU results and the resulting *OS* map. The introduction of more endmembers could have improved the LSU analysis, but it was unclear how they should be defined and to which regions or phenomena would correspond.

As previously stated, the exposure time of the experiment (33 ms) and the haemoglobin oxygen dynamics (3 ms) argue against seeing any oxygen distribution inside the RBC, especially when it is in equilibrium at 100% and 0% *OS*. Possible explanations for this spectral distributions could be defocused RBCs, tilted RBCs, directional effects from illumination and scattering from other RBCs[94], and defects from the optical system. In terms of *OD*, the information on the regions affected by gradients and the external parts of the RBCs were proven to be more different to the oxy- and deoxyhaemoglobin endmembers than the *OD* on the central regions of the RBC (Fig. 3.26). Future testing of this effects will be performed by using beads since they are have a simpler structure and are do not have surface defects as RBCs do.

3.8.5 Reducing *OS* error with different radius

Due to the existence of multiple sources of errors and the complexity of characterising and/or compensating them as described above, a more basic approach was performed. After the *OS* map of the RBCs was produced, the image was segmented in order to detect the RBC and its centroid. Starting from this centroid, different radius discs were used to calculate the mean and standard deviation of the RBCs oxygenation. The results are shown in Fig. 3.33. The objective was to find the maximum number of used pixels with the minimum standard deviation, for this reason, a radius of 4 pixels with 8.6% standard deviation was chosen, which corresponds to $\sim 30\%$ of a 9 pixels radius RBC. Although 3 pixels produced 7.8% standard deviation, the covered area was $\sim 15\%$ of the cell. Furthermore, when it was applied to the whole sample, both radius (3 and 4 pixels) have a standard deviation of 14%.

The analysis of the RBCs in a 4 pixels radius from the centroid reduces the standard deviation related to the systematic errors explained in the previous sections, which mostly affects the external parts (not the edges) of the RBCs.

3.8.6 Defocus

One concern about this technique was the effect of defocus on the oximetry results. In order to assess this problem, a 100% oxygenated horse blood sample was imaged between a microscope slide and a coverlside. The sample was then defocused $\pm 10\,\mu$m and recorded at 30 fps. The image sequence was obtained in 3 runs using *Nikon Elements* (Nikon, Japan). The first one run was performed from the image being focused to -10 μm defocused, shifting $1 \pm 0.025\,\mu$m every 200 ms. The second run covered the range from -10 μm to +10 μm, shifting $1 \pm 0.025\,\mu$m every 167 ms. Finally, the third run covered from +10 μm to focused

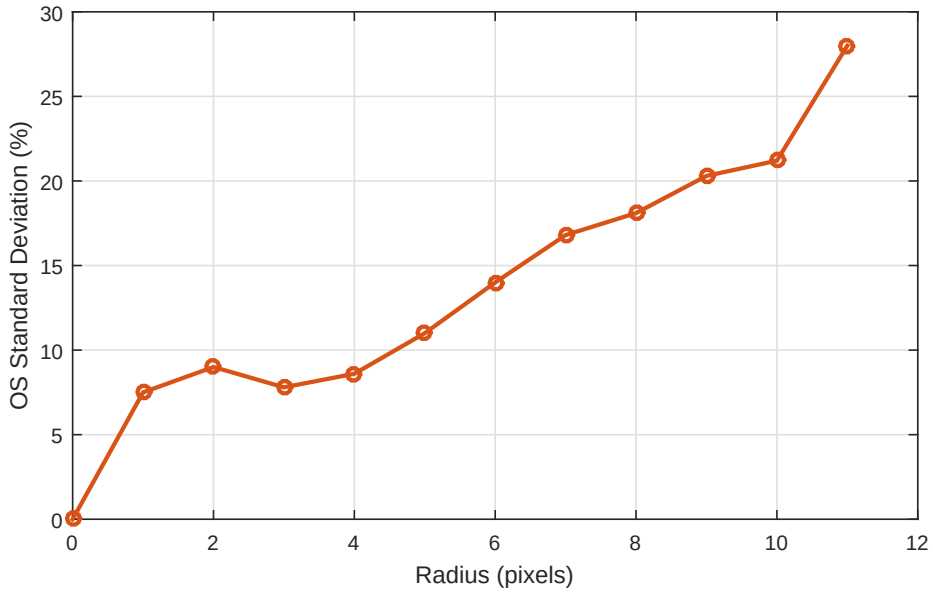

Figure 3.33: *OS* standard deviation for a single cell for different disc radius.

by translating $1 \pm 0.025\,\mu$m every 100 ms.

The resulting image sequence was then analysed applying the corresponding threshold to eliminate background and edges. As previously discussed, edges included the bright and dark effect from defocus[103]. The analysis was first done using a radius of 4 pixels (Fig. 3.34(a)) and then repeated without imposing any maximum analysable region (using all pixels in the RBC) (Fig. 3.34(b)). The idea behind this two methods is to show that defocus introduces changes in the RBC brightness in the external parts of the RBC, while the central regions remains approximately unchanged, for this reason the method using a disk centred in the RBC is expected to be more invariable to defocus than the one without disk. Defocused regions are expected to be included in the edges endmembers, so they can be excluded from the analysis. This experiments also aims to show the performance of oximetry after removing the edges from defocused RBCs.

The most critical features of both oximetry graphs are two minima marked with grey lines. These two events correspond to the maximum defocused images, as shown in Fig. 3.34(c). The difference in translation speed between the runs and the error associated with the microscope stage could explain why the first maximum defocus peak is broader than the second. Without considering the regions of maximum defocus, Fig. 3.34(a) has three main sections with $OS = 94 \pm 7\%$, $OS = 92 \pm 6\%$ and $OS = 91 \pm 7\%$. On the other hand, Fig. 3.34(b) has $OS = 92 \pm 7\%$, $OS = 89 \pm 7\%$ and $OS = 89 \pm 7\%$. Although comparing the means and standard deviations shows similar behaviours, when the figures are compared, Fig. 3.34(a) (with radius = 4 pixels) shows more stable results than using the whole RBC analysable area after the edges endmember is removed. In conclusion, this technique is also invariant to defocus when a maximum radius is included in the analysis. When the

defocus is too extreme, the technique fails to provide reliable *OS* values. Refractive effects produced by defocus mask the haemoglobin spectral information, being these regions larger with higher defocus, leaving only small usable areas (less than 3 pixels) inside the RBC to provide oxygenation results.

On Fig. 3.34(a)-(b) there is an oxygenation decreasing gradient. Although is not clear why the mean oxygenation decreased during the experiment, it could be explained by the length of the experiment ($\sim$ 2 minutes) and the solution volume ($\sim 10\,\mu$l). Under these circumstances and the use of a 100 W lamp, the solution might have heated during the experiment, shifting the haemoglobin oxygen affinity and modifying the amount of oxygen that can bind to haemoglobin[106].

3.8.7 Spectral variations due to RBC lensing

It is known that RBCs can be used as lenses due to their particular discoidal shape[112]. One concern in this project is the effect of the RBC refractive index on the produced image. Since refraction is wavelength dependent (Fig. 3.35), RBCs might propagate light differently, so some regions of the cells would be expected to have a different behaviour when compared to other wavelengths. These differences are expected to be magnified at blue wavelengths, since the refractive index shows more variation in wavelength than in the red[113].

In order to spot these differences, an RBC from a 100% *OS* imaged sample in the cell sample was selected, and the *OD* map at 571 nm was subtracted from the other wavebands in order to find differences. The 571 nm (isosbestic) was selected as a reference so any non-homogeneity could not be attributed to *OS* differences in the cell. Fig. 3.36 shows that the main difference is seen in the central region. This region is brighter on the long wavelengths because the *OD* difference is highest between these wavelengths and 571 nm. The main real difference happens on the edges and the internal regions close to them. As an example, at 576 nm the RBC bright region extends up to the limit of it, while on 591 nm and 599 nm the edges are well defined as dark regions. Differences can be also observed among the other RBCs.

The previous analysis of Fig. 3.36 is strictly qualitative and might be influenced by scattering, tilt of the RBC, non-uniformities and defects on the cell membrane. An attempt was made to simulate this effect on *Zemax* in order to verify spectral variations due to lensing and the refractive index. Since a correct model of horse RBC was not available, the simulations were done using a model of human RBC. The optical system contained a rectangular volume of $n = 1.33$ simulating water, a $f = 2.3\,$mm focal length lens, with $n = 1.5$ constant in the 560 nm to 599 nm spectral range (IRIS wavelengths) and a$100 \times 100\,\mu$m sensor with 500 pixels. In front of the lens an annulus of $200\,\mu$m was placed to reduce spherical aberrations. The system had a magnification of 10x. An STL RBC model was created on *OpenSCAD* (Fig. 3.37) and placed inside the rectangular volume. The RBC was $1.6\,\mu$m thick on the

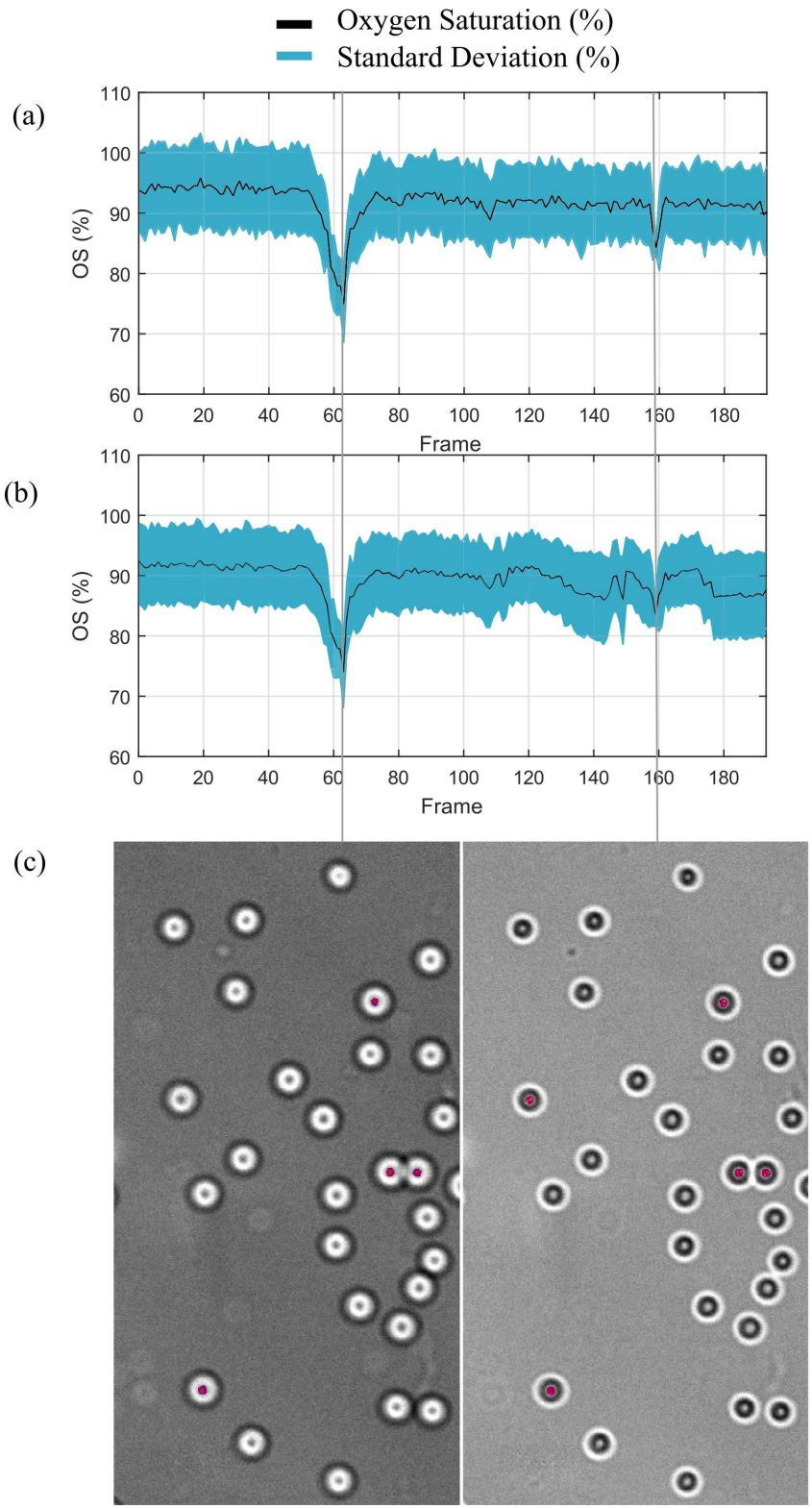

Figure 3.34: Defocus effect over an RBC sample. The sequence is shown in terms of frame since the defocus was performed under different steps and speeds during the experiment. (a) Oximetry results using a radius of 4 pixels. (b) Oximetry results without imposing a radius. (c) *OD* map with superimposed *OS* at 560 nm of the two maximum defocus, -10 μm on the left and +10 μm on the right. The grey lines on (a) and (b) show when the maximum defocus happens.

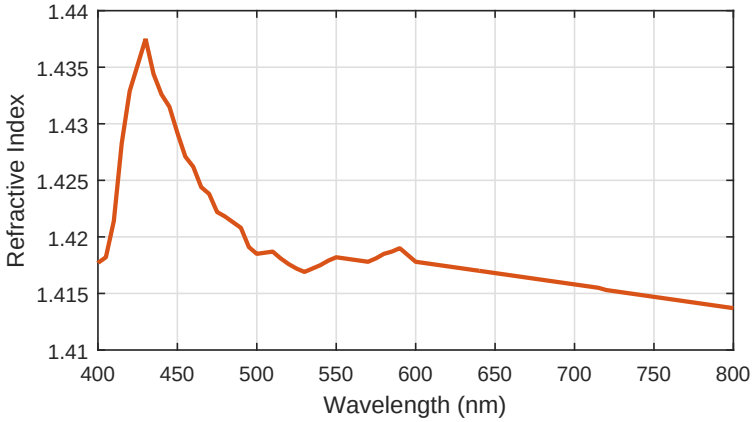

Figure 3.35: Haemoglobin refraction index for a 355.5 g/l concentration, which corresponds to the concentration on RBCs[4].

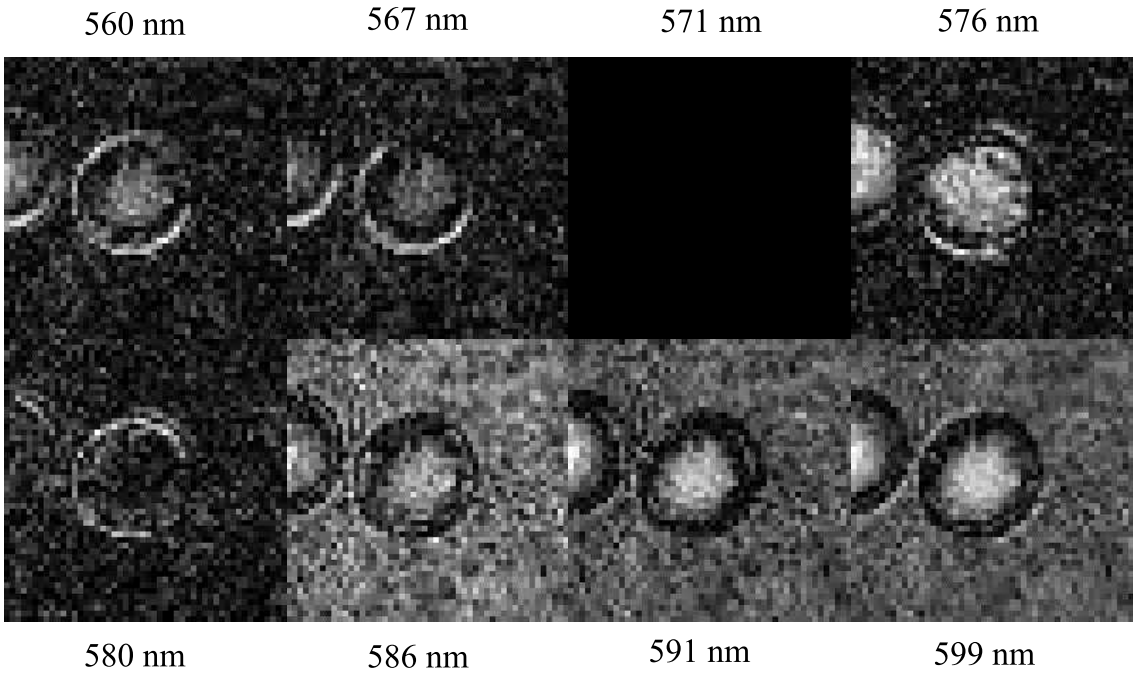

Figure 3.36: *OD* map subtraction of 571 nm waveband to all 8 wavelengths, highlighting the differences between them.

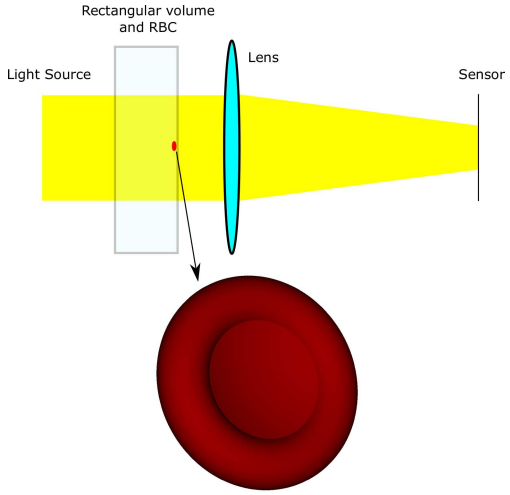

Figure 3.37: Diagram of the Zemax model used for the simulations (not on scale) including a STL model of an RBC with 1.6 μm thickness on the external part, 0.2 μm thickness on the centre and a diameter of 6 μm.

external part, 0.2 μm thick on the centre and had a diameter of 6 μm. A glass material with the refractive index from Fig. 3.35 was created for the RBC. The RBC also included the oxyhaemoglobin transmission spectrum. In reality a microscope such as the one used in this thesis uses Köhler illumination, but for this simulation collimated light corresponding to IRIS central wavelengths was directed towards the RBC, which was placed on the internal surface of the rectangular volume. The lens was placed 2.53 mm away from the RBC and the detector 25.3 mm away from the lens.

The simulations were done using the 8 IRIS central wavelengths by launching 10^8rays towards the RBC. The resulting incoherent radiance images on the detector were saved and then compared with the isosbestic reference (571 nm). The comparison was performed by making a composite of each image (in magenta) with the isosbestic reference (in green). The results show on grey the matching region between the reference and current image, and on magenta and green the difference between the selected wavelength and the reference respectively (Fig. 3.38). This figure shows how image formation through an RBC changes with refractive index since it is wavelength dependent. The main difference between the results is the change the in size of the RBC image due to changes in refractive index, which is then used to evaluate how much of the RBCs mismatch when image registration is performed. These regions do not provide reliable information since they show different structures and hence, different spectral signatures.

Although the refractive index has a maximum difference of 0.001 between 590 nm and 560 nm, these variations were enough to change the image formation. In particular, the most significant differences occurred when 571 nm was compared with 560 nm, 567 nm, 586 nm, 591 nm and 599 nm. The most extreme case was for 560 nm, in which the RBC bright part (before reaching the dark edges) is $\sim 7\%$ larger in radius than at 571 nm. This shows how towards the edges, the spectral information is not reliable, since, at different wavelengths,

the same pixels are displaying information from different regions of the RBCs.

One concern about this *Zemax* model is that raytracing is being applied over features $< 10\lambda$, a regime in which raytracing becomes unreliable. In such cases, it is advised to use a more rigorous approach such as finite-difference time-domain electromagnetic simulations.

3.9 Optical system chromatic aberrations

Another potential negative effect on the data analysis is the longitudinal chromatic aberration inherent to the optical system since this would change the focus of the RBC. This affects the image registration, since the generated image is wavelength dependant and produces a mismatch of the registered RBC with wavelength. The microscope-IRIS system consists of a CFI Plan Apochromat λ 100x oil immersion with NA 1.45 microscope objective, and 200 mm and 50 mm SLR lenses. The microscope objective is meant to be highly corrected for chromatic aberrations while the SLR lenses might perform worse than the microscope objective.

To assess the chromatic aberrations in the whole optical system a spoke target (Fig. 3.39(a)) was imaged at steps of 25 nm defocus (microscope resolution of 25 nm) for a set of 11 wavelengths, from 410 nm to 610 nm in steps of 20 nm by using a LCTF. Once the image stacks were generated, the variance of each was calculated for each wavelength (Fig. 3.39(b)). The variance of an image provides a metric of how sharp the edges of the image are, so it produces a maximum value when it is focused and produces low values when the image is defocused.

In the z-stack, the variance reached a maximum in the best-focused image. Fig. 3.39(c) shows a plot of the best focus point relative to the position at 410 nm. This shows that in the range 560 nm to 599 nm (IRIS range), there was a maximum longitudinal chromatic aberration of $\sim 0.4\,\mu$m between 570 nm and 590 nm for our microscope-IRIS system. This effect was considered negligible, since it was expected only to affect the most external regions of the RBC, especially the edges. Fig. 3.39(d) shows how the difference of registered images at 567 nm and 591 nm of a distortion target shows a mismatch on the edges of the dots, highlighted in brighter pixels. This is produced by the chromatic aberrations of the optical system, which produced a 20% increase in radius for the 591 nm band when compared to the 567 nm band.

3.10 Conclusions and future work

The accuracy and repeatability with which oximetry can be performed on single RBCs are important quantities to characterise; they determine how accurately one can measure the transfer of oxygen from an RBC to a tissue cell and at what rates one can measure it. For a single RBC, the standard error of measuring its oxygenation at 30 frames per second was

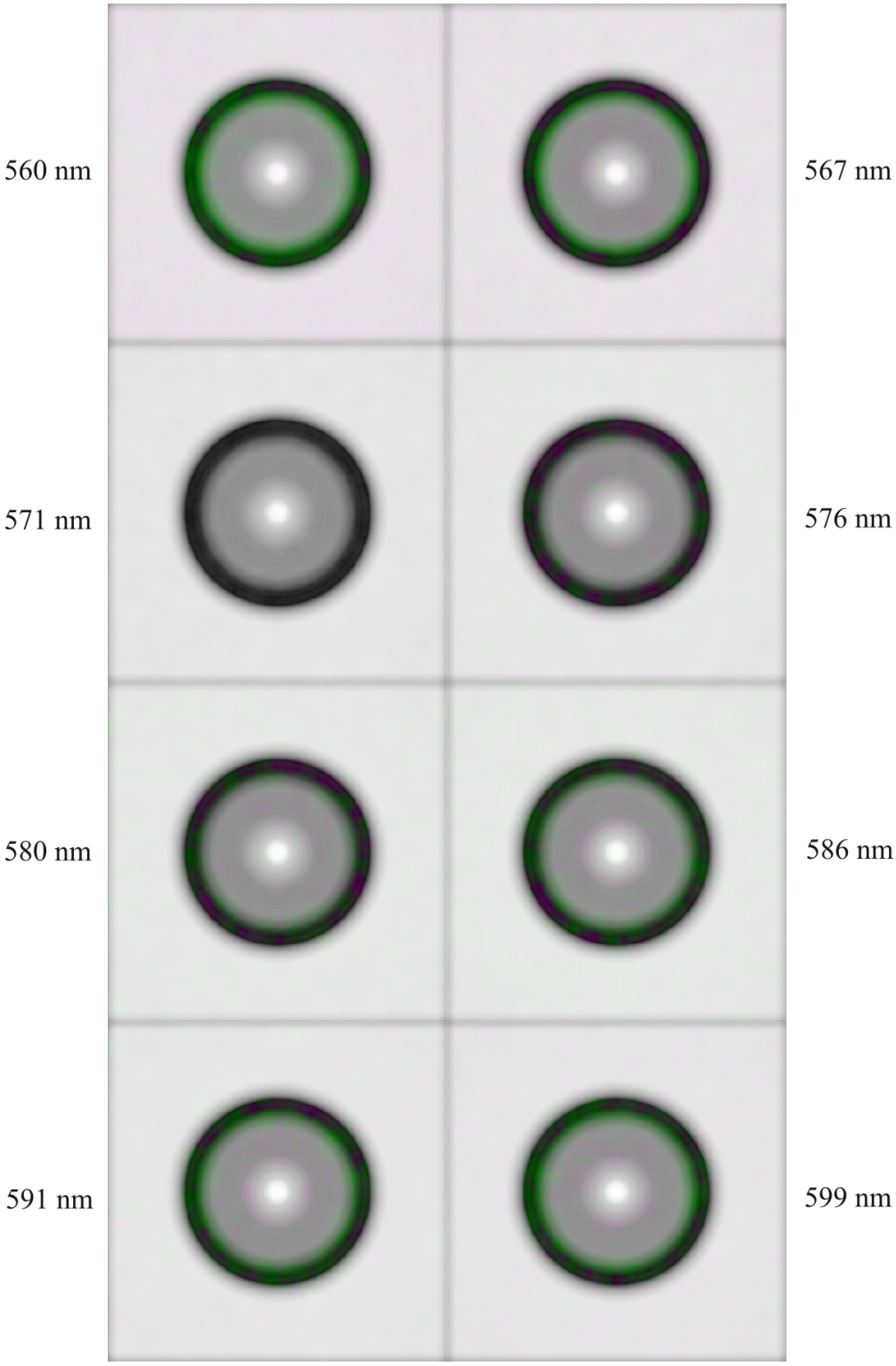

Figure 3.38: Fused *Zemax* simulation images of a model RBC at different wavelengths. Matched regions in grey. Mismatched regions in green (reference image) and magenta (selected wavelength).

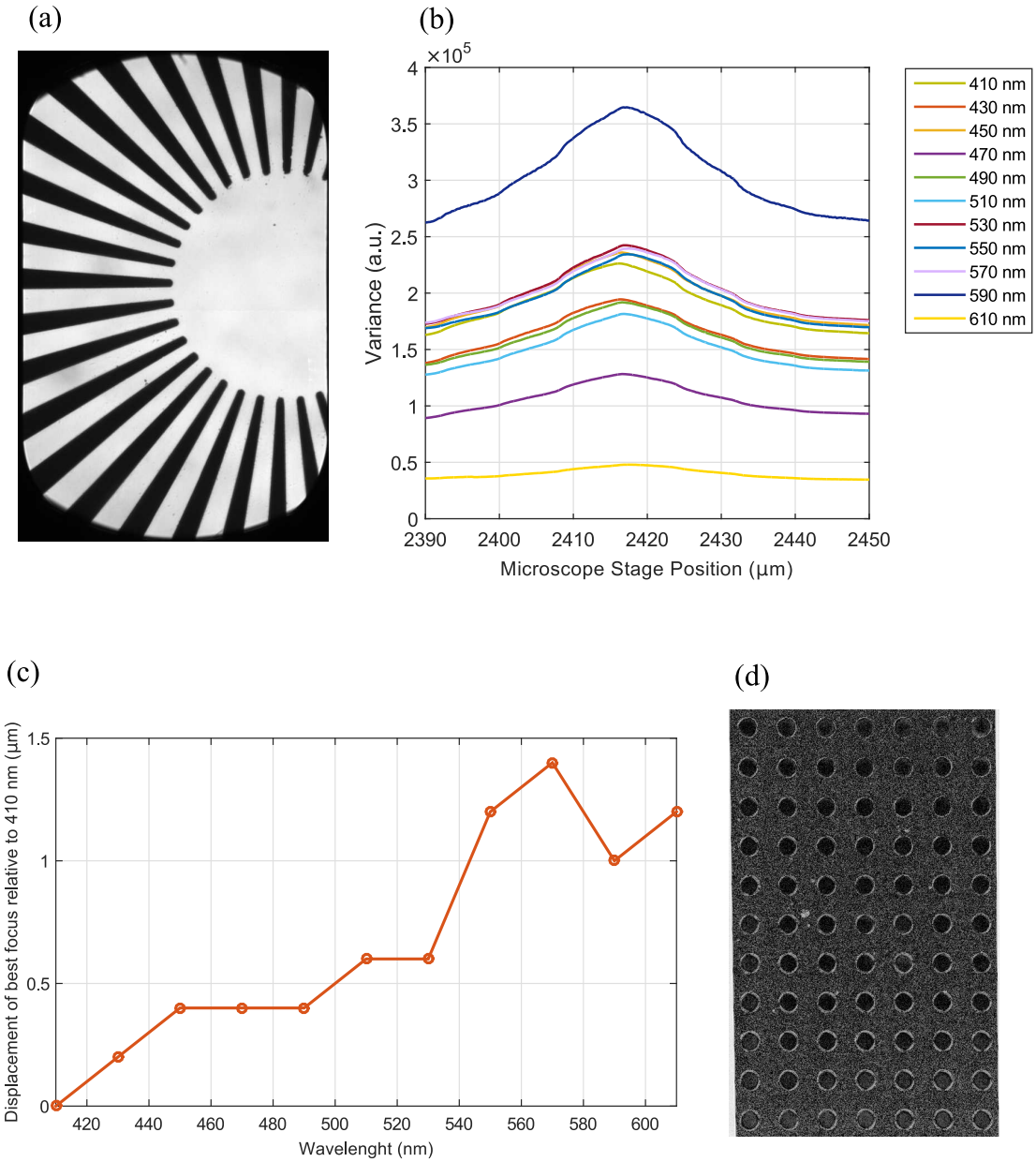

Figure 3.39: Chromatic aberration assessment. (a) Chrome on glass spoke target imaged through our microscope-IRIS system. (b) Variance of the spoke target by scanning in the z axis for different wavelengths. (c) Displacement of the best focus position relative to 410 nm. (d) Chromatic aberration effect compared through the difference of a distortion target image at 567 nm and 591 nm.

10.7% and the standard deviation averaged across seven different blood *OS* values was 6.7%. As previously stated, these values are obtained by comparing our results with the values obtained by a blood gas analyser, which is not a gold standard reference. We are not aware of other published measurements for the accuracy and precision of measuring the *OS* of a single RBC at video rates in vitro. Oximetry is traditionally accomplished using two wavelengths[57]. Analysing the same single RBC deoxygenation data at two wavelengths (λ = 571 nm, 599 nm) using the Lambert-Beer law yielded $OS = 284 \pm 875\%$ prior to deoxygenation and $OS = 20$ at the conclusion of deoxygenation. Eight wavelengths oximetry, therefore, provides enhanced sensitivity when the amount of light absorbed by single RBCs is small when compared with two-wavelengths calibration oximetry. This reason behind this is that using eight points provides less sensitivity to errors than using only two points. Because this technique provides snapshot multispectral video-rate oximetry, it avoids errors due to temporal misregistration. Additionally, the high spatial resolution allowed the use of only pixels in the centre third of each RBC for oximetry, resulting in significantly smaller standard deviations (mean $OS = 102 \pm 9\%$, versus mean $OS = 94 \pm 28\%$ using all the pixels in the cell). Although changes in the *OS* values should be observable at the diffraction limit (0.2 μm) as determined by the 1.45 NA 100x microscope objective, it was not possible to artificially produce a change in haemoglobin oxygenation on this time scale to verify this.

A series of possible source of errors were identified. The first identified source of errors is introduced by the sensor bit-depth. In this case, an 11-bit sensor was used, which is not capable of discriminating between two oxygenations 4-6% apart from each other. This source of error can be eliminated by using a high-speed 16-bit camera, which would have a resolution of 1% in oxygen saturation.

The second source of errors was introduced by the low absorption of RBCs in the 560-600 nm range. Low absorption signal was shown to be problematic as adjacent pixels displayed different spectral signatures and different endmembers abundances. The high noise also made it difficult any curve fitting attempt in order to completely characterise the *OD* distribution of the RBC, which would have taken into account different cell shapes and orientations, allowing a more accurate oximetry analysis of the cell. The solution for this would be to perform the experiment in the 410 nm to 450 nm of the spectrum, which is where light absorption by haemoglobin is the highest. This would be possible by designing a new filter plate in this region of the spectrum.

The third source of errors was a series of artefacts from IRIS that were identified as serrations from the manufacturing process. These defects occurred in different regions for each band, modifying the spectral signature of RBCs and introducing systematic errors in oximetry in different regions of the FoV. The effect was not found to be consistently repeatable between samples and it was not possible to distinguish between the effect of the serrations and physiological changes in the RBCs that would produce changes in oxygenation. The effect of the serrations could be evaluated using microbeads since their absorbance would

not change during the experiment and any change would be due to the serrations. This will be solved in the future by including a set of glass windows which will be index matched with the external surfaces of IRIS.

Other systematic errors included the introduction of longitudinal chromatic aberrations from the RBCs due to lensing and difference in refractive index. The difference in refractive index modified the dimensions of the imaged RBC with wavelength, meaning that once the image is registered, the same region of the same RBC does not occupy the same position in the (x,y) pixels of the 3D cube. In addition, the chromatic aberrations of the system produce a similar effect. The results of these effects are that the spectral information of the RBC is not reliable in the external regions, and that is more reliable to use only the central part of the cells, as shown by the analysis performed using different disk radius for oximetry.

Errors introduced by the LSU analysis and the used references were ruled out by analysing the data with an ICA approach. Independent Components Analysis is meant to identify the spectral components that contribute to the sample transmission. The ICA components were found to be similar to the abundance maps obtained with the LSU analysis, and the same oxygenation gradients were found in some RBCs. These gradients are systematic errors from the analysis and might be due to tilted cells, regions with different cell thicknesses, or changes in transmissions due to optical system defects. The use of OCT[107] would provide a better description of the RBC in terms of shape, thickness and orientation. This additional information would reduce errors through developing models that would include these variations. For example, by knowing the thickness of the RBC pixel by pixel it would be possible to directly apply the Beer-Lambert law (Eq. 1.5).

The edges of each RBC were excluded from analysis for a number of different reasons (Section 3.8). Measurements of RBC *OS* were affected by defocusing. Variation in the axial position of some RBCs in the open container was due to their incomplete attachment to the cover slide by poly-l-lysine. By varying the microscope stage holding the sample along the optical axis over a 10 μm range, the optical density at the edges of the RBCs was observed to change significantly, while the centre of the RBC remained unaffected and was included in oximetry measurements. The defocused parts of the RBCs were identified as edges by the LSU analysis, so they were excluded from the oximetry. However, using a small disk rather than the whole RBC showed more stability during the defocusing sequence, showing that relying on the edges endmember alone is not enough and that chromatic effects are not excluded from the analysis when the whole RBC is used. As for the future work, the defocusing sequence should be repeated with microbeads, in order to obtain a reference behaviour in terms of *OD* and be able to compare it with the behaviour shown by the RBCs.

The shape of RBCs was occasionally that of an echinocyte (spiky) due to the addition of sodium dithionite or present in unaltered horse blood from the date it was purchased. This resulted in greater numbers of pixels being rejected from the cell *OD* image during analysis due to its abnormal shape. The ability of this technique to image RBCs with high

spatial resolution was essential to evaluate which pixels contained abundances belonging exclusively to oxy- or deoxyhaemoglobin endmembers; these were used to calculate the cell's *OS* value.

Future experiments with RBCs should be preceded by controlled experiments. Such experiments would include the use of artificial packages of haemoglobin that would behave as RBCs[100] and it would also use microbeads. The use of artificial RBCs would facilitate the experiment in terms of having a more simple and controlled shape, whereas real RBCs can have inhomogeneities and there can be differences in shape among cells. On the other hand, microbeads can prove useful in terms of characterising how defects in the optical system can affect the transmission of the beads, and then it can be extrapolated to RBCs. Microbeads and artificial cells can also be used to study the effect of defocus and how to take it into account to calculate the oxygenation of cells. Finally, OCT[107] could be added to the technique to the thickness and shape of the RBCs could be identified, which would reduce systematic errors introduced by differences in thickness and the orientation of RBCs.

The edges effects could have been attenuated by using index-matching solution for the RBCs experiments[96, 108], this would eliminate reflection, scattering and refractive effects, which would improve results and the usable RBC surface. A drawback of this approach is that is not applicable for *in vivo* applications. G. Di Caprio *et al.* also published real time deoxygenation of RBCs[96] in a flow cell, but a 1.28 correction factor was applied in order to match their results to the expected oxygen saturation values.

The strength of this technique over two wavelength RBC oximeters is its higher accuracy and its ability to take into account simultaneously for other chromophores in addition to oxy- and deoxyhaemoglobin in RBCs, as long as they have unique spectral signatures as well as anisotropic scattering due to blood and tissue. Examples of other chromophores include methaemoglobin, carboxyhaemoglobin, and haemozoin[94], which is present in RBCs infected with malaria. Chromophores that can be imaged in other human cells include melanin and lipofuscin. A 16-band version of IRIS[3, 114] has been demonstrated, which will allow measurement of these additional RBC chromophores at video rates. In contrast to slower sequential RBC chromophore imagers[94], this technique will allow detection of RBC chromophores at rates relevant to oxygen metabolism of cells.

In addition, the current 8 wavelengths IRIS can be used with a different set of filters, in the blue and the red, in order to be able to perform oximetry measurements in small capillaries (< 20 μm) and larger capillaries in the retina or in other body parts with minimally invasive techniques. This is possible thanks to the replication of the IRIS transmission function along the free spectral range since it allows the selection of multiple spectral lobes on different wavelengths for each waveband. In this case, it is of interest to select a minimum of two wavelengths on the blue, which offer high haemoglobin absorption and hence, improved signal for RBCs.

Using this technique *in vivo* would require using IRIS in the 410 nm to 450 nm range,

which is where haemoglobin absorbs most of the light, making the RBCs to be easily distinguishable from the surrounding tissue. One of the difficulties of applying this technique *in vivo* is the high light scattering and absorption on the short range of the spectrum, which would difficult obtaining information from the microcirculation below the skin. However, this technique could be used in other situations such as nailfold capillaroscopy[115], in which RBCs can be easily imaged. Microendoscopes could be used as a minimally invasive imaging device that could be combined with IRIS. The use of microendoscopes would allow imaging the microcirculation below the skin and can be used in animals models to study diseases such as multiple sclerosis[14]. In terms of performing RBC oximetry in retinal vessels, commercial fundus cameras are unable to resolve RBCs, but adaptive optics and high-speed cameras can be used for such purpose[104] and they could be implemented with IRIS.

Chapter 4

Eight-Wavelength Retinal Oximetry

Summary: This chapter describes the application of IRIS to retinal oximetry. It describes how to optimise the spectral characteristics of the multispectral system to reduce errors in oximetry. A comparison between existing physical models applied to retinal oximetry and a phantom eye are shown. This chapter also shows how the use of 8 wavelengths increases the stability of oxygenation compared with the use of two wavelengths. Finally, this chapter describes an oximetry algorithm which enhances stability and reliability of oximetry *in vivo*.

4.1 Introduction

Section 1.4 provided an overview of retinal oximetry, its importance as a diagnosis technique and the different methods for performing it. From these techniques, the most successful has been two-wavelengths oximetry, which provides good repeatability and is being used as a monitoring tool for diabetic retinopathy[9, 64, 116–119], glaucoma[11, 120], Retinopathy of Prematurity (ROP)[121], retinitis pigmentosa[68] and Alzheimer's disease[69].

The use of physical models for calibration-free retinal oximetry has been proved challenging. Delori[62] (Subsection 1.4.2.2, Eq. 1.17 and Eq. 1.18) obtained an averaged oxygen saturation of $98 \pm 8\%$ for arteries and $45 \pm 7\%$ for veins and it was possible to detect oximetry changes in veins when hyperoxia was induced. This method required calibration in order to take into account the illumination bandwidth effect in the extinction coefficients. More detail on how this was achieved is given in Section 4.2. Values higher than 100% oxygenation were found due to variability in pigmentation, ocular medium turbidity, and eye movement.

Schweitzer *et al.*[78] (Subsection 1.4.2.3 and Eq. 1.19) did not apply their model to a human eye due to the complexity of light propagation in the fundus. Smith *et al.*[79] included a correction factor to account for light scattering for their *in vitro* data and then it was applied in swine eyes. This model was used later by Mordant *et al.*[80] without

calibration in healthy subjects. The results showed values higher than 100% for arteries and below 40% for veins, which are higher and lower respectively than previously reported values using two-wavelengths oximetry.

Oximetry tends to perform better in less complex media, such as windows through the skin on tumour hypoxia studies[10, 122]. In these cases light passes once trough the vessels, simplifying the physical model to be solved. In addition, high quality imaging can be achieved, since there is no turbid medium between the tissue and the sensor.

The eye acts as a window to the retina, which allows to easily image retinal vessels. The problems arise when an accurate physical model is developed in order to characterise light propagation and absorption through the different components of the eye. Pigmentation, eye diameter, choroid thickness, lens opacity, vessel thickness, transmitted light through vessels, light scattering in blood, illumination bandwidth and the spectral characteristics of the system are some of the factors which can modify the measured vessel transmission, and hence, the calculated *OS*. These effects and their associated errors are discussed in this chapter previous to the development of an eight-wavelength retinal oximetry algorithm that allows stable and calibration-free oximetry.

In this chapter, the IRIS-Filter plate system described in Chapter 3 is used. The collimating lens was an 80 mm $F\# = 1.8$ SLR lens and the imaging lens a 50 mm $F\# = 1.4$ SLR lens. A 5.8×12.5mm field stop aperture was used to limit the replicated IRIS images, so overlapping was avoided. The IRIS-Filter assembly was interfaced to a commercial fundus camera (*Topcon*, Japan). The sCMOS sensor used for imaging (*Zyla*, *Andor*) was synchronised with the fundus-camera flash by means of *LabView* (*National Instruments*, USA). The complete system is shown in Fig. 4.1.

This chapter analyses source of errors such as spectral bandwidth, spectral variations in illumination and how to minimise their associated errors. It also includes a method to estimate the fundus reflectance, while showing that using a fundus reflectance reference might not be suitable for all subjects due to different pigmentations degrees. Afterwards, blood wavelength-dependent scattering is introduced in the Beer-Lambert law and the different light paths in blood vessels in the retina are described. Finally, ocular scattering is modelled and introduced in existing physical models for calibration-free retinal oximetry. The modified models are then evaluated in terms of error propagation and finally they are applied to retinal oximetry by means of a retinal algorithm that uses the full potential of the eight-bands IRIS in order to increase the stability of oximetry along vessels.

4.2 Bandwidth effect

The first factor to be taken into account is the spectral bandwidth of the used multispectral technique, which can be a LCTF, a filter wheel, IRIS or any of the imaging spectral devices shown on Section 1.2 that does not output a continuous spectrum on the sensor. This section

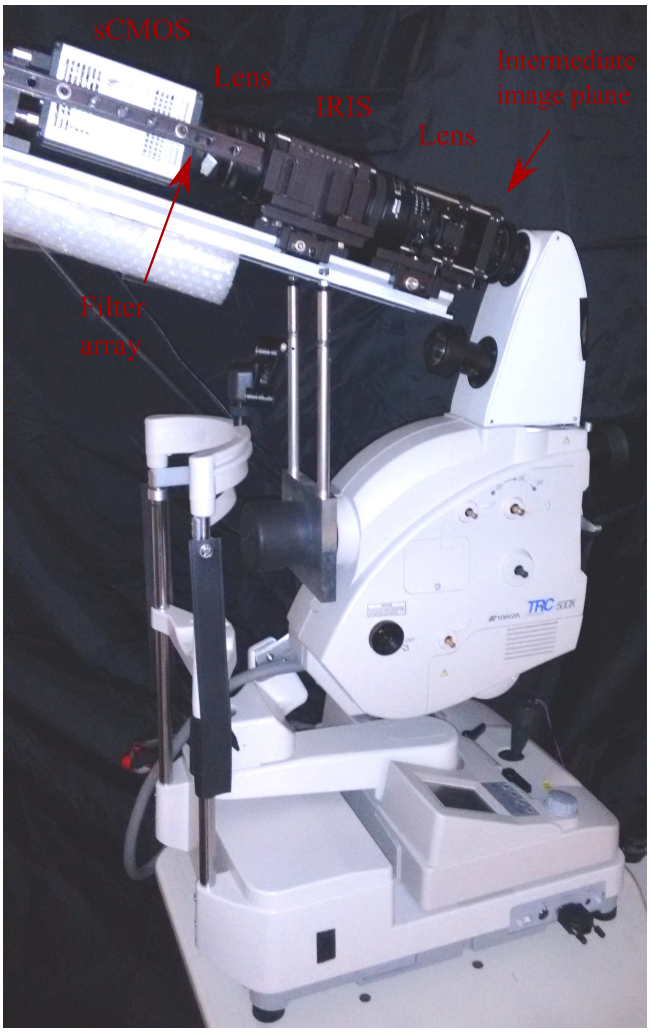

Figure 4.1: Modified fundus camera with the IRIS system. Includes the sCMOS sensor, the filter array, the collimating and imaging lens, IRIS and the stop aperture on the intermediate image plane.

shows how the spectral bandwidth modifies the transmitted intensity through blood, differing from the transmitted light obtained from monochromatic light and how it affects oximetry when is not taken into account.

In Subsection 1.4.2.4, Eq. 1.22 introduced the effect of multiple light paths on vessels. For simplicity, this section assumes only single pass and introduces broadband illumination:

$$T = \frac{T_s \int S(\lambda)\, 10^{-cd\left[\left(\varepsilon_{HbO_2}(\lambda)-\varepsilon_{Hb}(\lambda)\right)OS+\varepsilon_{Hb}(\lambda)\right]} d\lambda}{\int S(\lambda)\, d\lambda}, \tag{4.1}$$

where T_s represents light scattered away from the imaging path, being effectively lost, T_s is assumed to be wavelength independent and $S(\lambda)$ is the system spectral transmission, which includes illumination, filters, coatings and any element which has spectral dependences on transmissions such as IRIS. Eq. 4.1 has an integral form, which in the past compelled some authors to find ways to simplify the computation of this model. Nowadays, this can be easily solved by working with vectors with the system spectral information and the extinction

coefficients of blood. These data needs to be in small enough λ steps in order to approximate a continuous curve. Previous research found that steps of 0.1 nm were enough[3]. The system spectral information can be obtained using a spectrometer, and with this information Eq. 4.1 is expected to produce negligible errors when artificial data is fitted to the model.

As shown during this section, there are several methods for taking into account the spectral bandwidth. To evaluate them in the same way, several blood transmissions were calculated using different bandwidths. Since our interest is focused in the eight IRIS wavebands, the system spectral transmission was approximated by a Gaussian-like function in simulations:

$$S(\lambda) = e^{\left(-\left(\frac{\lambda-\lambda_i}{0.6\times\lambda_{FWHM}}\right)^2\right)}, \tag{4.2}$$

where λ_i is the central wavelength belonging to the 8 IRIS wavebands and λ_{FWHM} is the full-width at half maximum (FWHM) and is the same for each central wavelength, which increases in steps of 2 nm from 0 nm to 20 nm, where λ_{FWHM} = 0 nm is the monochromatic case. For simplicity, the following examples are assumed to have $T_s = 1$ and $OS = 100\%$. For each λ_{FWHM}, eight transmissions were calculated (one per IRIS waveband). A complete set of 11 blood-transmission profiles were generated (one per bandwidth (Eq. 4.2)) using Eq. 4.1. Once the eight-wavelength blood-transmission profiles were created, a global solver built-in *Matlab* was run, applying a non-linear-least-squares method which optimised Eq. 4.1 to the transmission profiles. To assess the effect of bandwidth, the optimisation model considered monochromatic light as the spectral transmission function $S(\lambda)$. Since the transmission data is generated with a certain spectral bandwidth and the model to be fitted assumes monochromatic light, errors in oxygenation are expected.

The results for λ_{FWHM} = 0 nm, FWHM = 10 nm and λ_{FWHM} = 20 nm are displayed on Fig. 4.2, clearly showing how the fits and associated *OS* worsens with higher λ_{FWHM} .

A more accurate description of the effect of not considering the λ_{FWHM} on Eq. 4.1 is shown in Fig. 4.3 for 0%, 50% and 100% oxygenated blood. This figure shows how the error increases with bandwidth. The associated error achieves values of 35.2%, 20.3% and 14.8% for $OS = 100\%$, $OS = 50\%$ and $OS = 0\%$ respectively. The error for $OS = 0\%$ increases more slowly than for the other oxygenations because with larger bandwidth T_s decreases in order to improve the fit.

The first known attempt to take this effect into account was performed by Cohen *et al.*[73] by introducing the concept of average absorbance coefficients. In this publication, the *OD* of the intensity of a retinal vessel divided by the intensity of the background was described as:

$$OD = \frac{1}{2}\log\frac{\int_{\lambda_1}^{\lambda_2} W(\lambda)\,d\lambda}{\int_{\lambda_1}^{\lambda_2} W(\lambda)\,10^{-2\left[\mu_{HbO_2}(\lambda)OS+\mu_{Hb}(\lambda)(1-OS)\right]}q_{tt}(\lambda)\,d\lambda}, \tag{4.3}$$

where λ_1 and λ_2 are the spectral boundaries defined by the filter transmission $W(\lambda)$ and

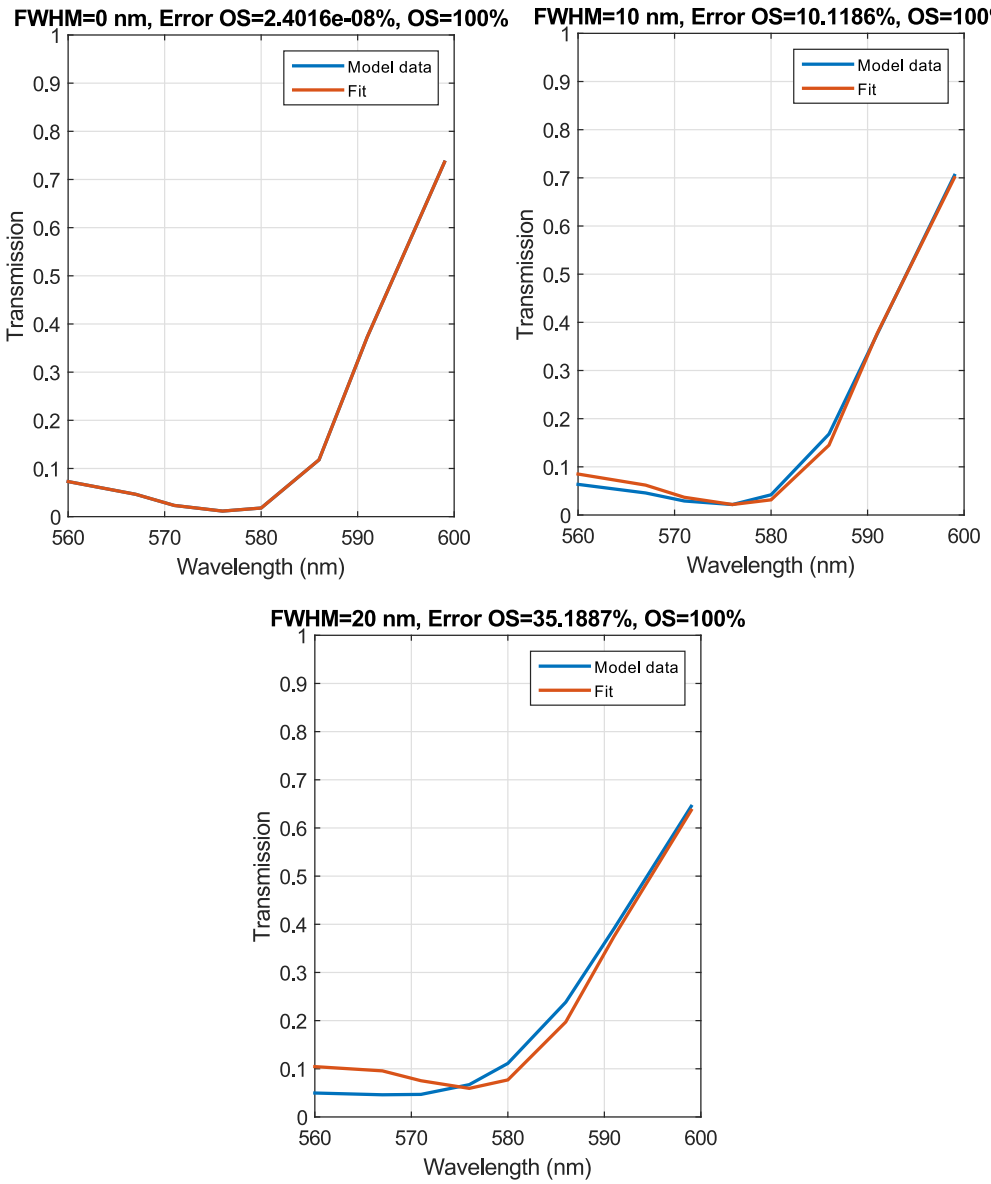

Figure 4.2: Artificial transmission data (blue) for different λ_{FWHM} and fit results considering monochromatic light (red), including the λ_{FWHM} , the OS error of the fit, and the oxygenation of the original transmission. For $\lambda_{FWHM} = 0\,\text{nm}$, the fit (Red) overlaps the model data (Blue) in every point, so this last one is not distinguishable from the fit.

$q_{tt}(\lambda)$ is the scattering component[73]. The idea behind the average extinction coefficients $\bar{\mu}_{HbO_2}(\lambda)$ and $\bar{\mu}_{Hb}(\lambda)$ is that they bypass the need of working with integrals, because they already take into account the spectral characteristics of the system. The OD expression used would then be:

$$OD = [\bar{\mu}_{HbO_2}(\lambda)\, OS + \bar{\mu}_{Hb}(\lambda)\,(1 - OS)] - \frac{1}{2}\log q_{tt}(\lambda)\,. \tag{4.4}$$

The average extinction coefficients are found (Eq. 4.5[73]) by solving Eq. 4.3 and Eq.

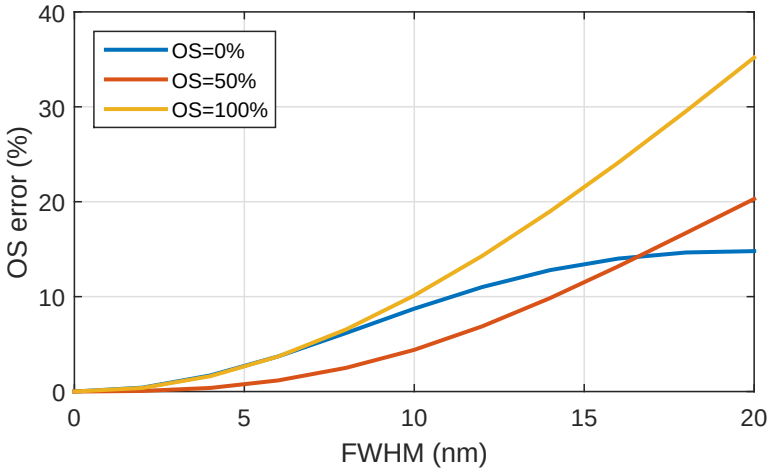

Figure 4.3: *OS* error against λ_{FWHM} for oxygenations 0%, 50% and 100%. Monochromatic light was used on the optimisation process.

4.4 for $OS = 1$ (100% oxygenated) and $OS = 0$ (0% oxygenated):

$$\begin{aligned}\bar{\mu}_{HbO_2}(\lambda) &= -\left(\frac{1}{2cd}\right)\log\frac{\int_{\lambda_1}^{\lambda_2} d\lambda W(\lambda)10^{-2\mu_{HbO_2}(\lambda)}}{\int_{\lambda_1}^{\lambda_2} d\lambda W(\lambda)},\\ \bar{\mu}_{Hb}(\lambda) &= -\left(\frac{1}{2cd}\right)\log\frac{\int_{\lambda_1}^{\lambda_2} d\lambda W(\lambda)10^{-2\mu_{Hb}(\lambda)}}{\int_{\lambda_1}^{\lambda_2} d\lambda W(\lambda)}.\end{aligned} \tag{4.5}$$

Eq. 4.5 has the drawback that it includes the vessels diameter. However, the vessel diameter can be measured in pixels[123] and then translated into microns by considering the eye refractive error[124] or the angular size[125]. Delori[62] removed the double pass assumption and switched it by a geometric factor $0 \leq s \leq 1$. An empirical calibration algorithm was introduced in order to avoid the recalculation of the averaged coefficients for each measured vessel. Delori's version was used to test the performance of the average extinction coefficients:

$$\begin{aligned}\bar{\varepsilon}_{HbO_2}(\lambda) &= -\left(\frac{1}{scd}\right)\log\frac{\int_{\lambda_1}^{\lambda_2} W(\lambda)10^{-scd\varepsilon_{HbO_2}(\lambda)}d\lambda}{\int_{\lambda_1}^{\lambda_2} W(\lambda)d\lambda},\\ \bar{\varepsilon}_{Hb}(\lambda) &= -\left(\frac{1}{scd}\right)\log\frac{\int_{\lambda_1}^{\lambda_2} W(\lambda)10^{-scd\varepsilon_{Hb}(\lambda)}d\lambda}{\int_{\lambda_1}^{\lambda_2} W(\lambda)d\lambda}.\end{aligned} \tag{4.6}$$

As in the previous example, 8 IRIS wavelengths were simulated with 11 different FWHM, from 0 nm to 20 nm in 2 nm steps and for 0%, 50% and 100% oxygenation using Eq. 4.1. The generated *OD*s were fitted to Eq. 1.17 using the averaged coefficients from Eq. 4.6. The *OS* error vs λ_{FWHM} is shown in Fig. 4.4. This figure shows how the averaged coefficients produce no error for $OS = 100\%$ and $OS = 0\%$. However, since the averaged extinction coefficients were obtained by solving Eq. 4.4 for $OS = 100\%$ and $OS = 0\%$, it

was expected that they would not perform well at other oxygenations. This can be observed in Fig. 4.4 for $OS = 50\%$, with a 6.5% OS error at λ_{FWHM} = 20 nm.

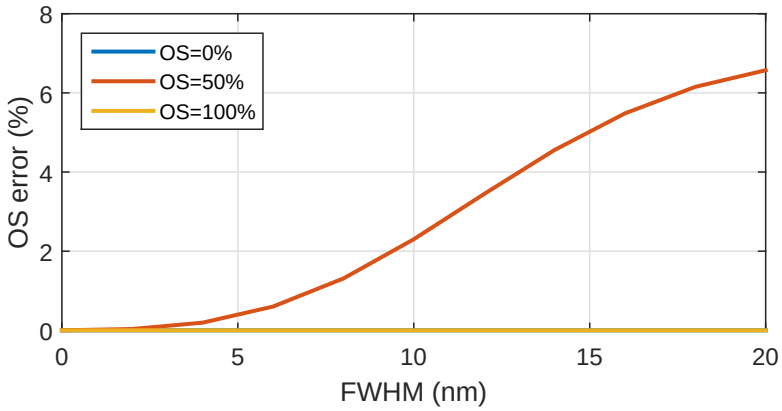

Figure 4.4: Oxygen saturation error vs bandwidth from using averaged extinction coefficients for $OS = 0\%$, $OS = 50\%$ and $OS = 100\%$. The transmissions were generated using Eq. 4.1 and then fitted to Eq. 1.17 with the average extinction coefficients from Eq. 4.6. The errors for $OS = 100\%$ (Yellow) and $OS = 0\%$ (Blue) overlap in each point, so only $OS = 100\%$ (Yellow) is visible.

Other authors spectrally weight the haemoglobin spectrum with the illumination spectrum, producing an effective extinction coefficient[108]:

$$\bar{\varepsilon}_{HbO_2}(\lambda) = \frac{\int_{\lambda_1}^{\lambda_2} W(\lambda)\varepsilon_{HbO_2}(\lambda)d\lambda}{\int_{\lambda_1}^{\lambda_2} W(\lambda)d\lambda},$$
$$\bar{\varepsilon}_{Hb}(\lambda) = \frac{\int_{\lambda_1}^{\lambda_2} W(\lambda)\varepsilon_{Hb}(\lambda)d\lambda}{\int_{\lambda_1}^{\lambda_2} W(\lambda)d\lambda}. \tag{4.7}$$

Following the same procedure as for Fig. 4.4 but using the coefficients from Eq. 4.7, the oxygen saturation was found and the produced errors were evaluated. The behaviour of OS errors with bandwidth is shown in Fig. 4.5. As expected, the error increases with bandwidth, especially for oxygenated blood. In the case of deoxygenated blood, the errors are smaller, partially due to compensation from the parameters c and S from Eq. 1.17 on the optimisation process. In this case, for bandwidths below 5 nm the error is smaller than 0.3%, which is smaller than the 2.7% achieved on Fig. 4.3 when no bandwidth correction was applied.

The best performing method is summarised in Fig. 4.4, which introduces a small error for oxygen saturations other than 100% and 0%. As an example, for λ_{FWHM} = 10 nm, the error in OS is 2.3% for $OS = 50\%$, while the error is $\sim 0\%$ for 100% and 0% oxygenated blood.

In practice, it is possible to use the system spectral data measured with a spectrometer and introduce it in Eq. 4.1 in vectorial form (steps of 0.1 nm or smaller to better simulate a continuous curve) and use the extinction coefficients also in vectorial form. This operation has the effective behaviour of an integral, it is easy to implement, is physically correct

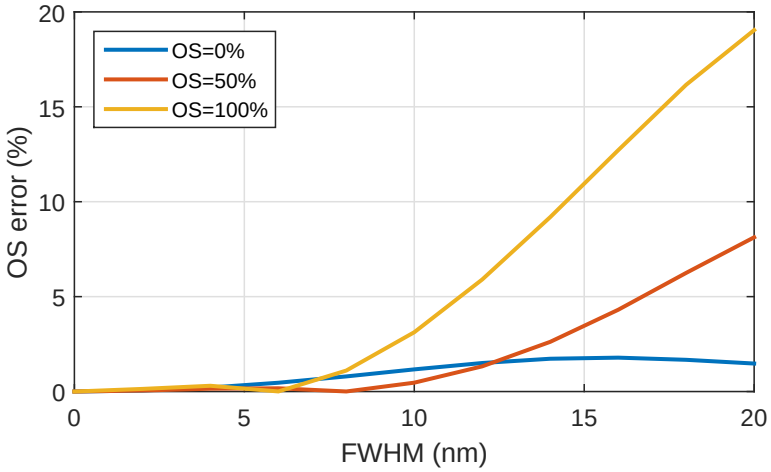

Figure 4.5: *OS* error with increasing bandwidth produced by the use of the weighted coefficients (Eq. 4.7). Transmission data was generated with Eq. 4.1 and then fitted to Eq. 1.17.

and produces *OS* errors $< 10^{-8}\%$ (physically 0) for any bandwidth and oxygenation when artificial data is introduced in the model.

Once the different approaches were evaluated, it was concluded that the best method was to measure with a spectrometer the IRIS transmission function, filters and light source, and use the integral form of Eq. 4.1 in order to minimise errors.

4.3 Spectral variations in illumination

The previous section showed how as long as the spectral data is integrated into the physical model, errors in the retrieved *OS* are expected to be zero if other sources of errors are not included. However, it is important to also consider the effect of spectral differences between the real spectrum and the one introduced in the physical model. For example, halogen lamps tend to shift color temperature with power: blue wavelengths at high power, while they have larger contributions in the red when low power is used. The flash lamp of a fundus-camera (xenon lamp) can also present spectral variations between subsequent pulses. As shown in the previous section, Eq. 4.1 includes $S(\lambda)$, which corresponds to the system spectral transmission and includes the illumination source. Since spectral variations in illumination can occur during an experiment, it is necessary to evaluate the effect it has on the *OS* calculation.

To show the effect of spectral variations on oximetry, a set of 13 illumination spectra, 11 artificial and two experimental from a halogen and xenon lamp (Fig. 4.6), are used in conjunction of IRIS and the filter plate transmission (Fig. 2.18) to generate a set of blood transmission profiles. These transmissions are the input data for the optimisation process of Eq. 4.1 to recover the *OS*. In order to see the effect of spectral variations, the considered illumination on the optimisation of Eq. 4.1 is the one corresponding to a halogen lamp (Fig. 4.6).

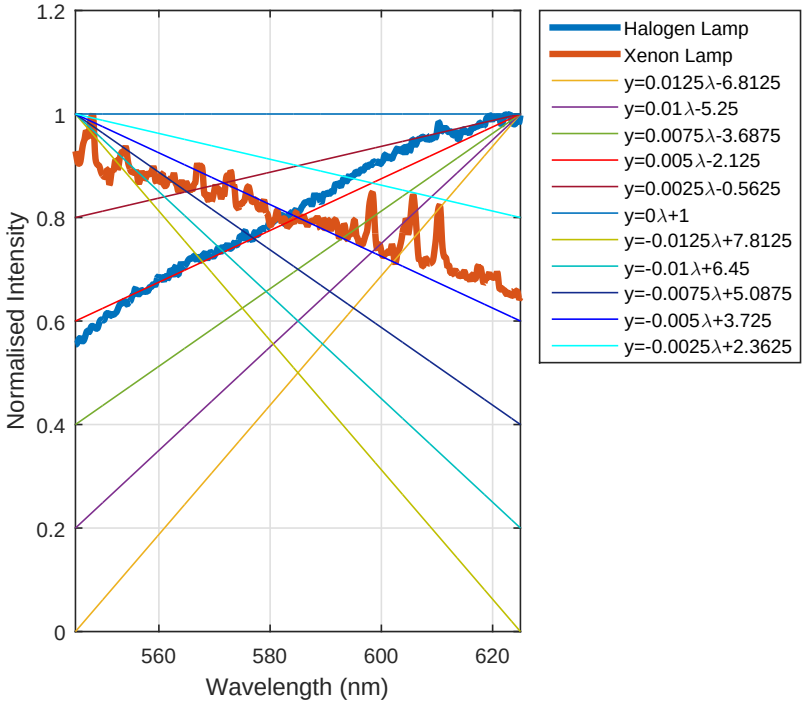

Figure 4.6: Light sources used in the simulations, being the xenon and halogen lamps highlighted while the other sources correspond to straight lines with slopes ranging from 0.0125 to 0 to -0.0025. λ corresponds to the wavelength.

The first characteristic to be observed is the difference between the artificially generated blood transmission with Eq. 4.1 and the resulting blood transmission of the optimisation process considering a halogen lamp as the illumination. The error on transmission is shown in Fig. 4.7(a). In this case, the highest error on transmission is 7.2% and corresponds to the 100% oxygenated case of the illumination $y = -0.0125\lambda + 7.8125$ on Fig. 4.6. This illumination spectral pattern has a correlation of $R = -0.9936$ with the halogen lamp spectrum and has higher contributions towards the blue and lower towards the red wavelengths, while the halogen lamp shows higher contributions in the red and lower in the blue wavelengths.

The second characteristic to be analysed is the error in *OS*. In this case, the maximum recovered *OS* error corresponds to 3.7% (Fig. 4.7(b)) for the 100% oxygenation case of the illumination $y = -0.0125\lambda + 7.8125$, the same illumination in which the maximum error in transmission happens, as expected.

These results show that even in the case of having extreme spectral variations of the illumination such as in the $y = -0.0125\lambda + 7.8125$ case (Fig. 4.6), the error in *OS* is $<$ 4%, which is not insignificant. This 4% could be the difference between 58% oxygenation of veins in a healthy subject and the 66% of a diabetic patient[118], which highlights the importance of using the right spectral system transmission.

Fig. 4.6 also includes spectra with minor variations compared with the halogen lamp spectrum. These are $y = 0.0025\lambda - 0.5626$, $y = 0.005\lambda - 2.125$ and $y = 0.0075\lambda - 3.6875$,

which produce *OS* errors at 100% oxygenation of 0.49%, 0.02% and 0.05% respectively. In general, pulse oximeters and blood gas analysers have an accuracy of 1% or 0.5%, so the obtained *OS* errors for small variations on the spectrum are negligible.

In conclusion, as long as the same illumination lamp is used in terms of spectrum for the data taking and the optimisation process, even small spectral variations during the experiment should not produce any significant errors in the recovered *OS*. The light source spectrum should be periodically measured in order the effect of variations during time, although this would not solve the issue of spectral variations due to power changes during the experiment.

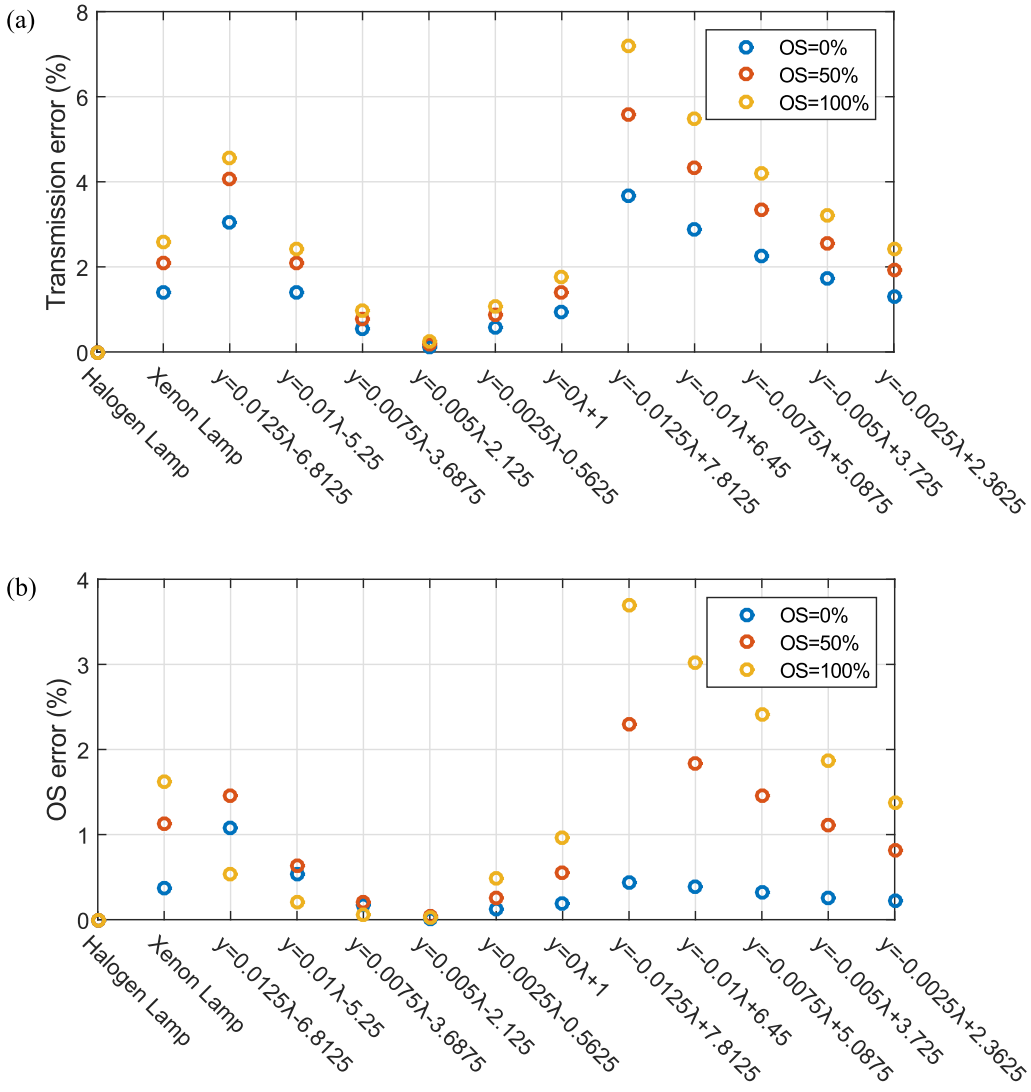

Figure 4.7: Effect of spectral variations in illumination using the illumination shown on Fig. 4.6 for 100%, 50% and 0% blood oxygenation. The halogen lamp spectrum is used in the physical model when the optimisation is performed. (a) Error in transmission (b) Error in *OS*.

4.4 Fundus reflectance

To characterise more accurately the spectral behaviour of the eye it is necessary to take into account the fundus reflectance of the eye. The main reflector on the eye is the sclera, but the albedo does not have any significant spectral signature in the IRIS working range from 560 nm to 599 nm[126]. The main spectral contributors for the fundus reflectance are the choroid, choroidal pigmentation and the RPE[5]. The choroid is a highly oxygenated and vascularised layer with a thickness ranging from 272 μm at the fovea, to 256 μm thickness at 1 mm from the fovea in the temporal region, to 248 μm thickness at 1 mm from the fovea in the nasal region[127]. The choroidal pigmentation correlates with the subjects' skin pigmentation while there is a low correlation between the RPE pigmentation and skin pigmentation[128]. Due to the high absorption of blood in the blue-green range, the choroid contributes to the reflectance less than the retinal layers[5], while in the red wavelengths the choroid is highly transparent, and the choroid structure is visible[129], contributing to non-uniformities in the background.

The importance of characterising the fundus reflectance can be better understood when observing arteries in retinal images of subjects with heavily pigmented eyes at red wavelengths. It has been shown in the past that back-scattered light from blood can be larger in terms of intensity than transmitted light[51] under certain haematocrit and sample depth conditions. In cases where pigmentation concentration is high, light is highly absorbed by the fundus and most of the collected intensity coming from the vessel is directly backscattered from blood in the vessel[71, 72, 79]. In these cases, images of a heavily pigmented fundus can show arteries with higher grey levels than the fundus (Fig. 4.8). When $I_{Fundus} < I_{Vessel}$ we have $T_{Vessel} = {}^{I_{Vessel}}/_{I_{Fundus}} > 1$, being T_{Vessel} the blood transmission of the analysed vessel. If the correct fundus reflectance is not used, the physical model might not be able to accurately replicate vessel transmissions higher than 1, increasing errors in the recovered oxygenation.

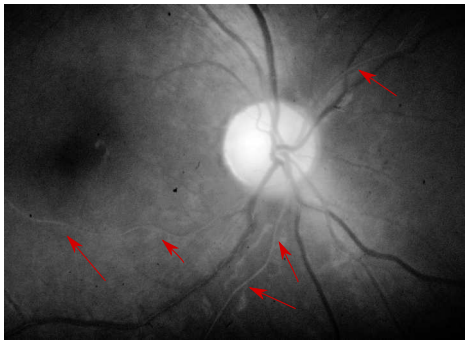

Figure 4.8: Intensity image obtained with IRIS at 599 nm of a darkly pigmented eye, showing some arteries being brighter than the background. In terms of transmission, this would mean that these arteries have transmissions higher than 1 at 599 nm and longer wavelengths.

To estimate the fundus reflectance, the ratio between the obtained fundus intensity and

the intensity obtained from a white spectral reference (Spectralon) at the same wavebands and under the same illumination conditions was performed. Under ideal circumstances in which a model eye behaves as a real eye, this ratio should provide the fundus reflectance when images are captured under equal illumination conditions. Since the conditions and similarities between a model and a real eye are limited, the calculated reflectance is expected to be only an approximation of the real fundus reflectance. The obtained reflectances for a set of different subjects with different degrees of pigmentation will be compared with fundus reflectance from the literature. The ratio of extravascular light reflection (EVR) between 571 nm and 599 nm[57] will be calculated to show its behaviour with increasing pigmentation degree. Finally, the calculated pigmentation will be introduced in an oximetry physical model to calculate the blood oxygenation and it will be compared with the effect of assuming a reference fundus reflectance.

In first place, nine subjects with different degrees of pigmentation were imaged using the IRIS system interfaced with a fundus camera (*Topcon*, Japan). The degrees of pigmentation were classified as "Light Pigmentation", which corresponded to subjects with blue eyes and light skin, "Medium Pigmentation", which corresponded to subjects with brown eyes and light skin, and finally "Heavy Pigmentation", which corresponded to subjects with dark eyes and dark skin.

Major vessels with diameters larger than $100\,\mu$m were selected, tracked and analysed. The background intensity of the vessels was averaged in order to obtain a spectral intensity profile for each retina representative of the fundus. After performing retinal imaging, a model eye (Fig. 2.20) filled with water and with Spectralon as a background was imaged with the same flash settings. Images taken of the model eye with Spectralon and without capillaries were used to obtain an intensity reference of the background at each waveband. This was achieved by averaging a region of interest of approximately 100 pixels for each IRIS image. The ratio between the retinal spectral intensity profiles and the intensity obtained from the Spectralon on the model eye provided an estimation of the fundus reflectance. The obtained reflectances were compared with the fundus reflectance reference from Delori *et al.*[5] on Fig. 4.9(a). In this experiment, the angle of incidence of the beam can be different in the human eye and in the model eye, which in return affects the collected intensity. As an example, if the model eye is slightly tilted, more light is reflected away from the imaging path, reducing the collected intensity and reducing the calculated fundus reflectance when the ratio between intensities is performed. Since the angle of illumination might change during the experiments, the sampled fundus reflectances can be affected by different scaling factors, which makes difficult a comparison with a fundus reflectance reference. A scaling factor was found for each calculated reflectance so the reflectance value at 571 nm would match the value of the fundus reflectance reference at 571 nm. 571 nm was selected due to its isosbestic behaviour. The adjusted reflectances are shown in Fig. 4.9(b). The adjusted reflectances show a decrease in reflectance with increasing pigmentation on the 591 nm

and 599 nm wavelengths while in the shorter wavelengths there is little difference among subjects, mainly due to the scaling at 571 nm and the absorption from the choroid. Delori's fundus reflectance[5] was added as a reference (sampled only at IRIS wavelengths).

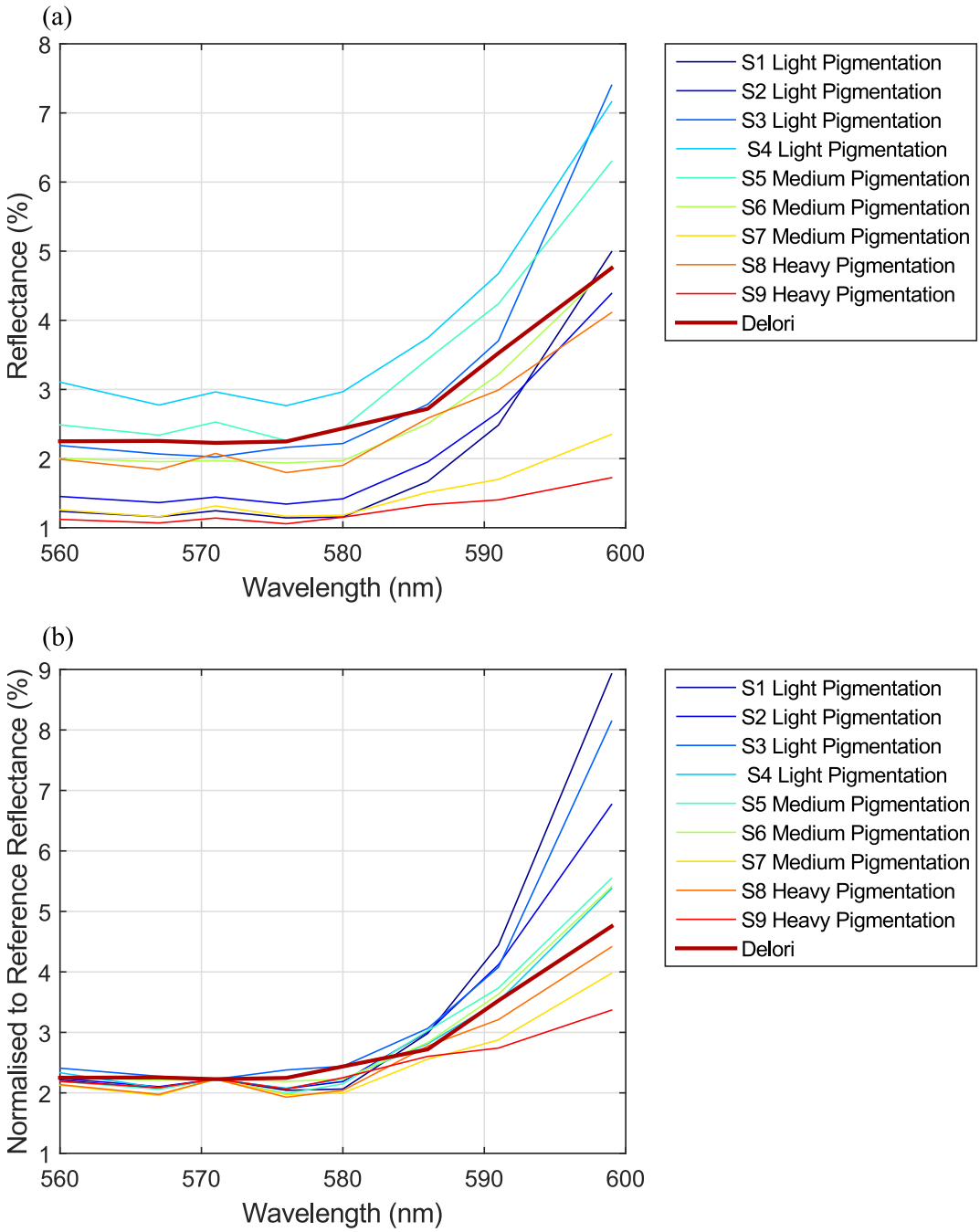

Figure 4.9: (a) Estimated fundus reflectances compared with the reference from Delori *et al.*[5]. (b) Adjusted reflectance to match the reference at 571 nm.

The pigmentation dependence was also evaluated by using the ratio of extravascular light reflection (EVR) between 571 nm and 599 nm[57] as shown in Subsection 1.4.1 and Eq. 1.13. The EVR for the obtained reflectance profiles was shown to increase with pigmentation (Fig. 4.10).

It is important to notice that the recovered fundus reflectance using this method is not a

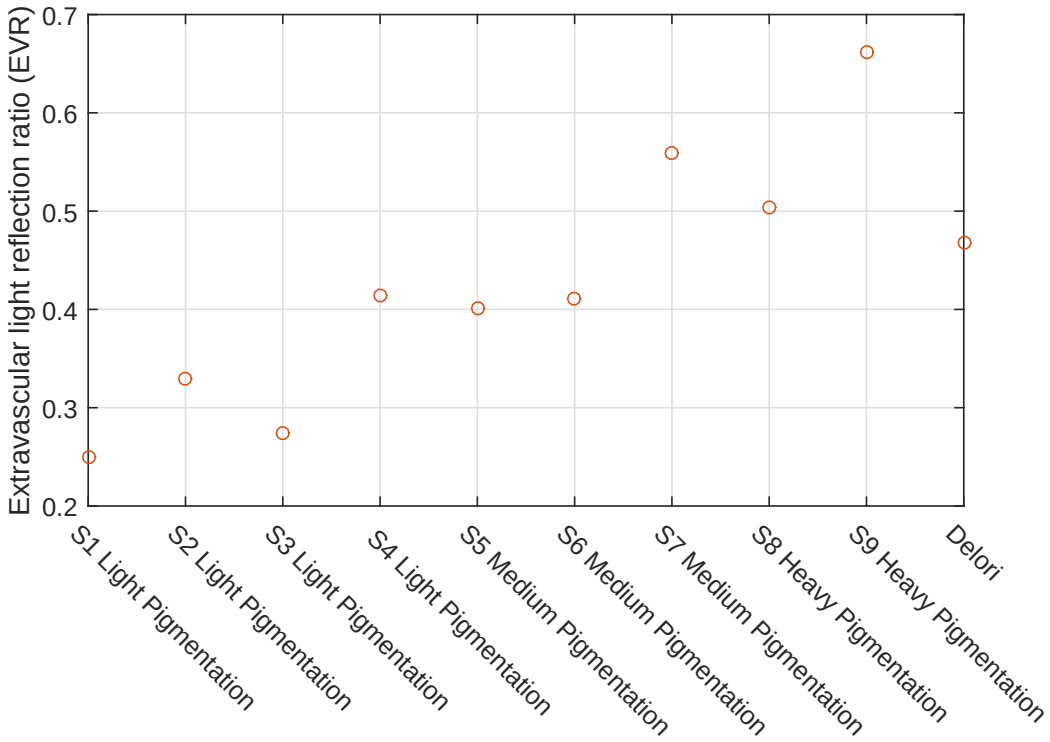

Figure 4.10: Extravascular light reflection ratio using 571 nm and 599 nm, showing how it increases with pigmentation. The reference fundus reflectance from Delori corresponds to medium pigmentation and is included at the end of the figure.

continuous spectral curve and that there are only data points at IRIS central wavelengths.

The error introduced by neglecting the continuous reflectance curve was evaluated. For this purpose Eq. 4.1 was used assuming single pass, $OS = 0\%$ to $OS = 100\%$ in 20% steps, $T_s = 1$, $c = 0.0023\,{}^{\text{mole}}/_{\text{litre}}$ (human blood haematocrit 45%), $d = 150\,\mu$m and $S(\lambda)$ including IRIS transmission, the filter plate, the broadband filter, the illumination spectrum from a xenon lamp and Delori's fundus reflectance[5] interpolated in the 545 nm to 625 nm at 0.1 nm steps. Eq. 4.1 was then optimised to find OS, c and T_s using the generated transmission and considering the reference fundus reflectance from Delori *et al.*[5] as if it was obtained by IRIS (Fig. 4.9), which only contains 8 wavelengths. The error in transmission between the artificial data and the data from the optimisation increased with higher OS to a maximum of 7.7% error at 100% OS (Fig. 4.11(a)). More important than the error in transmission is the OS error obtained from the optimisation. Fig. 4.11(b) shows relatively low errors for oxygenations, being 1.3% the maximum error in OS. This error in oxygenation is below the standard deviation obtained at two-wavelengths oximetry for veins and arteries[59, 63]. From the point of view of using this generated fundus reflectance (8 available wavelengths) rather than the complete fundus reflectance in the full used spectral range, the introduced errors are considered small, and this method can be considered to provide a good estimation of the fundus reflectance.

The main concern with introducing the fundus reflectance into the physical model

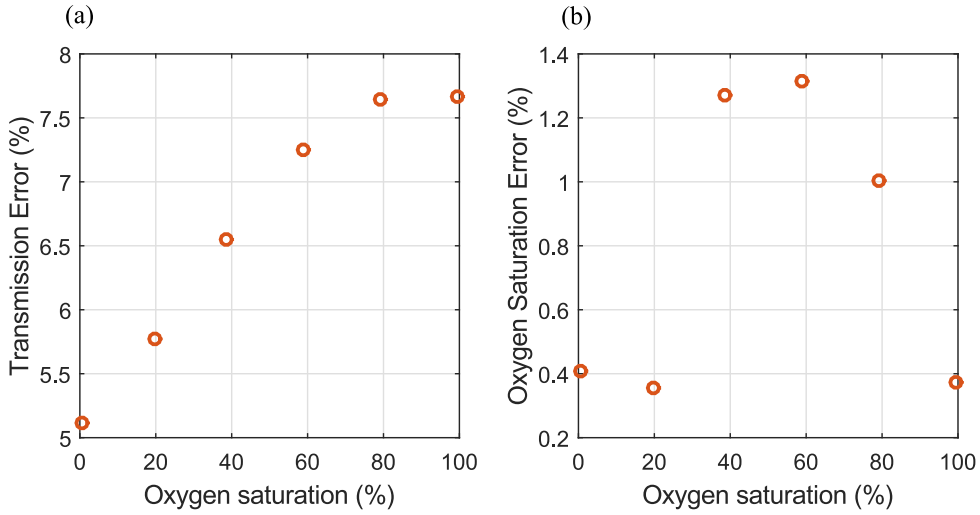

Figure 4.11: Errors introduced by using the reference fundus reflectance as obtained from retinal images with IRIS instead of using the continuous reference fundus reflectance. (a) Error in transmission. (b) Error in *OS*.

is the associated error generated when a different fundus reflectance than the real one is used. Since the generated fundus reflectance is not continuous and has only 8 data points (one per wavelength), it behaves as a scaling factor to the intensity integrals on Eq. 4.1 $\left(T = \frac{T_s \int S(\lambda) 10^{-cd\left[\left(\varepsilon_{HbO_2}(\lambda)-\varepsilon_{Hb}(\lambda)\right)OS+\varepsilon_{Hb}(\lambda)\right]} d\lambda}{\int S(\lambda) d\lambda}\right)$. This means that the obtained fundus reflectance cancels when the vessel and background intensities are divided. Eq. 4.1 would be independent of errors on the measured fundus reflectance as long as the reflectance is not a continuous. In the case of being continuous, it cannot be excluded from the integral and it would not cancel. However, when the blood reflectance[51, 79] is included (backscattered component) in the physical model, the fundus reflectance does not cancel for this component because the vessel intensity is not affected by the fundus. This case can be represented using Eq. 1.9 and Eq. 4.1 to simulate a case with single pass and backscattered light, which produces:

$$T = \frac{\int X_1 S(\lambda) F(\lambda) 10^{-cd\left[\left(\varepsilon_{HbO_2}(\lambda)-\varepsilon_{Hb}(\lambda)\right)OS+\varepsilon_{Hb}(\lambda)\right]} d\lambda}{\int S(\lambda) F(\lambda) d\lambda}, \\ + \frac{\int X_3 S(\lambda) + X_4 S(\lambda) 10^{-cd\left[\left(\varepsilon_{HbO_2}(\lambda)-\varepsilon_{Hb}(\lambda)\right)OS+\varepsilon_{Hb}(\lambda)\right]} d\lambda}{\int S(\lambda) F(\lambda) d\lambda}, \tag{4.8}$$

where X_1 the single pass scattering losses, X_3 and X_4 are constants for the backscattered component, $S(\lambda)$ includes the spectral transmission of IRIS and the filter plate and the illumination spectrum, $F(\lambda)$ is the fundus reflectance, which for this case it has only one value for each IRIS band. In the single pass section of the integral, the fundus reflectance is located in dividend and divisor, being then cancelled in the division because it is a single value per waveband rather than a continuous curve. The second part of Eq. 4.8 includes the backscattered component, and the part corresponding to the vessel does not include the

fundus reflectance, meaning that when is divided by the background, the fundus reflectance has an effect on the vessel transmission.

To assess the effect of using a fundus reflectance reference in the *OS* recovery in subjects with different pigmentation degrees, meaning different fundus reflectance, a set of blood transmission profiles using Eq. 4.8 was generated for each fundus reflectance on Fig. 4.9(b). The obtained transmissions were fitted to Eq. 4.8 in order to recover the *OS* by applying an optimisation process (non-linear data fitting) and using Delori's fundus reflectance (Fig. 4.9(b)) for all the generated transmission.

Since a sample of 9 subjects is small to draw any statistically significant conclusion and the definitions of the pigmentation degrees are broad and only based on eye and skin colour, the objective of this section is to show how errors are introduced when the wrong reflectance is used, and that these errors might become larger when the subject fundus reflectance differs more from the reference used in the *OS* recovery.

The errors introduced by not using the correct reflectance are shown in terms of the absolute error in transmission (Fig. 4.12(a)), which evaluates the absolute error between the input transmission generated with the subject fundus reflectance and the output transmission obtained from the fit using the reference reflectance. The error in transmission evaluates the ability of the fundus reflectance reference to fit the original blood transmission.

The absolute errors produced were also evaluated in terms of the retrieved oxygenation (Fig. 4.12(b)). The absolute error in *OS* was obtained by comparing the oxygenation used to generate each blood transmission for each subject using its own fundus reflectance and the oxygenation retrieved by fitting assuming a fundus reference.

In addition, the correlation coefficient between the fundus reflectance reference with the calculated fundus reflectances was calculated for comparison with the *OS* and transmission error.

The blood transmission produced by the optimisation process showed absolute errors between 2% and 5% from the original input transmission (Fig. 4.12(a)). The oxygenation recovery showed major absolute errors in all cases (Fig. 4.12(b)), being in general higher than 10% *OS*, which is not acceptable. Regarding the correlation between the reference and the subject fundus reflectance, it was expected to see a direct link between correlation and absolute errors in transmission and oxygenation, but this link was not observed, as seen in Fig. 4.12. As an example, the fundus reflectances of subjects S7, S8 and S9 had a lower correlation with the fundus reflectance than subject S2, however, the error in oxygenation of subject S2 is comparable to the errors of subjects S7, S8 and S9.

Although more fundus reflectance data of more subjects and a more accurate classification of pigmentation would be necessary to draw a more solid conclusion about errors in the recovered *OS* and the degree of pigmentation, this section shows that if a different reflectance than the one of the analysed retina is used, errors in oxygenation can be significant enough as to invalidate the oximetry results. If the subject fundus reflectance is not available, a ref-

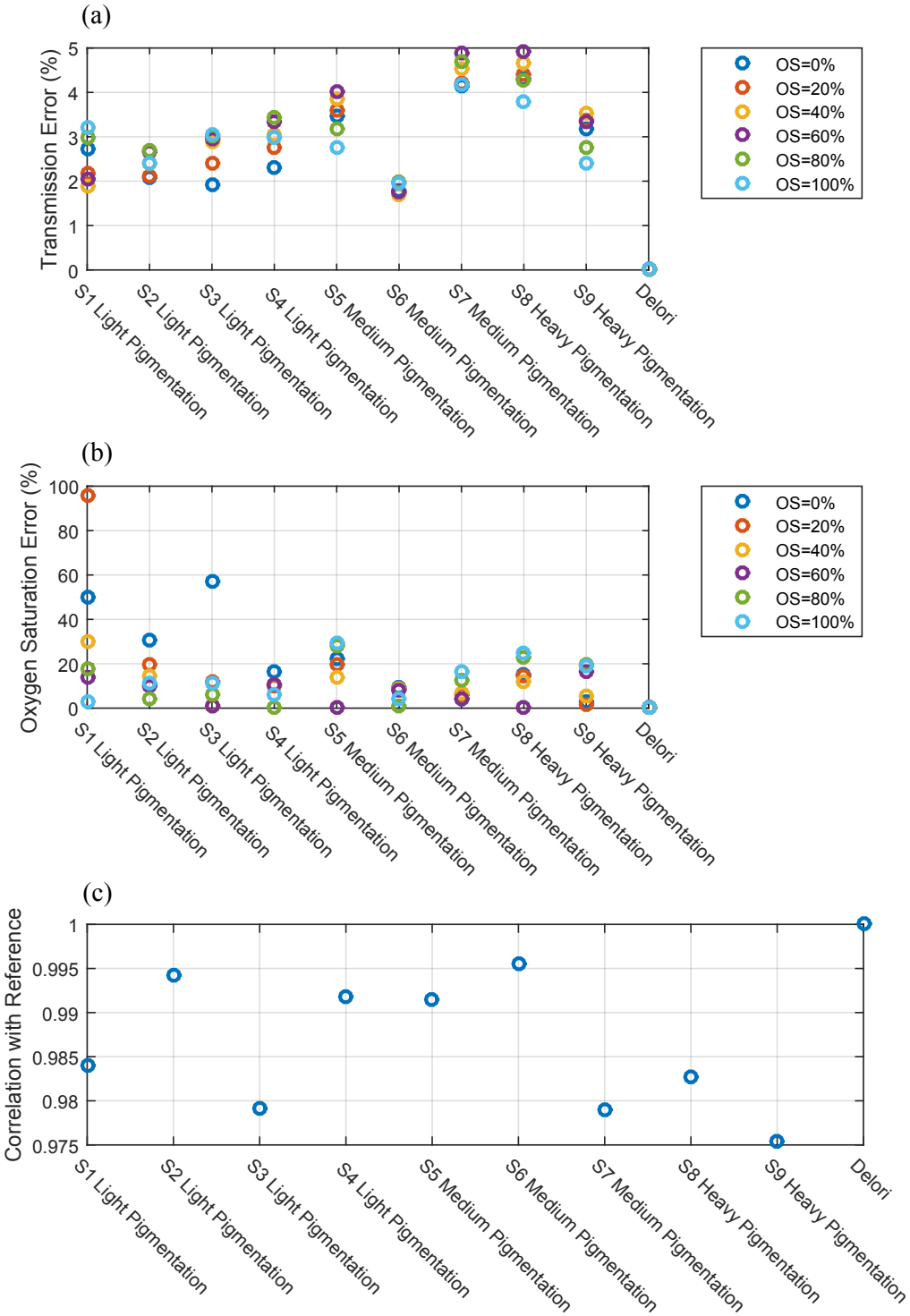

Figure 4.12: Effect of assuming the same fundus reflectance for a set of generated transmission under different reflectance conditions (Fig. 4.9(b)). (a) Absolute error in transmission. (b) Absolute error in oxygenation. (c) Correlation coefficient of experimental fundus reflectance with Delori's fundus reflectance.

erence should be used considering that errors are expected to be more relevant in a lightly pigmented retina than in a darkly pigmented retina.

4.5 Calibration-free physical model

Once the effects of spectral variations in illumination, bandwidth, and fundus reflectance have been discussed, it is possible to introduce them into the available calibration-free physical models from the literature on retinal oximetry. These models were described in Subsection 1.4.2 and correspond to Eq. 1.19, Eq. 1.21 and Eq. 1.22. The first model, Eq. 1.19[78], expands the Beer-Lamber law by including wavelength dependent and independent light scattering (S and $n\log\frac{1}{\lambda}$) and a geometric factor that depends on the illumination and the geometry of light collection (s). Eq. 1.21[79] introduces the different light pathlenghts that contribute to the collected intensity of the vessel. These pathlengths (Fig. 4.13) correspond to light reflected by the fundus and travels once through the vessel (single pass), light that passes through the vessel twice, being reflected once by the fundus (double pass) and backscattered light by the vessel that never reaches the fundus. Finally, Eq. 1.22 is a special case of Eq. 1.21 in which either the double pass or the backscattered component are considered to be negligible.

Since these equations are in integral form, applying the logarithm to obtain the optical density so the models could be simplified is not possible. Instead, it is more convenient to work with transmissions. These equations were rewritten as:

$$T_{SCW} = \frac{\int Y(\lambda)R(\lambda)\,10^{-S-n\log\left(\frac{1}{\lambda}\right)-scd\left[\left(\varepsilon_{HbO_2}(\lambda)-\varepsilon_{Hb}(\lambda)\right)OS+\varepsilon_{Hb}(\lambda)\right]}d\lambda}{\int Y(\lambda)R(\lambda)\,d\lambda}, \tag{4.9}$$

$$\begin{aligned} T_C = {} & \frac{\int X_1 Y(\lambda)R(\lambda)10^{-cd\left[\left(\varepsilon_{HbO_2}(\lambda)-\varepsilon_{Hb}(\lambda)\right)OS+\varepsilon_{Hb}(\lambda)\right]}d\lambda}{\int Y(\lambda)R(\lambda)d\lambda} \\ & + \frac{\int X_2 Y(\lambda)R(\lambda)10^{-2cd\left[\left(\varepsilon_{HbO_2}(\lambda)-\varepsilon_{Hb}(\lambda)\right)OS+\varepsilon_{Hb}(\lambda)\right]}d\lambda}{\int Y(\lambda)R(\lambda)d\lambda} \\ & + \frac{\int X_3 Y(\lambda)+X_4 Y(\lambda)10^{-cd\left[\left(\varepsilon_{HbO_2}(\lambda)-\varepsilon_{Hb}(\lambda)\right)OS+\varepsilon_{Hb}(\lambda)\right]}d\lambda}{\int Y(\lambda)R(\lambda)d\lambda}, \end{aligned} \tag{4.10}$$

$$T_{DN} = \frac{\int T_s Y(\lambda)R(\lambda)\,10^{-\chi cd\left[\left(\varepsilon_{HbO_2}(\lambda)-\varepsilon_{Hb}(\lambda)\right)OS+\varepsilon_{Hb}(\lambda)\right]}d\lambda}{\int Y(\lambda)R(\lambda)\,d\lambda}, \tag{4.11}$$

where $R(\lambda)$ the fundus reflectance and $Y(\lambda)$ the system transmission function including IRIS, filter plate, broadband filter and illumination.

Eq. 4.10[79] represents all the possible pathlengths in retinal vessels. X_1 and X_2 are the light contributions of single and double pass respectively, while X_3 and X_4 are the coefficients for backscattered light[51]. These pathlengths can be better understood by representing them in a simplified model of a retina (Fig. 4.13), in which the vessel is represented in red. Light is represented as being specularly reflected by the fundus while in reality the fundus diffuses light rather than reflecting it.

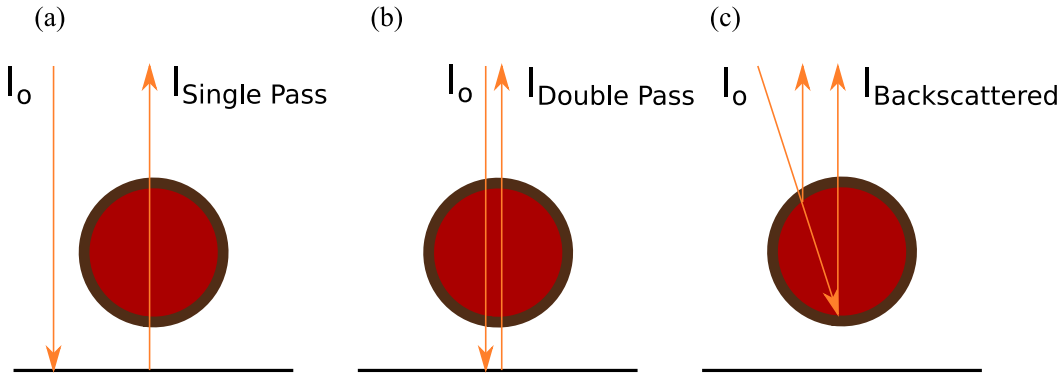

Figure 4.13: pathlengths in retinal vessels. (a) Single pass, X_1. (b) Double pass, X_2. (c) Backscattered, X_3 and X_4.

Eq. 4.11[79] is a simplification of Eq. 4.10. The considered approximations are partially possible due to the use of a confocal scanning laser ophthalmoscope () as a retinal imaging device. A cSLO restricts illumination and imaging to small volumes of blood and retinal tissue, allowing an improved light collection over a fundus camera by rejecting stray light from other parts of the eye. In addition, in a cSLO with the appropriate stop aperture or pinhole, the main collected components would be backscattered light when a vessel is imaged[82]. Under different pinhole configurations, a cSLO can collect nearly only single pass or double pass. In a fundus camera, this is not true since the collected light proceeds from different parts of the adjacent retina.

Regarding the pathlengths contributions to blood transmissions, Monte-Carlo simulations showed that for vessels with diameter higher than 50 μm and using a cSLO the main component is backscattered light and is the main contributor for larger vessels, while double pass is almost non-existent for larger vessels[71, 72]. These simulations were applied considering a complete model of the eye including the retina, choroid, RPE and sclera, taking into account their respective absorption, scattering coefficients and anisotropy factor. Monte Carlo simulations also showed how with an increase of pigmentation (RPE and/or choroid) the backscattered component dominates over the other components, double pass being almost negligible to vessel intensity[72].

On the other hand, Monte Carlo models considering the fundus as a layer which scatters and absorbs light (replicating the behaviour of Spectralon) showed that the main component is single pass[130].

In terms of the model to be used in this research, Eq. 4.9 does not take into account pathlengths contributions and only considers scattering from blood (more details in Subsection 1.4.2.3), and Eq. 4.11 is a simplification which might be only applicable in cases where there is some control over the illumination and pathlengths, such as using cSLO. Due to these reasons, Eq. 4.10 is the model applied in this thesis. However, the performance of the three models is tested in terms of error propagation and oximetry Subsection 4.5.3.

4.5.1 Whole blood wavelength dependent scattering

The models in Eq. 4.9, Eq. 4.10 and Eq. 4.11 lack the wavelength-dependent scattering component for whole blood. The scattering coefficient represents a scattering event a photon would suffer when travelling through a medium, but it does not considers the anisotropy of the medium or the occurrence of multiple scattering events. For the scattering to be correctly introduced in the physical model, it is necessary to use the reduced scattering coefficients, which are obtained from the scattering coefficients and the anisotropy factor. The reduced scattering coefficient describes the diffusion of light through tissue, taking into account multiple scattering events and the anisotropy of the medium[131].

$$\mu_s' = (1-g)\,\mu_s, \tag{4.12}$$

where μ_s' are the reduced scattering coefficients, g is the anisotropy factor and μ_s are the scattering coefficients.

The reduced scattering coefficient for oxy- and deoxyhaemoglobin can be found in the literature for a haematocrit of 33.2%[111] (Fig. 4.14). Since haematocrit can vary between subjects and among blood vessels, it is necessary to introduce a multiplying factor in order to scale them[132]:

$$\mu'_{s,hct2} = \frac{\gamma(hct2)}{\gamma(hct1)}\frac{hct2}{hct1}\mu'_{s,hct1}, \tag{4.13}$$

where hct the haematocrit and $\gamma(hct)$ is a non-linear scaling factor. The choice for $\gamma(hct)$ was done considering Mie scattering[132], since Mie scattering theory matches adequately the macroscopic scattering observed in whole blood[133]:

$$\gamma(hct) \approx (1-hct)^2. \tag{4.14}$$

By using Eq. 4.13 with Eq. 4.14 and considering that scattering is oxygen dependent[111], the scattering component of whole blood can be rewritten:

$$\alpha = -\frac{(1-hct2)^2}{(1-hct1)^2}\frac{hct2}{hct1}d\left[\left(\mu'_{s,HbO_2} - \mu'_{s,Hb}\right)OS + \mu'_{s,Hb}\right], \tag{4.15}$$

where

$$hct = c\frac{RBCmw}{m_{Hb}}. \tag{4.16}$$

In Eq. 4.16 c corresponds to haemoglobin concentration in whole blood, $m_{Hb} = 350\,\mathrm{g/litre}$[134] is the haemoglobin concentration in a human RBC and $RBCmw = 64500\,\mathrm{mole/litre}$[47] is the haemoglobin molar mass. The scattering component (Eq. 4.15) will then be included in physical models with the absorption coefficients.

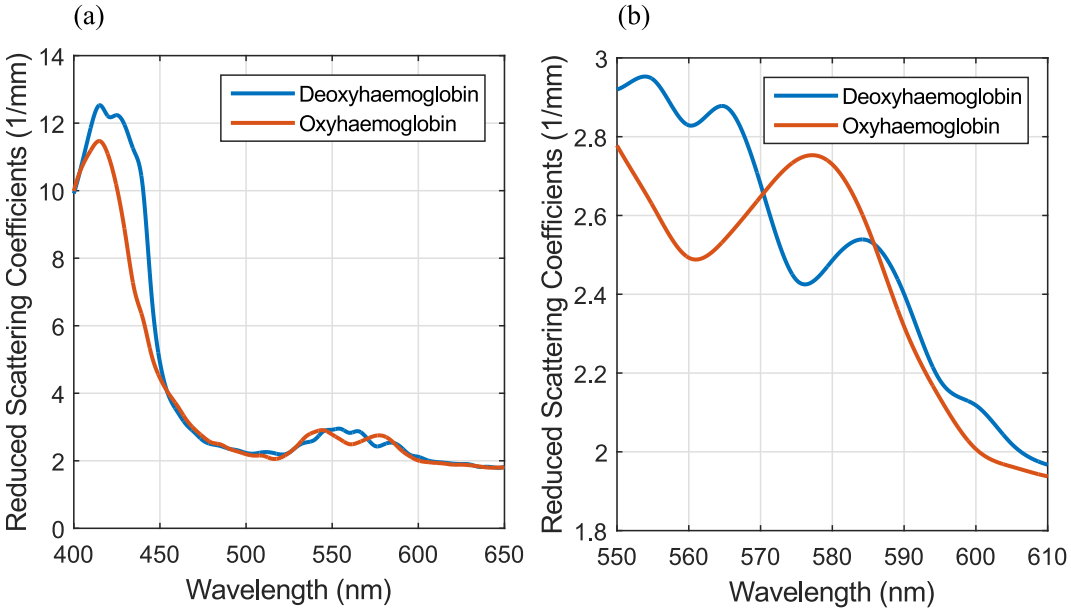

Figure 4.14: Reduced scattering coefficients at 33.2% haematocrit. (a) 400 nm to 650 nm range. (b) 550 nm to 610 nm, which is the spectral working range of the retinal IRIS.

4.5.2 Contrast reduction by ocular scattering

Another important factor to consider is the scattering introduced by ocular media, which reduces the contrast on retinal images. Some contrast reduction can occur in a fundus camera due to reflections and scattering from lenses. Potential sources of light scattering in the eye are the cornea, the lens, vitreous and retina[7] (Fig. 4.15). In addition, defects or pathologies in any ocular component increases scattering. This scattering is increased in elder patients[7]. In the retina, some vessels can go deeper into retinal tissue, producing local contrast variations in the vessel.

Ocular straylight is light scattered by the eye and it is potentially wavelength-dependent. It is known that for small illumination solid angles, the blood spectral absorption and pigmentation from the fundus introduces a wavelength dependence on the scattered light by the eye, while for larger angles, the fundus reflectance did not impact on the straylight wavelength dependency[135]. Other studies corroborate that the fundus has an effect on the wavelength dependence of scattered light by the eye, but there might be compensations between different phenomena, so some subjects might show wavelength dependencies on ocular straylight and other subjects might not show dependencies at all[136]. Due to these reasons, the contrast reduction due to ocular scattering was assumed to be wavelength independent in this thesis.

The effect of scattered light is an increase in the magnitude of the zero spatial frequency, which acts as and additive intensity component I_c in the image. This is added to the vessel intensity I_v and the fundus intensity adjacent to the vessel I_F (background). This additive constant modifies the transmission in the absence of contrast loss $T = {}^{I_v}/_{I_F}$ to $T' = {}^{(I_v+I_c)}/_{(I_F+I_c)}$.

The vessel transmission is then rewritten as:

$$T' = T\,(1-K)+K, \tag{4.17}$$

where $K = {}^{I_c}/_{(I_F+I_c)}$[3], with $K \to 1$ for worse case scenarios and $K \to 0$ in cases without contrast reduction. The intensity offset increases the obtained vessel transmission. In cases of low contrast, background and vessel intensities are expected to have a similar magnitude of grey levels, making it harder to recover adequately the *OS* information from a fitting process (Subsection 4.5.3).

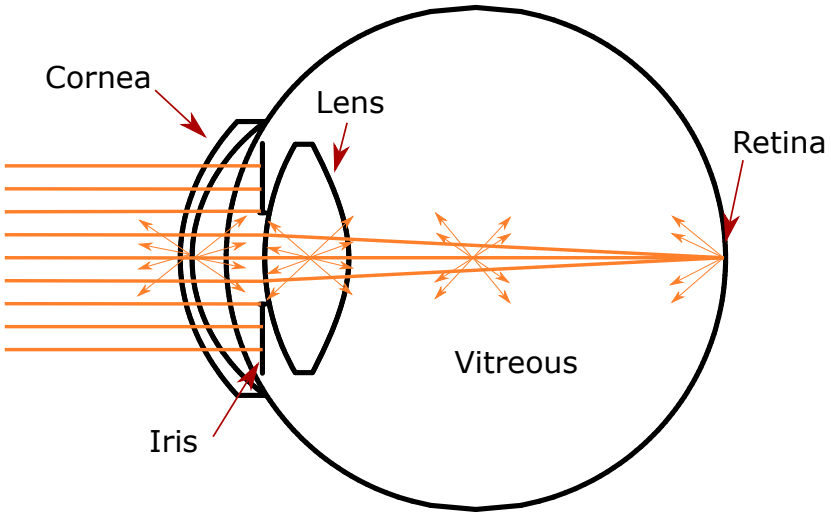

Figure 4.15: Simplified model eye[6] including the typical sources of scattering in the eye[7].

As an example of the effect of contrast reduction, the transmission of a 150 μm thickness vessel was simulated assuming single pass and without contrast reduction, 100% oxygenated blood, IRIS filtered wavebands and a set of intensity offsets from 0 to 5 a.u. in 0.5 steps. The offsets were added to the vessel and background intensity, and then the transmission was obtained from dividing both intensities. The background reflectance and illumination were assumed to be 100% and constant along the spectral range. Following the creation of the transmission profiles, Eq. 4.17 was then used to recover the *OS* and the K value of each generated transmission. The results in Fig. 4.16 show how K increased by increasing the intensity offset, approaching asymptotically to $K = 1$. The recovered *OS* was 100% for all cases, which shows that Eq. 4.17 replicates the effect of a constant intensity added to the background and vessel intensities.

Another applied test was performed by imaging a 100% oxygenated horse whole blood (BGA measured value) filled 150 μm quartz capillary in a model eye with Spectralon as background (Fig. 2.20). The capillary was imaged through a fundus camera interfaced with IRIS, the filter plate and broadband filter used in Chapter 3. The test was performed on the

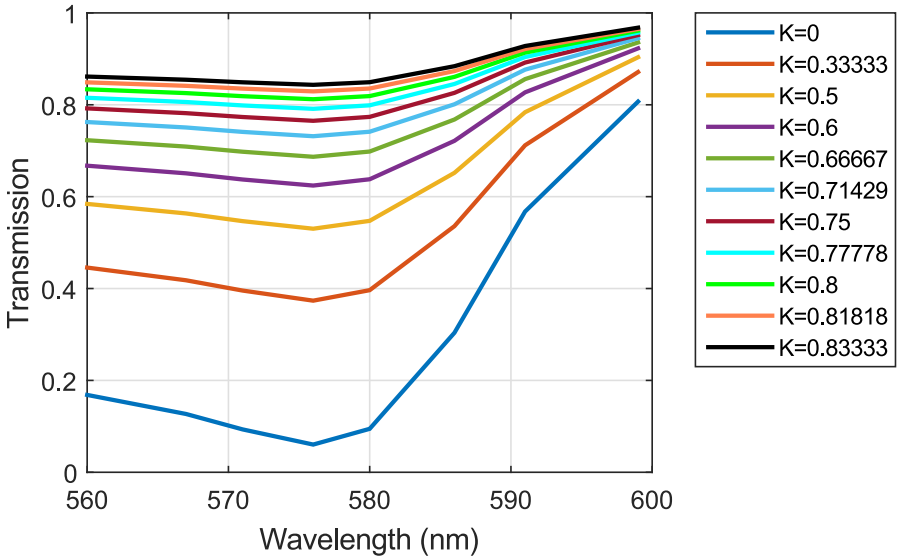

Figure 4.16: Generated single pass and 100% oxygenation transmission for a 150 μm thickness vessel, including the K value recovered in the optimization process.

mean transmission along the capillary, assuming single pass and no contrast reduction:

$$T = \frac{\int X_1 S(\lambda)\, 10^{-cd\left[\left(\varepsilon_{HbO_2}(\lambda)-\varepsilon_{Hb}(\lambda)\right)OS+\varepsilon_{Hb}(\lambda)\right]} d\lambda}{\int S(\lambda)\, d\lambda}, \tag{4.18}$$

$$T = \frac{\int X_1 S(\lambda)\, 10^{-cd\left[\left(\varepsilon_{HbO_2}(\lambda)-\varepsilon_{Hb}(\lambda)\right)OS+\varepsilon_{Hb}(\lambda)\right]} d\lambda}{\int S(\lambda)\, d\lambda}(1-K)+K. \tag{4.19}$$

In this case, the single pass assumption was valid since Monte Carlo simulations under Spectralon-like background conditions show that double pass and backscattered light are negligible[130]. The models used for the fit were Eq. 4.18 with X_1, c and OS variables and Eq. 4.19 with X_1, c, OS and K as variables. The optimisation was performed by fitting the two equations to the experimental transmission. This was done by a *multisearch* algorithm built in Matlab, which performs a non-linear-least-squares fit on 10 equally spaced points inside the predefined variable threshold. The maximum and minimum limits of the variables were -1 to 2 in units of intensity for OS, 0 to 1 for X_1, 0 to $11 \cdot 10^{-3}$ mole/litre for c and 0 to 1 for K. The displayed results in Fig. 4.17 show that the model including K produced $OS = 91.7\%$, while when K was not included, the result was $OS = 50.6\%$. In terms of concentration, the results are displayed as $C = c \cdot 64500$, with g/litre as units. In Fig. 4.17(a) the concentration was $C = 181.7$ g/litre, while in Fig. 4.17(b) was $C = 86.9$ g/litre. Usually horse blood has concentrations in the 100 g/litre to 150 g/litre range, but in this experiment, aggregation was observed even with flowing blood, so it was expected for the concentration to be higher than the usual values. These results demonstrate the need of having contrast losses in the physical model to obtain accurate oximetric results.

In terms of the models to be used in the retina, the wavelength-dependent scattering α (Eq. 4.17) and the contrast reduction K (Eq. 4.15) were implemented in Eq. 4.9, Eq. 4.10

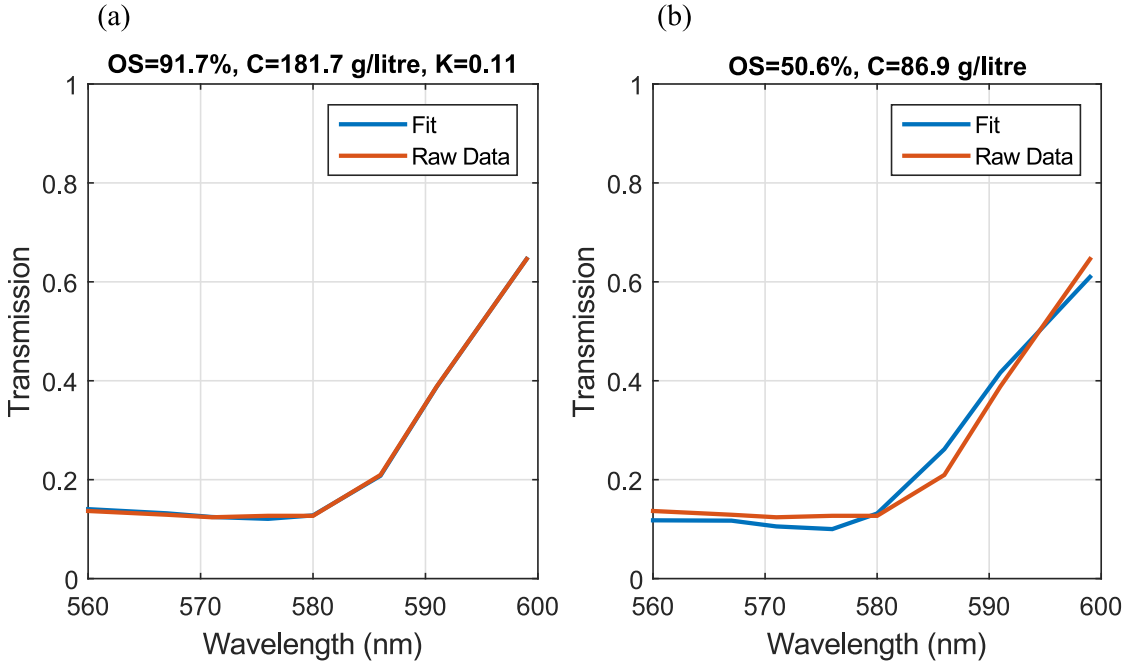

Figure 4.17: Optimisation results from fitting the models to the experimental data from a 150 μm quartz capillary filled with 100% oxygenation horse whole blood. (a) Considering contrast reduction factor K in the model (Eq. 4.19). In this case the raw data (Red) and the fit (Blue) overlap in some points. (b) Without considering contrast reduction in the model (Eq. 4.18).

and Eq. 4.11. The wavelength-dependent scattering α was added to the attenuation part of the Beer-Lambert law with the extinction coefficients, while the contrast reduction K was implemented as $T' = T\,(1-K)+K$, where T' is the transmission considering contrast losses and T is the transmission in the ideal case without contrast losses:

$$T_{SCW} = \frac{\int Y(\lambda)\,R(\lambda)\,10^{-S-n\log\left(\frac{1}{\lambda}\right)-scd\left[\left(\varepsilon_{HbO_2}(\lambda)-\varepsilon_{Hb}(\lambda)\right)OS+\varepsilon_{Hb}(\lambda)\right]-s\alpha}d\lambda}{\int Y(\lambda)\,R(\lambda)\,d\lambda}\,(1-K)+K, \tag{4.20}$$

$$T_C = \Big[\frac{\int X_1 Y(\lambda)R(\lambda)10^{-cd\left[\left(\varepsilon_{HbO_2}(\lambda)-\varepsilon_{Hb}(\lambda)\right)OS+\varepsilon_{Hb}(\lambda)\right]-\alpha}d\lambda}{\int Y(\lambda)R(\lambda)d\lambda}$$

$$+\frac{\int X_2 Y(\lambda)R(\lambda)10^{-2cd\left[\left(\varepsilon_{HbO_2}(\lambda)-\varepsilon_{Hb}(\lambda)\right)OS+\varepsilon_{Hb}(\lambda)\right]-2\alpha}d\lambda}{\int Y(\lambda)R(\lambda)d\lambda} \tag{4.21}$$

$$+\frac{\int X_3 Y(\lambda)+X_4 Y(\lambda)10^{-cd\left[\left(\varepsilon_{HbO_2}(\lambda)-\varepsilon_{Hb}(\lambda)\right)OS+\varepsilon_{Hb}(\lambda)\right]-\alpha}d\lambda}{\int Y(\lambda)R(\lambda)d\lambda}\Big]\,(1-K)+K,$$

$$T_{DN} = \frac{\int T_s Y(\lambda)\,R(\lambda)\,10^{-\chi cd\left[\left(\varepsilon_{HbO_2}(\lambda)-\varepsilon_{Hb}(\lambda)\right)OS+\varepsilon_{Hb}(\lambda)\right]-\chi\alpha}d\lambda}{\int Y(\lambda)\,R(\lambda)\,d\lambda}\,(1-K)+K. \tag{4.22}$$

Eq. 4.20 (Model 1) has S, n, s, c, OS and K as free parameters. Eq. 4.21 (Model 2) has

X_1, X_2, X_3, X_4, c, OS and K as free parameters. Eq. 4.22 (Model 3) has T_s, χ, c, OS and K as free parameters. The vessel thickness d is first measured in pixels along the vessel[123], and then converted in centimetres using the camera magnification and the refractive error of the eye[124].

Ocular scattering can be measured[7, 137], but the devices and methods used were not available and not used in this project. Instead, the contrast reduction was extracted from the optimization of the model. Knowing it in advance would reduce the dimensionality of the model by one and might reduce error propagation, as is shown in Subsection 4.5.3.

Some local contrast recovery used for haze (atmospheric phenomenon in which suspended particles in air reduce clarity) removal can enhance contrast in biomedical imaging applications[138, 139]. Although it can be potentially useful, there are some concerns over the output generated and how it would affect the measured vessel transmission. These algorithms can change the contrast in a way that the measured transmission of the vessels would be modified and the grey levels belonging to the vessel might be brought close to zero.

4.5.3 Error propagation

The models in Eq. 4.20, Eq. 4.21 and Eq. 4.22 were evaluated in terms of error propagation in order to know the expected behaviour of the recovered oxygenation when they were applied. Error propagation was first performed quantitatively by analysing the expected behaviour from the partial derivative $\frac{\partial OS}{\partial T}$. The second part included a perturbation analysis of the three models by introducing a small error in the blood transmission measured in a model eye, and finally, the same perturbation analysis is performed by modelling a blood transmission profile in a human retina.

The models are fairly complex, so in terms of doing it analytically, a simplified version of the models was used:

$$T(\lambda) = \left[X_1 10^{-cd\left[\left(\varepsilon_{HbO_2}(\lambda)-\varepsilon_{Hb}(\lambda)\right)OS+\varepsilon_{Hb}(\lambda)\right]}\right](1-K)+K. \tag{4.23}$$

The effect of errors in estimates of illumination, fundus reflectance and bandwidth have been addressed previously in Section 4.3. Furthermore, the model optimisation is usually applied over an experimentally measured transmission without having any previous knowledge of the analysed blood properties, so the error propagation is mainly focused on variations of OS to small changes in transmission. These small deviations are represented by the partial derivative of OS respect to the transmission on Eq. 4.23:

$$\frac{\partial OS}{\partial T} = \frac{1}{cd\left(\varepsilon_{Hb}(\lambda)-\varepsilon_{HbO_2}(\lambda)\right)}\frac{1}{\ln(10)}\frac{1}{T-K}. \tag{4.24}$$

The analysis of Eq. 4.24 provided a quantitative idea on how the model is expected to

behave:

1. When $K \to 1$, $\frac{1}{T-K} \to \infty$. This means that for low contrast conditions (high K) OS will greatly vary under small variations of T.

2. For the isosbestic case, Eq. 4.24 is invalid because T is independent of OS, so ideally the error should be small or non-existent. In reality, since we are fitting 8 wavelengths, an error on the isosbestic wavelength means that the model produces an error in OS by trying to find a curve that correctly fits the transmission on all wavelengths.

3. In our system we have $FWHM \sim 8$nm, meaning that point 2 might not be applicable to our case while case 4 would be more common.

4. For near-isosbestic cases, $(\varepsilon_{Hb}(\lambda) - \varepsilon_{HbO_2}(\lambda))$ becomes small, increasing the error propagation. At the same time, T is less sensitive to OS changes, so further analysis is required.

5. For wavelengths with high OS contrast, $(\varepsilon_{Hb}(\lambda) - \varepsilon_{HbO_2}(\lambda))$ should reduce the sensitivity to errors.

Eq. 4.24 shows the error propagation for a single-pass case, which is equally valid for double pass. Since in retinal vessels the backscattered component is more significant than single and double pass in the range of 560 nm to 600 nm, the sensitivity to errors of this component also needs to be analysed. In this case, the backscattered component R is written as:

$$R = \left[\frac{X_3}{R_F} + \frac{X_4}{R_F} 10^{-cd\left[\left(\varepsilon_{HbO_2}(\lambda) - \varepsilon_{Hb}(\lambda)\right)OS + \varepsilon_{Hb}(\lambda)\right]}\right](1-K) + K, \tag{4.25}$$

where X_3 and X_4 are fitting factors and R_F is the fundus reflectance. X_3 and X_4 can have maximum values of 0.13 and 0.7 respectively[51]. The OS sensitivity to small variations in R is then expressed as:

$$\frac{\partial OS}{\partial R} = \frac{1}{cd\left(\varepsilon_{Hb}(\lambda) - \varepsilon_{HbO_2}(\lambda)\right)} \frac{1}{\ln(10)} \frac{R_F}{(T-K)R_F - X_3(1-K)}. \tag{4.26}$$

The backscattered case represented by Eq. 4.26 is expected to behave in a similar way as to single pass:

1. In cases with $X_3 \to 0$, $(T-K)R_F \gg X_3(1-K)$ and we have the same situation as in single pass.

2. In cases with $X_3 \to 0$ and $R_F \to 0$, the error propagation is expected to be close to 0 as long as K$\nrightarrow$ 1. In that case a $\frac{\partial OS}{\partial R} \sim \frac{0}{0}$ indetermination would happen.

Error propagation is more clearly illustrated by doing a perturbation analysis. From Eq. 4.24 and Eq. 4.26, high K values and near-isosbestic wavelengths are likely to be the most

critical cases in which sensitivity to errors are high. This analysis was applied on Model 1 (Eq. 4.20), Model 2 (Eq. 4.21) and Model 3 (Eq. 4.22). The principle behind perturbation analysis is to introduce a small error in an artificially generated blood transmission and fit the perturbed data with the same model used to generate the original transmission. The recovered *OS* indicates the sensitivity of the model to small error in transmission. This process was tested under a range of contrast conditions. Model 2 (Eq. 4.21) is the most complete of the models, since it includes all the pathlengths and scattering contributions, while Model 3 (Eq. 4.22) is a simplification of this model, and Model (Eq. 4.20) does not take into account any different pathlengths, specially backscattered light, which is the biggest contributor in retinal vessels. Because of this reasons, the three models might generate different output transmissions when the same common values are used. To avoid errors from using the wrong artificially generated transmission in the wrong model, experimental data was used for the perturbation analysis as described next.

To obtain data from a well-controlled environment, experimental blood transmission data was obtained using a model eye (Fig. 2.20) and a fundus camera interfaced with IRIS (Fig. 4.1). 100% oxygenated (BGA measured) defibrinated whole horse blood was flowed at $5\,{}^{\mathrm{mm}}/_{\mathrm{s}}$ through a 150μm diameter FEP capillary in the model eye, using Spectralon to simulate the sclera and water as the vitreous. Blood was 39% haematocrit, but this was expected to differ during the experiment due to aggregation. A xenon source was used as a flash lamp for the illumination. Once the image was obtained and the wavebands registered, 224 intensity sections were obtained along the vessel and then averaged. The corresponding vessel minimum intensity was identified as the vessel intensity and a linear fit was applied to the background intensity pixels in order to obtain the background value (More details on the transmission acquisition are given on Subsection 4.6.2). The contrast reduction was generated by applying Eq. 4.17 for K ranging from 0 to 0.9 at 0.1 steps as shown in Fig. 4.18. $K = 0$ would mean no light scattered, which is not a realistic situation. Measurements using a metallic piece of black-painted steel instead of the blood capillary produced $K = {}^{I_c}/_{(I_F+I_c)} = 0.04$. In this case, $I_c \approx 800$ grey counts was the intensity level at the image of the black metallic piece (cross polarisation was used, so reflections were minimised.) and the grey level on the adjacent Spectralon was $I_F \approx 18000$ grey counts. This low value of K showed little light scattering in the model eye, so the obtained images were considered to have no contrast reduction in order to simplify the analysis.

Once the transmission profiles under different contrast reduction were generated, a 1% error in transmission was independently added to each wavelength, generating a total of 8 transmission profiles per K. Model 1 (Eq. 4.20), Model (Eq. 4.21) and Model 3 (Eq. 4.22) were fitted to the resulting 8×10 ((perturbed transmission) x (contrast reduction K)) transmission profiles, and the recovered *OS* was compared with the BGA measured *OS* of 100% in order to obtain the oxygenation error. Fig. 4.19(a) shows the error in *OS* against K when small errors in transmission are introduced for each of the three used models. As seen in this

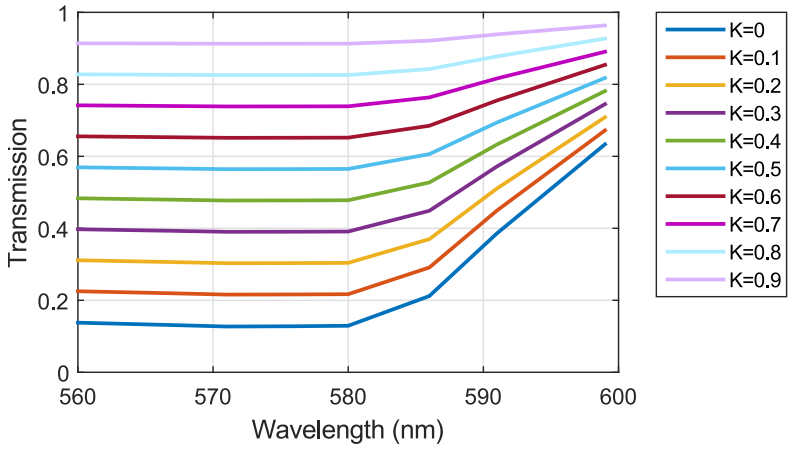

Figure 4.18: 150 μm horse blood filled quartz capillary retrieved transmission ($K = 0$), including the generated transmission for different contrast conditions.

figure, errors are enhanced under low contrast conditions. Further error analysis was done considering K as a known parameter to test error propagation by reducing the dimensionality of the problem. The introduced K was the same used to generate the transmission profiles, thus reducing the dimensionality of the problem. Fig. 4.19(b) shows errors in OS against K when small errors in transmission are added to the three models and when the contrast reduction is known, reducing the amount of free parameters by one in the optimisation process. When K is known, Model 1 (Eq. 4.20) and Model 3 (Eq. 4.22) have $> 50\%$ OS error at $K = 0$. The optimisation of the transmission with $K = 0$ (no added contrast reduction) in Fig. 4.19(a) produced $K = 0.11$ for Models 1 and 3. This implies that these two models do not accurately represent light propagation on vessels, at least for a model eye. On the other hand, for the case without added contrast reduction, Model 2 produced $K = 0.037$, which was similar to the $K \approx 0.04$ found when a black metallic piece was imaged through the model eye. The problem might be derived from the fact that Model 1 does not include double pass and backscattered light, and that Model 3 is a simplification of Model 2 for cases in which light and pathlengths are under controlled conditions such as when a cSLO or structured illumination is used. From Fig. 4.19(a)-(b) it is observed that Models 1 and 3 had a standard deviation of the OS error of 22% and 24% respectively for $K = 0.9$ when K was a fitting parameter, while when K was know, the standard deviations became 6% for both models. Model 2 did not show any appreciable improvement when K was introduced as a known parameter. In summary, Fig. 4.19(a) show how under lower contrast conditions there is an increase in oxygenation error for the three models and that when K is unknown they show the same behaviour. In the case in which K is known, Models 1 and 3 introduce an offset in error for the $K = 0$ case, which discourages their use when K is known.

More results on error propagation is given in Fig. 4.20, which focuses on the perturbation analysis of Model 2 applied to the transmission data obtained form a 100% oxygenated capillary on a model eye. This figure shows how the error tends to increase with lower

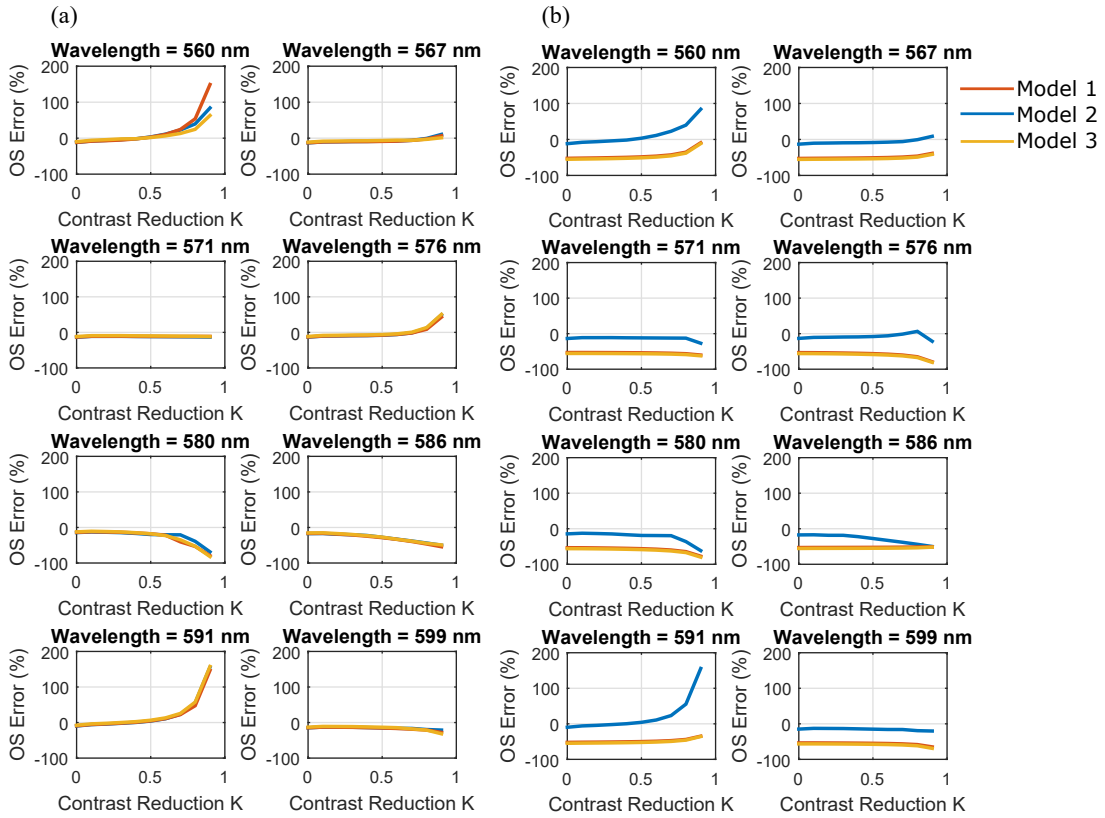

Figure 4.19: Error propagation under a 1% perturbation. (a) Maintaining K as a fitting parameter. The three models tend to overlap, being Model 3 (Yellow) the one represented on top. (b) Introducing K as a known parameter, the same used to generate the corresponding transmission profile. In this case Model 1 (Red) and Model 3 (Yellow) overlap, being Model 3 the one represented over Model 1.

contrast. The wavelengths with less sensitivity to errors with decreasing contrast were 571 nm, 599 nm and 567 nm. The reason why the previous assumptions are not confirmed by Fig. 4.20 is that Model 2 is more complex than Eq. 4.23, meaning that they might respond differently to perturbations.

The model eye experiment was also performed by adding a scattering layer made of *Parafilm* on the model eye lens. The model optimisation produced contrast reduction values of $K > 0.9$ and oxygenations >150% for all samples. Fig. 4.20 (a) shows how for $K = 0.9$ the error in oxygenation can achieve values >100%, which supports the results shown in this experiment.

Finally, the perturbation analysis was performed by modelling the transmission of a vessel on a human retina, which was expected to produce different results than in a model because of the higher impact of the backscattered component compared with the model eye, in which single-pass is the main contribution to the vessel intensity. This analysis was not performed due to the impossibility of measuring the retinal vessel oxygenations with an independent device which would serve as a reference oxygenation. However, a blood transmission profile was generated using Model 2 and $X_1 = 1$, $X_2 = 1$, $X_3 = 0.01$, $X_4 = 0.1$, $OS = 1$, $D = 150\,\mu$m as parameters. Delori's fundus reflectance[5] was used. A set of con-

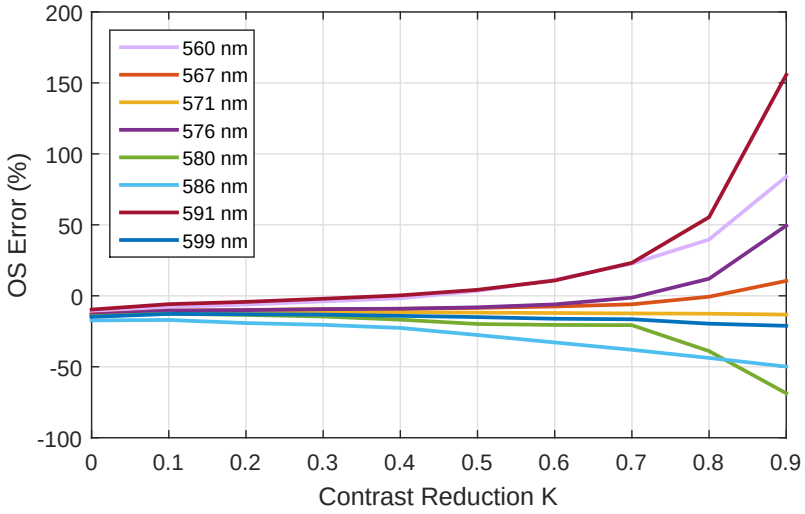

Figure 4.20: Oxygenation error propagation for Eq. 4.21 using transmission data from a 100% oxygenated capillary on a model eye. Obtained from adding 1% error in transmission.

trast reductions from 0 to 0.9 in 0.1 steps was used to generate the set of transmissions and finally a 1% perturbation was added to each wavelength independently. The results of the optimisation process for Model 2 are shown in Fig. 4.21. This figure shows that perturbations are expected to produce larger errors in the isosbestic and quasi-isosbestic wavelengths when is compared with the perturbation analysis on model eye under low contrast conditions. As is shown in the following sections, fitting to retinal vessels tends to produce values of K between 0.4 and 0.8, so high errors in OS are to be expected.

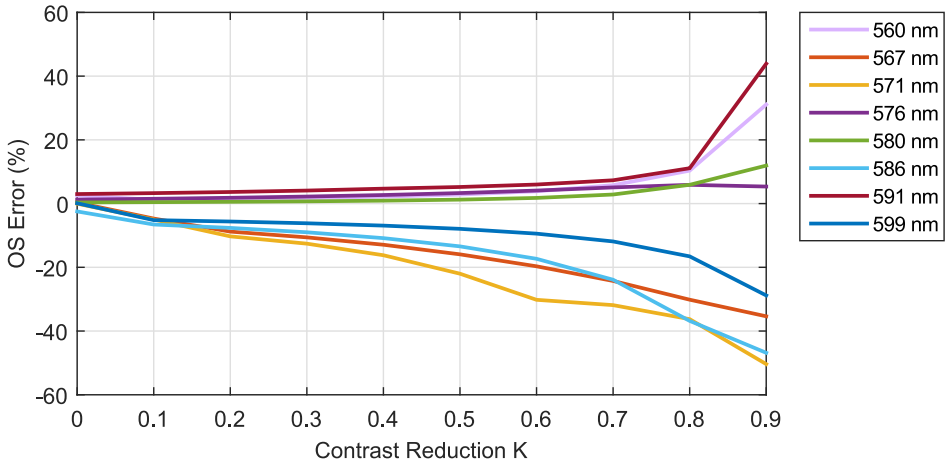

Figure 4.21: Oxygenation error propagation for Eq. 4.21 when the fundus reflectance is introduced.

The conclusion of this section is that Models 1 and 3 perform poorly when K is a known parameter and that they are not able to find the correct K when it is treated as a fitting parameter. In terms of recovering the correct OS, the three models perform similarly when K is a fitting parameter. In terms of comparing the error propagation between a model eye and a human retina, the analysis were shown to produce different results mainly to the different

pathlength contributions, being single pass higher for a model eye and backscattered higher on a human retinal in the range of wavelengths used in this thesis.

4.6 Retinal oximetry algorithm

The physical models shown in the previous section are complex in terms of free variables to be fit. A model with too many variables, even if is overdetermined, can provide different solutions for the parameters when similar input transmissions are introduced. Another issue is that these models are only simplifications of how light is propagated, scattered and absorbed in the eye and the use of models that are too simple might produce less accurate results.

This section shows how to calculate the vessel diameter, so one variable is fixed on the model, how to calculate the vessel transmission, and finally an algorithm based on a set of physiological assumptions in order to increase the stability of the oximetric measurements along the vessel.

4.6.1 Vessel size

Measuring the vessel calibre is important for oximetry since it is one of the parameters involved in the Beer-Lambert law. Vessel diameter is a significant parameter for assessing blood flow autoregulation in retinal vessels under hypoxic conditions[57, 63] because they tend to modify their diameter in order to allow changes in blood flow and compensate oxygen supply.

Vessel diameter can be measured by means of OCT[140], which showed high correlation ($r = 0.9812$) between width and vertical diameter. However, this technique was not available, so it had to be performed over the captured spectral images using an intensity-based technique.

To accurately measure the vessel diameter, an existing method based in Image-J for meningeal vessels measurements[123], and tested in retinal vessels[141], was implemented in *Matlab*. An example of how the algorithm works is shown is Fig. 4.22. Although this technique only measures depth, previous research using OCT[140] shows that is safe to assume that width and vertical length have similar dimensions.

As a first step, an intensity section across the vessel is extracted (Fig. 4.22(a)). This profile is then processed in the following method (shown in Fig. 4.22(b)):

1. Find the left and right reference (background, green and purple crosses) values and positions and the minimum vessel intensity (blue circle). The minimum positions are obtained from a Gaussian filtered profile (red profile), which tends to be more accurate in terms of locating the minimum. These positions provide the minimum intensity value in the raw vessel profile (black profile) (Fig. 4.22(b)).

2. The average between the reference and the minimum intensity values provides a first estimation of the vessel intensity on its boundaries. This intensity value is used to find the vessel boundaries by finding the vessel positions corresponding to these intensities.

3. A linear fit is applied to each estimated boundary on step 2. For this purpose, 4 intensity values are added to each side of the estimated boundary. These intensity values correspond to adjacent vessel intensities. The fits are shown in green in Fig. 4.22(b).

4. The positions where the linear fits cross the raw interpolated intensity profile are the accurate vessel boundaries, which are represented as red and yellow circles in Fig. 4.22(b).

5. The vessel boundaries found in point 4 are the vessel diameter. Since we are working with an interpolated vessel profile, it is necessary to identify their corresponding pixels in the registered spectral 3-D cube.

This vessel-calibre algorithm calculates the thickness of the blood column in pixels, which is necessary to translate to microns or centimetres.

The magnification of the retinal system was first evaluated using a model eye (Fig. 2.20) with a $f = 22\,\text{mm}$ lens, filled with water and a 1.3 mm thickness piece of black-painted steel as a reference. From the image size, the estimated magnification of the system was $M = 0.67$ when a FoV of 50° was used. Eyes are expected to have different axial length, refractive errors and corneal curvatures. In order to estimate the magnification introduced by the eye, these parameters should be known, either by keratometry or ultrasonography[124] or using OCT[142]. In this research these techniques were not available, instead, all the subjects were assumed to have 22 mm of axial length, the same of the used model eye. Adjustments from subject to subject were possible by using the refractive error of the eye[124], which is usually known by the subjects. In this case, the system-eye magnification is expressed as[124]:

$$M = k\,(D + A)\,, \tag{4.27}$$

where k is a calibration constant found from the camera magnification, D is the dioptre for a $f = 22\,\text{mm}$ eye and A is the refractive error of the subject's eye.

This algorithm was successfully applied for collaboration at the measurement of vessel thickness (in pixels) under acute mild induced hypoxia, showing an increase in vessel diameter, suggesting an autoregulatory response to hypoxia[63].

4.6.2 Vessel transmission

Traditionally, the minimum vessel intensity can be obtained either by identifying the minimum value of the intensity profile[57] or by fitting a parabolic function. These two methods should be capable of bypassing the effect of specular reflections over vessels. Simulations of

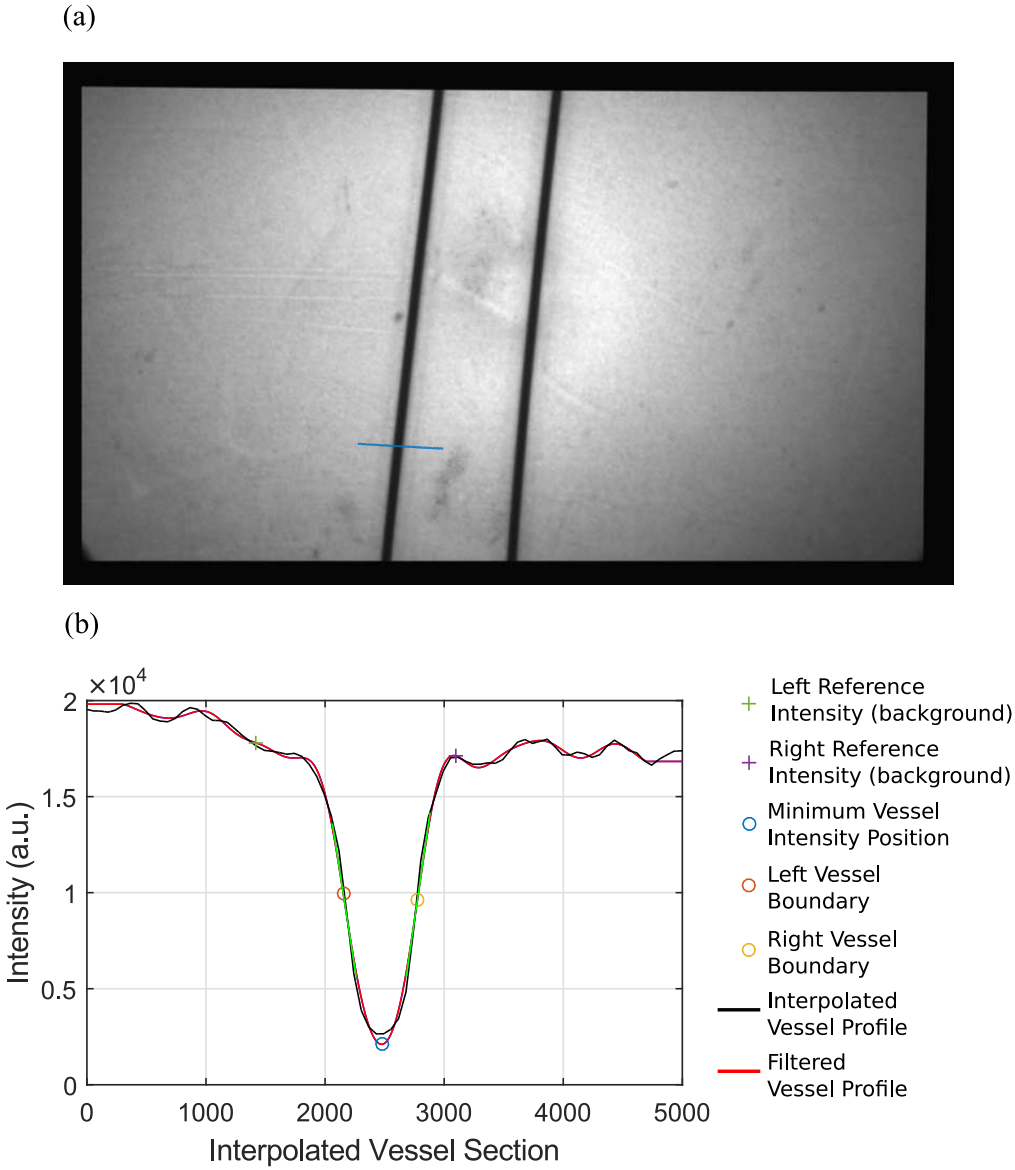

Figure 4.22: (a) Model eye image with a cross-section (blue line) over a blood-filled capillary. (b) Vessel intensity profile (black line), highlighting the points involved in the vessel size algorithm. The results of the algorithm are the left and right vessel boundary. The position of the minimum vessel intensity is easily obtained from a filtered (red line) version of the raw intensity profile.

a cylindrical vessel, of 150 μm, 100% oxygenated blood, assuming single pass and constant reflectance (Fig. 4.23) show that the transmission profile across the vessel becomes flatter at higher absorptions, making a parabolic function unsuitable for these cases.

In this section, a parabolic function, a hyperGaussian and an exponential approach are used as vessel fitting functions. The exponential approach fits an exponential to each side of the vessel, from the detected vessel boundaries to the detected minimum:

$$y = l + Ae^{((((x-d)/w)^2)^n)}, \tag{4.28}$$

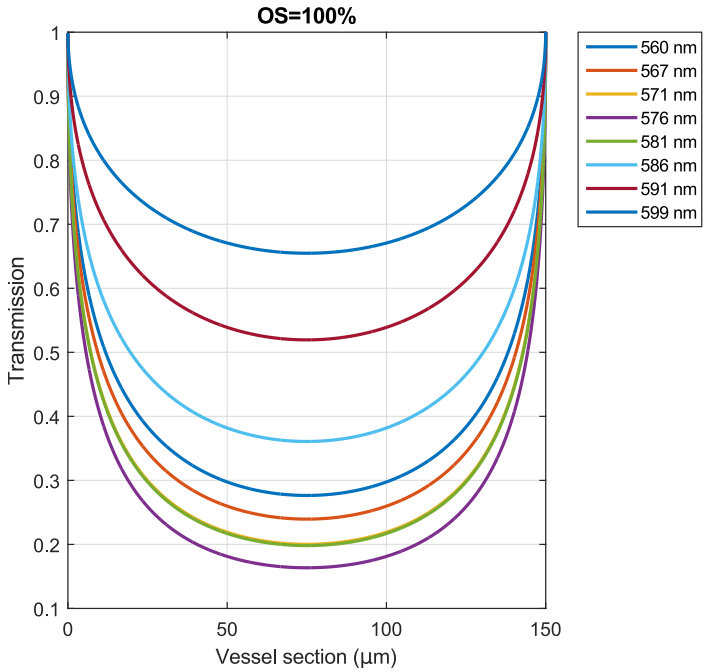

Figure 4.23: Theoretical transmission across a 150 μm diameter vessel at 100% oxygenation, assuming only single pass.

$$y_{left} = a10^{(-x/b)} + k, \tag{4.29}$$

$$y_{rigth} = a10^{((x-r)/b)} + k, \tag{4.30}$$

where l, A, d, w and n fitting parameters for the hyperGaussian (Eq. 4.28) and k, a, r and b fitting parameters for the exponential model (Eqs. 4.29 and 4.30). The idea behind Eq. 4.29 and Eq. 4.30 is that if one side of the vessel is poorly defined due to noise, reflections or tissue, the other half is used to determine the minimum intensity, while the hyperGaussian fit would produce a poor fit (Fig. 4.25).

The three models were tested with profiles obtained with a blood filled quartz capillary and then for retinal vessels. First, using a model eye, the different fits showed how a parabolic function tended to underestimate the intensity of the shorter wavelengths since they tend to produce flatter profiles in the centre of the vessel (Fig. 4.24(a)). In terms of transmission, Fig. 4.24(b) shows how the transmission from hyperGaussian and exponential fits differed in a 16% while the parabolic and the exponential differed in an average of 99% in transmission. In terms of goodness of the fit on the vessel, the results on Table 4.1 showed that the exponential fit (Eq. 4.29 and Eq. 4.30) adjusted better to the raw data.

In the case of the retina, a vein with a strong central reflection (Fig. 4.25(a)) was selected and the same procedure as in the model eye capillary was followed. In this case, the vessel transmission profiles obtained with the three methods showed different behaviours in the short wavelengths, as seen in Fig. 4.25(b). This differences in the obtained transmission are

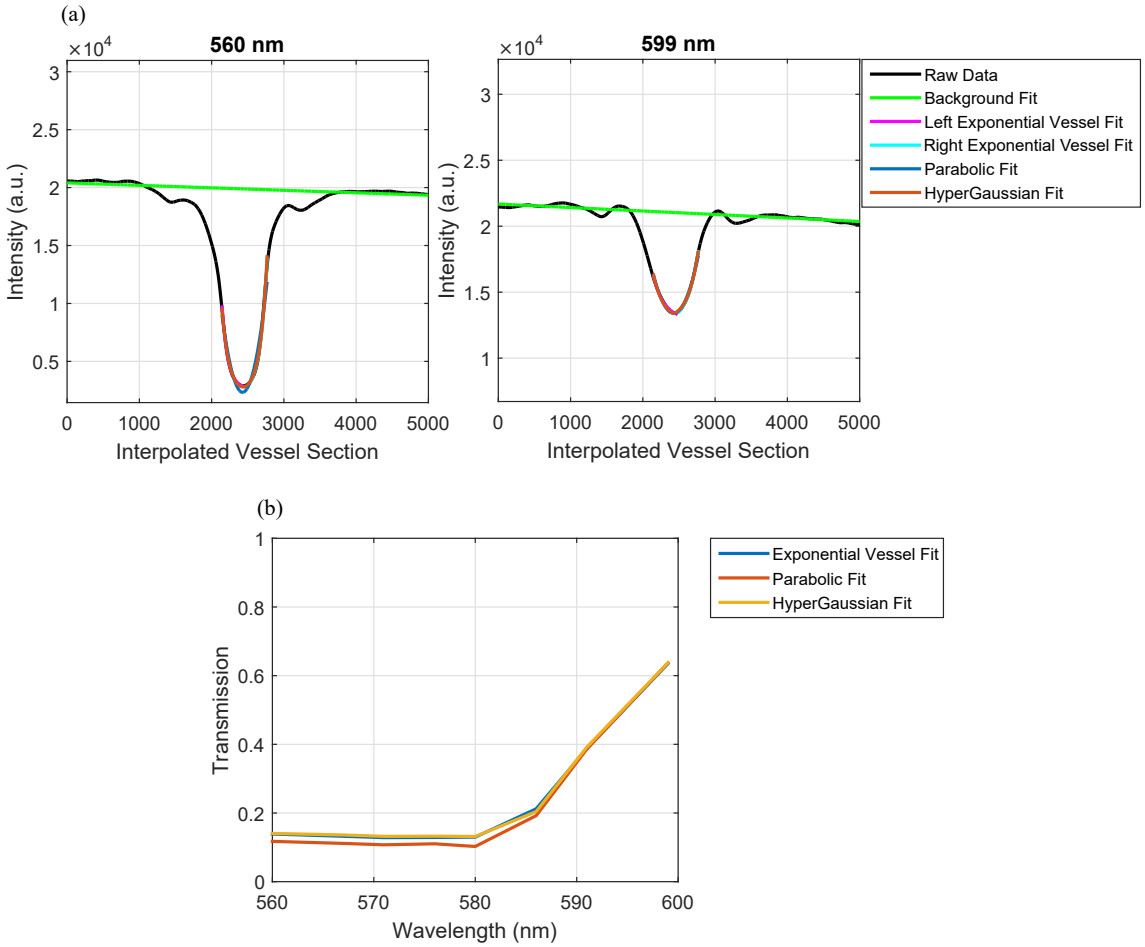

Figure 4.24: Blood filled quartz capillary section analysis. (a) Intensity profiles with the different section fit. The profiles tend to overlap, being the Exponential Fit on top of the others, which shows a good fit of the three methods. (b) Transmission profiles obtained from the fits on (a).

	r^2 (560 nm)	r^2 (599 nm)
Exponential Fit	0.997	0.9975
HyperGaussian Fit	0.996	0.9951
Parabolic Fit	0.9578	0.9903

Table 4.1: Goodness of fit displayed by fitting a hyperGaussian, an exponential and a parabola to a vessel intensity profile in a model eye.

produced by the central reflection on the short wavelengths, which is not visible in the long wavelengths (Fig. 4.25(a)). In terms of goodness of fit, the r^2 values on Table 4.2 showed how the exponential fit provided a better vessel fit, and it was able to produce a better vessel minimum estimate than the other two methods when specular reflections were present.

Ideally, specular reflections should be removed by using cross-polarisation, but as seen in Fig. 4.25(a), the reflection was only attenuated, not eliminated. Another explanation to this effect could be that RBCs are aligned and change their shape to more ellipsoidal under flow conditions, which increases reflected light by the cells at the 560 nm range[143].

This section compared different methods to fit a vessel intensity profile to extract the

	r^2 (560 nm)	r^2 (599 nm)
Exponential Fit	0.9041	0.9958
HyperGaussian Fit	0.594	0.9158
Parabolic Fit	0.5267	0.9074

Table 4.2: Goodness of fit displayed by fitting a hyperGaussian, an exponential and a parabola to a vessel intensity profile in a human eye.

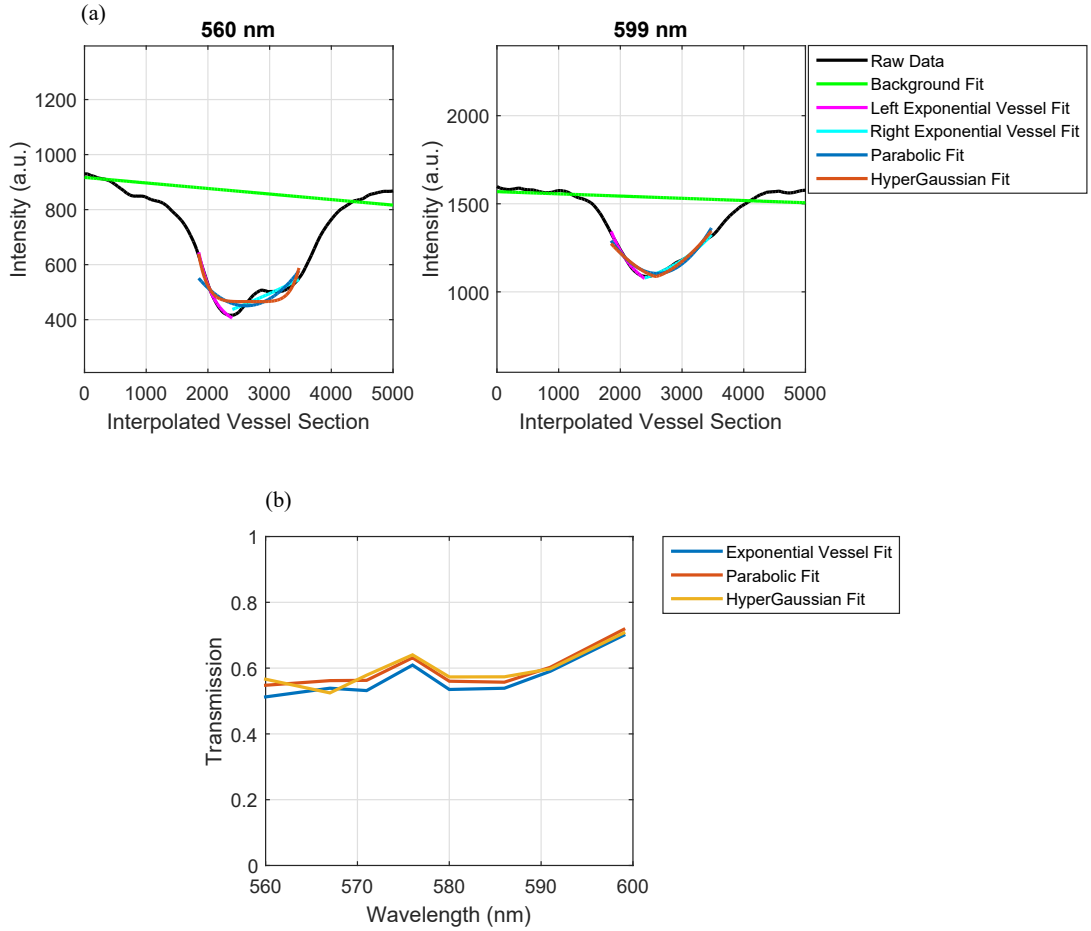

Figure 4.25: Retinal vein section analysis. (a) Intensity profiles with the different section fit at 560 nm and 599 nm. (b) Transmission profiles obtained from the fits on (a).

transmission. The conclusion was that using an exponential fit to each side of the vessel intensity profile produced more accurate result in retinal vessels than more traditional methods such as fitting a parabola or a hyperGaussian. The lack of accuracy is specially critical in the short range of the IRIS wavelengths, where specular reflections are more relevant than in the long range of wavelengths.

4.6.3 Oximetry algorithm

On the previous sections, the diameter was eliminated as a free parameter and the vessel transmission was calculated as accurately as possible. Even with these improvements, Model 1 (Eq. 4.20), Model 2 (Eq. 4.21) and Model 3 (Eq. 4.22) have 6, 7 and 5 fitting variables

respectively. These variables can have dependencies among them, and error propagation can produce considerable errors in the retrieved *OS*. This means that the oximetry applied along a vessel can be highly unstable. To introduce stability along the vessel and minimise interactions between the different variables, an algorithm was developed for retinal oximetry (Algorithm 4.1). The curve fitting of the model to the transmission data was performed by a non-linear least square optimisation built-in Matlab. To reduce the chances of finding a local minimum, a global solver was used. In this case, the global solver was a Matlab function that generated a certain number of starting points for the non-linear least square optimisation to solve. For our models, 10 starting points were selected, since it was a good balance between accuracy and computing time.

This algorithm uses the full potential of IRIS 8 wavelengths and a set or physiological assumptions applied in different steps (Algorithm 4.1) :

1. As a pre-step, the diameter, transmission and fundus reflectance along the vessel are smoothed by using a moving average of 10 pixels. By doing so, noise and systematic errors are reduced.

2. The physical models are fit to the transmissions along the vessel, including the obtained data for the diameter and fundus reflectance. After the results are generated, the following assumptions are applied:

    - c is assumed to be constant along the analysed vessel as long as no branches occur in the analysed length. Mass conservation makes this assumption to be highly reliable because without branches there is no added or subtracted blood in the analysed vessels. The algorithm calculates c for each vessel independently, without assuming that it is equal in all retinal vessels. Due to flow rate distributions between parent and child vessels and the viscosity of blood, the haematocrit concentration can differ between vessels, especially between large and small vessels[144, 145]. The difference in haematocrit between parent and child branches is produced by a phenomenon known as plasma skimming: A child branch is fed by the periphery of the parent vessel, which is usually poor in RBCs, so the branching capillary has a lower haematocrit. However, depending of the flow conditions, haematocrit can increase in the branching capillaries[144].
    - *OS* is assumed constant along the vessel. Analysed vessels tend to be below 3 mm long and larger than 40 μm. Oxygen delivery occurs in the microvasculature, where RBCs are aligned flowing through the vessel and these vessels cannot be resolved by our current imaging system. Along retinal vessels, gradients have not been observed in the typical vessel length analysed in this research[146, 147]. However, this assumption might be invalid in cases where arteries and veins are adjacent due to a counter-current mechanism in which oxygen diffuses from arteries to adjacent veins[118].

- K is assumed constant. For healthy subjects, the contrast reduction from scattered light by the cornea, vitreous and retina is considered uniform. This assumption should be reviewed on patients with cataracts since the contrast reduction might not be uniform[148].

3. Keeping c, OS and K constant, the physical models are fit again to the transmission along the vessel. This step finds the variations of the other parameters along the vessel. Pigmentation and non-uniformities from the choroid might change pathlengths contributions in different parts of the vessel. Vessel sections over the optic disc might show different parameter values since the reflectance of the optic disc and other regions of the retina are different. The calculated parameters are smoothed by calculating the running average of 10 sections to increase stability.

   Regarding the pathlengths in Eq. 4.21, the condition $X_1 + X_2 + X_3 + X_4 = 1$ should be satisfied. The implementation of this condition resulted in long computing times using a global solver, with an average of one day per vessel section. The use of this condition was unfeasible, since the collected retinal data contained 150 vessels with an average of ~ 100 vessel sections. To speed up the solver no relation was imposed between the pathlengths. In principle, the other two models would not require such extra conditions.

4. Keeping c and OS constant, including X_1, X_2, X_3 and X_4 along the vessel, local variations on K along the vessel are calculated. This might be useful in cases when the vessel is deeper in the retina, although is unlikely to occur in retinal vessels. However, it is useful for other non-retinal oximetry applications where exposed vessels change in depth, having regions with more tissue over them.

5. Finally, the oxygenation OS is found along the vessel by using the previously found values for the other parameters.

With the application of the algorithm shown above (summarized in Algorithm 4.1 in the following page), the number of free parameters is reduced in each step, eliminating possible dependencies among them.

The free parameters for Model 1, Model 2 and Model 3 are limited by lower and upper boundaries. For Model 1, S, n, and s have limits 0 and 1[78]. For Model 2, X_1 and X_2 have limits 0 and 1[79], X_3 has limits 0 and 0.13 while X_4 has limits 0 and 0.7[51]. For Model 3, T_s has limits 0 and 10 while χ has limits 0 and 2[79]. The upper limit for T_s is not limited under backscattered conditions but is not expected to be higher than 10. On the side of the common parameters, OS has limits -1 to 2 to take into account error propagation (Fig. 4.20 and Fig. 4.21), c has limits 0 and $11 \cdot 10^{-3}$mole/litre, and K has limits 0 and 1.

This section has described the necessary assumptions and steps to follow in order to increase stability and accuracy on retinal oximetry. The implementation of this algorithm

Algorithm 4.1 Retinal Oximetry Algorithm for Eq. 4.21. The same procedure is followed with the other two models using their own variables.

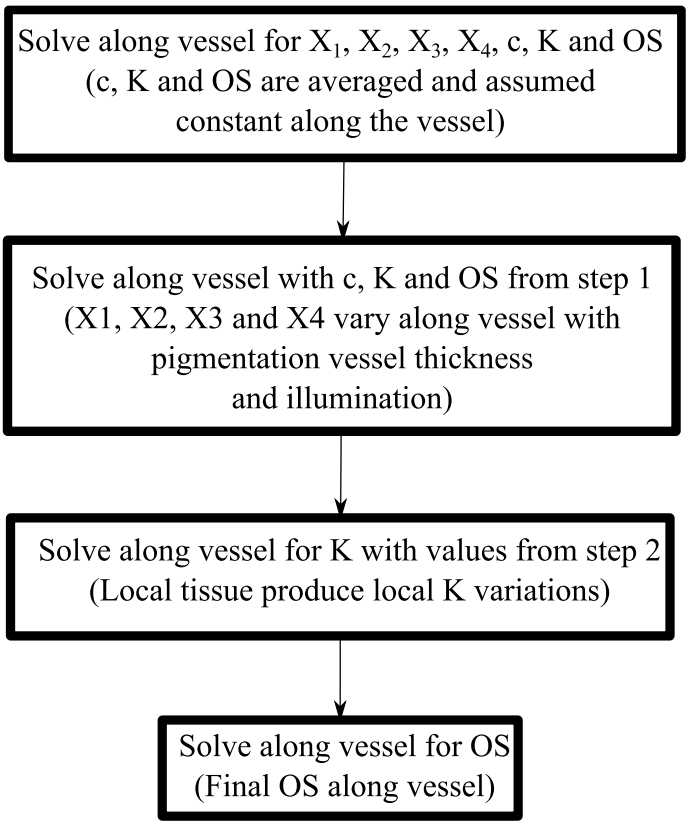

was then tested in a blood transmission data obtained from a model eye and human retinas

4.7 Model validation

The retinal algorithm developed was first tested using a fundus camera interfaced with IRIS as shown in Fig. 4.1 on Section 4.1 and a model eye (Fig. 2.20, Section 2.3). A set of 16 blood samples were imaged using this system. Blood was flowed at $5\,^{\mathrm{mm}}/_{\mathrm{s}}$ through a $150\,\mu$m inner-diameter FEP tubing (Fig. 4.26). Defibrinated horse blood with 39% haematocrit was deoxygenated using sodium dithionite and the oxygenation measured with a blood gas analyser (BGA).

Once the IRIS images were registered, the vessels tracked, the diameter measured and the transmission calculated, the retinal oximetry algorithm (Algorithm 4.1) was applied for Model 1, Model 2 and Model 3. A constant 99% reflectance was used to simulate the Spectralon background.

Fig. 4.27 shows the *OS* calculated for each physical model and a linear fit to the corresponding physical model. The results from the linear fit are shown on Table 4.3, where it is seen that Model 3 had the lowest performance with an oxygenation standard deviation of $42 \pm 17\%$ when compared with the *OS* measured by a blood gas analyser and a $r^2 = 0.5019$. On the other hand, Models 2 and 3 showed similar behaviours.

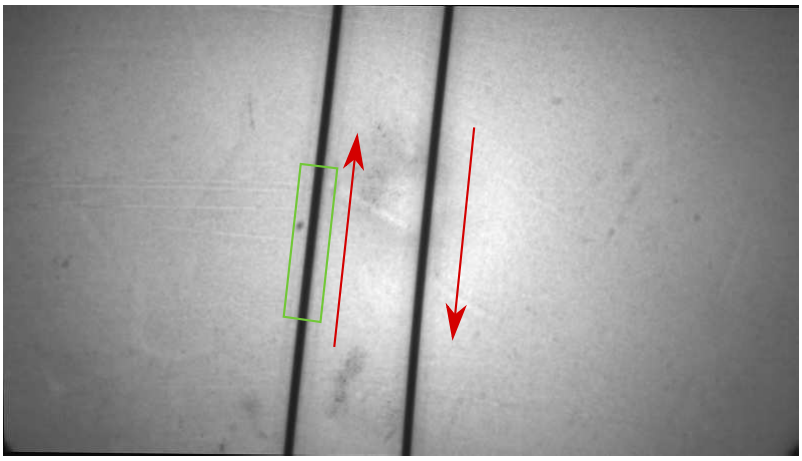

Figure 4.26: Registered IRIS image at 560 nm of a blood filled 150 μm tubing, indicating the flow in red and the analysed tubing region in green.

	Oxygenation Standard Deviation (%)	Linear Fit	r^2
Model 1	$42 \pm 17\%$	$y = 0.3841x - 32.67$	0.5019
Model 2	$1.3 \pm 0.4\%$	$y = 1.174x - 23.59$	0.9438
Model 3	$1.4 \pm 0.4\%$	$y = 1.169x - 24.02$	0.9411

Table 4.3: Standard deviation, fit and goodness of fit of each model applied to the measured data with a model eye.

From these results, it can be concluded that Model 2 and Model 3 are equivalent in results for data obtained on a model eye, while the results from using Model 1 have high spread per vessel and performs poorly in terms of measuring the mean *OS*. Following these results, Model 2 and 3 showed the best performance in a model eye, meaning that they were good candidates for performing retinal oximetry because they represent more accurately the physical behaviour of light in a model eye, and hence, in a human eye.

The condition $X_1 + X_2 + X_3 + X_4 = 1$ for Model 2 was not implemented and the oximetry results matched the ones obtained by using Model 3, which does not require any similar condition. This shows that the pathlength contribution for Model 2 do not need any extra conditions apart from the imposed upper and lower boundaries.

A common characteristic of the results for Model 2 and Model 3 was an underestimation in the calculated *OS* with deoxygenation. The deoxygenation of blood was performed using sodium dithionite, which has the side effect of increasing the osmolarity of the solution. The osmolarity of a solution is expressed as:

$$O = \sum_i \varphi_i n_i C_i \, {}^{\text{osmol}}/_{\text{L}}, \tag{4.31}$$

where $\varphi$the osmotic coefficient ($\varphi = 1$ means 100% dissociation), n is the number of particles into which the substance dissociates and C is the molar concentration of the solute. The osmolarity units are ${}^{osmol}/_{L}$, where *osmol* is the number of solute moles contributing on the

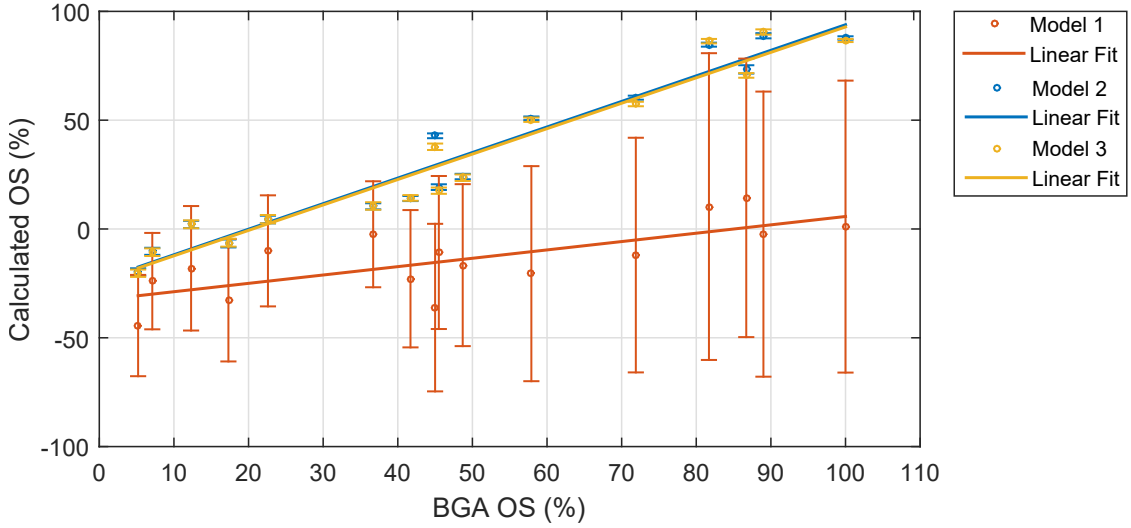

Figure 4.27: Eight wavelengths algorithm oxygenation results for Model 1 (Eq. 4.20), Model 2 (Eq. 4.21) and Model 3 (Eq. 4.22) compared with the values obtained using a Blood Gas Analyser (BGA). Includes a linear fit to the calculated *OS*.

osmotic pressure of a solution. In our case, sodium dithionite $Na_2S_2O_4$ has a molar mass of $174.107\,\mathrm{g/mol}$ and dissociates into $2Na$ and $2S_2O_4$, which makes $n = 4$. φ was assumed to be equal to one. In order to completely deoxygenated whole blood, a concentration of $C = 3\,\mathrm{mg/L}$ was required. Using Eq. 4.31 with the previously specified parameters produced an osmolarity of $O = 69\,\mathrm{mosmol/L}$, where *mosmol* stands for milliosmols. The added sodium dithionite then increased the osmolarity of the solution, which in return was added to the own whole blood osmolarity, which is around $300\,\mathrm{mosmol/L}$[149]. A change in the osmolarity of blood means that the haemoglobin concentration in RBCs is modified, thus modifying the absorption and scattering properties of blood[149].

This section shows how in our case the osmolarity increased due to the addition of sodium dithionite, producing an increase in the scattering and absorption coefficients. Since an osmolarity increase was not taken into account in our model, the non-linear squares fit underestimated the *OS* of the sample. In order to avoid osmolarity effects in the future, blood oxygenation should be controlled by using gases such as CO_2, O_2 and N_2[150].

4.8 Application to *in vivo* retinal oximetry

After applying the algorithm to data obtained from a model eye, the next step was to test IRIS and the algorithm with human retinas. Nine young healthy subjects volunteered, with an average age of 28 ± 5 years. This study was approved by Heriot-Watt University Ethics Committee. All procedures were performed according to the Tenets of declaration of Helsinki. The volunteer consent form and additional information can be found in Appendix D. Their pupils were dilated using tropicamide 0.5% eye drops and then the retina was imaged with a commercial fundus camera interfaced with IRIS (Fig. 4.1). In order to as-

sess the ability of our system to detect oxygen changes in the retina, the subjects were imaged under different systemic oxygenations conditions, more specifically, 5 data sets were taken: normoxia-hypoxia-normoxia-hypoxia-normoxia. Hypoxia was achieved using a hypoxia generator (*Everest Summit II Hypoxic Generator, Hypoxico Inc*., New York, U.S.) by reducing the oxygen partial pressure. Systemic *OS* was monitored using a finger pulse oximeter (*Biox 3740 Pulse Oximeter, Ohmeda*). The response of different subjects to the same oxygen partial pressure was found to differ in terms of measured oxygenation by the pulse oximeter. In order to minimise disparities between subjects, oxygen partial pressure was varied between 21% and 15% in order to induce a 5 minutes long hypoxic state of $85 \pm 3\%$ systemic oxygen saturation. After 5 minutes being hypoxic, it was considered that retinal arteries had the same average *OS* displayed by the pulse oximeter. After hypoxia, subjects were left to achieve normoxia for 10 minutes and the hypoxia-normoxia process was repeated once more. The 9 subjects had different eye pigmentation, as shown in Fig. 4.10. An average of 22 vessels (11 arteries and veins) per subject were tracked and analysed.

Exclusion criteria were applied to reject problematic vessels or regions:

1. Vessels towards the edges of the image were rejected since some bands suffered vignetting introduced by the filter plate.

2. Vessel sections which crossed paths with other vessels were ignored. The vessel diameter in these regions did not provide reliable results. Oxygen diffusion between close vessels can occur, so it is better to consider the vessel before and after the crossing as different vessels.

3. Vessels smaller than 4 pixels or $\sim 62\,\mu$m were rejected. Aliasing, high transmission, low contrast and noise made them unreliable in terms of extracting information.

4. Vessel sections separated by fewer than 4 pixels were rejected. This is due to the possibility of having *OS* diffusion between them in those regions, but mainly because the algorithms to extract the vessel profile, diameter and transmission tended to produce wrong results in these vessel sections. Adjacent vessels appeared in the obtained vessel section, interfering with the background and vessel profile fit to calculate the vessel diameter and transmission.

4.8.1 Independent Component Analysis (ICA)

Prior to the application of the oximetry algorithm, it is informative to do an Independent Components Analysis (ICA) on the retrieved optical densities for all subjects with 2 and 8 wavelengths. This would allow assessing the performance of both methods only by spectral methods, rather than by fitting the data to physical models.

The transmission of the tracked vessels was calculated, which was then calculated as *OD*, creating a 3-D matrix in which x was the distance along the vessel in pixels, y was the

vessel number and z was the 8 IRIS wavelengths. Using *ENVI*, ICA was applied to each 3-D cube of each subject for the eight and two wavelengths cases. The two selected wavelengths were 571 nm and 599 nm, which are the standard used in retinal oximetry. The output components of the ICA analysis was fixed at two since no more than two spectral components have a main role in blood absorbance. These two components would be oxyhaemoglobin and deoxyhaemoglobin and their variance along the vessels provided a metric of variability along the vessel. The stability of the measurement was compared by calculating the standard deviation for each vessel and then each retina. The standard deviation of the ICA components for nine subjects are displayed in Fig. 4.28, showing a decrease in standard deviation for 8 wavelengths when compared with 2 wavelengths. Considering the nine subjects, there is a 13% standard deviation reduction for the first ICA component and a 10% reduction in standard deviation for the second ICA component. ICA results show that along vessels, 8 wavelengths provides more stability than 2 wavelengths. In this case, the improvement in stability might be due to having 8 points representing the spectral signature rather than only 2 points, which could be more sensitive to errors. On the other hand, repeating the measurement several times using two wavelengths would reduce this sensitivity to errors and might provide a similar enhancement as using 8 wavelengths.

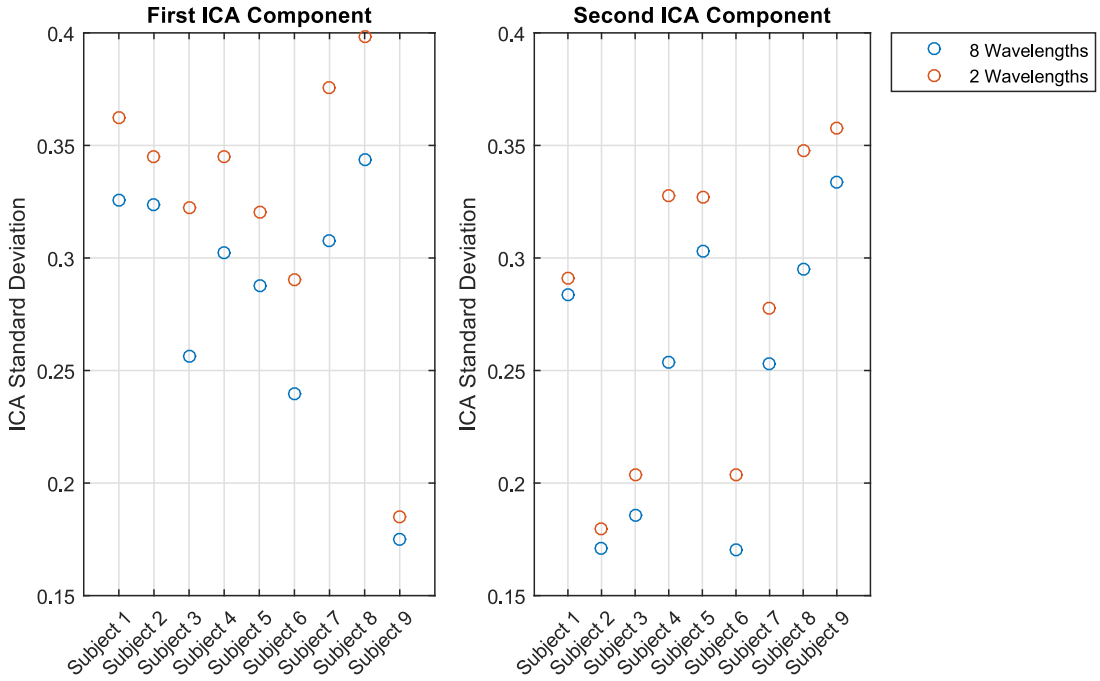

Figure 4.28: Retinal vessels ICA standard deviation of the first and second ICA components, with the subjects sorted from lower to higher pigmentation.

4.8.2 Eight-wavelength retinal oximetry algorithm

The retinal algorithm (Algorithm 4.1) was applied to data obtained from 9 subjects with a range of pigmentations (Fig. 4.10) using Model 1 (Eq. 4.20), Model 2 (Eq. 4.21) and

Model 3 (Eq. 4.22) (Equations shown on Subsection 4.5.2). Two-wavelength oximetry was performed using Eq. 1.8 (Section 1.3), setting the *OS* thresholds to 96% and 54% for arteries and veins respectively[59].

The oximetric maps obtained from each of the above-mentioned models are shown in Appendix A, including their corresponding tabulated data with the mean *OS* for arteries and veins and the mean of the standard deviation of each vessel. An example of an oximetry map is shown here in Fig. 4.29, including the vessel number on Fig. 4.29(a).

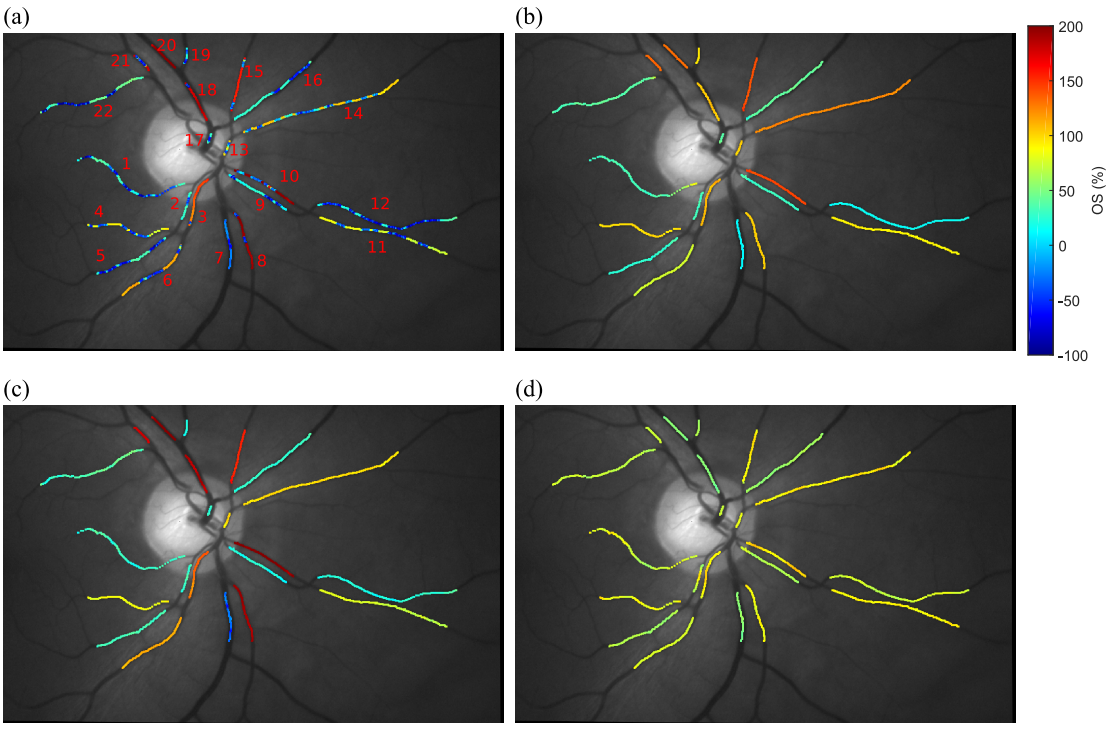

Figure 4.29: Subject 5 *OS* maps from different models at normoxia (98% *OS*, pulse oximeter). (a) Model 1 (Eq. 4.20). (b) Model 2 (Eq. 4.21). (c) Model 3 (Eq. 4.22). (d) two-wavelengths oximetry (Eq. 1.8).

The performance of the models was assessed in terms of the mean *OS* values of all retinas for the normoxia-hypoxia-normoxia-hypoxia-normoxia sequence considering first the standard deviation of the mean *OS* of the individual vessels (Fig. 4.30(a)) and then the mean standard deviation of the *OS* along the individual vessels (Fig. 4.30(b)).

Fig. 4.30(a) shows the mean *OS* of all vessels, separated in arteries and veins. The error bars in this figure corresponds to the standard deviation of the mean oxygenation of all vessels, so it represents the distribution of vessel oxygenations of all subjects. Model 1, Model 2, Model 3 and two-wavelengths oximetry had a standard deviation of $\sim 17\%$, $\sim 13\%$, $\sim 20\%$ and $\sim 4\%$ *OS* respectively (Fig. 4.30(a)). These values were calculated by first averaging the oxygenation along the vessels of all subjects and then calculating the standard deviation of all the oxygenations. This shows that two-wavelengths oximetry had the lowest variability between vessels and subjects, mainly due to its calibration-based and linear nature, which tends to constrain the calculated *OS*. From the three calibration-free methods, Model 2

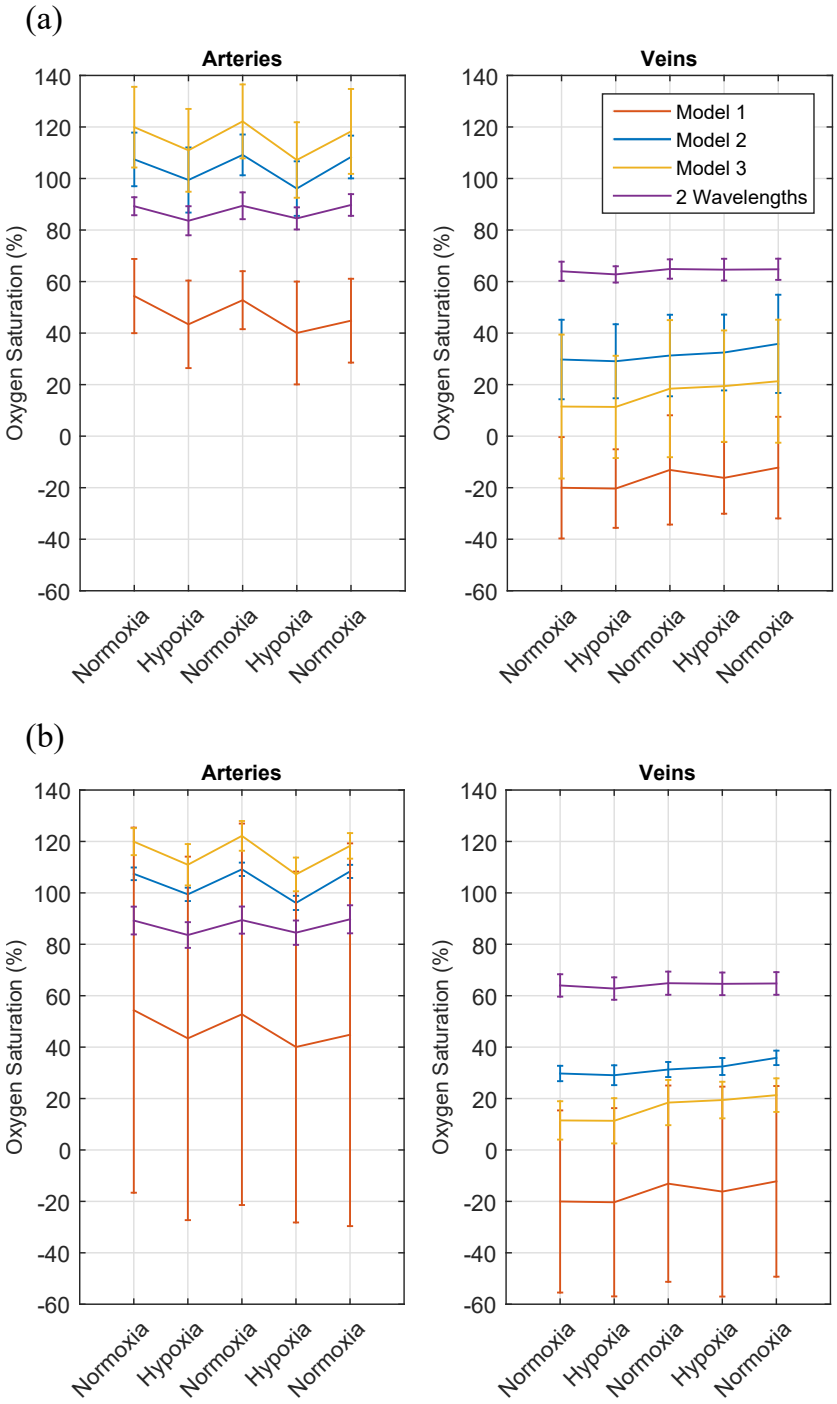

Figure 4.30: Oximetry-model comparison of the normoxia-hypoxia-normoxia-hypoxia-normoxia sequence. (a) Mean *OS* and standard deviation of the mean oxygenation of all vessels, showing the distribution of mean vessel oxygenations found in all subjects. (b) Mean *OS* and mean of the standard deviation of the oxygenation along the vessels of all subjects, showing how stable are the oximetry measurements along the vessels.

presented the best performance, while Model 3 showed the highest variability of mean vessel oxygenations. The main difference between Model 2 and Model 3 when applied on a model eye (Fig. 4.27) and on human retinas (Fig. 4.30) is that Model 3 is a simplification of Model 3 and it is meant to work in conditions where either the backscattered or the double pass are

neglected, while Model 3 considers all three contributions to the vessel transmission (single pass, double pass, backscattered)[79].

Fig. 4.30(b) shows the mean *OS* of all vessels and the error bars correspond to the mean of the standard deviation of the oxygenation along all the vessels, so it represents how stable is the oxygen calculation along the vessels. Model 1, Model 2, Model 3 and two-wavelengths oximetry had a mean standard deviation of the oxygenation along vessels of $\sim 55\%$, $\sim 3\%$, $\sim 7\%$ and $\sim 5\%$ *OS* respectively, where Model 2 had the lowest standard deviation, having a 2% *OS* reduction of variability along vessels when compared with two-wavelengths oximetry. These values were obtained by first calculating the standard deviation of the oxygenation along all the vessels of all subjects, and then calculating the average of these values.

The four models were also compared using the mean *OS* (Fig. 4.30) where the results from two-wavelength oximetry were used as a reference. In this context, Model 1 produced *OS* values below 60% for arteries and below 0% for veins, which are abnormally low. At this point, Model 1 had been demonstrated to produce low *OS* and high *OS* variability in vessels, so it was excluded from any future analysis. Table 4.4 shows a summary of the main oxygenation features for the three remaining models, including the mean *OS* and standard deviation for arteries and veins, the arteriovenous difference (A-V) under hypoxia and normoxia conditions, and finally the *OS* difference between normoxia and hypoxia for arteries and veins.

Table 4.4 shows Model 2 and Model 3 having oxygenations on arteries higher than the oxygenations found using two-wavelengths oximetry under normoxia and hypoxia conditions, while *OS* on veins is below the two-wavelength oximetry reference. However, in terms of detecting a change in *OS*, Model 2 and Model 3 seemed to perform better than two-wavelengths oximetry. During the experiment, measured systemic *OS* with the pulse oximeter was $97.7 \pm 0.9\%$ under normoxia and $84.3 \pm 1.5\%$ under hypoxia conditions, meaning a difference of $12 \pm 2\%$ *OS* on arteries between normoxia and hypoxia conditions. The information displayed on Table 4.4 shows an oxygenation change of $5.4 \pm 1.5\%$ for two-wavelengths oximetry, while Model 2 and Model 3 show an *OS* difference of $10.5 \pm 5.3\%$ and $11.8 \pm 4.7\%$ respectively, where these values were closer to the measured oxygenation via the pulse oximeter. Evaluation of venular *OS* changes with an external reference (not retinal oximetry) was not possible since the pulse oximeter measures only arterial systemic *OS*.

When Model 2 (Eq. 4.21) and Model 3 (Eq. 4.22) were compared, the second one produced higher *OS* for arteries: $120.1 \pm 2.8\%$(Model 3) > $108.3 \pm 2.0\%$(Model 2), on normoxia conditions. For veins, The second model produced lower *OS* than the first model: $17.1 \pm 5.1\%$(Model 3) < $32.3 \pm 3.5\%$(Model 2). Although the obtained *OS* for Model 2 was 18.8% and 32.3% off compared with the two-wavelengths reference for arteries and veins respectively, they are closer than the obtained oxygenations from Model 3, which means that

Model 2 produced the most precise oximetric values of the three proposed calibration-free models.

Regarding the arteriovenous difference, two-wavelength oximetry showed oxygenation differences of $25 \pm 1.7\%$ for normoxia and $20.4 \pm 2.1\%$ for hypoxia. Previous studies using two-wavelengths oximetry with subjects breathing a fixed O_2 showed that the difference remains approximately constant[63, 151]. The performed experiment on this chapter used 9 subjects under different O_2 concentrations in order to make the subjects hypoxic at approximately the same systemic oxygenation. An experiment with a higher number of subjects will be required in order to obtain more reliable data about the arteriovenous difference. The difference in methodology might also explain why the *OS* change on veins between normoxia and hypoxia is $1.5 \pm 5.2\%$ for Model 2, $1.7 \pm 9.2\%$ for Model 3 and $0.8 \pm 1.9\%$ for two-wavelength oximetry (Table 4.4). According to the literature[151], the induced *OS* difference between normoxia and hypoxia on veins by breathing 10% O_2 should be $18 \pm 22\%$ and $28 \pm 7\%$ for arteries. Other authors[63] report $8.3 \pm 3.5\%$ and $8.2 \pm 2.6\%$ oxygenation difference for veins and arteries respectively using different imaging systems but applying the same methodology and breathing 15% O_2.

Oxygen Saturation	Model 2	Model 3	Two-wavelength oximetry
Arteries Normoxia	$108.3 \pm 2.0\%$	$120.1 \pm 2.8\%$	$89.5 \pm 0.7\%$
Veins Normoxia	$32.3 \pm 3.5\%$	$17.1 \pm 5.1\%$	$64.5 \pm 1.5\%$
Arteries Hypoxia	$97.8 \pm 4.9\%$	$108.3 \pm 3.8\%$	$84.1 \pm 1.3\%$
Veins Hypoxia	$30.8 \pm 3.9\%$	$15.4 \pm 7.7\%$	$63.7 \pm 1.2\%$
A-V Normoxia	$76 \pm 4\%$	$103 \pm 6\%$	$25 \pm 1.7\%$
A-V Hypoxia	$67 \pm 6\%$	$92.9 \pm 8.5\%$	$20.4 \pm 2.1\%$
Arteries N-H	$10.5 \pm 5.3\%$	$11.8 \pm 4.7\%$	$5.4 \pm 1.5\%$
Veins N-H	$1.5 \pm 5.2\%$	$1.7 \pm 9.2\%$	$0.8 \pm 1.9\%$

Table 4.4: *OS* for subjects under normoxia and hypoxia conditions, arteriovenous difference (A-V) and normoxia-hypoxia difference (N-H) for arteries and veins.

The oximetric calculations displayed in this section shows that Model 2 performs better than Model 3 in terms of stability along the vessel and mean *OS*. When Model 2 was compared with two-wavelength oximetry, the first one produced values above 100% for arteries, which can be explained by error propagation, while veins tend to produce values around 30% oxygenation, below the average 54% defined in the literature[59]. Model 2 also had a higher

standard deviation of *OS* on veins and arteries ($\sim 13\%$ *OS*) than two-wavelengths oximetry ($\sim 4\%$ *OS*). However, one advantage of Model 2 over two-wavelength oximetry was a lowest oxygenation standard deviation along vessels, being $\sim 3\%$ in front of the $\sim 5\%$ produced by the calibration-based model.

Regarding the *OS* obtained with two-wavelengths oximetry, the mean oxygenation for arteries on normoxia was $OS = 89.5 \pm 0.7\%$ while the pulse oximeter showed $OS = 97.7 \pm 0.9\%$. Two-wavelengths oximetry performed with the same optical system showed $OS = 98.5 \pm 1.6\%$ while the pulse oximeter showed $OS = 98.6 \pm 0.7\%$ in a previous research[63], showing an similar behaviour between both values. In the latest case, stricter exclusion criteria were applied, among them the elimination of vessels with high background reflectance variations, which yielded the highest errors in oximetry. In additions, vessels with a thickness below 12 pixels were also rejected. In this thesis, under a more relaxed exclusion criteria, two-wavelength oximetry showed a mismatch of 8.25% oxygenation between the calculated and measured with the pulse oximeter. However, Model 2 also showed a mismatch, in this case of 9.7% *OS*. This thesis wanted to show the superior performance of calibration-free oximetry under conditions usually excluded from analysis in other research such as the above mentioned. This has been shown with the arteriovenous difference and the stability of the vessels. Some examples of performance along vessels are shown in the next section.

4.8.2.1 Oximetry stability along vessels

Further stability analysis was performed by plotting the *OS* results for Model 2 (Eq. 4.21), two-wavelengths oximetry (Eq. 1.8) and the transmission along the vessel. 571 nm was used to plot the transmission, in order to discard any oxygenation-sensitive effects on the transmission. This comparison allowed assessing how the different methods deal with changes in background reflectance, proximity to other vessels or long vessels. Long vessels can cross different parts of the retina with different melanin concentrations and different choroidal structure (non-homogeneous background), so they can be subjected to artificial *OS* variations along them.

Subsection 4.6.3 introduced the retinal algorithm used in this chapter. This algorithm (Algorithm 4.1) assumes the oxygenation to be constant in the second step, which could artificially lead to an increase in oxygenation stability along the vessel. This step is based on the assumption that changes in oxygenation should not happen in the typical length of the analysed vessels, which are below 3 mm[146, 147]. However, the last step of the retinal algorithm solves the oximetry models for the oxygen saturation along the vessel by fixing all the parameters previously found. This last step should account for any oxygenation changes along the vessels. In addition, when the three physical models are compared in Fig. 4.30(b), it can be observed that the forcing the oxygenation to be constant in the second step of the algorithm does not stabilise the final oxygenation obtained from the algorithm for Model 1.

This effect is better represented in Fig. 4.29 where the retinal algorithm produces results with different stabilities along the vessels because the models are solved for *OS* along with the vessels in the last step.

To check the oximetry stability along vessels, three vessels of different subjects were selected: vessel 19 of subject 2 (Fig. A.2) for the change on background, since it passes from the optic disc to the retina; vessel 12 of subject 5 (Fig. A.5), a vein which passes ~ 3 pixels away from an artery; vessel 9 of subject 7 (Fig. A.7), which was the longest vessel processed with 207 pixels ($\sim 3.2\,$mm).

Fig. 4.31(a) shows the results for vessel 19 of subject 2 (Fig. A.2). In this artery, the standard deviation of the transmission at 571 nm was 8.2%. The vessel transmission increased when it changed from the optic disc to the retina. This might be due to an increase in the X_3 backscattered component as obtained from Model 2, which was 0.0009 ± 0.0015 over the optic disc, and increased to 0.0064 ± 0.0015 over the retina. The oxygenation values from two-wavelength oximetry had a standard deviation of 7.3% along the vessel, with a clear increase in oxygenation in the region where the change from optic disc to retina occurs (Fig. 4.31(a)). Model 2 shows a lower variation along the vessel with a standard deviation of 5.1% and with no apparent relation to changes in transmission. In the case of using Model 2 on a pixel based method, the oxygenation standard deviation was 19.94% and was clearly affected by the transition from optic disc to retinal tissue.

Fig. 4.31(b) shows the results for vessel 12 of subject 5 (Fig. A.5). The transmission of this vein had a standard deviation of 5.2%. These variations might be due to changes in the choroid and pigmentation. Two-wavelengths oximetry shows a variation of 5.1% in oxygenation, while for Model 2 is 1.9%. In the case of using Model 2 on a pixel based method the oxygenation standard deviation was 23.81%.

Fig. 4.31(c) shows the results for vessel 9 of subject 7 (Fig. A.7). The transmission of this artery had a standard deviation of 5%, while two-wavelengths oximetry and Model 2 had 3.2% and 0.6% standard deviation on *OS* respectively. In the case of using Model 2 without on a pixel based method the oxygenation standard deviation was 36.37%.

The plots in Fig. 4.31 show a higher variability along vessels for two-wavelengths oximetry than for Model 2. As stated before, the eight-wavelength retinal oximetry algorithm for all nine subjects presented a mean oxygenation standard deviation of $\sim 3\%$, while it was $\sim 5\%$ for two-wavelengths oximetry. Considering the 150 processed vessels of all 9 subjects, 86% of the vessels had lower oxygenation standard deviation with the retinal oximetry algorithm than the mean oxygenation standard deviation of all vessels for two-wavelengths oximetry ($\sim 5\%$). This figure also shows the need of using the retinal algorithm rather than applying Model 2 directly to the transmission data. In the latest case, the mean *OS* standard deviation along vessels was $\sim 25.19\%$, which shows larger variability than the $\sim 3\%$ achieved when the retinal algorithm was applied.

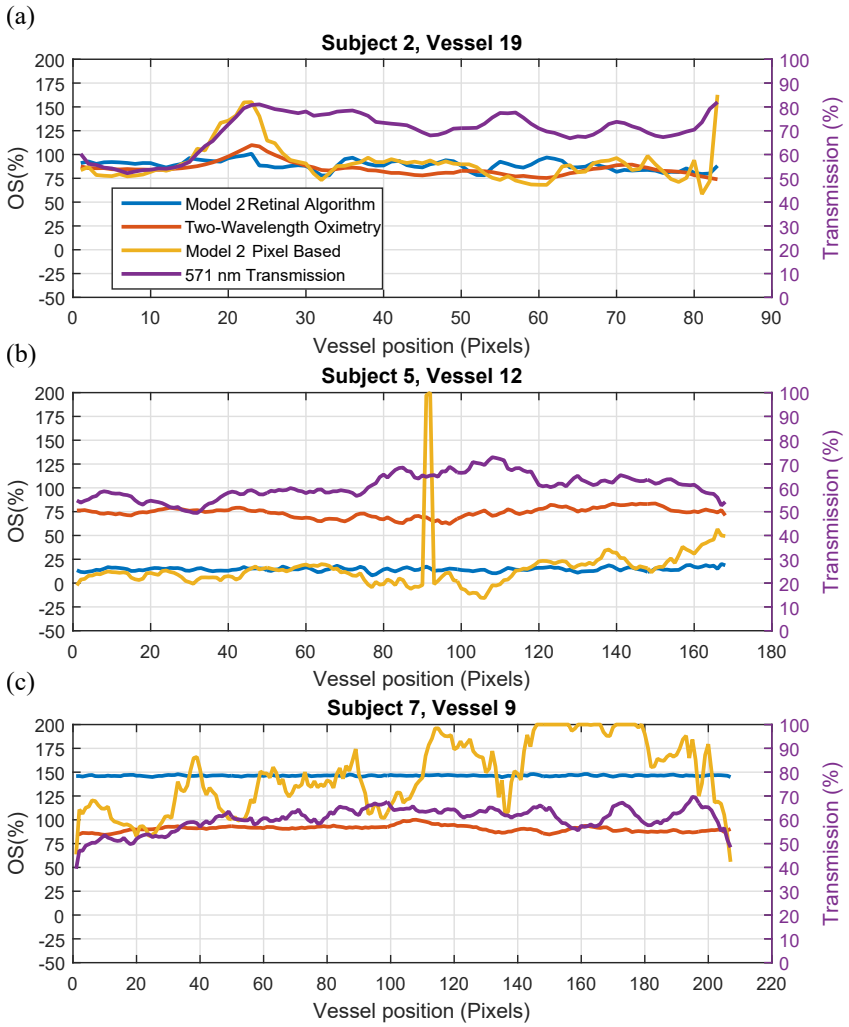

Figure 4.31: Oximetry stability along vessels for Model 2 (Eq. 4.21) applying the retinal algorithm (blue), two wavelengths oximetry (Eq. 1.8)(red) and Model 2 applying it on a pixel based system (yellow). Includes the vessel transmission at 571 nm (purple). (a) Subject 2, vessel 19 (Fig. A.2) corresponds to an artery which analysed path passes from the optic disc to the retinal tissue. (b) Subject 5, vessel 12 (Fig. A.5) corresponds to a vein which contains regions ~ 3 pixels away from an artery. (c) Subject 7, vessel 9 (Fig. A.7) corresponds to the longest processed vessel on all subjects, with 207 pixels long, which corresponds to $\sim 3.2\,\text{mm}$.

4.8.2.2 Oximetry parameters relation with vessel diameter

On two-wavelengths oximetry, it has been observed a relation of decreasing *OS* with increasing diameter[58]. This might be produced by Eq. 1.8 not including spectral bandwidth effects. The vessel thickness or pathlength does not cancel on the *ODR* when the spectral bandwidth is introduced.

In the case of 8 wavelengths oximetry, the use of a physical model which includes the diameter and spectral bandwidth should remove any systematic errors. In this section, possible relations of K, c and OS on Model 2 (Eq. 4.21) were analysed against vessel diameter. The pathlength contributions were not analysed since it is not possible to discriminate between them from an intensity map and might not produce reliable results. The results were analysed

by showing the mean value of K, c and OS with diameter for each vessel and subject under the first normoxia sample.

Fig. 4.32 shows a scatter plot with the mean contrast reduction of all analysed vessels of all subjects versus diameter and the corresponding linear fit to the whole data. The mean contrast reduction calculated for all vessels and subjects was $K = 0.42 \pm 0.05$. The linear fit was $y = -0.003x + 0.7$ with $r^2 = 0.2711$. Although the r^2 was low, there was an increase of K with small diameters. This effect might be due to the larger thickness of the inner limiter membrane (ILM) over thinner vessels. This added tissue would increase light scattering and reduce the contrast. OCT images obtained by other groups suggest that this could be the case[140, 152, 153], since thinner vessels are deeper on the ILM, while on larger vessels the ILM is thinner.

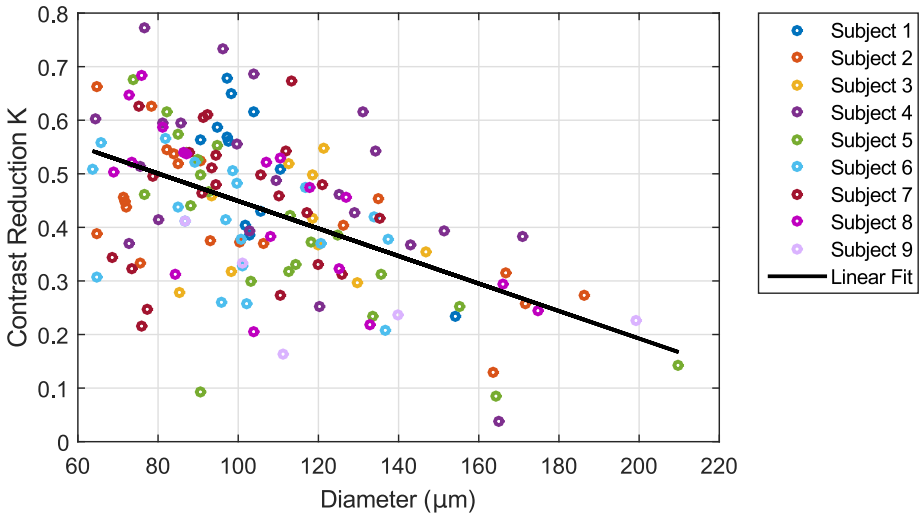

Figure 4.32: Contrast reduction K behaviour with diameter per subject and the linear fit to all subjects.

In terms of haemoglobin concentration, Fig. 4.33 shows little to no effect and the spread of the concentration values was likely to be an artefact from the algorithm.

Regarding the OS, vessels were separated between arteries (Fig. 4.34(a)) and veins (Fig. 4.34(b)) and then analysed in function of their diameter. The linear fit for arteries was $y = 0.3x + 83$ and with $r^2 = 0.0536$, while for veins fit was $y = -0.17x + 46$, with $r^2 = 0.0642$. Both show a small trend, but the r^2 was small enough to be considered negligible, so the diameter would not have an effect on the calculated OS.

4.9 Conclusions and future work

This chapter has shown the application of the modified IRIS to retinal oximetry. First, it was shown the need of correctly using the spectral transmission function of the system (bandwidth and illumination) and the subject's own fundus reflectance to minimise errors.

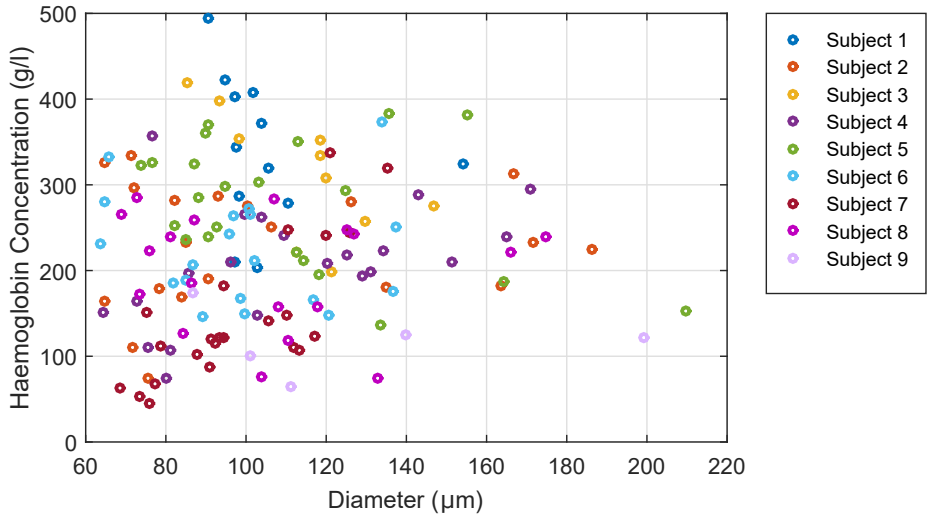

Figure 4.33: Haemoglobin concentration behaviour with diameter per subject.

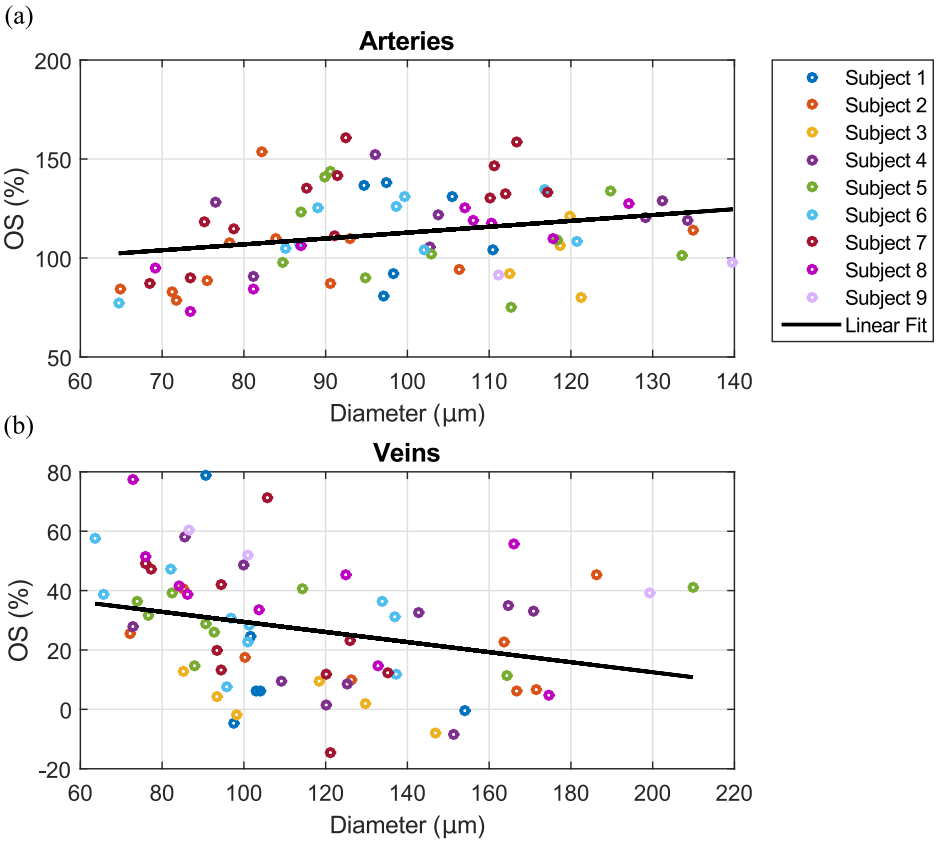

Figure 4.34: Oxygenation behaviour with diameter per subject and the linear fit to all subjects. (a) Arteries. (b) Veins.

Secondly, a modification of existing physical models was applied in order to take into account contrast reduction from ocular scattering. The introduction of contrast reduction in the model increased the error sensitivity of *OS* with small perturbations on transmission, especially under medium contrast conditions such as the eye. Errors in transmission were reduced by fitting an exponential function to each side of the vessel, rather than using more conventional methods such as fitting a parabola. Finally, an eight-wavelength oximetry algorithm

was developed by introducing physiologically feasible assumptions in order to reduce oxygenation variability along vessels. A 10% increase in the stability of the *OS* calculation was first found by means of an Independent Components Analysis using 8 wavelengths when compared with two-wavelengths oximetry.

In the case of the oximetry algorithm, three calibration-free models were used: Model 1 (Eq. 4.20), Model 2 (Eq. 4.21) and Model 3 (Eq. 4.22). The results showed Model 1 underestimating the *OS* and having a mean standard deviation of $\sim 55\%$ oxygenation along vessels, which might be mainly due to the lack of considering backscattered light. Model 3 showed an oxygenation standard deviation of $\sim 7\%$, still larger than the $\sim 5\%$ for two-wavelengths oximetry, but tended to overestimate *OS* in arteries and underestimate it on veins. The behaviour of this model might be due to the fact that is a simplification of a more complex model, which was designed to be used with systems such as a cSLO, in which the pathlengths contributions on vessels can be controlled. Finally, Model 2 showed an oxygenation standard deviation of $\sim 3\%$, smaller than the obtained with two-wavelength oximetry.

In terms of comparing the change in *OS* for arteries between normoxia and hypoxia, Model 2 and Model 3 showed $10.5 \pm 5.3\%$ and $11.8 \pm 4.7\%$ respectively, which was within the $12 \pm 2\%$ oxygenation measured by the pulse oximeter. These two models performed better than two-wavelengths oximetry, which showed an oxygenation difference of $5.4 \pm 1.5\%$ between normoxia and hypoxia for arteries.

Error propagation was an important issue since in general the algorithm calculated a contrast reduction of $K = 0.42 \pm 0.05$. Under these conditions errors higher than 20% were to be expected for small errors in transmission, and as it has been shown, the used physical models tended to produce errors of this magnitude (see Appendix A). In the future, error propagation could be reduced by improving the vessel characterisation and reducing the dimensionality of the problem or by increasing the contrast by computational means.

In terms of improving the vessel characterisation, the implementation of an OCT system would allow measuring vessel thickness with better accuracy, since from retinal images it is only possible to measure the width, not the depth of the vessel. An OCT system would also eliminate the need of estimating the eye magnification, which is dependent on the axial length and refractive error of the eye.

The use of structured illumination would eliminate the backscattered component, which would reduce the need of estimating the fundus reflectance and the associated errors. Furthermore, a better control over the pathlengths would allow reducing the dimensionality of the problem, increasing the stability and accuracy of the calculations.

The retinal algorithm was adapted to perform oximetry on two collaboration projects. The first one performed *in vivo* oximetry of rats dorsal spinal cord vasculature under different inspired oxygen concentration air. Since the imaged medium was less complex than retinal tissue, oximetric results showed physiologically feasible values (below 100%) and showed a

good response to changes on inspired O_2. Oximetry showed values of $67.8 \pm 10.4\%$ *OS* for 21% O_2 and $29.2 \pm 24.6\%$ *OS* for 15% O_2[154]. The involved authors on this work were: Marieke A. van der Putten[1], Lewis E. Mackenzie[1], Javier Fernandez Ramos[1], Roshni Desai[2], Andrew L. Davies[2], Kenneth J. Smith[2] and Andrew R. Harvey[1]. In the future it will be applied to rat dorsal spinal cord vasculature in order to assess the role of hypoxia in diseases such as multiple sclerosis and rheumatoid arthritis. The second collaboration project in which the algorithm was applied was performed by Marieke A. van der Putten[1] on mice tendon microvasculature to assess hypoxia on autoimmune diseases such as rheumatoid arthritis. In this system, only single pass intervenes for vessel transmission, which simplifies the physical model and improves oximetric results, without producing values higher than 100% oxygenation. Preliminary results showed a decrease in oxygen saturation in the diseased model mice.

[1]School of Physics and Astronomy, University of Glasgow, Glasgow, United Kingdom

[2]Department of Neuroinflammation, University College London Institute of Neurology, London, United Kingdom

Chapter 5

Conclusions

5.1 Summary of thesis

This work has shown the improvement of IRIS as a snapshot multispectral imaging device and its application to oximetry.

Chapter 1 describes existing imaging multispectral devices, from scanning to snapshot devices, providing special emphasis on the latter. IRIS is then introduced and its advantages over other techniques such as CTIS or CASSI are explained. Among the advantages, the most relevant are the 100% light transmission of polarised light, no need of inversion for the 3-D cube recovery, offering high SNR and its compactness. This chapter briefly introduces some spectral analysis techniques such as Independent Components Analysis and Linear Spectral Unmixing. The chapter then continues with a review of retinal oximetry. It includes the basics of oximetry, starting with a brief description of the Beer-Lambert law and the spectral behaviour of blood at different oxygenations. Several calibration-based methods to calculate oxygen saturation from the optical density of retinal vessels are described. Then calibration-free methods developed by other groups are described. The chapter then finishes with a review of oximetry applied to red blood cells, which includes techniques such as Raman spectrography, photoacoustics, OCT and two-wavelength oximetry.

Chapter 2 describes the inherent issues of IRIS and how they are solved. The main problem of IRIS is the existence of spectral side lobes, which contaminates the spectrum and the spatial information from PSF smearing introduced by the dispersion of the Wollaston prisms. The sidelobes are removed with the implementation of individual filter tiles in front of the detector array. The sidelobe removal allows accurate image registration and spectral characterisation of chromophores.

Chapter 3 describes the application of the modified IRIS to video-rate oximetry of red blood cell. First, the image registration technique used is described, which improves the subpixel accuracy when compared with previous image registration methods. Second, it describes the experimental system and sample preparation, which includes the use of a cell

chamber and a PLL-coated microscope cover slide. Finally, a linear spectral unmixing technique is applied to the recorded videos of deoxygenating red blood cells in order to recover the deoxygenation process. The same technique is applied to blood samples deoxygenated to a determined oxygen saturation. The results show a measurement repeatibility below 1% during the oxygenated and deoxygenated states in the recorded video.

Chapter 4 finally applies the improved IRIS to retinal oximetry. In order to do so, first, several factors such as bandwidth, fundus reflectance, and illumination are analysed in order to assess their correct application and the consequences of not doing it correctly. The second part includes the introduction of ocular scattering in existing calibration-free physical models, including error perturbation analysis in order to assess the effect of 1% error on transmission on the calculated oxygen saturation. An algorithm is developed to increase stability on the oxygen saturation calculations and reduce the possible relations and dependencies between the fitting parameters of the calibration-free physical models. After applying the algorithm to data obtained from blood on a model eye and on human retinas, oximetry performance was improved in terms of stability along vessels of one of the calibration-free compared to the two-wavelength oximetry model. However, error propagation introduces an overestimation of the oxygen saturation, producing values above 100% oxygenation.

5.2 Conclusions and future work

This thesis has shown how with the elimination of spectral side lobes on IRIS it is possible to perform oximetry of RBCs *in vitro* and of human retinal vessels. However, the results for retinal vessels only showed better performance than other techniques in terms of oxygen saturation stability along vessels. The spectral improvement allowed a better spectral characterisation of different substances. When it was applied to oximetry, the recovered 3-D cube provided a spectrally accurate transmission of blood, which in return allowed the use of physical models to extract the oxygen saturation from blood transmission without the need for calibration. The retrieval of oxygen saturation of blood can be used as a tool to detect and treat hypoxia and gain further knowledge of diseases in which hypoxia is developed. Some examples of diseases in which hypoxia is developed are diabetes[9], tumour hypoxia[10], glaucoma[11], sickle cell anaemia[12], Alzheimer's disease[13] and multiple sclerosis[14].

The introduction of the filter plate using a 3-D printed holder increased the versatility of IRIS since the filters can be swap and changed in order to select multiple wavelengths of the free spectral range of IRIS, limited only by the illumination source. This opens the use of IRIS to other spectral imaging applications.

The application of IRIS to RBC oximetry yielded accurate and precise oxygen saturation values. Oximetry on single RBCs has been performed using OCT[87] with the introduction of a corrective factor. Another optical technique measured the mass of oxy and deoxyhaemoglobin at two wavelengths in order to calculate the oxygen saturation, but it also required a

corrective factor[96]. Finally, photoacoustics allowed measurement of the oxygenation of single RBCs *in vivo[91],* but with no subcellular resolution and with high data averaging to obtain a good oxygen saturation characterisation. On the other hand, IRIS allowed subcellular resolution, with standard deviations of $\sim 10\%$ for single RBCs and no need of corrective factors thanks to the use of spectral references (endmembers) to calculate the oxygen saturation. Another important result was the stability of the measurement during the oxygenated and deoxygenated states, which were 1.17% and 0.88% oxygenation for the oxy- and deoxygenated cases for the single cell, and 0.66% and 0.56% for the oxygenated and deoxygenated regions on the whole sample. In theory, it should have been possible to observe subcellular oxygen saturation changes, but it was not possible due to the timescales for deoxygenation being faster than the camera framerate and the ability to change oxygenation in a controlled way. This can be easily solved by using a camera with a higher frame rate. In the future, the filter plate will combine a set of filters in the blue region of the spectrum and another set in the red in order to be able to perform oximetry on individual RBCs and in the microvasculature simultaneously. Future work will include the use of a 16-bit and high frame rate camera, which would allow higher oxygenation resolution and capturing oxygen release and uptake by RBCs. It is also recommended to do a test of the system using microbeads or artificial RBCs[100] to characterise defocus effects, which would then allow analysing defocused RBCs. Finally, implementing OCT[107] would give relevant information about the RBC shape. Knowing the shape of the RBC would allow taking into account different thickness and orientations of the RBCs, which would in return increase the accuracy of the method. The use of this technique *in vivo* would require imaging in the 410-450 nm range of the spectrum since it is where haemoglobin has its maximum absorption and it would be possible to distinguish individual RBCs from surrounding tissue. However, high light scattering from tissue means that in can be applied where there is little or no tissue over the vessels such as nailfold capillaroscopy[115]. RBC oximetry could also be performed in the microvasculature below the skin using microendoscopes, which would be minimally invasive. These two approaches could be proved useful to monitor oxygen saturation in the microvasculature, which can be disrupted by diabetes. Microendoscopes can be used in animals models to study diseases such as multiple sclerosis[14]. This approach is being currently developed by Marieke A. van der Putten[1]. This technique could be applied to RBCs in retinal vessels using adaptive optics[155] since regular fundus cameras do not achieve cellular resolution.

IRIS was applied to retinal oximetry thanks to the development of a retinal oximetry algorithm. The implementation of the contrast reduction and the use of the retinal algorithm allowed the reduction of the oxygenation standard deviation on vessels from $\sim 5\%$ on two-wavelengths oximetry to $\sim 3\%$, which means that the retrieved oxygen saturation along vessels was more stable using the retinal algorithm than two-wavelengths oximetry. This oxygenation vessel stability was better in 86% of the 150 analysed vessels when eight-

[1]School of Physics and Astronomy, University of Glasgow, Glasgow, United Kingdom

wavelength oximetry was compared with two-wavelength oximetry. However, the retinal oximetry algorithm produced oxygenation values higher than 100% for arteries at normoxia and hypoxia. In the retinal testing, three calibration-free models were tested and compared with two-wavelength oximetry. Model 1 considered wavelength-dependent and wavelength-independent scattering but did not consider multiple paths of lights on vessels. Model 2 considered single and double pass and backscattered light from blood. Finally, Model 3 was a simplification of Model 2 done by assuming that backscattered light or double pass events can be neglected. Model 3 is expected to perform better under controlled illumination conditions such as using a cSLO. Models 1 and 2 were shown to be too simple or inadequate for 8 wavelengths retinal oximetry performed with a fundus camera, since Model 1 had standard deviations of up to 50%, and Model 2 tended to overestimate (and underestimate for veins) the oxygenation for arteries with mean values higher than 120%. Model 3 (Eq. 4.21) produced more stable results thanks to considering the contributions of multiple light pathlengths, which the other two models did not consider or were approximations. Model 3 also tended to overestimate oxygenation with values higher than 100%. This overestimation was mainly due to error propagation from the model, which was quite sensitive to small perturbations in transmission for medium contrast situations such as in retinal vessels. In the future, the contrast could be enhanced computationally which would reduce the loss of contrast and error propagation. Another problem is the different light pathlengths involved in the retinal vessel transmission. The contribution of these pathlengths have been shown in the past to vary for different vessel diameter and pigmentation conditions[71, 72] and it is not possible to know the contributions of each pathlength from an image obtained using a fundus camera. However, light pathlengths in retinal vessels can be controlled using a cSLO[82], which would reduce the dimensionality of the models and increase accuracy. Regarding the control of the pathlengths in a conventional fundus camera, it could be achieved using structured illumination, which would be used to shadow the retinal vessels while the rest of the retina is illuminated. This could be performed by introducing a spatial light modulator (SLM) in the illumination path of a fundus camera. The method would require an initial snapshot of the retina, which would be used to generate a binary mask of the retina after segmenting the vessels. This mask would be introduced in the SLM and projected over the retina. Real-time translation and rotation transformation would be required to match the projected pattern with the retina. With the retinal vessels being shadowed, the only contribution to the vessel transmission would be single pass, which would simplify the physical models and eliminate any possible compensation effects between pathlengths contributions when the models are solved. With an increase in contrast and a reduction in dimensionality, the retinal oximetry algorithm would improve its reliability and it would be closer to being an effective clinical tool.

The validation of the retinal oximetry algorithm on a model eye produced a linear behaviour, with $r^2 = 0.9411$, however, it underestimated oxygen saturation values when com-

pared with the measured values with a BGA, mainly due to an increase in osmolarity by the added sodium dithionite. In the future, a system using nitrogen should be implemented in order to deoxygenate blood.

The application of IRIS to measure oxygen diffusion between two laminar flows in a flow cell resulted in invalid results (Appendix B). Although laminar flow such as the observed in retinal vessels was replicated, faults in the flow cell design produced higher oxygen diffusion results and even reoxygenation of a flow composed only of deoxygenated blood. The reason behind this was the use of PDMS, which has an oxygen diffusion coefficient comparable in magnitude to that of haemoglobin. In the future it is recommended to coat the channels with PTFE, to manufacture a flows cell completely of PTFE or glass, or 3-D print a flow cell with a material such as PLA, which has a low oxygen diffusion coefficient.

Chapter 6

List of Publications

Journal articles (Published)

- T. Choudhary, D. Ball, J. Fernandez Ramos, A. I. McNaught, A. R. Harvey. "Assessment of Acute Mild Hypoxia on Retinal Oxygen Saturation Using Snapshot Retinal Oximetry", *Investigative Ophthalmology & Visual Science*, doi:10.1167/iovs.13-12624 (2013).[63]

- M. A. v. d. Putten, L. MacKenzie, A. Davies, J. Fernandez-Ramos, R. Desai, K. Smith, and A. Harvey, "A multispectral microscope for *in vivo* oximetry of rat dorsal spinal cord vasculature," Physiological Measurement (2016).[154]

Conference publications

- J. Fernandez Ramos, L. Brewer, A. Gorman, A Harvey, "Video-Rate Multispectral Imaging: Application to Microscopy and Macroscopy" *Computational Optical Sensing and Imaging*, Optical Society of America, 2014. [114]

Presentations

- J. Fernandez Ramos, L. Brewer, A. Harvey. "Cognate applications of biomedical oximetry: 8 wavelength oximetry in red blood cells". Oximetry Workshop (Birmingham), 2014.

- J. Fernandez Ramos, L. Brewer, A. Gorman, A. Harvey. "High-speed oximetry of individual red blood cells using multispectral analysis". Photon14 (UK), 2014.

- Javier Fernandez Ramos, T. Choudhary, L. Brewer1, A. Harvey. "Multispectral Snapshot Imaging Applied to Oximetry Using IRIS". Photonex (Heriot-Watt), 2014.

- J. Fernandez Ramos, L. Brewer, A. Gorman, A. Harvey. "Eight wavelength calibration-free oximetry". Oximetry Workshop (Glasgow), 2016.

References

[1] Q. Li, X. He, Y. Wang, H. Liu, D. Xu, and F. Guo, "Review of spectral imaging technology in biomedical engineering: achievements and challenges," J Biomed Opt **18**, 100901 (2013).

[2] N. Hagen and M. W. Kudenov, "Review of snapshot spectral imaging technologies," Optical Engineering **52**, 090901–090901 (2013).

[3] A. S. Gorman, "Snapshot spectral imaging using image replication and birefringent interferometry : principles and applications," PhD Thesis, Heriot-Watt University (2011).

[4] M. Friebel and M. Meinke, "Model function to calculate the refractive index of native hemoglobin in the wavelength range of 250-1100 nm dependent on concentration," Appl Opt **45**, 2838–42 (2006).

[5] F. C. Delori and K. P. Pflibsen, "Spectral reflectance of the human ocular fundus," Appl Opt **28**, 1061–77 (1989).

[6] "Zemax Models of the Human Eye | Zemax - Zemax," Http://www.zemax.com/support/resource-center/knowledgebase/zemax-models-of-the-human-eye.

[7] D. P. Pinero, D. Ortiz, and J. L. Alio, "Ocular scattering," Optom Vis Sci **87**, E682–96 (2010).

[8] W. F. Boron and E. L. Boulpaep, *Medical Physiology: A Cellular and Molecular Approach* (Saunders/Elsevier, 2009). Google-Books-ID: lxJrtQAACAAJ.

[9] J. S. Tiedeman, S. E. Kirk, S. Srinivas, and J. M. Beach, "Retinal oxygen consumption during hyperglycemia in patients with diabetes without retinopathy," Ophthalmology **105**, 31–36 (1998).

[10] B. S. Sorg, B. J. Moeller, O. Donovan, Y. Cao, and M. W. Dewhirst, "Hyperspectral imaging of hemoglobin saturation in tumor microvasculature and tumor hypoxia development," J Biomed Opt **10**, 44004 (2005).

[11] G. Michelson and M. Scibor, "Intravascular oxygen saturation in retinal vessels in normal subjects and open-angle glaucoma subjects," Acta Ophthalmol Scand **84**, 289–95 (2006).

[12] I. Halphen, C. Elie, V. Brousse, M. Le Bourgeois, S. Allali, D. Bonnet, and M. de Montalembert, "Severe nocturnal and postexercise hypoxia in children and adolescents with sickle cell disease," PLoS One **9**, e97462 (2014).

[13] S. Minoshima, B. Giordani, S. Berent, K. A. Frey, N. L. Foster, and D. E. Kuhl, "Metabolic reduction in the posterior cingulate cortex in very early Alzheimer's disease," Annals of Neurology **42**, 85–94 (1997).

[14] A. L. Davies, R. A. Desai, P. S. Bloomfield, P. R. McIntosh, K. J. Chapple, C. Linington, R. Fairless, R. Diem, M. Kasti, M. P. Murphy, and K. J. Smith, "Neurological deficits caused by tissue hypoxia in neuroinflammatory disease," Annals of Neurology **74**, 815–825 (2013).

[15] R. O. Green, M. L. Eastwood, C. M. Sarture, T. G. Chrien, M. Aronsson, B. J. Chippendale, J. A. Faust, B. E. Pavri, C. J. Chovit, M. S. Solis, M. R. Olah, and O. Williams, "Imaging spectroscopy and the Airborne Visible Infrared Imaging Spectrometer (AVIRIS)," Remote Sensing of Environment **65**, 227–248 (1998).

[16] C.-C. Yu, C. Lau, G. O'Donoghue, J. Mirkovic, S. McGee, L. Galindo, A. Elackattu, E. Stier, G. Grillone, K. Badizadegan, R. R. Dasari, and M. S. Feld, "Quantitative spectroscopic imaging for non-invasive early cancer detection," Optics Express **16**, 16227–16239 (2008).

[17] S. A, "Multispectral pushbroom array imager," in "Sensor Systems for the 80's Conference," (American Institute of Aeronautics and Astronautics, 1980), Meeting Paper Archive.

[18] M. M. Meyers, I. Ferreira, P. Fomitchov, and R. Filkins, "Multispectral line confocal imaging microscope for fluorescence applications," (International Society for Optics and Photonics, 2011), pp. 79020I–79020I–11.

[19] M. E. Gehm, M. S. Kim, C. Fernandez, and D. J. Brady, "High-throughput, multiplexed pushbroom hyperspectral microscopy," Opt Express **16**, 11032–43 (2008).

[20] A. R. Harvey, J. E. Beale, A. H. Greenaway, T. J. Hanlon, and J. W. Williams, "Technology options for imaging spectrometry," (International Society for Optics and Photonics, 2000), pp. 13–24.

[21] A. D. Meigs, E. W. Butler, B. A. Jones, L. J. O. Iii, R. G. Sellar, and B. Rafert, "Airborne visible hyperspectral imaging spectrometer: optical and system-level description," (International Society for Optics and Photonics, 1996), pp. 278–284.

[22] A. Barducci, D. Guzzi, C. Lastri, P. Marcoionni, V. Nardino, and I. Pippi, "Theoretical aspects of Fourier Transform Spectrometry and common path triangular interferometers," Opt Express **18**, 11622–49 (2010).

[23] L. W. Schumann and T. S. Lomheim, "Infrared hyperspectral imaging Fourier transform and dispersive spectrometers: comparison of signal-to-noise-based performance," (International Society for Optics and Photonics, 2002), pp. 1–14.

[24] A. Harvey and D. Fletcher-Holmes, "Birefringent Fourier-transform imaging spectrometer," Opt Express **12**, 5368–74 (2004).

[25] M. W. Kudenov and E. L. Dereniak, "Compact real-time birefringent imaging spectrometer," Opt Express **20**, 17973–86 (2012).

[26] D. W. Fletcher-Holmes and A. R. Harvey, "Real-time imaging with a hyperspectral fovea," Journal of Optics a-Pure and Applied Optics **7**, S298–S302 (2005).

[27] A. A. Wagadarikar, N. P. Pitsianis, X. Sun, and D. J. Brady, "Video rate spectral imaging using a coded aperture snapshot spectral imager," Optics Express **17**, 6368 (2009).

[28] P. M. W. French, M. J. Dayel, K. Dowling, S. C. W. Hyde, M. J. Lever, P. Vourdas, A. K. L. Dymoke-Bradshaw, and J. D. Hares, "Two-dimensional fluorescence lifetime imaging for in-vitro and in-vivo application," (International Society for Optics and Photonics, 1998), pp. 150–157.

[29] J. Hunicz and D. Piernikarski, "Investigation of combustion in a gasoline engine using spectrophotometric methods," (International Society for Optics and Photonics, 2001), pp. 307–314.

[30] W. R. Johnson, D. W. Wilson, W. Fink, M. Humayun, and G. Bearman, "Snapshot hyperspectral imaging in ophthalmology," J Biomed Opt **12**, 014036 (2007).

[31] T. Okamoto and I. Yamaguchi, "Simultaneous acquisition of spectral image information," Optics Letters **16**, 1277 (1991).

[32] M. R. Descour, C. E. Volin, E. L. Dereniak, T. M. Gleeson, M. F. Hopkins, D. W. Wilson, and P. D. Maker, "Demonstration of a computed-tomography imaging spectrometer using a computer-generated hologram disperser," Appl Opt **36**, 3694–8 (1997).

[33] W. R. Johnson, D. W. Wilson, and G. Bearman, "All-reflective snapshot hyperspectral imager for ultraviolet and infrared applications," Opt Lett **30**, 1464–6 (2005).

[34] A. Wagadarikar, R. John, R. Willett, and D. Brady, "Single disperser design for coded aperture snapshot spectral imaging," Appl Opt **47**, B44–51 (2008).

[35] M. E. Gehm, R. John, D. J. Brady, R. M. Willett, and T. J. Schulz, "Single-shot compressive spectral imaging with a dual-disperser architecture," Opt Express **15**, 14013–27 (2007).

[36] L. Gao, J. Liang, C. Li, and L. V. Wang, "Single-shot compressed ultrafast photography at one hundred billion frames per second," Nature **516**, 74–7 (2014).

[37] R. Shogenji, Y. Kitamura, K. Yamada, S. Miyatake, and J. Tanida, "Multispectral imaging using compact compound optics," Optics Express **12**, 1643–1655 (2004).

[38] J. Downing and A. R. Harvey, "Multi-aperture hyperspectral imaging," in "Imaging and Applied Optics," (Optical Society of America), OSA Technical Digest (online), p. JW2B.2.

[39] L. Gao, R. T. Kester, and T. S. Tkaczyk, "Compact Image Slicing Spectrometer (ISS) for hyperspectral fluorescence microscopy," Opt Express **17**, 12293–308 (2009).

[40] L. Gao, R. T. Kester, N. Hagen, and T. S. Tkaczyk, "Snapshot Image Mapping Spectrometer (IMS) with high sampling density for hyperspectral microscopy," Opt Express **18**, 14330–44 (2010).

[41] D. Ren and J. Allington-Smith, "On the Application of Integral Field Unit Design Theory for Imaging Spectroscopy," Publications of the Astronomical Society of the Pacific **114**, 866–878 (2002).

[42] A. Gorman, D. W. Fletcher-Holmes, and A. R. Harvey, "Generalization of the Lyot filter and its application to snapshot spectral imaging," Opt Express **18**, 5602–8 (2010).

[43] R. H. Yuhas, A. F. H. Goetz, and J. W. Boardman, "Discrimination among semi-arid landscape endmembers using the Spectral Angle Mapper (SAM) algorithm," in "JPL, Summaries of the Third Annual JPL Airborne Geoscience Workshop," , vol. 1 (1992), vol. 1, pp. 147–149.

[44] J. B. Adams, M. O. Smith, and P. E. Johnson, "Spectral Mixture Modeling - a New Analysis of Rock and Soil Types at the Viking Lander-1 Site," Journal of Geophysical Research-Solid Earth and Planets **91**, 8098–8112 (1986).

[45] S. Wold, K. Esbensen, and P. Geladi, "Principal Component Analysis," Chemometrics and Intelligent Laboratory Systems **2**, 37–52 (1987).

[46] A. Hyvarinen and E. Oja, "Independent component analysis: algorithms and applications," Neural Netw **13**, 411–30 (2000).

[47] S. Prahl, "Tabulated Molar Extinction Coefficient for Hemoglobin in Water," Http://omlc.org/spectra/hemoglobin/summary.html.

[48] J. B. Hickam and R. Frayser, "Spectrophotometric determination of blood oxygen," Journal of Biological Chemistry **180**, 457–465 (1949).

[49] K. Kramer, J. O. Elam, G. A. Saxton, and J. Elam, W. N., "Influence of oxygen saturation, erythrocyte concentration and optical depth upon the red and near-infrared light transmittance of whole blood," Am J Physiol **165**, 229–46 (1951).

[50] N. M. Anderson and P. Sekelj, "Light-absorbing and scattering properties of nonhaemolysed blood," Phys Med Biol **12**, 173–84 (1967).

[51] N. M. Anderson and P. Sekelj, "Reflection and transmission of light by thin films of nonhaemolysed blood," Phys Med Biol **12**, 185–92 (1967).

[52] V. Twersky, "Multiple scattering of waves and optical phenomena," J Opt Soc Am **52**, 145–71 (1962).

[53] V. Twersky, "Absorption and multiple scattering by biological suspensions," J Opt Soc Am **60**, 1084–93 (1970).

[54] R. N. Pittman and B. R. Duling, "A new method for the measurement of percent oxyhemoglobin," J Appl Physiol **38**, 315–20 (1975).

[55] R. N. Pittman and B. R. Duling, "Measurement of percent oxyhemoglobin in the microvasculature," J Appl Physiol **38**, 321–7 (1975).

[56] J. B. Hickam, R. Frayser, and J. C. Ross, "A study of retinal venous blood oxygen saturation in human subjects by photographic means," Circulation **27**, 375–85 (1963).

[57] J. M. Beach, K. J. Schwenzer, S. Srinivas, D. Kim, and J. S. Tiedeman, "Oximetry of retinal vessels by dual-wavelength imaging: calibration and influence of pigmentation," J Appl Physiol (1985) **86**, 748–58 (1999).

[58] M. Hammer, W. Vilser, T. Riemer, and D. Schweitzer, "Retinal vessel oximetry-calibration, compensation for vessel diameter and fundus pigmentation, and reproducibility," J Biomed Opt **13**, 054015 (2008).

[59] S. H. Hardarson, A. Harris, R. A. Karlsson, G. H. Halldorsson, L. Kagemann, E. Rechtman, G. M. Zoega, T. Eysteinsson, J. A. Benediktsson, A. Thorsteinsson, P. K. Jensen, J. Beach, and E. Stefansson, "Automatic retinal oximetry," Invest Ophthalmol Vis Sci **47**, 5011–6 (2006).

[60] D. Schweitzer, M. Hammer, J. Kraft, E. Thamm, E. Konigsdorffer, and J. Strobel, "In vivo measurement of the oxygen saturation of retinal vessels in healthy volunteers," IEEE Trans Biomed Eng **46**, 1454–65 (1999).

[61] J. de Kock, L. Tarassenko, C. Glynn, and A. Hill, "Reflectance pulse oximetry measurements from the retinal fundus," IEEE Transactions on Biomedical Engineering **40**, 817–823 (1993).

[62] F. C. Delori, "Noninvasive technique for oximetry of blood in retinal vessels," Appl Opt **27**, 1113–25 (1988).

[63] T. R. Choudhary, D. Ball, J. Fernandez Ramos, A. I. McNaught, and A. R. Harvey, "Assessment of acute mild hypoxia on retinal oxygen saturation using snapshot retinal oximetry," Invest Ophthalmol Vis Sci **54**, 7538–43 (2013).

[64] E. Stefansson, S. H. Hardarson, and O. B. Olafsdottir, "Retinal Oxygenation in Patients with Diabetic Retinopathy," European Journal of Ophthalmology **20**, 635–636 (2010).

[65] T. Bek, "Retinal oximetry in diabetic retinopathy," Acta Ophthalmologica **92**, 0–0 (2014).

[66] O. B. Olafsdottir, S. H. Hardarson, M. S. Gottfredsdottir, A. Harris, and E. Stefansson, "Oxygen metabolism in glaucoma," Acta Ophthalmologica **88**, 43–43 (2010).

[67] A. Mcnaught, "Retinal oximetry in glaucoma," Acta Ophthalmologica **92**, 0–0 (2014).

[68] T. Eysteinsson, S. H. Hardarson, D. Bragason, and E. Stefánsson, "Retinal vessel oxygen saturation and vessel diameter in retinitis pigmentosa," Acta Ophthalmologica **92**, 449–453 (2014).

[69] A. B. Einarsdottir, S. H. Hardarson, J. V. Kristjansdottir, D. T. Bragason, J. Snaedal, and E. Stefánsson, "Retinal Oximetry Imaging in Alzheimer's Disease," Journal of Alzheimer's Disease **49**, 79–83 (2015).

[70] M. H. Smith, "Optimum wavelength combinations for retinal vessel oximetry," Appl Opt **38**, 258–67 (1999).

[71] M. Hammer, S. Leistritz, L. Leistritz, and D. Schweitzer, "Light paths in retinal vessel oxymetry," IEEE Trans Biomed Eng **48**, 592–8 (2001).

[72] W. Liu, S. Jiao, and H. F. Zhang, "Accuracy of retinal oximetry: a Monte Carlo investigation," J Biomed Opt **18**, 066003 (2013).

[73] A. J. Cohen and R. A. Laing, "Multiple scattering analysis of retinal blood oximetry," IEEE Trans Biomed Eng **23**, 391–400 (1976).

[74] G. S. Brindley and E. N. Willmer, "The reflexion of light from the macular and peripheral fundus oculi in man," The Journal of Physiology **116**, 350–356 (1952).

[75] I. J. Hodgkinson, P. B. Greer, and A. C. Molteno, "Point-spread function for light scattered in the human ocular fundus," J Opt Soc Am A Opt Image Sci Vis **11**, 479–86 (1994).

[76] D. L. Drabkin and R. B. Singer, "Spectrophotometric studies VI. A Study of the absorption spectra of non-hemolyzed erythrocytes and of scattering of light by suspension of particles, with a note upon the spectrophotometric determination of the pH within the erythrocyte," Journal of Biological Chemistry **129**, 739–757 (1939).

[77] O. W. v. Assendelft, *Spectrophotometry of Haemoglobin Derivatives* (C. C. Thomas, 1970). Google-Books-ID: 6H_0cQAACAAJ.

[78] D. Schweitzer, L. Leistritz, M. Hammer, M. Scibor, U. Bartsch, and J. Strobel, "Calibration-free measurement of the oxygen saturation in human retinal vessels," (International Society for Optics and Photonics, 1995), pp. 210–218.

[79] M. H. Smith, K. R. Denninghoff, A. Lompado, and L. W. Hillman, "Effect of multiple light paths on retinal vessel oximetry," Appl Opt **39**, 1183–93 (2000).

[80] D. J. Mordant, I. Al-Abboud, G. Muyo, A. Gorman, A. Sallam, P. Ritchie, A. R. Harvey, and A. I. McNaught, "Spectral imaging of the retina," Eye (Lond) **25**, 309–20 (2011).

[81] K. R. Denninghoff, R. A. Chipman, and L. W. Hillman, "Oxyhemoglobin saturation measurements by green spectral shift," Opt Lett **31**, 924–6 (2006).

[82] K. R. Denninghoff, K. B. Sieluzycka, J. K. Hendryx, T. J. Ririe, L. Deluca, and R. A. Chipman, "Retinal oximeter for the blue-green oximetry technique," J Biomed Opt **16**, 107004 (2011).

[83] K. R. Denninghoff, R. A. Chipman, and L. W. Hillman, "Blood oxyhemoglobin saturation measurements by blue-green spectral shift," J Biomed Opt **12**, 034020 (2007).

[84] I. P. Torres Filho, J. Terner, R. N. Pittman, E. Proffitt, and K. R. Ward, "Measurement of hemoglobin oxygen saturation using Raman microspectroscopy and 532-nm excitation," J Appl Physiol (1985) **104**, 1809–17 (2008).

[85] H. A. Rinia, M. Bonn, E. M. Vartiainen, C. B. Schaffer, and M. Muller, "Spectroscopic analysis of the oxygenation state of hemoglobin using coherent anti-Stokes Raman scattering," J Biomed Opt **11**, 050502 (2006).

[86] K. Ramser, E. J. Bjerneld, C. Fant, and M. Kall, "Importance of substrate and photo-induced effects in Raman spectroscopy of single functional erythrocytes," J Biomed Opt **8**, 173–8 (2003).

[87] J. Yi and X. Li, "Estimation of oxygen saturation from erythrocytes by high-resolution spectroscopic optical coherence tomography," Optics Letters **35**, 2094 (2010).

[88] J. Yi, Q. Wei, W. Liu, V. Backman, and H. F. Zhang, "Visible-light optical coherence tomography for retinal oximetry," Opt Lett **38**, 1796–8 (2013).

[89] T. Christen, D. S. Bolar, and G. Zaharchuk, "Imaging brain oxygenation with MRI using blood oxygenation approaches: methods, validation, and clinical applications," AJNR Am J Neuroradiol **34**, 1113–23 (2013).

[90] T. Christen, P. Bouzat, N. Pannetier, N. Coquery, A. Moisan, B. Lemasson, S. Thomas, E. Grillon, O. Detante, C. Rémy, J.-F. Payen, and E. L. Barbier, "Tissue oxygen saturation mapping with magnetic resonance imaging," Journal of Cerebral Blood Flow & Metabolism **34**, 1550–1557 (2014).

[91] L. Wang, K. Maslov, and L. V. Wang, "Single-cell label-free photoacoustic flowoxigraphy in vivo," Proc Natl Acad Sci U S A **110**, 5759–64 (2013).

[92] L. Li, C. Yeh, S. Hu, L. Wang, B. T. Soetikno, R. Chen, Q. Zhou, K. K. Shung, K. I. Maslov, and L. V. Wang, "Fully motorized optical-resolution photoacoustic microscopy," Optics Letters **39**, 2117–2120 (2014).

[93] S. Hu and L. V. Wang, "Photoacoustic imaging and characterization of the microvasculature," Journal of Biomedical Optics **15**, 011101–011101–15 (2010).

[94] L. Ji Youn, M. L. Clarke, F. Tokumasu, J. F. Lesoine, D. W. Allen, R. Chang, M. Litorja, and H. Jeeseong, "Absorption-Based Hyperspectral Imaging and Analysis of Single Erythrocytes," Selected Topics in Quantum Electronics, IEEE Journal of **18**, 1130–1139 (2012).

[95] C. G. Ellis, M. L. Ellsworth, and R. N. Pittman, "Determination of red blood cell oxygenation in vivo by dual video densitometric image analysis," Am J Physiol **258**, H1216–23 (1990).

[96] G. D. Caprio, C. Stokes, J. M. Higgins, and E. Schonbrun, "Single-cell measurement of red blood cell oxygen affinity," Proceedings of the National Academy of Sciences **112**, 9984–9989 (2015).

[97] G. Wong, R. Pilkington, and A. R. Harvey, "Achromatization of Wollaston polarizing beam splitters," Optics Letters **36**, 1332–1334 (2011).

[98] K. B. Saebvarnothing and A. Bjvarnothingrnerud, "Accurate de-oxygenation of ex vivo whole blood using sodium Dithionite," in "Proc. Intl. Soc. Mag. Reson. Med.", , vol. 8 (2000), vol. 8.

[99] J. T. Coin and J. S. Olson, "The rate of oxygen uptake by human red blood cells," J Biol Chem **254**, 1178–90 (1979).

[100] K. D. Vandegriff and J. S. Olson, "Morphological and physiological factors affecting oxygen uptake and release by red blood cells," J Biol Chem **259**, 12619–27 (1984).

[101] J. Peetermans, I. Nishio, S. T. Ohnishi, and T. Tanaka, "Light-scattering study of depolymerization kinetics of sickle hemoglobin polymers inside single erythrocytes." Proceedings of the National Academy of Sciences of the United States of America **83**, 352–356 (1986).

[102] L. M. Coronado, C. T. Nadovich, and C. Spadafora, "Malarial hemozoin: From target to tool," Biochimica et Biophysica Acta (BBA) - General Subjects **1840**, 2032–2041 (2014).

[103] L. G. Mesquita, U. Agero, and O. N. Mesquita, "Defocusing microscopy: An approach for red blood cell optics," Applied Physics Letters **88**, 133901–3 (2006).

[104] P. Bedggood and A. Metha, "Direct visualization and characterization of erythrocyte flow in human retinal capillaries," Biomedical Optics Express **3**, 3264–3277 (2012).

[105] D. G. Lowe, "Distinctive Image Features from Scale-Invariant Keypoints," International Journal of Computer Vision **60**, 91–110 (2004).

[106] T. Clerbaux, P. Gustin, B. Detry, M. L. Cao, and A. Frans, "Comparative study of the oxyhaemoglobin dissociation curve of four mammals: man, dog, horse and cattle," Comp Biochem Physiol Comp Physiol **106**, 687–94 (1993).

[107] K. Kim, H. Yoon, M. Diez-Silva, M. Dao, R. R. Dasari, and Y. Park, "High-resolution three-dimensional imaging of red blood cells parasitized by Plasmodium falciparum and in situ hemozoin crystals using optical diffraction tomography," J Biomed Opt **19**, 011005 (2014).

[108] E. Schonbrun, R. Malka, G. Di Caprio, D. Schaak, and J. M. Higgins, "Quantitative absorption cytometry for measuring red blood cell hemoglobin mass and volume," Cytometry A **85**, 332–8 (2014).

[109] U. Agero, C. H. Monken, C. Ropert, R. T. Gazzinelli, and O. N. Mesquita, "Cell surface fluctuations studied with defocusing microscopy," Phys Rev E Stat Nonlin Soft Matter Phys **67**, 051904 (2003).

[110] U. Agero, L. G. Mesquita, B. R. Neves, R. T. Gazzinelli, and O. N. Mesquita, "Defocusing microscopy," Microsc Res Tech **65**, 159–65 (2004).

[111] M. Friebel, J. Helfmann, U. Netz, and M. Meinke, "Influence of oxygen saturation on the optical scattering properties of human red blood cells in the spectral range 250 to 2,000 nm," J Biomed Opt **14**, 034001 (2009).

[112] L. Miccio, P. Memmolo, F. Merola, P. A. Netti, and P. Ferraro, "Red blood cell as an adaptive optofluidic microlens," Nature Communications **6**, 6502 (2015).

[113] O. Zhernovaya, O. Sydoruk, V. Tuchin, and A. Douplik, "The refractive index of human hemoglobin in the visible range," Phys Med Biol **56**, 4013–21 (2011).

[114] J. Fernandez Ramos, L. R. Brewer, A. Gorman, and A. R. Harvey, "Video-Rate Multispectral Imaging: Application to Microscopy and Macroscopy," in "Classical Optics 2014 (2014), paper CW1C.3," (Optical Society of America, 2014), p. CW1C.3.

[115] P. T. Goedhart, M. Khalilzada, R. Bezemer, J. Merza, and C. Ince, "Sidestream Dark Field (SDF) imaging: a novel stroboscopic LED ring-based imaging modality for clinical assessment of the microcirculation," Optics Express **15**, 15101 (2007).

[116] J. M. Beach, J. S. Tiedeman, M. F. Hopkins, and Y. S. Sabharwal, "Multispectral fundus imaging for early detection of diabetic retinopathy," (International Society for Optics and Photonics, 1999), pp. 114–121.

[117] M. Hammer, T. Riemer, W. Vilser, S. Gehlert, and D. Schweitzer, "A new imaging technique for retinal vessel oximetry: principles and first clinical results in patients with retinal arterial occlusion and diabetic retinopathy," (International Society for Optics and Photonics, 2009), pp. 71630P–12.

[118] S. H. Hardarson and E. Stefánsson, "Retinal oxygen saturation is altered in diabetic retinopathy," British Journal of Ophthalmology pp. bjophthalmol–2011–300640 (2011).

[119] R. E. Man, M. B. Sasongko, J. Xie, R. Kawasaki, W. J. Best, J. E. Noonan, C. D. Luu, J. J. Wang, and E. L. Lamoureux, "Associations of retinal oximetry in persons with diabetes," Clinical & Experimental Ophthalmology **43**, 124–131 (2015).

[120] S. H. Hardarson, M. S. Gottfredsdottir, G. H. Halldorsson, R. A. Karlsson, J. A. Benediktsson, T. Eysteinsson, J. M. Beach, A. Harris, and E. Stefansson, "Glaucoma

filtration surgery and retinal oxygen saturation," Invest Ophthalmol Vis Sci **50**, 5247–50 (2009).

[121] W. B. Vehmeijer, V. Magnusdottir, T. S. Eliasdottir, S. H. Hardarson, N. E. Schalij-Delfos, and E. Stefánsson, "Retinal Oximetry with Scanning Laser Ophthalmoscope in Infants," PLoS ONE **11**, e0148077 (2016).

[122] B. S. Sorg, M. E. Hardee, N. Agarwal, B. J. Moeller, and M. W. Dewhirst, "Spectral imaging facilitates visualization and measurements of unstable and abnormal microvascular oxygen transport in tumors," J Biomed Opt **13**, 014026 (2008).

[123] M. J. Fischer, S. Uchida, and K. Messlinger, "Measurement of meningeal blood vessel diameter in vivo with a plug-in for ImageJ," Microvasc Res **80**, 258–66 (2010).

[124] B. Bengtsson and C. E. Krakau, "Correction of optic disc measurements on fundus photographs," Graefes Arch Clin Exp Ophthalmol **230**, 24–8 (1992).

[125] T. D. Williams, "Determination of the True Size of an Object on the Fundus of the Living Eye," Optometry and Vision Science **69**, 717–720 (1992).

[126] A. N. Bashkatov, E. A. Genina, V. I. Kochubey, and V. V. Tuchin, "Optical properties of human sclera in spectral range 370–2500 nm," Optics and Spectroscopy **109**, 197–204 (2010).

[127] V. Manjunath, M. Taha, J. G. Fujimoto, and J. S. Duker, "Choroidal Thickness in Normal Eyes Measured Using Cirrus-HD Optical Coherence Tomography," American journal of ophthalmology **150**, 325–329.e1 (2010).

[128] J. J. Weiter, F. C. Delori, G. L. Wing, and K. A. Fitch, "Retinal pigment epithelial lipofuscin and melanin and choroidal melanin in human eyes," Invest Ophthalmol Vis Sci **27**, 145–52 (1986).

[129] J. V. Kristjansdottir, S. H. Hardarson, G. H. Halldorsson, R. A. Karlsson, T. S. Eliasdottir, and E. Stefansson, "Retinal oximetry with a scanning laser ophthalmoscope," Invest Ophthalmol Vis Sci **55**, 3120–6 (2014).

[130] P. I. Rodmell, J. A. Crowe, A. Gorman, A. R. Harvey, G. Muyo, D. J. Mordant, A. I. McNaught, and S. P. Morgan, "Light path-length distributions within the retina," J Biomed Opt **19**, 36008 (2014).

[131] V. V. Tuchin, "Light scattering study of tissues," Physics-Uspekhi **40**, 495–515 (1997).

[132] N. Bosschaart, G. J. Edelman, M. C. Aalders, T. G. van Leeuwen, and D. J. Faber, "A literature review and novel theoretical approach on the optical properties of whole blood," Lasers Med Sci **29**, 453–79 (2014).

[133] J. M. Steinke and A. P. Shepherd, "Comparison of Mie theory and the light scattering of red blood cells," Appl Opt **27**, 4027–33 (1988).

[134] V. V. Tuchin, *Handbook of Optical Biomedical Diagnostics* (Society of Photo Optical, 2002).

[135] H. S. Ginis, G. M. Perez, J. M. Bueno, A. Pennos, and P. Artal, "Wavelength dependence of the ocular straylight," Invest Ophthalmol Vis Sci **54**, 3702–8 (2013).

[136] J. E. Coppens, L. Franssen, and T. J. van den Berg, "Wavelength dependence of intraocular straylight," Exp Eye Res **82**, 688–92 (2006).

[137] R. M. Boynton and F. J. Clarke, "Sources of Entoptic Scatter in the Human Eye," J Opt Soc Am **54**, 110–9 (1964).

[138] E. Peli and T. Peli, "Restoration of retinal images obtained through cataracts," IEEE Trans Med Imaging **8**, 401–6 (1989).

[139] J. Yang, B. Zhang, and Y. Shi, "Scattering removal for finger-vein image restoration," Sensors (Basel) **12**, 3627–40 (2012).

[140] Y. Ouyang, Q. Shao, D. Scharf, A. M. Joussen, and F. M. Heussen, "Retinal vessel diameter measurements by spectral domain optical coherence tomography," Graefe's Archive for Clinical and Experimental Ophthalmology **253**, 499–509 (2014).

[141] R. Blondal, M. K. Sturludottir, S. H. Hardarson, G. H. Halldorsson, and E. Stefansson, "Reliability of vessel diameter measurements with a retinal oximeter," Graefes Arch Clin Exp Ophthalmol **249**, 1311–7 (2011).

[142] Izatt JA, Hee MR, Swanson EA, and et al, "MIcrometer-scale resolution imaging of the anterior eye in vivo with optical coherence tomography," Archives of Ophthalmology **112**, 1584–1589 (1994).

[143] L.-G. Lindberg and P. A. Oberg, "Optical properties of blood in motion," Optical Engineering **32**, 253–257 (1993).

[144] P. Gaehtgens, "Distribution of flow and red cell flux in the microcirculation," Scandinavian Journal of Clinical and Laboratory Investigation. Supplementum **156**, 83–87 (1981).

[145] P. Ganesan, S. He, and H. Xu, "Analysis of retinal circulation using an image-based network model of retinal vasculature," Microvascular Research **80**, 99–109 (2010).

[146] J. P. Paul, R. A. O'Connell, S. L. Hosking, A. J. Anderson, and B. V. Bui, "Retinal oxygen saturation: novel analysis method for the oxymap," Optom Vis Sci **90**, 1104–10 (2013).

[147] A. M. Shahidi, S. R. Patel, J. G. Flanagan, and C. Hudson, "Regional variation in human retinal vessel oxygen saturation," Exp Eye Res **113**, 143–7 (2013).

[148] R. Michael and A. J. Bron, "The ageing lens and cataract: a model of normal and pathological ageing," Philosophical Transactions of the Royal Society B: Biological Sciences **366**, 1278–1292 (2011).

[149] M. Friebel, J. Helfmann, and M. C. Meinke, "Influence of osmolarity on the optical properties of human erythrocytes," J Biomed Opt **15**, 055005 (2010).

[150] K. R. Denninghoff and M. H. Smith, "Optical model of the blood in large retinal vessels," J Biomed Opt **5**, 371–4 (2000).

[151] J. B. Hickam and R. Frayser, "Studies of the retinal circulation in man. Observations on vessel diameter, arteriovenous oxygen difference, and mean circulation time," Circulation **33**, 302–16 (1966).

[152] D. Y. Kim, J. Fingler, J. S. Werner, D. M. Schwartz, S. E. Fraser, and R. J. Zawadzki, "In vivo volumetric imaging of human retinal circulation with phase-variance optical coherence tomography," Biomed Opt Express **2**, 1504–13 (2011).

[153] Y. Ouyang, Q. Shao, D. Scharf, A. M. Joussen, and F. M. Heussen, "An easy method to differentiate retinal arteries from veins by spectral domain optical coherence tomography: retrospective, observational case series," BMC Ophthalmology **14**, 1–9 (2014).

[154] M. A. v. d. Putten, L. E. MacKenzie, A. L. Davies, J. Fernandez-Ramos, R. A. Desai, K. J. Smith, and A. R. Harvey, "A multispectral microscope for in vivo oximetry of rat dorsal spinal cord vasculature," Physiological Measurement **38**, 205 (2017).

[155] P. Bedggood and A. Metha, "Direct visualization and characterization of erythrocyte flow in human retinal capillaries," Biomed Opt Express **3**, 3264–77 (2012).

[156] D. Bragason, "Intravascular saturation gradients: Model and meaurements," (2014). Birmingham Oximetry Workshop 2014, https://astonreplay.cloud.panopto.eu/Panopto/Pages/Viewer.aspx?id=c8422fb3-6d7a-489a-816e-f1b42f4b7b89.

[157] D. E. MCMILLAN, "Chapter 4 - Hemorheology: Principles and concepts," in "Levin and O'Neal's The Diabetic Foot (Seventh Edition)," (Mosby, Philadelphia, 2008), pp. 75–88.

[158] C. D. Murray, "The Physiological Principle of Minimum Work I. The Vascular System and the Cost of Blood Volume," Proceedings of the National Academy of Sciences of the United States of America **12**, 207–214 (1926).

[159] T. F. Sherman, "On connecting large vessels to small. The meaning of Murray's law," J Gen Physiol **78**, 431–53 (1981).

[160] P. R. Preussner, G. Richard, O. Darrelmann, J. Weber, and I. Kreissig, "Quantitative measurement of retinal blood flow in human beings by application of digital image-processing methods to television fluorescein angiograms," Graefe's Archive for Clinical and Experimental Ophthalmology = Albrecht Von Graefes Archiv Für Klinische Und Experimentelle Ophthalmologie **221**, 110–112 (1983).

[161] D. Hershey and T. Karhan, "Diffusion Coefficients for Oxygen Transport in Whole Blood," Aiche Journal **14**, 969–& (1968).

[162] H. C. Berg, *Random Walks in Biology* (Princeton University Press, Princeton, N.J, 1993).

[163] G. Garhofer, R. Werkmeister, N. Dragostinoff, and L. Schmetterer, "Retinal blood flow in healthy young subjects," Invest Ophthalmol Vis Sci **53**, 698–703 (2012).

[164] G. Mehta, K. Mehta, D. Sud, J. W. Song, T. Bersano-Begey, N. Futai, Y. S. Heo, M. A. Mycek, J. J. Linderman, and S. Takayama, "Quantitative measurement and control of oxygen levels in microfluidic poly(dimethylsiloxane) bioreactors during cell culture," Biomed Microdevices **9**, 123–34 (2007).

[165] D. K. Wood, A. Soriano, L. Mahadevan, J. M. Higgins, and S. N. Bhatia, "A biophysical indicator of vaso-occlusive risk in sickle cell disease," Sci Transl Med **4**, 123ra26 (2012).

[166] T. C. Merkel, V. I. Bondar, K. Nagai, B. D. Freeman, and I. Pinnau, "Gas sorption, diffusion, and permeation in poly(dimethylsiloxane)," Journal of Polymer Science Part B-Polymer Physics **38**, 415–434 (2000).

[167] R. Lima, S. Wada, S. Tanaka, M. Takeda, T. Ishikawa, K. Tsubota, Y. Imai, and T. Yamaguchi, "In vitro blood flow in a rectangular PDMS microchannel: experimental observations using a confocal micro-PIV system," Biomed Microdevices **10**, 153–67 (2008).

[168] K. Ren, W. Dai, J. Zhou, J. Su, and H. Wu, "Whole-Teflon microfluidic chips," Proceedings of the National Academy of Sciences **108**, 8162–8166 (2011).

[169] R. A. Pasternak, M. V. Christensen, and J. Heller, "Diffusion and Permeation of Oxygen, Nitrogen, Carbon Dioxide, and Nitrogen Dioxide through Polytetrafluoroethylene," Macromolecules **3**, 366–371 (1970).

[170] L. Bao, J. R. Dorgan, D. Knauss, S. Hait, N. S. Oliveira, and I. M. Maruccho, "Gas permeation properties of poly(lactic acid) revisited," Journal of Membrane Science **285**, 166–172 (2006).

Appendix A

Oximetry Results

A.1 Subject 1

Two-wavelengths oximetry calibration $OS = 112.13 - 80.82 * ODR$.

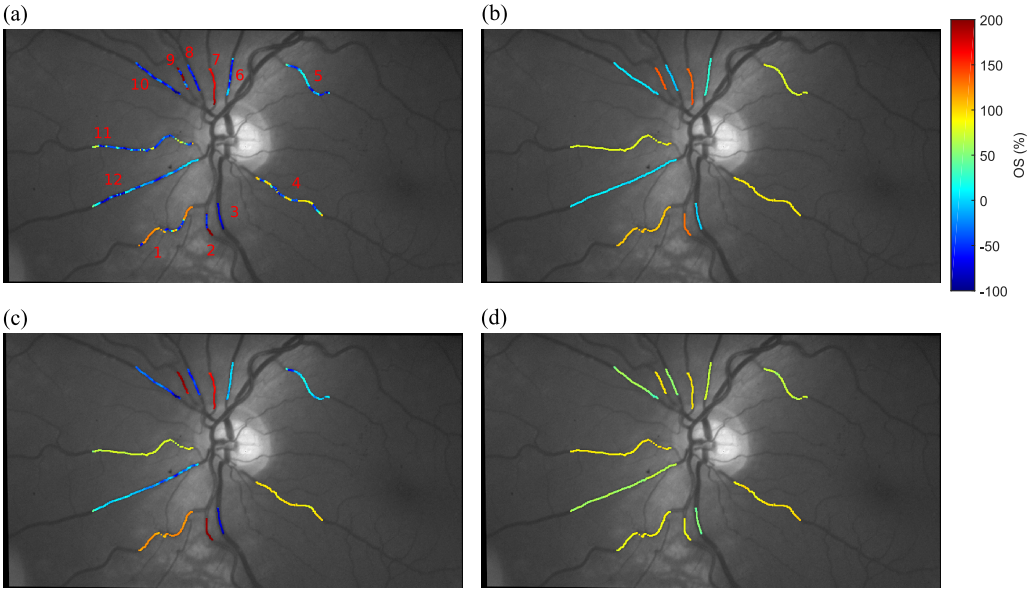

Figure A.1: Subject 1 *OS* maps from different models at the first normoxia: (a) Model 1 (Eq. 4.20). (b) Model 2 (Eq. 4.21). (c) Model 3 (Eq. 4.22). (d) Two-wavelengths oximetry (Eq. 1.8).

Arteries(A)/Veins(V)		Normoxia	Hypoxia	Normoxia	Hypoxia	Normoxia
Pulse Oximeter		95%	85%	96%	83%	97%
Model 1	A	$114 \pm 2\%$	$93 \pm 1\%$	$111 \pm 2\%$	$100 \pm 1\%$	$108 \pm 2\%$
	V	$18 \pm 3\%$	$24 \pm 3\%$	$15 \pm 2\%$	$21 \pm 3\%$	$21 \pm 3\%$
Model 2	A	$62 \pm 77\%$	$65 \pm 65\%$	$67 \pm 83\%$	$84 \pm 60\%$	$46 \pm 80\%$
	V	$-48 \pm 23\%$	$-36 \pm 32\%$	$-38 \pm 30\%$	$-30 \pm 30\%$	$-30 \pm 30\%$
Model 3	A	$141 \pm 5\%$	$122 \pm 5\%$	$130 \pm 3\%$	$125 \pm 5\%$	$128 \pm 4\%$
	V	$-32 \pm 15\%$	$-10 \pm 10\%$	$-7 \pm 7\%$	$-6 \pm 9\%$	$-4 \pm 7\%$
Two-wavelengths oximetry	A	$91 \pm 3\%$	$88 \pm 3\%$	$93 \pm 3\%$	$89 \pm 3\%$	$93 \pm 5\%$
	V	$61 \pm 5\%$	$65 \pm 4\%$	$65 \pm 4\%$	$67 \pm 5\%$	$68 \pm 4\%$

Table A.1: Subject 1 mean *OS* and mean standard deviation.

A.2 Subject 2

Two-wavelengths oximetry calibration $OS = 99.01 - 69.46 * ODR$.

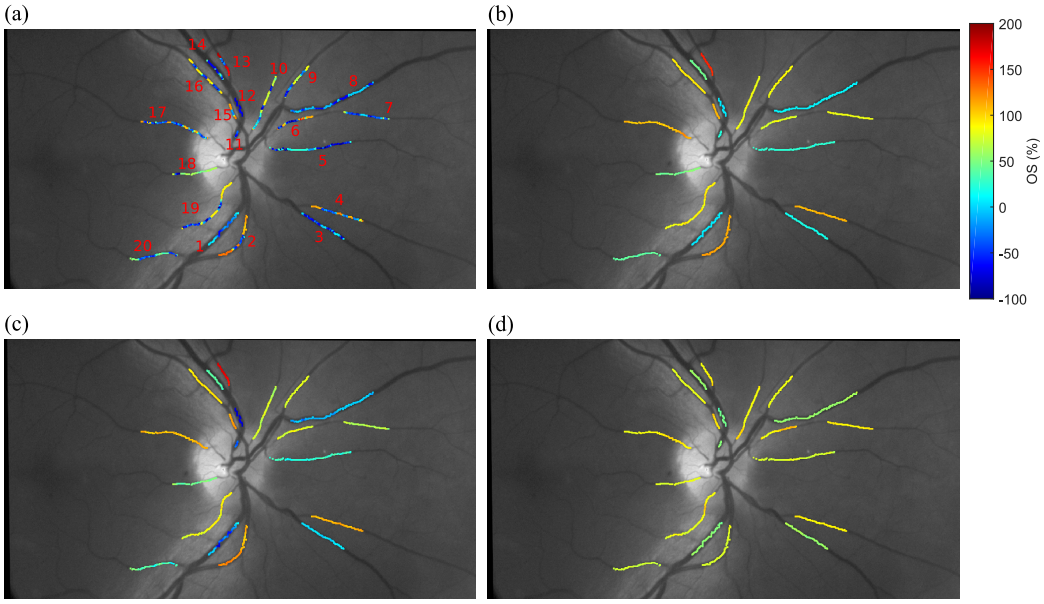

Figure A.2: Subject 2 *OS* maps from different models at the first normoxia: (a) Model 1 (Eq. 4.20). (b) Model 2 (Eq. 4.21). (c) Model 3 (Eq. 4.22). (d) Two-wavelengths oximetry (Eq. 1.8).

Arteries(A)/Veins(V)		Normoxia	Hypoxia	Normoxia	Hypoxia	Normoxia
Pulse Oximeter		99%	87%	98%	86%	99%
Model 1	A	$97 \pm 3\%$	$79 \pm 3\%$	$93 \pm 2\%$	$89 \pm 3\%$	$91 \pm 3\%$
	V	$22 \pm 2\%$	$22 \pm 2\%$	$27 \pm 3\%$	$34 \pm 2\%$	$10 \pm 2\%$
Model 2	A	$35 \pm 68\%$	$18 \pm 62\%$	$29 \pm 64\%$	$21 \pm 65\%$	$21 \pm 66\%$
	V	$-36 \pm 30\%$	$-25 \pm 39\%$	$-23 \pm 32\%$	$-23 \pm 36\%$	$-42 \pm 28\%$
Model 3	A	$95 \pm 5\%$	$82 \pm 6\%$	$94 \pm 6\%$	$90 \pm 6\%$	$93 \pm 5\%$
	V	$-6 \pm 9\%$	$11 \pm 11\%$	$3 \pm 10\%$	$7 \pm 8\%$	$-12 \pm 8\%$
Two-wavelengths oximetry	A	$88 \pm 4\%$	$85 \pm 5\%$	$88 \pm 4\%$	$85 \pm 4\%$	$88 \pm 5\%$
	V	$59 \pm 3\%$	$61 \pm 3\%$	$62 \pm 3\%$	$61 \pm 3\%$	$62 \pm 3\%$

Table A.2: Subject 2 mean *OS* and mean standard deviation.

A.3 Subject 3

Two-wavelengths oximetry calibration $OS = 122.36 - 91.12 * ODR$.

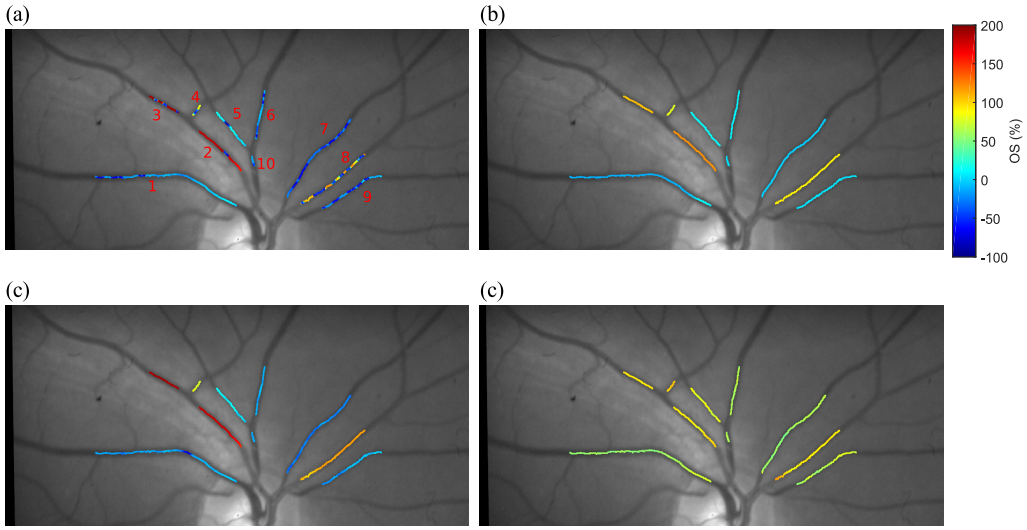

Figure A.3: Subject 3 *OS* maps from different models at the first normoxia: (a) Model 1 (Eq. 4.20). (b) Model 2 (Eq. 4.21). (c) Model 3 (Eq. 4.22). (d) Two-wavelengths oximetry (Eq. 1.8).

Arteries(A)/Veins(V)		Normoxia	Hypoxia	Normoxia	Hypoxia	Normoxia
Pulse Oximeter		98%	83%	98%	83%	98%
Model 1	A	$100 \pm 1\%$	$85 \pm 1\%$	$107 \pm 1\%$	$82 \pm 2\%$	$115 \pm 2\%$
	V	$3 \pm 2\%$	$4 \pm 3\%$	$2 \pm 3\%$	$5 \pm 3\%$	$24 \pm 3\%$
Model 2	A	$79 \pm 81\%$	$64 \pm 68\%$	$58 \pm 85\%$	$27 \pm 71\%$	$23 \pm 77\%$
	V	$-26 \pm 23\%$	$-25 \pm 29\%$	$-26 \pm 27\%$	$-22 \pm 27\%$	$-44 \pm 40\%$
Model 3	A	$139 \pm 4\%$	$128 \pm 11\%$	$136 \pm 4\%$	$98 \pm 4\%$	$146 \pm 8\%$
	V	$-12 \pm 6\%$	$-8 \pm 10\%$	$-6 \pm 10\%$	$0 \pm 6\%$	$16 \pm 15\%$
Two-wavelengths oximetry	A	$96 \pm 4\%$	$90 \pm 3\%$	$99 \pm 5\%$	$92 \pm 2\%$	$99 \pm 7\%$
	V	$67 \pm 5\%$	$67 \pm 5\%$	$72 \pm 5\%$	$71 \pm 5\%$	$71 \pm 5\%$

Table A.3: Subject 3 mean *OS* and mean standard deviation.

A.4 Subject 4

Two-wavelengths oximetry calibration $OS = 101.79 - 77.53 * ODR$.

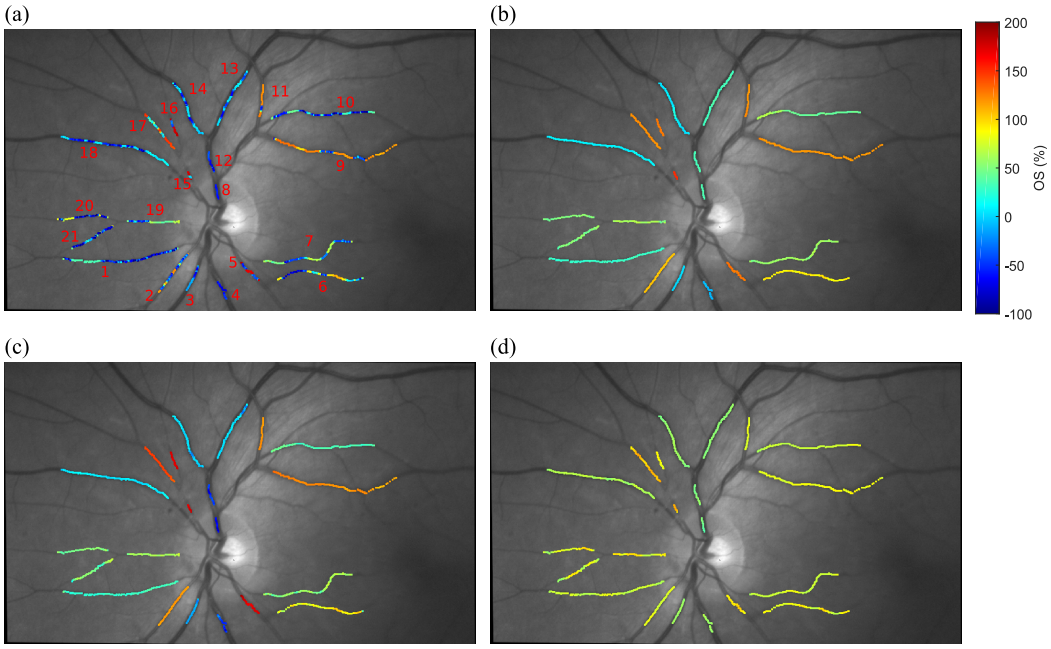

Figure A.4: Subject 4 *OS* maps from different models at the first normoxia: (a) Model 1 (Eq. 4.20). (b) Model 2 (Eq. 4.21). (c) Model 3 (Eq. 4.22). (d) Two-wavelengths oximetry (Eq. 1.8).

Arteries(A)/Veins(V)		Normoxia	Hypoxia	Normoxia	Hypoxia	Normoxia
Pulse Oximeter		98%	83%	98%	85%	97%
Model 1	A	$103 \pm 3\%$	$98 \pm 2\%$	$114 \pm 3\%$	$110 \pm 3\%$	$112 \pm 3\%$
	V	$25 \pm 3\%$	$27 \pm 3\%$	$32 \pm 2\%$	$46 \pm 3\%$	$50 \pm 2\%$
Model 2	A	$43 \pm 74\%$	$45 \pm 73\%$	$52 \pm 73\%$	$33 \pm 76\%$	$26 \pm 84\%$
	V	$-33 \pm 30\%$	$-33 \pm 28\%$	$-31 \pm 36\%$	$-17 \pm 42\%$	$-9 \pm 40\%$
Model 3	A	$116 \pm 6\%$	$109 \pm 15\%$	$122 \pm 10\%$	$127 \pm 8\%$	$119 \pm 7\%$
	V	$-6 \pm 8\%$	$-13 \pm 9\%$	$-10 \pm 11\%$	$16 \pm 12\%$	$-20 \pm 8\%$
Two-wavelengths oximetry	A	$88 \pm 7\%$	$80 \pm 7\%$	$87 \pm 10\%$	$83 \pm 10\%$	$87 \pm 7\%$
	V	$61 \pm 4\%$	$59 \pm 4\%$	$60 \pm 4\%$	$59 \pm 4\%$	$59 \pm 5\%$

Table A.4: Subject 4 mean *OS* and mean standard deviation.

A.5 Subject 5

Two-wavelengths oximetry calibration $OS = 105.42 - 90.1 * ODR$.

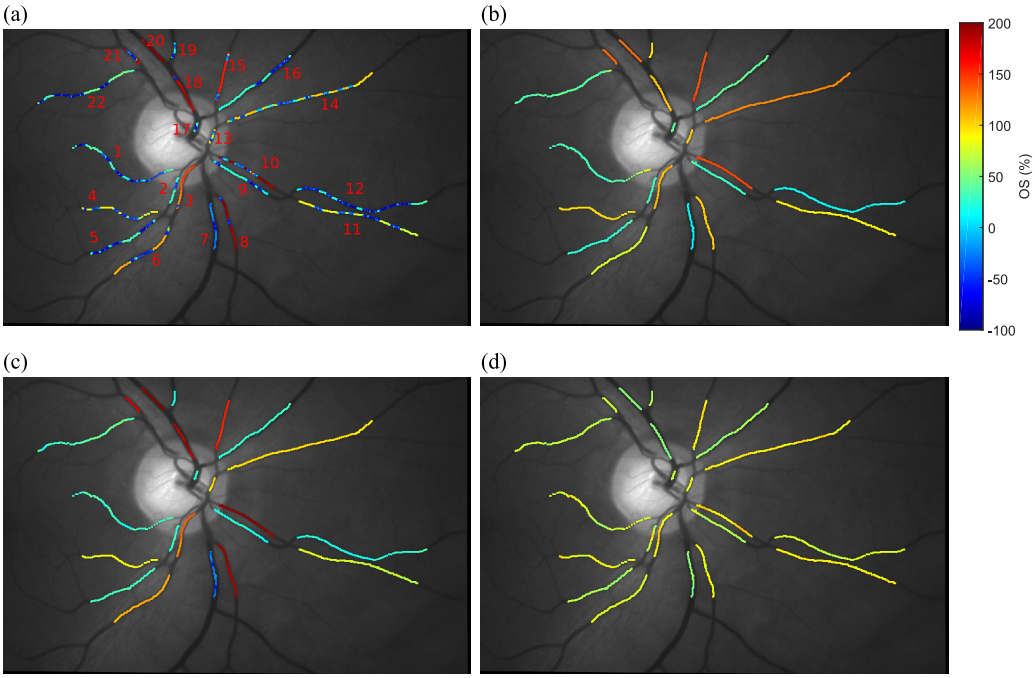

Figure A.5: Subject 5 *OS* maps from different models at the first normoxia: (a) Model 1 (Eq. 4.20). (b) Model 2 (Eq. 4.21). (c) Model 3 (Eq. 4.22). (d) Two-wavelengths oximetry (Eq. 1.8).

Arteries(A)/Veins(V)		Normoxia	Hypoxia	Normoxia	Hypoxia	Normoxia
Pulse Oximeter		98%	85%	98%	82%	98%
Model 1	A	$112 \pm 2\%$	$113 \pm 2\%$	$107 \pm 2\%$	$104 \pm 2\%$	$120 \pm 2\%$
	V	$50 \pm 3\%$	$56 \pm 3\%$	$55 \pm 2\%$	$50 \pm 3\%$	$62 \pm 3\%$
Model 2	A	$67 \pm 78\%$	$57 \pm 90\%$	$67 \pm 83\%$	$55 \pm 79\%$	$55 \pm 86\%$
	V	$16 \pm 41\%$	$15 \pm 44\%$	$30 \pm 47\%$	$11 \pm 53\%$	$30 \pm 43\%$
Model 3	A	$132 \pm 4\%$	$143 \pm 4\%$	$142 \pm 4\%$	$125 \pm 4\%$	$143 \pm 4\%$
	V	$49 \pm 5\%$	$47 \pm 11\%$	$67 \pm 6\%$	$53 \pm 5\%$	$63 \pm 7\%$
Two-wavelengths oximetry	A	$86 \pm 4\%$	$82 \pm 4\%$	$86 \pm 4\%$	$80 \pm 4\%$	$87 \pm 4\%$
	V	$65 \pm 5\%$	$62 \pm 6\%$	$65 \pm 6\%$	$64 \pm 6\%$	$63 \pm 5\%$

Table A.5: Subject 5 mean *OS* and mean standard deviation.

A.6 Subject 6

Two-wavelengths oximetry calibration $OS = 102.74 - 75.02 * ODR$.

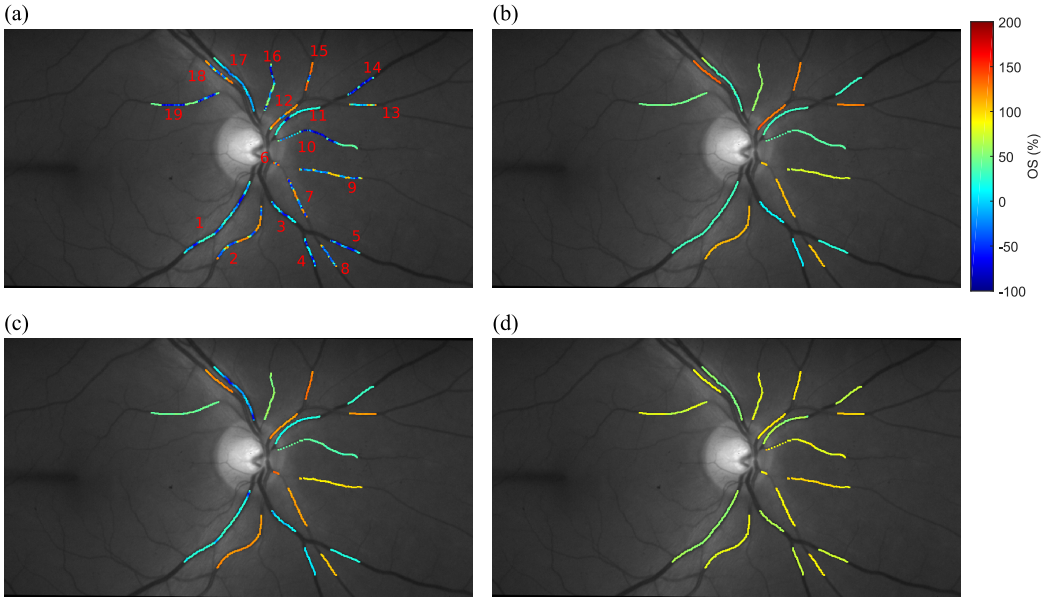

Figure A.6: Subject 6 *OS* maps from different models at the first normoxia: (a) Model 1 (Eq. 4.20). (b) Model 2 (Eq. 4.21). (c) Model 3 (Eq. 4.22). (d) Two-wavelengths oximetry (Eq. 1.8).

Arteries(A)/Veins(V)		Normoxia	Hypoxia	Normoxia	Hypoxia	Normoxia
Pulse Oximeter		98%	85%	98%	85%	99%
Model 1	A	$113 \pm 2\%$	$100 \pm 2\%$	$113 \pm 3\%$	$94 \pm 3\%$	$107 \pm 2\%$
	V	$31 \pm 3\%$	$26 \pm 4\%$	$29 \pm 3\%$	$33 \pm 3\%$	$42 \pm 2\%$
Model 2	A	$48 \pm 67\%$	$23 \pm 65\%$	$54 \pm 66\%$	$31 \pm 63\%$	$31 \pm 65\%$
	V	$-16 \pm 39\%$	$-19 \pm 41\%$	$-17 \pm 43\%$	$-24 \pm 41\%$	$-13 \pm 40\%$
Model 3	A	$117 \pm 4\%$	$106 \pm 5\%$	$123 \pm 5\%$	$95 \pm 4\%$	$108 \pm 4\%$
	V	$21 \pm 7\%$	$18 \pm 7\%$	$18 \pm 8\%$	$20 \pm 8\%$	$27 \pm 6\%$
Two-wavelengths oximetry	A	$92 \pm 3\%$	$90 \pm 3\%$	$93 \pm 4\%$	$87 \pm 2\%$	$90 \pm 3\%$
	V	$69 \pm 4\%$	$68 \pm 3\%$	$68 \pm 3\%$	$69 \pm 3\%$	$70 \pm 4\%$

Table A.6: Subject 6 mean *OS* and mean standard deviation.

A.7 Subject 7

Two-wavelengths oximetry calibration $OS = 97.89 - 69.52 * ODR$.

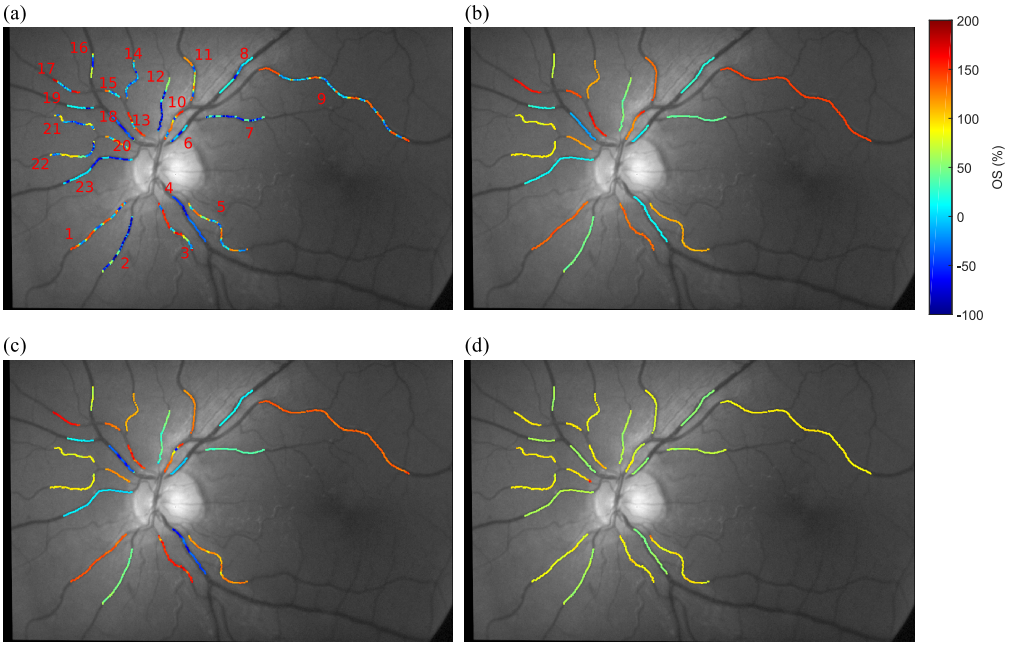

Figure A.7: Subject 7 *OS* maps from different models at the first normoxia: (a) Model 1 (Eq. 4.20). (b) Model 2 (Eq. 4.21). (c) Model 3 (Eq. 4.22). (d) Two-wavelengths oximetry (Eq. 1.8).

Arteries(A)/Veins(V)		Normoxia	Hypoxia	Normoxia	Hypoxia	Normoxia
Pulse Oximeter		96%	84%	97%	87%	97%
Model 1	A	$128 \pm 4\%$	$116 \pm 6\%$	$123 \pm 5\%$	$111 \pm 6\%$	$117 \pm 5\%$
	V	$28 \pm 4\%$	$22 \pm 4\%$	$45 \pm 3\%$	$23 \pm 4\%$	$40 \pm 3\%$
Model 2	A	$58 \pm 66\%$	$44 \pm 70\%$	$53 \pm 70\%$	$40 \pm 64\%$	$53 \pm 62\%$
	V	$-22 \pm 40\%$	$-31 \pm 37\%$	$0 \pm 52\%$	$-23 \pm 37\%$	$-3 \pm 40\%$
Model 3	A	$125 \pm 11\%$	$112 \pm 18\%$	$126 \pm 12\%$	$104 \pm 18\%$	$113 \pm 8\%$
	V	$13 \pm 7\%$	$9 \pm 7\%$	$44 \pm 18\%$	$8 \pm 7\%$	$22 \pm 7\%$
Two-wavelengths oximetry	A	$91 \pm 11\%$	$84 \pm 5\%$	$90 \pm 6\%$	$85 \pm 7\%$	$90 \pm 6\%$
	V	$60 \pm 4\%$	$59 \pm 3\%$	$60 \pm 4\%$	$59 \pm 4\%$	$63 \pm 5\%$

Table A.7: Subject 7 mean *OS* and mean standard deviation.

A.8 Subject 8

Two-wavelengths oximetry calibration $OS = 101.63 - 87.43 * ODR$.

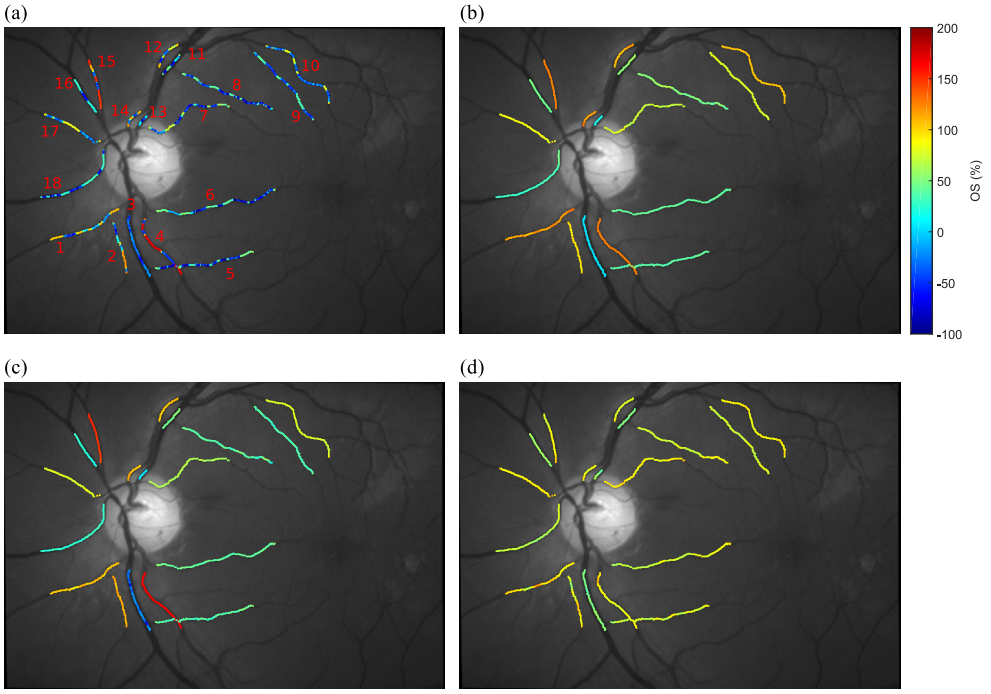

Figure A.8: Subject 8 *OS* maps from different models at the first normoxia: (a) Model 1 (Eq. 4.20). (b) Model 2 (Eq. 4.21). (c) Model 3 (Eq. 4.22). (d) Two-wavelengths oximetry (Eq. 1.8).

Arteries(A)/Veins(V)		Normoxia	Hypoxia	Normoxia	Hypoxia	Normoxia
Pulse Oximeter		98%	84%	98%	85%	98%
Model 1	A	$107 \pm 4\%$	$97 \pm 3\%$	$108 \pm 4\%$	$90 \pm 3\%$	$107 \pm 4\%$
	V	$40 \pm 4\%$	$37 \pm 3\%$	$37 \pm 4\%$	$32 \pm 4\%$	$43 \pm 4\%$
Model 2	A	$38 \pm 69\%$	$30 \pm 66\%$	$47 \pm 71\%$	$22 \pm 69\%$	$44 \pm 68\%$
	V	$-17 \pm 43\%$	$-14 \pm 41\%$	$-15 \pm 41\%$	$-21 \pm 42\%$	$-17 \pm 46\%$
Model 3	A	$107 \pm 4\%$	$102 \pm 5\%$	$121 \pm 5\%$	$97 \pm 5\%$	$112 \pm 5\%$
	V	$25 \pm 5\%$	$19 \pm 7\%$	$25 \pm 7\%$	$21 \pm 6\%$	$30 \pm 7\%$
Two-wavelengths oximetry	A	$87 \pm 8\%$	$80 \pm 7\%$	$89 \pm 8\%$	$81 \pm 7\%$	$88 \pm 9\%$
	V	$65 \pm 6\%$	$62 \pm 6\%$	$67 \pm 6\%$	$65 \pm 6\%$	$70 \pm 5\%$

Table A.8: Subject 8 mean *OS* and mean standard deviation.

A.9 Subject 9

Two-wavelengths oximetry calibration $OS = 106.7 - 87.7 * ODR$.

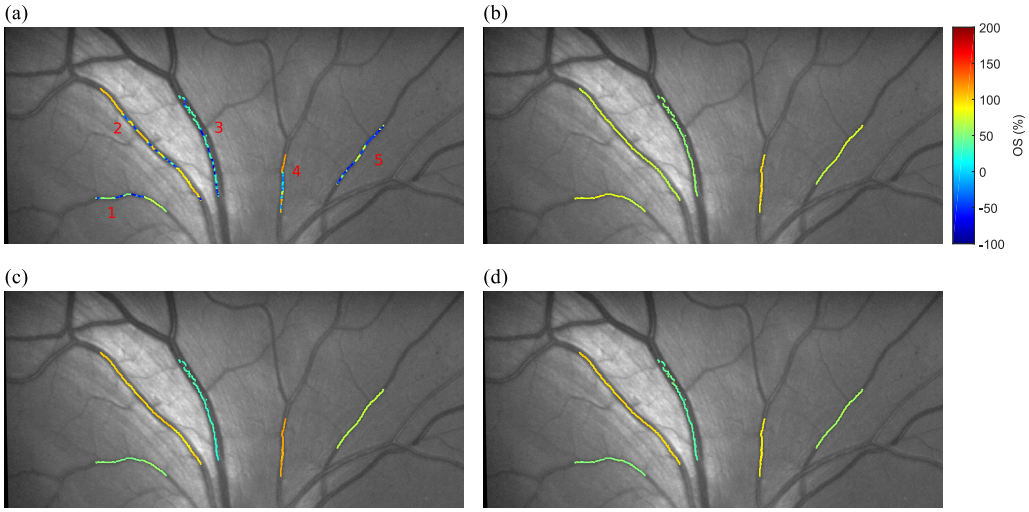

Figure A.9: Subject 9 *OS* maps from different models at the first normoxia: (a) Model 1 (Eq. 4.20). (b) Model 2 (Eq. 4.21). (c) Model 3 (Eq. 4.22). (d) Two-wavelengths oximetry (Eq. 1.8).

Arteries(A)/Veins(V)		Normoxia	Hypoxia	Normoxia	Hypoxia	Normoxia
Pulse Oximeter		98%	82%	99%	83%	98%
Model 1	A	$95 \pm 2\%$	$112 \pm 2\%$	$106 \pm 2\%$	$85 \pm 2\%$	$106 \pm 2\%$
	V	$51 \pm 3\%$	$40 \pm 8\%$	$39 \pm 4\%$	$48 \pm 4\%$	$48 \pm 4\%$
Model 2	A	$59 \pm 61\%$	$45 \pm 79\%$	$49 \pm 74\%$	$47 \pm 68\%$	$62 \pm 65\%$
	V	$2 \pm 50\%$	$-15 \pm 41\%$	$3 \pm 45\%$	$4 \pm 58\%$	$-16 \pm 45\%$
Model 3	A	$107 \pm 5\%$	$110 \pm 4\%$	$107 \pm 4\%$	$103 \pm 5\%$	$108 \pm 4\%$
	V	$50 \pm 4\%$	$29 \pm 8\%$	$34 \pm 5\%$	$55 \pm 4\%$	$45 \pm 5\%$
Two-wavelengths oximetry	A	$85 \pm 4\%$	$73 \pm 5\%$	$81 \pm 4\%$	$79 \pm 4\%$	$85 \pm 4\%$
	V	$68 \pm 4\%$	$62 \pm 5\%$	$64 \pm 4\%$	$66 \pm 4\%$	$69 \pm 5\%$

Table A.9: Subject 9 mean *OS* and mean standard deviation.

Appendix B

Oximetry in microchannels under laminar flow conditions

Summary: This chapter describes how blood shows a laminar flow behaviour on retinal vessels. This can affect oximetry in the sense that two merging veins can have different *OS* and they do not mix together due to laminar flow conditions. However, oxygen is expected to diffuse between both flows. In this chapter, we attempted to replicate this effect in a PDMS microchannel in order to estimate oxygen diffusion between to blood streams under laminar flow conditions and to understand the possible consequences on retinal oximetry.

B.1 Introduction

During the 2014 Birmingham Oximetry Workshop David Bragason[1] presented model and preliminary data[156] on how oxygen gradients occur in retinal veins under laminar flow conditions. Laminar flow in retinal vessels is possible due to low Reynolds number ($Re < 1$[157]) and can be observed during fluorescein angiogram, where due to high Peclet number (ratio between advection rate and diffusion rate), fluorescein does not diffuse. Laminar flow in retinal vessels means that if two veins with different *OS* join, the two created streams keep their oxygenation downstream, with oxygen slowly diffusing. According to Bragason's model and oximetric preliminary data, laminar flow with different *OS* is particularly relevant when veins from the macula join other veins. The macula is a highly metabolic active region of the eye, due to the high concentration of cones and rods. Because of this, most of its oxygen needs are supplied by the choroid, meaning that it consumes less oxygen from retinal vessels than other retinal regions.

Working in collaboration with David Bragason and Laurence Brewer[2] it was decided to

[1]Ophthalmology, University of Iceland/Landspitali University Hospital, Reykjavik, Iceland
[2]SUPA Advanced Fellow, School of Physics and Astronomy, University of Glasgow

simulate *in vitro* the conditions of a vein confluence in order to provide further proof and insight on the phenomena.

B.2 Experimental system and methods

For this experiment, we used the same microscope-IRIS with a 40x 0.75NA microscope objective system and the LSU data analysis explained in Chapter 3. For the *in vitro* simulation, a flow cell was designed by Laurence Brewer and manufactured on PDMS by Marc Rodriguez[3] (Fig. B.1). The flow cell had two channels, one 100 μm wide and the other 50 μm wide that joined each other forming a common channel that was 100 μm wide. The depth of the channels was 40 μm and the length of the flow cell was approximately 30 mm. The flow cell was 5 mm thick. To simulate the behaviour of retinal vessels and vessel branches, the channel should have followed Murray's law[158, 159], but at the moment of the design this was not considered:

$$r_p^3 = r_{d_1}^3 + r_{d_2}^3, \tag{B.1}$$

where r_p is the radius of the parent branch, and r_{d_i} is the radius of the daughter branch i. Eq. B.1 relates the radii of the daughter branches to the radii of the parent vessel. This expression represents Murray's law and is derived from the assumption that flow in vessels occurs with the minimum possible work in terms of a fluid suffering from drag and the required energy to maintain the tissue and blood volume involved in the flow.

For this chapter, Eq. B.1 is relevant because if the radii relation is not satisfied, the volumetric flow of the daughter branches will be modified when they join. In these circumstances, the assumed relative velocity between the two streams will be different, producing unreliable results in terms of oxygen diffusion between both flows.

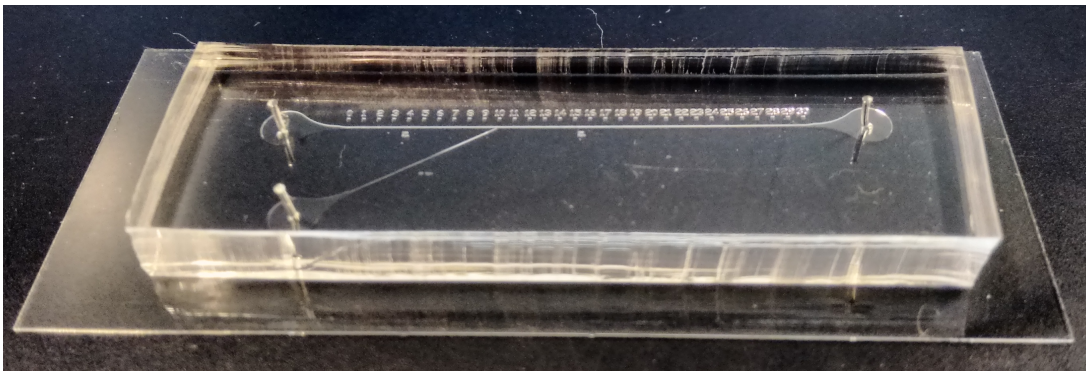

Figure B.1: PDMS flow cell. 30 mm long with two channels of 50 μm and 100 μm width joining at 10 mm in a 100 μm width channel. All the channels had a depth of 40 μm. The main channel included a 30 mm scale in steps of 1 mm.

[3]WestCHEM, School of Chemistry, University of Glasgow, University Avenue, Glasgow G12 8QQ, UK

To simulate the flow, a KDS270 syringe pump (*KD Scientific*, US) was used. Two 5 ml syringes were connected to the flow cell by means of polytetrafluoroethylene (PTFE) tubing of 150 μm inner diameter to the two input ports of the flow cell (Fig. B.1, left ports). Blood velocity in retinal vessels can vary from 0.24 mms^{-1}[104] for the smaller vessels to 13.5 mms^{-1}[160] for larger vessels. In our case, we chose 7 mms^{-1} as an intermediate case for our 100 μm channel, which produced a 100 μlhour^{-1} flow. 100% oxygenated (BGA measured) defibrinated horse blood flowed through the 50 μm while 0% oxygenated horse blood (deoxygenated with sodium dithionite and checked with BGA) flowed through the 100 μm channel. Using a microscope with a 40x and 0.75 NA objective did not allow capturing the whole channel length. The calculated FoV from the imaged IRIS wavebands was 822 × 515 pixels, which considering the Zyla pixel size of 6.5 μm, the 0.25x demagnification from the SLR lenses and 40x magnification from the microscope objective translates into a FoV of 534 × 335 μm. A 20x objective would have provided a larger field of view, but he interface between the two flows would have contained less pixels. The importance of having more pixels in the interface is that it provides a better characterisation of the oxygen diffusion between the two flows.

In order to capture the whole flow behaviour on the channel, images were recorded at 10 mm, 12 mm, 15 mm, 17 mm, 20 mm, 22 mm, 25 mm, 27 mm and 30 mm along the channel, where 10 mm was the position where both channels merge. An example of *OD* generated maps are shown in Fig. B.2, where 560 nm, 591 nm and 599 nm were more transmissive for oxygenated blood while at 576 nm and 580 nm there is an inversion and deoxygenated blood transmits more light. 567 nm, 571 and 586 nm have an apparent isosbestic behaviour.

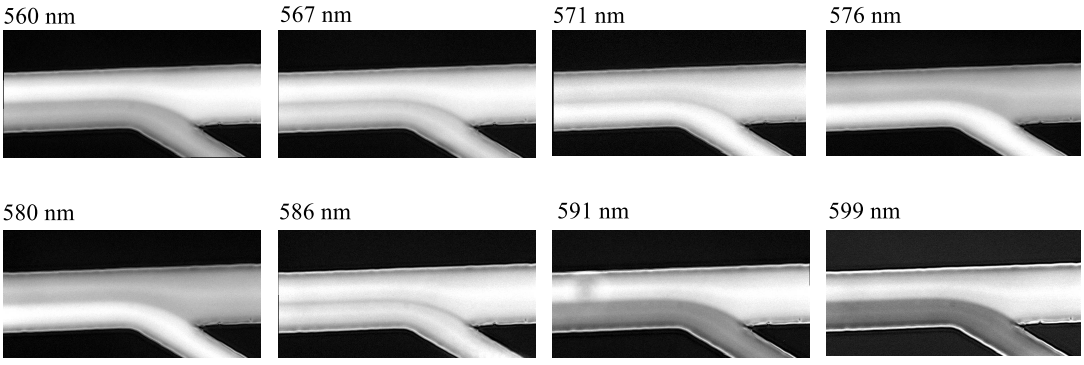

Figure B.2: *OD* map of the flow channel at the junction, showing the characteristic behaviour of 100% an 0% oxygenated blood with wavelength.

Once an image was obtained, a second image of the adjacent region to the channel was recorded to be used as background. The images along the channel were then divided by their corresponding background and the $-\log_{10}$ was applied in order to obtain the optical density of the channel.

$$OD = -\log_{10}\left(\frac{I_{Channel}}{I_{Background}}\right), \tag{B.2}$$

where $I_{Channel}$ is the intensity on the channel and $I_{Background}$ is the intensity on the background. This procedure is the same used in Chapter 3, using Eq. 3.1 to calculate the optical densities. The endmembers (Fig. B.3(a)) were taken at the position 10 mm (Fig. B.3(b)), where the channels merged. The oxyhaemoglobin and deoxyhaemoglobin endmembers were obtained from the 100% and 0% *OS* channels before they joined in the main channel to avoid possible interactions between them.

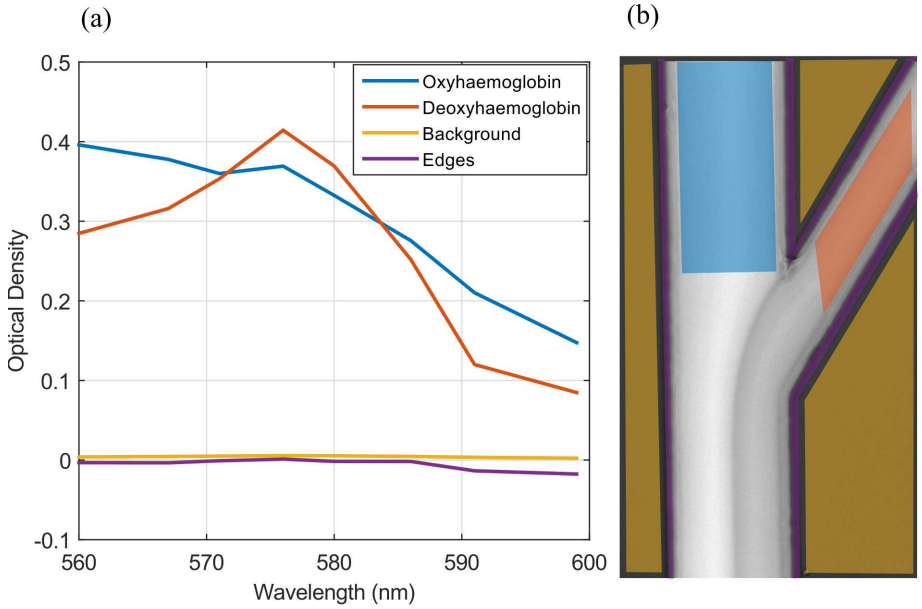

Figure B.3: (a) Endmembers used for the LSU analysis of the flow cell. (b) Selected ROIs for the endmember collection.

As in Subsection 3.8.1, the SNR can be calculated using Eq. 3.7 by considering that the noise is 0.005 *OD*, which corresponds to the standard deviation of the highlighted background on Fig. B.3(b). Once this value is obtained, the SNR is calculated as the ratio of the *OD* of blood on the channel and the background noise.

$$SNR(\lambda) = \frac{OD_{Channel}(\lambda)}{SD(background)}, \tag{B.3}$$

where $OD_{100\%}(\lambda)$ is the mean optical density of the 100% oxygenated channel (red in Fig. B.3) and $SD(background)$ is the standard deviation of the background (yellow in Fig. B.3). Table B.1 shows the SNR calculated with Eq. B.3 for the *OD* signal of oxygenated blood at $L = 10\,\text{mm}$ in this experiment. At 576 nm a SNR of 82 is achieved, this being the highest of all IRIS wavelengths. In general, the SNR is high, although it could be problematic in the 591 nm and 599 nm since a $40\,\mu\text{m}$ thickness blood column is still highly transparent on this wavelength regime. On Chapter 3, the calculated SNR for a single RBC (Table 3.1) ranged from a maximum 9 to a minimum of 0.014, which introduced significant variations and errors in the calculated oxygenation. In the case of the microchannel, a blood thickness of $40\,\mu\text{m}$ is expected to produce a better absorption signal than a single RBC. This improved signal is

shown on Table B.1, with a maximum SNR of 82 and a minimum of 16. The relevance of these values is that noise is expected to produce minimal errors on the performed oximetry.

Wavelength (nm)	Optical Density	SNR
560	0.28	56
567	0.32	64
571	0.35	70
576	0.41	82
580	0.37	74
586	0.25	50
591	0.12	25
599	0.08	16

Table B.1: SNR of the flow cell signal considering the Optical Density of the oxyhaemoglobin endmember and a noise of 0.005 *OD*.

Once the endmembers were obtained, a Linear Spectral Unmixing (LSU) was applied in order to detect background, edges, oxyhaemoglobin and deoxyhaemoglobin. Then a threshold was applied in order to reject pixels belonging to background and edges, which tend to have $\geqq 1$ abundance of these endmembers. The remaining pixels belonged to blood on the channels and were used to calculate the *OS* using Eq. 3.6.

B.3 Results

The results of the oxygen saturation map on the flow cell are shown in Fig. B.4. The *OS* maps show how the deoxygenated channel shifts to purple, which corresponds to $\sim 50\%$ *OS*. The *OS* change is better characterised in the form of histograms, in which is shown how the deoxygenated channel *OS* peak (maximum pixel abundance) shifted from -3% to 49%, while the peak of the oxygenated channel changed only from 96% to 94% *OS* from the junction to the end of the channel.

Once the *OS* values were generated and after analysing Fig. B.4, it was clear that oxygen diffusion was not following the expected behaviour. Although there was diffusion, it was expected that both channels would shift to 50% in approximately equal terms along the channel due to oxygen diffusion from the 100% to the 0% *OS* channel. The behaviour of Fig. B.4 was later on identified as a side effect of oxygen diffusion through the PDMS channel, which acted as an active source of oxygen to the blood on the channels. More details about this effect are explained on Section B.4.

Although the behaviour was not the expected, Fig. B.4 still showed oxygen diffusion. The next step was to characterise the *OS* gradient between both channels along the flow cell and adjust our data to a macroscopic diffusion model. The used model was Fick's law[161,

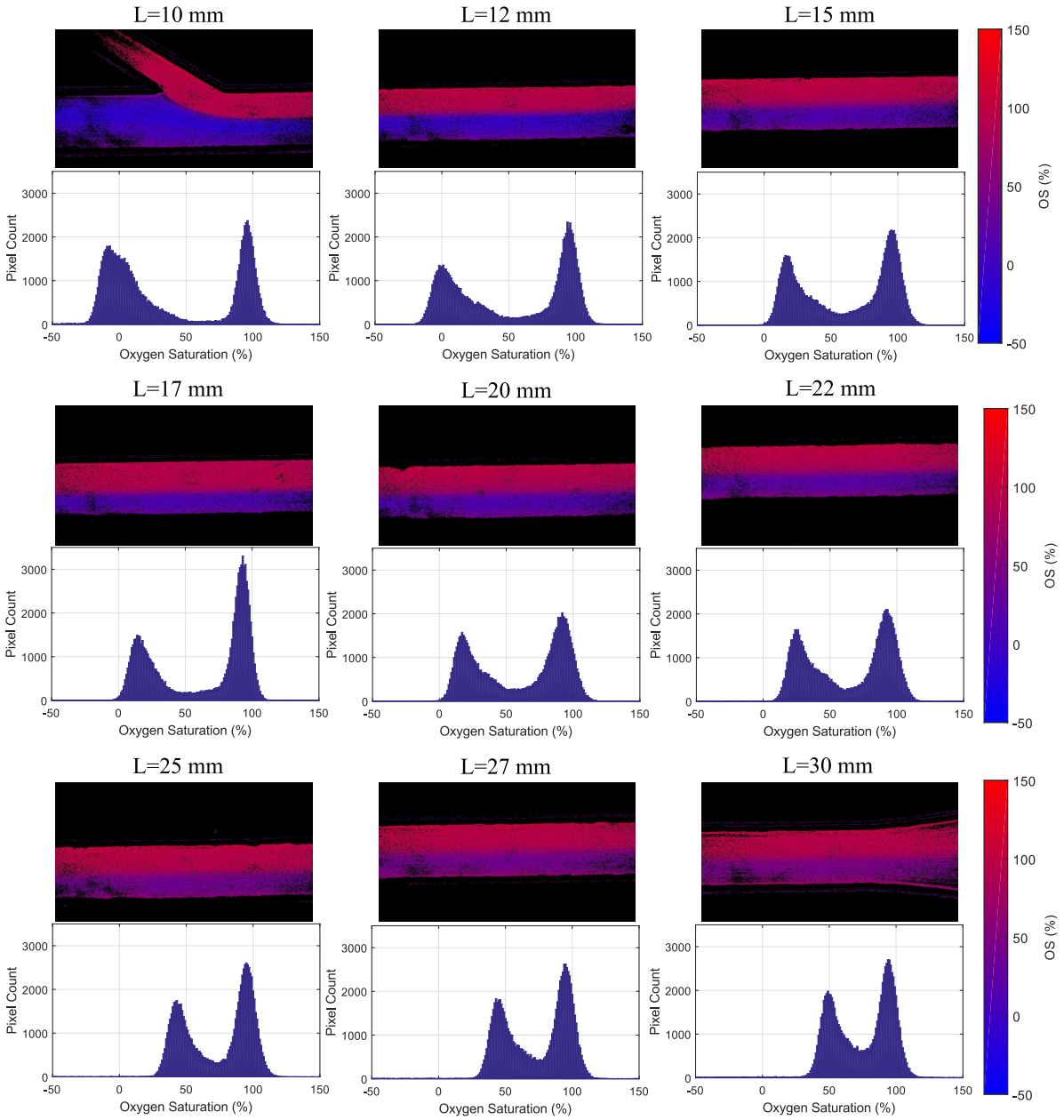

Figure B.4: *OS* map and pixel histogram along the flow channel. The sequence shows how the deoxygenated channel reoxygenates with distance until reaching approximately 50% *OS* at $L = 30\,\text{mm}$.

162]:

$$C(x,t) = \frac{C_0}{2}\left[erfc\left(\frac{x}{(4Dt)^{1/2}}\right)\right], \tag{B.4}$$

where C is the concentration in distance and time, C_0 the initial concentration, $erfc$ the error function, x the distance in one dimension, t the time and D the diffusion coefficient.

In our case, the interface between both flows was not always at the same value of x so a constant had to be added to the x variable. In addition, an *OS* offset in the 0% channel might be introduced from the LSU analysis (Fig. B.4), so an additive constant was added. Due to

these reasons, Eq. B.4 was modified so it could be adjusted to our data:

$$OS(x,y) = \frac{1}{2a} erfc\left(\frac{x-b}{\left(4D\frac{y}{v}\right)^{1/2}}\right) + c, \tag{B.5}$$

where OS is the oxygen saturation across x and along y on the channel, a, b, and c are fitting parameters, D is the oxygen diffusion coefficient and $\frac{y}{v} = t$, being v the blood velocity and y the position along the channel in mm. $y = 0\,\text{mm}$ corresponds to the position $L = 10\,\text{mm}$ on the flow channel scale. This equation was fitted to find a, b, D and c.

From the OS maps on Fig. B.4, 170 pixels profiles were taken across the channel and along the FoV, being the channel ~ 180 pixels wide. The deoxygenated stream on Fig. B.4 became thinner than the oxygenated stream along the channel, so from the centre of the channel, ~ 90 pixels belonged to the oxygenated flow while ~ 80 were for the deoxygenated one.

Once the OS profiles were obtained, Eq. B.5 was fitted individually to each profile on each picture, each picture having a mean of 376 section profiles, excluding the images at $L = 10\,\text{mm}$ (image at the confluence) and $L = 30\,\text{mm}$ (end of the channel and beginning of the output port) , which had 144 and 120 cross-sections respectively. Once the fits were obtained, they were averaged for each channel position, obtaining a total of 9 curves, one per picture. Finally, in order to obtain the oxygen diffusion coefficient, the 9 curves were again fitted to Eq. B.5 (Fig. B.5(a)). These fits gave back the value for the oxygen diffusion D, which is shown on Fig. B.5(b). The value goes from $D = 4.97 \times 10^{-5}\,\text{cm}^2\text{s}^{-1}$ at $y = 0\,\text{mm}$, to $D = 2.39 \times 10^{-7}\,\text{cm}^2\text{s}^{-1}$ at $y = 10\,\text{mm}$ and $D = 9.91 \times 10^{-8}\,\text{cm}^2\text{s}^{-1}$ at $y = 20\,\text{mm}$. According to the literature[161], the oxygen diffusion coefficient of whole blood is:

$$D = (1.98 - 0.0085H) \times 10^{-5}\text{cm}^2/\text{s}, \tag{B.6}$$

where H is the haematocrit. In this case, $H = 40\%$, which using Eq. B.6 produces $D = 1.9766 \times 10^{-5}\text{cm}^2/\text{s}$. In addition to the fact that the diffusion coefficient should not change along the channel, the values are too small in all the points with the exception of the confluence of both channels.

Fig. B.5(a) shows again how the OS on the oxygenated channel remains constant, while only the OS on the deoxygenated channel changes from ~0% to ~50%. As previously stated, the expected behaviour was that both flows would reach an oxygenation equilibrium by the end of the channel. This effect was produced by the own oxygen diffusion of the PDMS microchannel (more details on Section B.4).

In order to provide a more robust analysis, the process was repeated using the gradient of the OS map. As in the first step, the cross-sections of each OS image was fitted to Eq. B.5, and the results were averaged along each image, obtaining a total of 9 oxygenation diffusion curves. The gradient of these curves was performed and then fitted to the derivative of Eq.

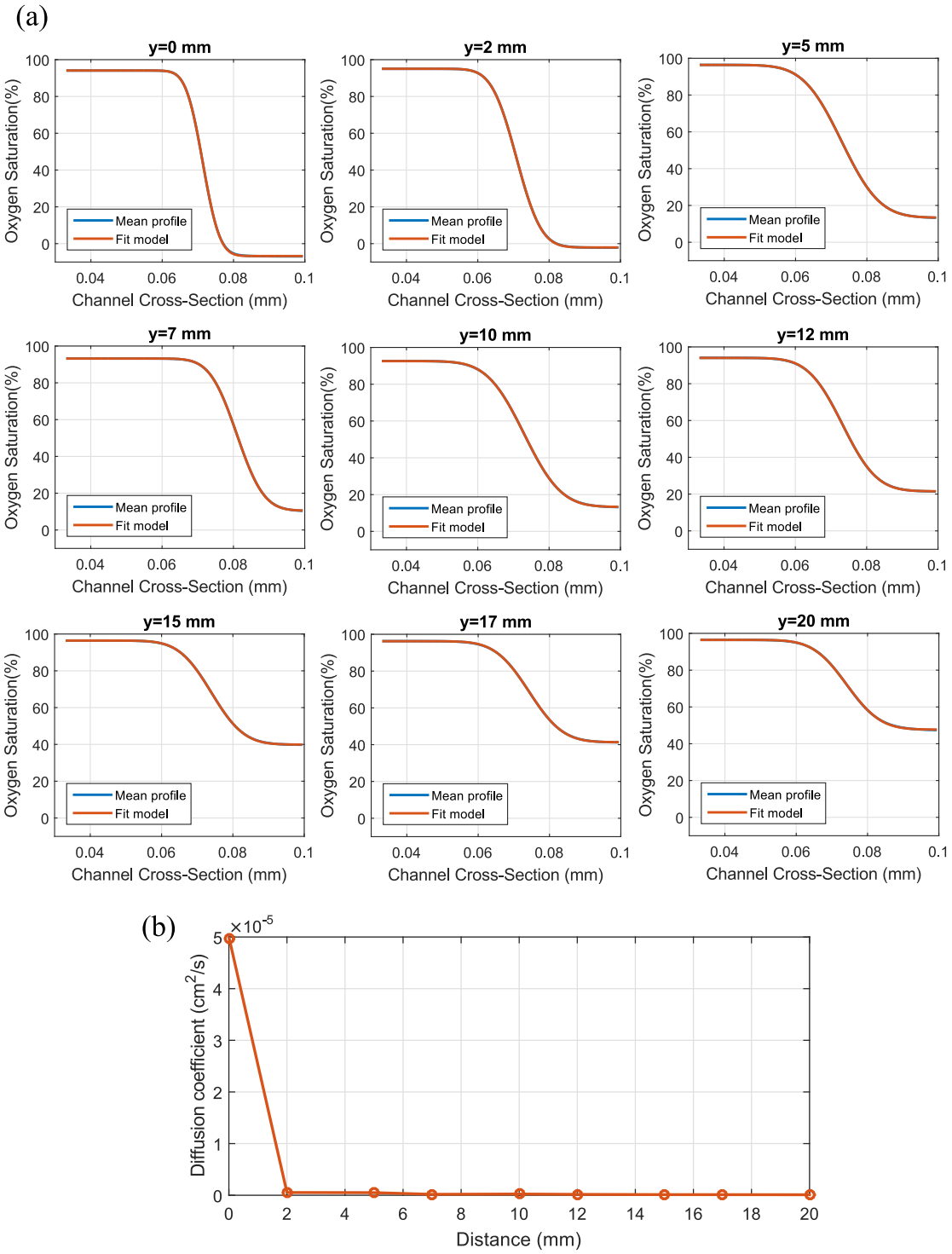

Figure B.5: (a) Mean *OS* cross-section and fit model (Eq. B.5) for the 9 positions along the flow channel. The fit model (Red) overlaps the mean profile (Blue) in every point, so the mean profile is not distinguishable from the fit model. (b) Diffusion coefficient extracted from fits along the channel.

B.5 (Fig. B.6(a)). This partial derivative[162], has only three fit parameters, a, D and b, in

contrast with Eq. B.5, which had four parameters to fit:

$$\frac{\partial OS(x,y)}{\partial x} = \frac{a}{\sqrt{4\pi D\frac{y}{v}}} e^{\left(-\frac{(x-b)^2}{4D\frac{y}{v}}\right)}. \tag{B.7}$$

The gradients and their corresponding fits are shown in Fig. B.6(a). From these fits, the diffusion constant D is extracted (Fig. B.6(a)). The obtained values are $D = 9.76 \times 10^{-6}\,\mathrm{cm^2/s}$ at $y = 0\,\mathrm{mm}$, to $D = 2.38 \times 10^{-7}\,\mathrm{cm^2/s}$ at $y = 10\,\mathrm{mm}$ and $D = 9.74 \times 10^{-8}\,\mathrm{cm^2/s}$ at $y = 20\,\mathrm{mm}$, showing a similar behaviour as in Fig. B.5(b).

From Fig. B.6(a), the maximum *OS* gradient with distance from the junction was calculated, which provided a qualitative evaluation on diffusion. This figure shows how the interface between both flows became more diffuse further from the junction (Fig. B.7), which means that oxygen was being diffused between both flows. In this figure there is a jump in the *OS* gradient at 7 mm, meaning that the interface between both flows was sharper at that point. From the point of view of diffusion, this is not possible, but it can be attributed to a sharp increase in pumped blood, or to a temporal change in the properties of blood. The two syringes used were held in the syringe pump during the whole experiment, being gently shaken every 30 seconds, but RBCs tend to aggregate fast, so it could be possible that at 7 mm the channel contained blood with different haematocrit, changing the flow interface and oxygen diffusion (Eq. B.6).

B.4 Errors discussion

As seen in Fig. B.5(b) and Fig. B.6(b), the oxygen diffusion coefficients obtained greatly differ from the theoretical one at 40% haematocrit. High haematocrit due to aggregation does not explain this since it would not change the diffusion coefficient in such a dramatic way (Eq. B.6). However, the channel was not designed following Murray's law (Eq. B.1), and in fact, the two merging channels of thickness 100 μm and 50 μm joined in a 100 μm thickness channel. This means that there were two flows trying to fit in a channel the size of one of them. This would inevitably increase the velocity of both streams, and by analysing Eq. B.5, if a smaller velocity than the actual velocity is introduced in the model, the fit will produce a smaller diffusion constant in order to adjust the model to the experimental data. Future experiments should include laser Doppler velocimetry[163] as a tool to control the flow speed between both blood streams.

The second main issue with the data is observed in Fig. B.4. This shows that only the deoxygenated channel changes the *OS*, going from $-7 \pm 17\%$ to $48 \pm 8\%$, while the oxygenated channel shifts from $94 \pm 7\%$ to $96 \pm 7\%$, effectively remaining constant along the channel. From an experiment like the shown here, the expected behaviour would be that both channels would finally have an oxygenation close to 50%, or at least they would shift in that

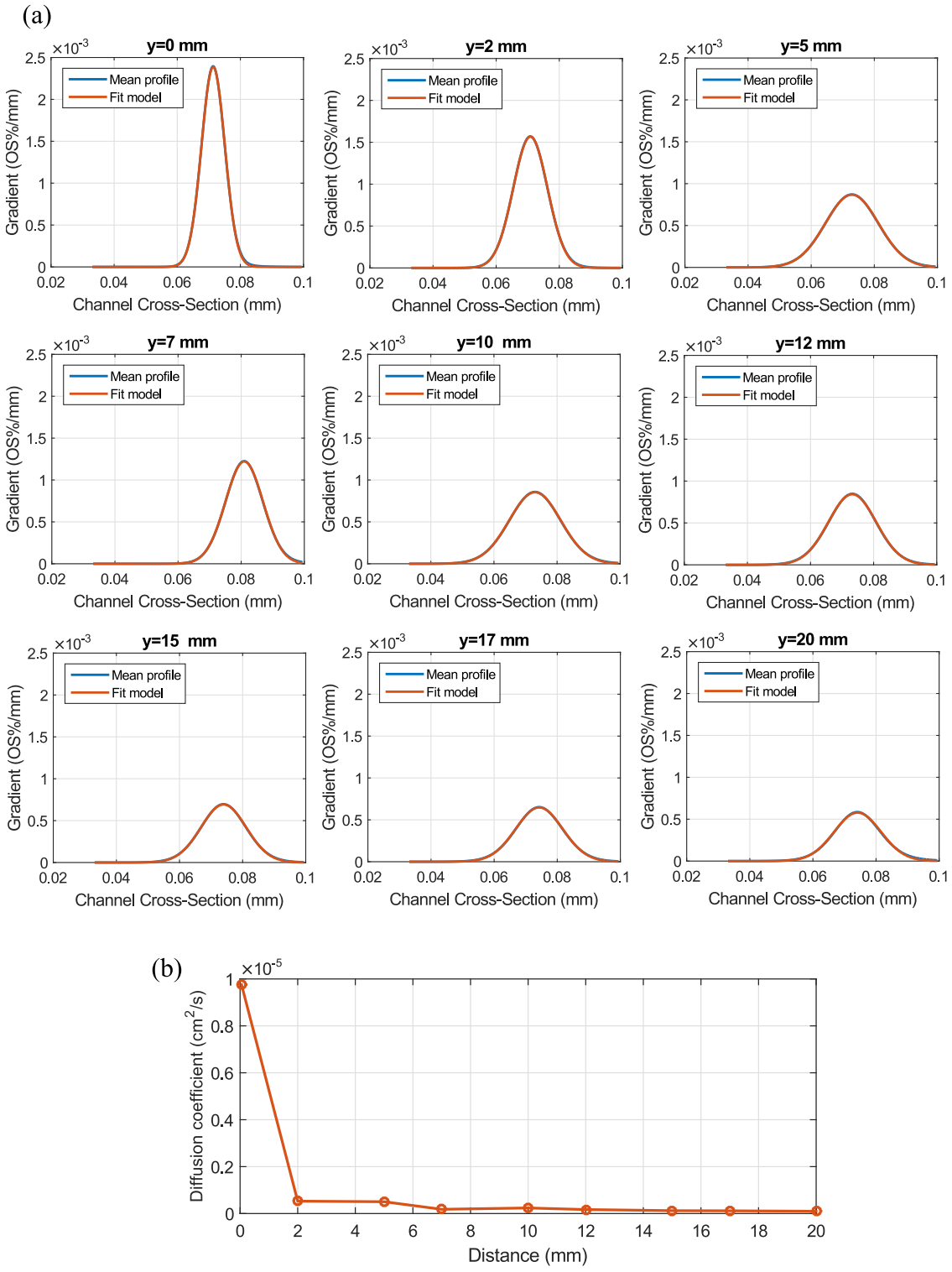

Figure B.6: (a) Mean *OS* gradient across the channel and fit model (Eq. B.7) for the 9 positions along the flow channel. The fit model (Red) overlaps the mean profile (Blue) in every point, so the mean profile is not distinguishable from the fit model. (b) Oxygen diffusion coefficient extracted from fits along the channel.

direction. The effect of having an excess of sodium dithionite would contribute to the faster deoxygenation of the oxygenated channel, which would then increase the oxygen diffusion coefficient. Since the amount of sodium dithionite was carefully measured and the explained

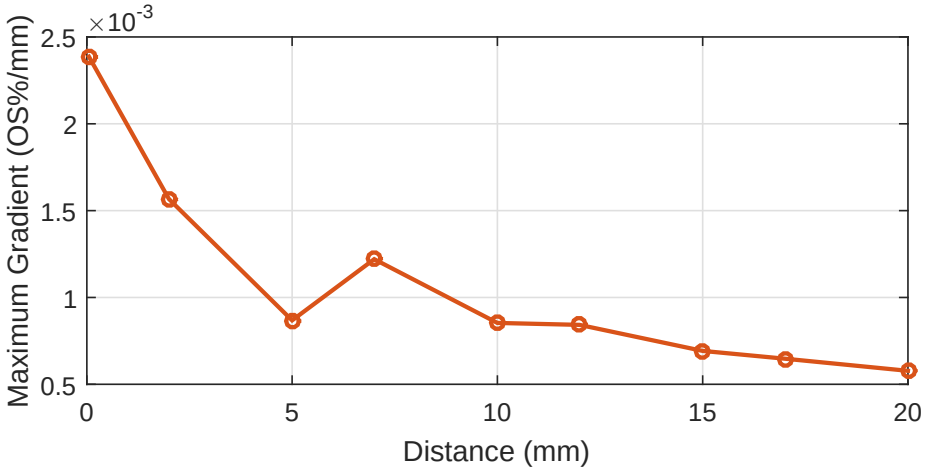

Figure B.7: Maximum gradient with distance from the junction, showing a general decrease.

behaviour did not happen, this was discarded as a possible cause of the reoxygenation of the channel.

Following a more detailed study of our flow cell, it was learned that PDMS is often used in flow channels systems for oxygenation and deoxygenation of cells due to its high oxygen (and other gases) diffusion coefficient[96, 164, 165]. PDMS (poly (dimethylsiloxane)) has a oxygen diffusion coefficient $D_O(PDMS) = 3.4 \times 10^{-5}\text{cm}^2/\text{s}$[166], which is higher than the $D_O \approx 2 \times 10^{-5}\text{cm}^2/\text{s}$ for whole blood 45% haematocrit (Eq. B.6).

In order to experimentally test the hypothesis of the reoxygenation, a $20\,\text{mm} \times 40\,\mu\text{m} \times 100\,\mu\text{m}$ PDMS channel was designed, with only one input and one output. Whole horse blood deoxygenated with sodium dithionite to be 0% was pumped at $7\text{mm}/\text{s}$ through the channel. Fig. B.8(a) shows the *OS* map of the flow cell with distance while Fig. B.8(b) is the *OS* histogram of these images. The histogram shows how the pixel population shifted from 0% at the beginning of the channel, to $\sim 50\%$ and $\sim 75\%$ oxygenation at the end of the channel. The experiment was repeated a total of 9 times with the same sample, acquiring snapshots in the same positions $y = 0\,\text{mm}$, $y = 10\,\text{mm}$ and $y = 20\,\text{mm}$, every minute. In each set, the results were in accordance with Fig. B.8, reoxygenation happens along the channel. It is interesting to see how near the walls of the channel, *OS* is higher than in the central regions. This could be explained by the existence of a plasma layer on the channel walls[167], which would mean these high *OS* values on the edges are an artefact from the LSU analysis. Another reason would be the oxygen diffused through PDMS. This would reoxygenate the blood in contact with the walls. The effect would not be visible in the central parts of the channel since there is 40 μm of blood that is not in contact with the channel walls. This last explanation would be adequate since blood reoxygenation appears to extend from the lateral walls of the channel (Fig. B.8(a) and Fig. B.4).

The effect of having a higher velocity than the assumed and the high PDMS oxygen diffusion invalidated the experiment in terms of calculating the oxygen diffusion.

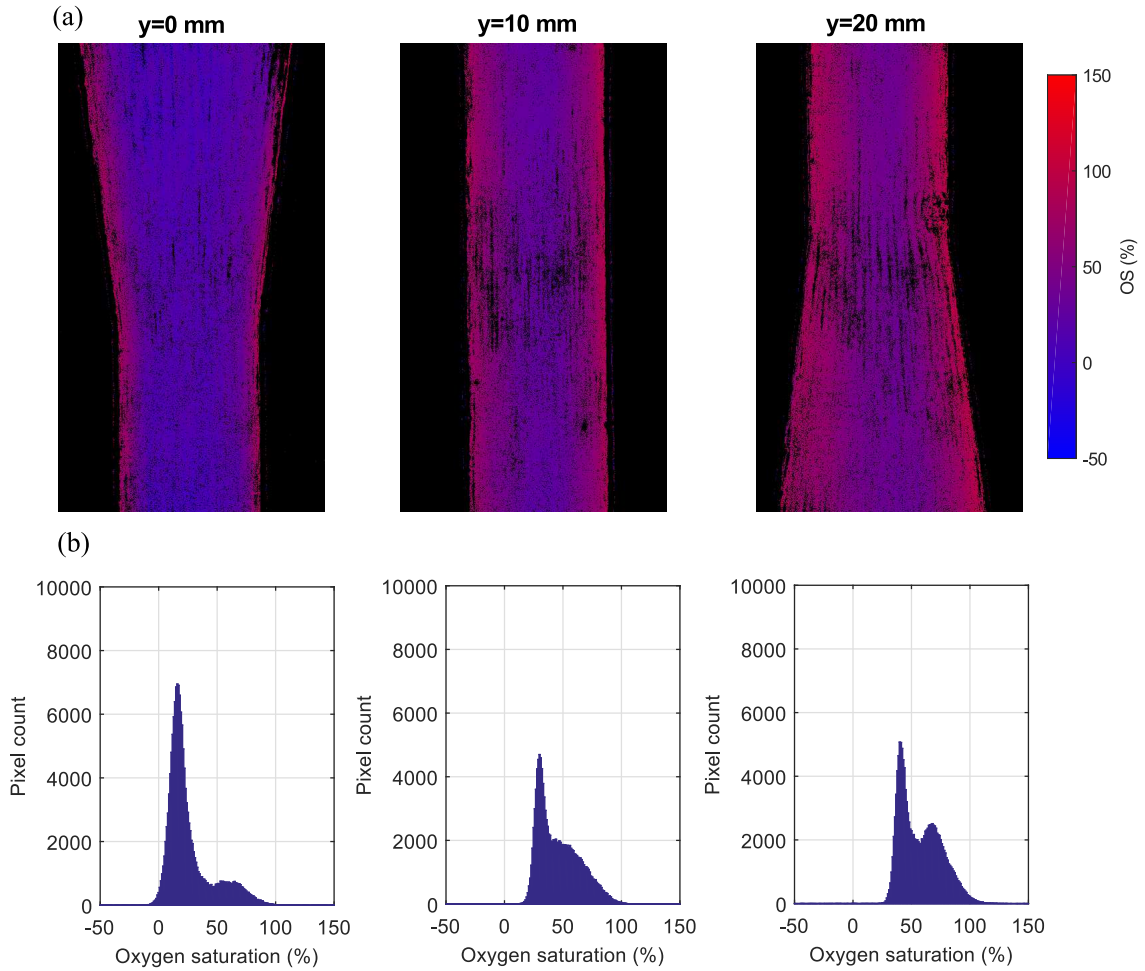

Figure B.8: Reoxygenation along a PDMS channel. (a) *OS* map of three images taken along a 20 mm channel. (b) *OS* histogram of all the pixels in (a).

B.5 Conclusions and future work

In this chapter, the laminar flow found in retinal vessels has been replicated. From the experimental data, it was possible to fit a diffusion model and calculate the diffusion constant. This oxygen diffusion coefficient was shown to be smaller than expected, mainly due to an underestimation of the flow velocity because the joint channel was smaller than what it should have been according to Murray's law. The reoxygenation due to oxygen diffusion through PDMS also cast doubt on the validity of the results obtained, since the *OS* gradient on Fig. B.7 could be affected by the extra oxygen coming through the channel walls. At the time we realised the faults in the experiment, the project had already moved onto retinal oximetry and the faults were not properly addressed.

Possible solutions to these issues are the use of glass channels, which have a lower oxygen diffusion coefficient, but are more difficult to work with from the point of view of manufacture[167]. It is also possible to design a channel using *Parafilm* and seal it between two coverslides, but the difficulty of making 100 μm channels accurately and straight would

introduce perturbations in the flow and the estimated velocities might change. A possible solution is to coat the channels with Teflon (PTFE) or to manufacture it completely of Teflon[168]. Teflon (PTFE) has an oxygen diffusion coefficient $D_O = 1.52 \times 10^{-7} \mathrm{cm}^2/\mathrm{s}$[169], which is lower than that of PDMS. A third option is the use of 3-D printing. With resolutions of up to 16 µm, and the use of gas impermeable polymers such as PLA ($D_O \sim 5 \times 10^{-8} \mathrm{cm}^2/\mathrm{s}$[170]), producing an oxygen impermeable flow cell should be easily achievable and would allow to accurately replicate *in vitro* the laminar flow observed in retinal vessels.

Appendix C

Experimental data and code locations

The data on this thesis is available for future research on the Imaging Concepts Group shared drive on the University of Glasgow \\ICGSERVE\ICG\Javier\.

Chapter 2

\\ICGSERVE\ICG\Javier\Thesis data and codes\IRIS improvement\

Chapter 3

\\ICGSERVE\ICG\Javier\Thesis data and codes\RBC Oximetry\

Chapter 4

\\ICGSERVE\ICG\Javier\Thesis data and codes\Retinal Oximetry\

Appendix B

\\ICGSERVE\ICG\Javier\Thesis data and codes\Oxygen Diffusion\

Appendix D

Ethical Approval Information

D.1 Subject Information

Study: Assessing retinal oxygenation using hyperspectral wave analysis and the effect of hypoxic stress

The aim of this study

To measure retinal blood oxygenation using hyperspectral image analysis during conditions of normoxia and hypoxia (simulated altitude).

Background

Assessing the vascular structure of the retina is a routine procedure conducted during an examination of the eye. Additional information about the vascular health of the eye may be gained by using techniques that analyse the image across a range of wavelengths. The technique known as hyperspectral image analysis has the potential to provide information about the oxygen content of the retinal vessels. There are few if any studies that have been conducted to compare the effects of breathing a hypoxic gas mixture (lower oxygen content) on the oxygen saturation values in the periphery and in the retinal vessels. However, some studies have shown that breathing a hypoxic gas mixture results in vasodilation (relaxation) of the skins' blood vessels and this may have a measurable effect in the retinal circulation. This study aims to measure the effects of hypoxic exposure on oxygen saturation and blood vessel diameter in a healthy population.

What will I do if I take part?

We are looking to recruit healthy male volunteers who can commit themselves to attending the laboratory on 2 separate occasions. During the initial visit a full explanation of the study

will be provided and we will measure your height, weight and blood pressure and heart rate (if these latter measures are too high we are unable to let you participate). We will ask you to sit quietly for a period of 30-40 minutes during which time we will take a series of measurements assessing the oxygen saturation of your blood, the blood flow through at the skin on an arm and the oxygen saturation of the blood vessels or your eye. All the measures are non-invasive, the oxygen saturation of your blood is measured using a simple probe placed over the tip of the finger and the oxygen saturation in the eye is obtained by taking a picture of the back of the eye. Skin blood flow will be obtained using a probe placed on the inner surface of the forearm. During each of the experimental trials we will ask you to breathe through a mouthpiece that provides you with either room air or a reduced amount of oxygen that would be equivalent to going to an altitude of 1500 and 3000m. The total period of time you will be required to breathe the hypoxic gas mixture is 30 minutes. We ask that you refrain from participating in any heavy strenuous exercise, smoking and drinking alcohol 24 hours prior to each test and avoid the consumption of caffeine containing beverages 2 hours prior to each trial.

Are there any risks involved?

There are minimal risks from participating in this study. Some subjects may experience blurred vision or headaches during the hypoxia trial and we will monitor you throughout each trial. Should this occur the trial will be stopped and you will be withdrawn from the study.

If I decide to take part can I later change my mind?

Your participation is voluntary and as such you are free to stop your involvement within this study at any point without giving any reason for doing so.

The information that is obtained during this experiment will be treated as privileged and confidential. It will not be released or revealed to any person without your written consent. However, the information may be used for statistical or scientific purposes with your right to privacy retained.

Thank you for considering taking part in this research which is designed to promote medical and scientific knowledge but may be of no benefit to you personally. Please discuss this information sheet with your family, friends or GP if you wish.

D.2 VOLUNTEER CONSENT FORM

CONSENT BY VOLUNTEER TO PARTICIPATE IN THE FOLLOWING STUDY:

Assessing retinal oxygenation using hyperspectral wave analysis and the effects of hypoxic stress

Name of Volunteer:

Principal Investigator: Dr Andy Harvey

I have read the volunteer information sheet on the above study and have had the opportunity to discuss the details with the principal investigator as named above and ask questions. As such I understand fully what is proposed to be done.

I have agreed to take part in the study as it has been outlined to me, but I understand that I am completely free to withdraw entirely or from any part of the study at any time I wish.

The information that is obtained during this experiment will be treated as privileged and confidential. It will not be released or revealed to any person without your written consent. However, the information may be used for statistical or scientific purposes with your right to privacy retained.

I understand that these trials are part of a research project designed to promote scientific knowledge, which has been approved by the School of Life Sciences Research Ethics Committee, and may be of no benefit to me personally.

I hereby fully and freely consent to participate in the study which has been fully explained to me.

Signature of Volunteer:

Date:

I confirm that I have explained to the volunteer named above, the nature and purpose of the tests to be undertaken.

Signature of Investigator:

Date: